

This work is protected by copyright and other intellectual property rights and duplication or sale of all or part is not permitted, except that material may be duplicated by you for research, private study, criticism/review or educational purposes. Electronic or print copies are for your own personal, non-commercial use and shall not be passed to any other individual. No quotation may be published without proper acknowledgement. For any other use, or to quote extensively from the work, permission must be obtained from the copyright holder/s.



**Architectural elements in fluvial multi-storey
sandbodies: deposition, preservation and
numerical representation**

Andrew James Mitten

Supervisors:

Dr. Stuart M. Clarke

Dr. Jamie K. Pringle

This thesis is submitted in accordance with the requirements of the University of Keele for
the degree of Doctor of Philosophy

31st March 2021

Acknowledgements

First, I would like to thank my family for all of the support that they have provided me in the writing of this thesis. Thank you to my Mum especially for her love, understanding and support that this would not have been possible without. To my Dad, his attitude of “get it done” has really helped me.

The people of the BDRG are thanked for their insightful contributions, support and most importantly friendship. To those of the Utah field team: Charlotte (the lunge) Priddy, David (the grenade) Cousins and Ross (the lettuce) Pettigrew. Louis Howell deserves a special mentioning for being an all-round solid friend and colleague.

I would also like to thank my supervisory team of Stu and Jamie. Without them I would not have learnt what I have or had the opportunity to present this thesis. Further thanks go to all of the people who have collaborated on this research (and show extraordinary patience): John Howell, James Mullins, David Hodgetts, Graham Leslie, Eileen Callaghan, Mike Browne, John Bilton and Sam Kirton.

Finally, I would like to thank Gary Nichols and Stuart Egan for taking the time to review and examine this thesis.

Thank you all!

Abstract

The recoverable proportion of known mobile resources from fluvial multi-storey sandbodies (MSBs) reservoirs is relatively low. The low recovery proportion can be attributed to a lack of a three-dimensional understanding of the reservoir architecture, a lack of consideration of meso-scale heterogeneity, and a lack of geological realism within reservoir models. This thesis considers the architectural nature of unconfined and confined MSBs. The work will: 1) develop an understanding of the main controls upon preservation and deposition of architectural elements within unconfined and confined MSBs and determine key diagnostic features attributed to them. Finally, this work will determine best-practice stochastic reservoir modelling practices for the simulation of unconfined and confined MSBs.

The works presented here use terrestrial photogrammetry, sedimentary logging and palaeohydrodynamic reconstructions from unconfined and confined multi-storey sandbodies to determine key architectural diagnostic criteria. Multi-point statistics, object-based models and sequential indicator simulation are used to determine the most appropriate algorithm to represent the two systems.

Results indicate that unconfined MSBs show complex barform architectures with compound bar formation. This is highlighted by the presence of upstream accretion elements, developed by variable discharge. In confined MSBs large water depths relative to sediment supply indicate that local accommodation is not being filled and that compound bar formation and upstream accretion elements are impeded. It is therefore proposed that unconfined MSBs can be identified by the presence of complex barform geometries and upstream accretion elements, whereas confined MSBs, due to their larger water depths can

be identified by the lack of upstream accretion elements and a lack of correlation between maximum flow depth reconstructions and the thickness of bars. Reservoir model tests suggest that the best method of representing these systems is through the use of three-dimensional multi-point statistics simulations, which provide the most realistic statistical and visual representation of the fluvial environment.

Contents

Acknowledgements	ii
Abstract.....	iii
Figure Contents	ix
Table Contents	xxii
1 Introduction.....	1
1.1 Multi-storey fluvial sandbodies.....	2
1.2 Research aims and objectives	5
1.3 Thesis sign-posting	7
1.3.1 Chapter 2: Literature Review and Scientific Background	7
1.3.2 Chapter 3: The sedimentary architecture of an unconfined fluvial system:example from the Lower Castlegate Sandstone, Utah.....	7
1.3.3 Chapter 4: The sedimentary architecture of a confined fluvial system: example from the Spireslack Sandstone, Scotland.....	8
1.3.4 Chapter 5: Geologically realistic representation of fluvial sedimentary architecture in stochastic reservoir models.....	8
1.3.5 Chapter 6: Discussion	8
1.3.6 Chapter 7: Conclusions	9
1.4 List of Publications.....	9
2 Fluvial sedimentology: a review	10
2.1 Bedforms and facies in fluvial sediments	11
2.2 Bounding surfaces	17
2.3 Sedimentary architecture	21
2.3.1 Unit bars.....	22
2.3.2 Downstream accretion elements.....	25
2.3.3 Lateral accretion elements	27
2.3.4 Compound bars	29
2.3.5 Channel fill elements.....	32
2.4 Plan-view fluvial styles.....	34
2.5 Allogenic controls and products on fluvial strata	39
2.5.1 The graded fluvial profile.....	39
2.5.2 Sequence stratigraphy in fluvial deposits.....	41
2.5.3 Systems tracts of fluvial sequence stratigraphy	43
2.6 Stratigraphic architecture	48
2.7 Summary	51

3	The sedimentary architecture of an unconfined fluvial system: example from the Lower Castlegate Sandstone, Utah.....	52
3.1	Introduction	53
3.2	Geological setting of the Castlegate Sandstone	54
3.2.1	Palaeogeography.....	54
3.2.2	Lithostratigraphy	56
3.3	Methodology.....	60
3.3.1	Terrestrial photogrammetry	63
3.3.2	Photogrammetric data acquisition and processing	65
3.3.3	Barform analysis from photogrammetric data	66
3.3.4	Palaeoflow reconstructions	67
3.4	Architectural elements identified	70
3.4.1	Channel fill elements.....	74
3.4.2	Downstream accretion elements.....	78
3.4.3	Lateral accretion elements	79
3.4.4	Upstream accretion elements.....	80
3.4.5	Overbank elements	81
3.5	Downstream variations Lower Castlegate.....	82
3.5.1	Downstream distribution of facies.....	82
3.5.2	Downstream variations in architecture.....	85
3.5.3	Downstream variations in accretionary element preservation.....	89
3.5.4	Downstream variations in palaeoflow reconstructions	90
3.6	Subsidence rates across the Lower Castlegate Sandstone.....	95
3.6.1	Burial history methodology	95
3.6.2	Burial history results.....	97
3.7	The influence of subsidence rates on fluvial architecture preservation.....	102
3.8	Palaeogeography of the unconfined Lower Castlegate	105
3.9	Discussion.....	109
3.9.1	Implications for reservoir quality.....	110
3.9.2	Implications for sequence stratigraphy	111
3.9.3	Implications for architectural elements in unconfined multi-storey sandbodies	112
3.10	Summary	113
4	The sedimentary architecture of a confined fluvial system: example from the Spireslack Sandstone, Scotland.	115
4.1	Introduction	116

4.2	Geological Setting of the Spireslack Sandstone	117
4.2.1	The Midland Valley, Ayshire, Scotland	118
4.2.2	The Carboniferous succession of the SGP	120
4.3	Methodology.....	127
4.4	The architecture of the Spireslack Sandstone	129
4.4.1	Channel element	136
4.4.2	Lateral accretion element.....	138
4.4.3	Downstream accretion element	139
4.4.4	Chute channel	141
4.4.5	Sheetflood.....	142
4.4.6	Overbank.....	143
4.5	Depositional model	145
4.6	Regional Correlation.....	150
4.6.1	Method of regional correlation	151
4.6.2	Results of regional correlation.....	155
4.7	Evolution of the confined Spireslack Sandstone.....	159
4.8	Discussion.....	163
4.8.1	Confined multi-storey sanbodies	163
4.9	Summary	165
5	Geologically realistic representation of fluvial sedimentary architecture in stochastic reservoir models.....	167
5.1	Introduction	168
5.2	Stochastic reservoir modelling.....	170
5.2.1	Object-based models.....	171
5.2.2	Sequential indicator simulations.....	173
5.2.3	Multi-point statistics.....	177
5.3	Modelling elements.....	180
5.4	Methodology.....	183
5.4.1	Model analysis tests	186
5.5	Two-dimensional training images	187
5.5.1	MPS from a deterministic two-dimensional training image	188
5.5.2	Generating two and a half-dimensional training images	190
5.6	Two-dimensional conditioned reservoir models	197
5.7	Three-dimensional training image	203
5.7.1	Depositional conditioning.....	204
5.7.2	The Jamuna River, northern India.....	205

5.7.3	Constructing a three-dimensional training image	209
5.8	Three-dimensional conditioned reservoir model	214
5.8.1	Object-based models of the Lower Castlegate.....	214
5.8.2	Sequential indicator simulations of the Lower Castlegate.....	217
5.8.3	Multi-point statistics models of the Lower Castlegate based upon a three-dimensional training image.....	218
5.8.4	Static connectivity tests.....	219
5.9	Discussion.....	223
5.9.1	The reproducibility of geologically realistic data	225
5.9.2	Constructing an MPS model for a confined fluvial system	228
5.10	Summary	230
6	Discussion.....	232
6.1	Multi-storey sandbodies	232
6.1.1	Unconfined multi-storey sandbodies	232
6.1.2	Confined multi-storey sandbodies	238
6.1.3	Unconfined and confined multi-storey sandbodies.....	245
6.2	Reservoir modelling of multi-storey sandbodies	247
6.2.1	Training image development for confined multi-storey sandbodies	248
6.3	Study limitations.....	249
7	Conclusions.....	253
7.1	Further work	255
7.1.1	Multi-storey sandbodies.....	255
7.1.2	Reservoir modelling.....	256
7.2	Summary	258
8	References.....	259
	Appendix A – Castlegate facies photoplates.....	286
	Appendix B – Castlegate bounding surface analysis	294
	B.1 - Castle Gate	294
	B.2 - Sunnyside	295
	B.3 - Tuscher Canyon	296
	Appendix C – High Resolution bounding surface analysis.....	297
	C.1 - Bounding surface hierarchy and erosional surfaces – Castle Gate North	297
	C.2 – Bounding surface analysis of the Main Tuscher Canyon Outcrop.....	298

Figure Contents

- Figure 1.1** – Methods of multi-storey sandbody formation (modified from Chamberlin and Hajek 2015). Annotation and formal nomenclature has been taken from Gibling (2006) and Miall (2014). Intra-channel belt processes form MSBs through such mechanisms as aggradation and meandering. Avulsion and reoccupation of topographical lows, compensational avulsion (Bridge and Leeder 1979; Straub et al. 2009), can generate MSBs; finally, lateral confinement, such as topographical confinements like incised valleys, can generate MSBs. Note, nomenclature labels do not suggest that their occurrence is limited to the mechanism of MSB generation they are depicted in. 4
- Figure 2.1** – A hierarchy of Fluvial architectural elements showing the scales at which fluvial systems are studied. The diagram illustrates facies-scale interpretations through to larger scale architectural element construction and the distribution of these elements within a basin fill complex (After Miall 2014). Note the definition used herein of sedimentary and stratigraphic architecture. 11
- Figure 2.2** – Phase diagram for bedforms produced by various grain sizes (mm) and mean flow velocities (cm s^{-1}) within a confined flow 20cm deep and at 10°C. Diagram compiled from in-text property ranges from Southard (1971), Ashley (1990), Leeder (1982; 2011), Hsu (2004) and Collinson et al. (2006). 12
- Figure 2.3** – Schematic representation of ripple formation and downstream migration. A) The formation of eddy currents within the trough between two bedforms, and the sedimentary grains in transport reaching the crest of the bedform. B) The avalanche of these grains down the lee slope of the bedforms and their subsequent downstream accretion (After Collinson et al. 2006; Nichols 2009). 14
- Figure 2.4** – Bounding surface hierarchy within a fluvial system, numbers correlate to the bounding surface hierarchy shown in Table 2.2 and in the text below (modified from Miall 2010). 19
- Figure 2.5** – Unit bar development and their internal structure (After Herbert et al. 2020). A) The migration of dune scale bedforms creating forests, with back-flow ripples from eddy currents forming toeset strata. Topset preserved strata are superimposed ripples and dune forms carrying material onto the lee slope. B) I) Plane foreset development in consistent flow; II) Low angle accretionary development within a unit bar; III) Minor reactivation scours 24
- Figure 2.6** – Examples of schematic representations of downstream accretion elements. A) A generalised schematic of internal architecture and build-up of downstream accretion elements (Miall 1985). B) An example of a preserved downstream accretion element from the Rockcave Member, Yungang Formation, China (Li et al. 2015), possibly also representing a compound barform in the rock record. C) Schematic representation of downstream accretion in Almeida et al. (2016). 26
- Figure 2.7** – A) Schematic representation of lateral accretion elements and their formation. A) An example of the facies distribution within a lateral accretion element. The notable facies here are blues show cross-bedded sands, pinks fine-grained silts and browns represent ripple laminated sandstone facies (After Colombera et al. 2013). B) Lateral accretion element from the Brahmaputra River. Note the oblique migration of 28

dune-scale bedforms on the margin of the element and the upstream accretion present on the upstream portion of the bar (Bristow 1995).

Figure 2.8 – A) Schematic representation of compound barform growth from the Torredonian Applecross Formation, Scotland (Ghinassi and Ielpi 2018), showing the complex interaction of lateral accretion elements and downstream accretion elements (much like in Figure 2.5B) around a central parent core unit bar. The image also provides evidence of upstream accretion on the upstream margin of the southernmost barform, similar to that shown in Figure 2.6B. B) Fence diagram of a GPR survey taken from the Jamuna River (Best et al. 2003). The barform is dominated (on the downstream section) by downstream accreting cosets of cross-bedding. The flanks of the element are dominated by lateral accretion and the tops by upstream and vertical accretion strata. C) Examples of compound and unit bar development from the South Saskatchewan River (Ashworth et al. 2011). 30

Figure 2.9 – A) Channel fill deposits from the Yungang Formation (Li et al. 2015). B) Schematic representations of channel fills in fluvial deposits (Miall 1985; Ghazi and Mountney 2009). C) Quarry face showing channel fill elements with both gradational and erosional tops, example from the Upper Triassic Stubensanstein, Germany (Honrung and Aigner 1999). 33

Figure 2.10 – A) Schematic representation of a braided river, example from the Sherwood Sandstone of the UK midlands (After Wakefield et al. 2015). B) Aerial image of the Jamuna River, northern India taken from Google Earth showing the multiple active channels and complex compound architecture formation associated with braided fluvial deposits. C) Panel section of an outcrop from the Yungang Formation, China, showing complex channel stacking and avulsions, with the presence of compound and unit barforms (Li et al. 2015). 36

Figure 2.11 – A) Schematic representation of perennial meandering fluvial system (After Miall 1996). B) Digital elevation model from the Allier River, France (Viero et al. 2018). Image shows multiple meanders and point bar deposits and how the fluvial system has migrated across its channel reach. C) A seismic amplitude stratigraphic slice through the McMurray Formation (Hubbard et al. 2011). Image highlights the complex nature of meander belts and shows the dominance of lateral accretion point bar elements. D) Outcrop panel interpretation of the Dinosaur Park Formation (Durkin et al. 2017). Image highlights the inclined internal bounding surface framework of point bar deposits and the heterolithic nature of their facies assemblages. 38

Figure 2.12 – Simplified model of downstream variations in plan-view fluvial style proximal of the fluvial marine transition zone (FMTZ), where marine base-level becomes the dominant allogenic control upon deposition (After Li et al. 2015). This margin is known as the buttress of the fluvial system. The gradient associated with fluvial systems and the graded profile is highlighted in red showing the buffer and preservation space associated with fluvial deposition (After Holbrook et al. 2006, Li et al. 2015). Basin-scale allogenic controls extensional and foreland basin controls on accommodation space and their spatial distribution through a basin. Note the “y-axis” indicates the relative proportion of a control’s influence at a point in the basin (After Catuneanu 2006). 41

Figure 2.13 – Fluvial stratigraphic architectures across the four traditional systems tracts. The falling stage systems tract creates erosional down-cutting forming valley fill; lowstand systems tract material shows incised valley fill of stacked channels; the transgressive systems tract consists of overbank deposition (brown) and tidally influenced isolated channels (yellow); finally, the highstand systems tract showing 47

stacked channel complexes over a wider spatial distribution. Note: the main black line at the base of each image is the incised valley and sequence boundary, to the right of each image is the position of the systems tract superimposed in red upon a eustatic sea level curve, HST – highstand systems tract, LST – lowstand systems tract (After Shanley & McCabe 1993; Cantuneanu 2006).

Figure 2.14 – The distributary fluvial system (DFS). A) Schematic representation of a DFS running from an apex down onto the alluvial plain within the basin. The schematic highlights the radial abandonment and activation of channel reaches (or tracts) across the fan-like system. Proximal medial and distal zones are highlighted and progradation of these is shown. Approximate architectural make-ups of the DFS are shown in the table, representing channel stacking and overbank preservation for each zone. Estimations of the proportion of architectures found within each zone are also included (modified from Nichols and Fisher 2007; Owen et al. 2015, 2017). B) The northern Quilian Mountains DFS from China is shown and annotated according to its zonations shown in A (modified from Hartley et al. 2010).

50

Figure 3.1 - Lithostratigraphic and chronostratigraphic context of the Campanian Lower Castlegate Sandstone MSB, Utah. (A) A geological map of the Book Cliffs in the area between Price and Green River (modified from Watkind 1995), showing the distribution of the Mesaverde Group outcrops. (B) A palaeogeographic reconstruction of the Sevier Orogeny and sediment supply pathway (red arrows), feeding the Western Interior Seaway (WIS) that spanned across North America (modified from Van de Graff, 1972; Chan and Pfaff, 1991). (C) Generalised vertical section detailing the lithostratigraphic make-up of the Upper Cretaceous and Lower Paleogene of the study area, west and east of Green River (modified from Pitman et al., 1987; Seymour and Fielding, 2013; Burns et al., 2017).

57

Figure 3.2 – A) Correlation of the study area (modified from Pattinson 2018). Showing the parasequence stacking of the Blackhawk Formation and its intertonguing with the distal marine shales of the Mancos Shale. The fluvial deposits highlighted on the correlation comprise the Castlegate Sandstone. The top Grassy Member of the Blackhawk Formation is used as a datum. Locations on the correlation are from Pattinson (2018; Figure 4), localities used in this study are highlighted in red. B) Correlation of sea-level variation to the sediments of the Mesaverde Group (modified from Howell et al. 2018), correlations of the lithostratigraphy presented in Figure 3.1C matched to the rate of sea-level change and the height of Campanian sea-level above the present day sea-level. C) Fluvial channel mixing and flow contamination pathways based upon provenance analysis (modified from Pettit et al. 2019). Note, not to scale.

60

Figure 3.3 - (A) Location of the wells (red) and outcrops (yellow) (GoogleEarth image acquired on 12/31/2016) (B) Data collection map from the proximal Castle Gate study site (GoogleEarth image acquired on 10/16/2013). (C) Data collection map from the medial Sunnyside study site (GoogleEarth image acquired on 08/08/2015). (D) Data collection map from the distal Tuscher Canyon study site (GoogleEarth image acquired on 07/28/2015). Note, key in Figure 3.3A applies to all.

61

Figure 3.4 – The photogrammetry method. A) Workflow for implementing structure from motion from field photos (modified from Bemis et al. 2014). Black arrows indicate workflow pathways, red arrows indicate the position of the created model relative to the workflow. Images on the right show the Castle Gate north outcrop model created using structure from motion the, and demonstrate stages in the process. B) Schematic of the overlap required for generating photogrammetric models (modified from Bemis et al. 2014), showing the ideal overlap required to

64

construct photogrammetric models and how it enables the rugosity of the outcrop to be imaged.

Figure 3.5 - A) Digital dense point cloud data from the outcrop dataset. Note: the outcrop overview shows the study location Tuscher Canyon. B) and C) show sedimentary dip and azimuth measurements (coloured surfaces) on the digital surface within the VRGS software (see text). D) Bounding surface analysis on the digitally-textured mesh surface. 66

Figure 3.6 – Plan form examples of sinuosity reconstruction. A) Schematic of Bridge et al. (2000) reconstruction method of a sine-generated meander. See text for details. B) La Roux (1992; Figure 3) Showing the assumption of sinuosity as a function of the deviation of individual palaeocurrents from a local mean or valley axis. See text for details. 68

Figure 3.7 – Field collected sedimentary log through the Lower Castle Gate, collected from the Castle Gate type locality. 72

Figure 3.8 - Facies photoplate from the Lower Castlegate, Utah. (A) Two sets of asymmetrical ripple laminated sandstone from the Castle Gate log at approximately 52 m, pen for scale. (B) Large trough crossbedded sandstone sets showing downlapping onto basal channel surface, highlighted is a pencil for scale. Clast moulds can be seen along the set surfaces. Image is taken from the Castle Gate log at approximately 33 m. (C) Smaller scale trough cross-bedded sets from Horse Canyon log at approximately 31 m. (D) Asymmetrical channel fill from the Castle Gate log at approximately 36 m. (E) Planar cross-bedded sandstone from 9-Mile Canyon log at approximately 28 m. At the base of the cross bedded facies an erosional base has been interpreted overlying fine-grained material, this erosive surface is overlain by a minor channel lag consisting of small extra- and intra-formational clast material. (F) Horizontally laminated sandstone erosionaly overlain by trough crossbedded sandstone from Tuscher Canyon log, at approximately 5 m. (G) Structureless structureless sandstone with some rip-up clasts, comprised of siltstone that have been deformed due to compaction. Photo is from the Castle Gate log at approximately 18 m. (H) Fine grained siltstones and structureless sandstones in the overbank succession of the Castle Gate log, from approximately 15 m. 75

Figure 3.9- The genetic units of the most common sedimentary facies found within the Castlegate Sandstone. The numbers indicate bounding surfaces hierarchy (Miall, 1985). A) Representative section of the bounding surface framework within the Lower Castlegate at Tuscher Canyon, and bounding surface hierarchy interpreted from that framework. B) Sandstone (St) facies showing pebble-lined foreset and set surfaces stacking below and above a third-order erosional scour surface. C) Third-order erosional surfaces bounding conformable packages of St and Sm facies. D) Sm facies within third-order scours (see Table 3.1 for facies codes). 76

Figure 3.10 - Field-obtained sedimentary logs and mean palaeocurrent directions of architectures collected in the field for each study locality. Logs are ordered (left to right) from west to east, highlighting the thickness variations observed across the Lower Castlegate Sandstone. A stacked bar graph of facies proportions is shown, proportions are obtained from the vertical thickness of the facies in the logs shown. A graph of erosional surfaces shows the number of erosional surfaces per metre, for each logged locality, and the number of channel bases per metre preserved across the Castlegate. This highlights the lack of preservation of in channel material towards the more distal portion of the basin. 83

- Figure 3.11** - The abundance of architectural elements across the three photogrammetric datasets across the Book Cliffs derived from the photogrammetric analysis of the proximal (Castle Gate), medial (Sunnyside) and distal (Tuscher Canyon) sections. 85
- Figure 3.12** - Outcrop interpretation images with (inset) location map, with palaeocurrent data and n values of individual elements (15° bins). (A) Castle Gate north outcrop (509831, 4400284) from McLaurin and Steel (2007) showing the proximal section of the Castlegate MSB. (B) Sunnyside west outcrop (553925, 4379887) for the medial section. (C) Tuscher Canyon south (584290, 4327974), note mid-sized SUV for scale (highlighted). (D) Inset map showing the locations of the outcrops and the Book Cliffs classic outcrop outline in Figure 3.3. For more detailed analysis of photogrammetry please refer to Appendix B and C. 85
- Figure 3.13** - (A) Scatter log-log plot showing the relationship of corrected width to thickness for each of the major constituent architectural elements within the Lower Castlegate Sandstone. (B) The corrected width against thickness for each of the major constituent architectural elements of the Lower Castlegate, shown as data envelopes (Gibling, 2006) highlighting the area in which corrected widths and thicknesses will occur. (C) Mean complete and partial element thickness for each field site relative to the palaeo-coastline. (D) Mean complete and partial element widths for each field site relative to the palaeo-coastline. (E) Mean complete and partial element width:thickness ratio for each field site relative to the palaeo-coastline. 87
- Figure 3.14** - Three preserved barforms from the Lower Castlegate Sandstone in the studied log sections. The images show a downstream accretion barform and to the right there is an interpretation of the bounding surface nature for each barform, along with a rough quantification of erosional surfaces against clinof orm top (Hajek and Heller, 2012) to highlight the degree of barform preservation. 89
- Figure 3.15** - Reconstructed flow depths from set thicknesses in each VOM locality. (A) The Castle Gate locality, showing mean maximum flow depth of each element relative to a single set thickness measurement. The green dashed line represents where data from one outcrop ends and another begins. Each element has been assigned a number; the numbers assigned to elements increase upsection (elements 1-7 make up the northern outcrop, 8-16 make up the type locality). Histograms based on the probability density of set thicknesses are provided with the cumulative frequency (%), (orange). (B) The Sunnyside locality (elements 1-9 make up the western outcrop, 10-19 make up the eastern), showing mean maximum flow depth of each element relative to a single set thickness measurement. (C) The Tuscher Canyon locality (elements 1-12 make up the northern outcrop, 13-21 make up the southern), showing mean maximum flow depth of each element relative to a single set thickness measurement. (D) The mean maximum reconstructed flow depths of each locality plotted with the coefficient of variance (secondary y-axis) of those means as a proxy of variable maximum flow depths. 90
- Figure 3.16** – Plots of palaeocurrent vector magnitude and circular standard deviation (modified from Curray 1956). Plot shows channel only and total palaeocurrent data results from each locality. 92
- Figure 3.17** - Palaeocurrent summary of the Lower Castlegate MSB, divided by architectural elements at each location. Note, n = number of measured forests, v_m = mean azimuth, r = dispersion as a percent, sn = sinuosity value. Note, 15° bin size. 93

Figure 3.18 - Information used in the creation of the burial history plots. Thicknesses of the overburden and environment of deposition have been taken from Pitman et al. (1987), Olsen et al. (1995), Miall and Arush (2001), Aschoff and Steel, 2011a,b) and Seymour and Fielding (2013). 95

Figure 3.19 - Gamma ray correlations of the Mesaverde Group to the top of the Lower Castlegate (correlation datum; (based upon Hampson et al. 2005). Inset map shows the outline of the Book Cliffs and the profile of the log transect represented in the correlation. Correlation plot shows the thinning of the Lower Castlegate moving distally in the basin (eastwards from Green River). Numbers of well locations are: 1 = Matt's Summit State A1, 2 = Shimmin Trust 10-11, 3 = Shimmin Trust 2, 4 = Slemaker A1, 5 = Iriart Fee 1, 6 = Keel Ranch 1-16, 7 = Stone Cabin 1, 8 = Wilcox 1-24, 9 = Butler Canyon Unit USA 33-12 and 10 = Rattlesnake Canyon 2-12 respectively. Note, abbreviations of formation tops are as follows: SC = Spring Canyon, A = Aberdeen Member, K = Kenilworth Member, and BH = Blackhawk Formation undivided. 99

Figure 3.20 - Burial history analysis of the Lower Castlegate Sandstone, Utah. (A) Thickness map from the down-hole logs from Figure 11. Subsidence rate map based upon burial history from down-hole formation thicknesses. (B) One dimensional burial history curves for four of the wells. (C) Subsidence rate for each down-hole log based upon their respective burial history analysis, plotted relative to the well positions across the basin (Figure 12). Numbers of well locations are: 1 = Matt's Summit State A1, 2 = Shimmin Trust 10-11, 3 = Shimmin Trust 2, 4 = Slemaker A1, 5 = Iriart Fee 1, 6 = Keel Ranch 1-16, 7 = Stone Cabin 1, 8 = Wilcox 1-24, 9 = Butler Canyon Unit USA 33-12 and 10 = Rattlesnake Canyon 2-12. 100

Figure 3.21 - Summary figure of the Lower Castlegate Sandstone MSB. Image is comprised of a cross-sectional view of the Western Interior Seaway during the Lower Castlegate deposition and higher resolution view of the profile within the fluvial profile. Descriptive interpretations of the fluvial strata and architectural elements making the idealised profile are highlighted, relative to their position downstream. This assumes constant avulsion frequency. A top-down view is also given showing the relative size and complexity of the channel and barform architecture within the Castlegate MSB. Finally, a brief summary of the critical changes observed downstream are highlighted and their controls stated. 103

Figure 3.22 – Palaeogeographic plan view reconstruction of the Lower Castlegate Formation. Showing stream capture of DFS-like run-off systems from the Sevier Orogeny and the more mature Mogollon Highlands fluvial system. Note, not to scale. 107

Figure 4.1 - The ENE-WSW striking Midland Valley Graben, Scotland (after Ellen et al. 2019). Bound to the north by the Highlands Boundary Fault and to the south by the Southern Uplands Fault. The location of the SGP coal mine is indicated by the labelled triangle. 116

Figure 4.2 - The Carboniferous stratigraphic framework for the Midland Valley of Scotland, showing the International and British chronostratigraphic subdivisions. The lithostratigraphic subdivisions of the Clackmannan Group and their associated informal unit subdivisions of the SGP succession (Modified from Ellen et al. 2019; Howell et al. 2019) are shown on the right of the Midland Valley lithostratigraphic column. The GVS also shows a eustatic sea-level curve for the Serpukovian (Haq et al. 2008), referenced to the present day sea-level. 120

Figure 4.3 – Map of the central Midland Valley, highlighting the Serpukovian strata exposed in the region and the location of the SGP site geological map. A) Regional 124

geological map and Google Earth Image showing the area surrounding the SGP field site. B) Geological map of the yellow boxed area shown in (A). Black box highlights the exposure of the studied area and the location of figure 4.5. C) Inset map showing the location of the central Midland Valley map relative to Scotland.

Figure 4.4 - Ortho-rectified image from a photogrammetric survey of the Main Void High Wall, with an accompanying interpretation panel (Modified from Ellen et al. 2019). The succession clearly shows several thick sandstone units and an obvious cyclic succession of mudstone, sand, limestone and coal. There are several faults that cut through the High Wall at a normal to oblique angle. These faults are mapped in Figure 4.3A, and are strike-slip in nature. Two Palaeogene? basaltic dykes cut through the succession on the south western side of the High Wall. Below the High Wall image is an interpreted image showing the pick of an unnamed sandstone that forms a major component of the Hosie Cyclothem, and is consistent with the sandstones above the 9ft Coal. Conformably overlying the mudstone? above the unnamed sandstone is the Index Limestone (2-4m). Erosionally down-cutting into the mudstones at the base of the Index Cyclothem is the Spireslack Sandstone, indicated by the pale sandy colour illustrated in Figure 4.2. 125

Figure 4.5 – Study location highlighting the location of the four major outcrops in the SGP area and the location of data collection. A) DEM and ordnance survey map (OS MasterMap 2019) with annotations of SGP mined faces and borehole locations, along with highlighted (black square) outline of arial image. B) Aerial image of the Main Void and B1 Face, photogrammetry collection paths and GPS locations have been marked on the image (Bing Maps 2015). 127

Figure 4.6 - Sedimentary log data of the Spireslack Sandstone collected from the exposure adjacent to the Main Void High Wall shown in Figure 4.5B (from Ellen et al. 2019). 131

Figure 4.7 – Photoplate highlighting the various facies of the Spireslack Sandstone and overlying succession. A) Planar crossbedded sandstone with heavily cleaved siltstone and coal, cleavage is inherited from syn-sedimentary movement sinistral faults. B) Close up of trough crossbedded sandstone facies highlighting its coarse and sub-subangular nature. Black flecks in here are intraformational coals. C) Poor preservation of trough cross bedded facies in base of image, with overlying set showing better preservation and exposure of cross bedded sandstone facies. Scale bar is in centimetres. D) Transition from planar bedded sandstones to planar laminated to structureless sandstones over 30 cm. This is as a result of increasingly reducing water depth, transitioning through the lower flow regime towards the higher end of the lower flow regime, see text for further description. E) Inclined heterolithics of structureless bioturbated sandstone and siltstone couplets. F) Spireslack Sandstone trough cross bedded sandstone strata, typical of the unit. G) Bioturbated sandstone at the top of the inclined heterolithic section. Top of the image shows the top of the Spireslack Sandstone with a locally correlatable siltstone 132

Figure 4.8 - Ortho-rectified projection of the photogrammetric dataset collected from the B1 Face. The data shown is for the fluvial portion of the Spireslack Sandstone, the top two images are interpreted below. The image shows two distinct channel sets with one eroding down into the other preserving distinctly more cut-and-fill channel elements than the previous bar-form dominated channel set (Ellen et al. 2019). Note, there is some syn-sedimentary faulting cutting obliquely through the outcrop. 134

Figure 4.9 – Schematic three-dimensional representations of the six architectural elements that make-up the Spireslack Sandstone. The channel element can be seen to erode through overbank material transporting bedload dominated material downstream in a north-western direction, as dunes and gravel lag deposits. Preserving trough cross-bedding and conglomerate lenses within erosional channel scour surfaces. Downstream accretion elements show trough cross bedded sandstones built into sets and cosets with major slip faces and reactivation surfaces punctuating. Chute channels can be seen to erode into the top of barforms at periods of peak discharge, these show little internal architecture. Lateral accretion elements are commonly developed on the flanks of such mid-channel bars and contain inclined draped sandstone strata. The final model shows the overbank hosted elements such as sheet flood and overbank elements which are composed of fine grained, clay rich sedimentation, along with abundant coal formation indicating a perennially high water table.	143
Figure 4.60 – Images from the B1 Face showing how the Spireslack Sandstone’s stratigraphic architecture lies within the context of the outcrop and the rest of the Upper Limestone Formation. A) The fluvial portion of the Spireslack Sandstone lies at the base of the outcrop, with a large inclined heterolithic architecture above it and finally the remaining outcrop overlying this is the marine portion of the Upper Limestone Formation. Note people for scale and the location of images 4.10b and c have been located with reference to the rest of the outcrop. B) Planar erosional base of the fluvial Spireslack Sandstone which is subsequently eroded by a second smaller scale erosion and the deposition of a second channel set. Channel set 2 shows onlapping set surfaces helping to pick out the second channel set. The top of the fluvial portion is picked by the downlapping of the inclined heterolithic clinofolds from the above architecture. C) Complex trough crossbedded sandstone set and coset scale architecture characterising the bar development of the homogeneous channel set 1 in the fluvial Spireslack Sandstone.	147
Figure 4.71 - Schematic representation of the two channel sets of the Spireslack Sandstone. The lower channel set shows limited bedform development and a much higher energy flow, the upper channel set is characterised by bedform development and bar-form growth (Ellen et al. 2019).	149
Figure 4.12 – Borehole map of the central Midland Valley with inset map showing where the outlined area lies in the Midland Valley of Scotland (Ordinance survey, 2002). All boreholes have been aligned to a correlation line. For details of each borehole see Table 4.3.	151
Figure 4.13 - Generalized vertical sections take from the SGP log sites (Ellen et al. 2019). All sections are aligned to the top Index Limestone datum, highlighting the differences in thickness and occurrence of the fluvial channel sets of the Spireslack Sandstone. The incision of these channels indicates that the valley is orientated north-west to south-east.	152
Figure 4.14 – Examples of two sets of borehole data used in the correlation of the Spireslack Sandstone, Grasshill 24 (left) and Annfield 2 (right). Logs show notes from chippings and the major correlated limestone and coal units within the area.	153
Figure 4.85 – Borehole correlation panel of the central Midland Valley. Panel has been referenced to the Index Limestone, a laterally correlatable, conformable unit across the Midland Valley Basin. Key stratigraphic units have been picked (Table 5.3) to show how the Spireslack Sandstone thins to the	157

south west. This south east thinning trend shows the unit pinching out as the fluvial strata are juxtaposed against the paralic portion of the Upper Limestone Formation. Inset map shows where the correlation line lies relative to the rest of the Scotland. Thickness inset map shows the lateral variation in the thickness of the Spireslack Sandstone, and how it thickens dramatically towards the Douglas 1 well, and then thins again to the north east.

Figure 4.96 – Evolution of the Spireslack Sandstone stratigraphic architecture as a result of relative sea-level fall and the position of each schematic image relative to a eustatic and relative (assuming linear subsidence and sediment input rate) sea level curves. A) Highstand deposition of coastal plain facies and distributary channels, during normal regression. B) Initial stages of forced regression, moderate base level fall producing slowly changing fluvial gradients forming wide incision. C) Final phase of forced regression, steep fluvial gradients generated by the more rapid change in base level form concentrated incision and the formation of an incised valley. D) Initial early lowstand normal regression backfilling phase of the valley, Spireslack Sandstone channel set one and two. E) Late lowstand high sinuosity incised valley fill formed by moderate backstepping of the fluvial system as normal regression transitions into transgression. 159

Figure 5.1 – The scales of typical fluvial reservoir heterogeneity (modified from Tyler and Finley, 1991; Morad et al., 2010). Note the 1 m - 10 m meso-scale of this study: zonation of permeability is within genetic units (Morad et al., 2010; Mitten et al., 2018). In giga- to meso-scale, the yellow indicates sandstone and the grey mud and siltstone, the red lines indicate faulting. In the micro-scale image, the black and grey represent quartz grains and the light blue indicates pore space. 168

Figure 5.2 – Object-based model example generated in Schlumberger Petrel v.2016 software, illustrating discrete geobody reproduction within a background facies. The objects inputted in this example are channels with two different dimensions, the pink and the blue. These have an inputted sinuosity to them, highlighted by the pink channels. The channels are added into a green (in this case floodplain) facies. 171

Figure 5.3 – Example of a semi-variogram showing the nugget, range and sill with associated axis (Ringrose and Bentley 2015). The sill indicates total variance, the range is the distance or lag when the sill is achieved and the nugget represents sub-lag distance variance 173

Figure 5.4 – Examples of unconditional sequential indicator simulations based upon variable variogram attributes, generated in Schlumberger Petrel v.2016 software. A) A large range variogram yields large geobodies. B) A smaller range produces smaller geobodies. C) A large nugget, representing sub-model scale heterogeneity, shows non-discrete geobody boundaries, a common effect of gradational transitions between sedimentary bodies. 175

Figure 5.5 - Example of MPS SNESIM algorithm and what the search tree obtains A) Shows a simple block two-dimensional training image, with three types of data. B) A training image of channelised sandstones in a mudstone background facies used to borrow data events from. A simulation grid with conditioning data showing the predetermined facies at those give node locations. Finally, the output of the SNESIM algorithm. Where channel sands have been projected between conditioning node points (Modified from Strebelle and Cavelius 2013). C) The use of Communian (2012) method of probability projection, using z-axis coordinate based probabilities to project 177

outcrops into three-dimensions. The lower four images show gridded models based upon differing probability weightings between the two outcrops.

Figure 5.6 – Complete interpretation of the Lower Castlegate Tuscher Canyon outcrop, Utah, USA (see Figure 3.3D for location). Schematic shows the distribution of architectural elements and dominance of the downstream accretion element. Pseudo-well logs have also been incorporated to show positions of wells used to condition reservoir models. Measured palaeocurrent data (respective positions marked) of individual sedimentary architectural elements are also shown. Note the 2.5x vertical exaggeration. 181

Figure 5.7 – Indicator variograms (coloured lines) showing the variance of the four architectural elements (DA = Downstream accretion element; CH = Channel element; LA = Lateral accretion element; TB = Thalweg bedform complex) across both data sets, providing input conditions for the SIS model iterations. Respective experimental variograms (black lines) are also shown, see text for details. 184

Figure 5.8 – Digitally painted two-dimensional training image of Tuscher Canyon, Utah, USA, for multi-point statistics simulations. This is a painted grid (using the 1 x 10 x 0.5 m cell size) of the interpreted Tusher Canyon outcrop seen in Figure 5.6. 187

Figure 5.8 – Test product of two-dimensional training image used in the production of three-dimensional multi-point statistics generated in Schlumberger Petrel v.2016 software, see text for details. 189

Figure 5.9 – Smoothed digital surfaces showing the relative proportions of the Downstream accretion element (DA) across the three model zones. 191

Figure 5.10 – Smoothed digital surfaces showing the relative proportions of channel element (CH) and thalweg bedform complex (TB) element across the three model zones. 192

Figure 5.11 – Smoothed digital surfaces showing the relative proportions of lateral accretion (LA) element across the three model zones. 193

Figure 5.12 – Histogram showing the trend data for each modelled element (see key) across all model zones showing into a normal Gaussian distribution. The x-axis shows gaussian transformed values for the relative proportions of elements across the trended surface. The y-axis, N, is the frequency of those values. Notice the values are now in a stationary gaussian space enabling the use of kriging. The legend shows the elements plotted on the histogram. 194

Figure 5.13 – Kriged trend models using the probability surfaces shown in figures 5.9, 5.10 and 5.11. A) Trend across zones for DA element. B) Trends across zones for CH and TB. C) Trends across zones for LA. 195

Figure 5.14 – Resulting multi-point statistics two and a half-dimensional training image developed from the original two-dimensional training image and the trended volumes shown in Figure 5. 196

Figure 5.15 – A) MPS-generated, three-dimensional reservoir model developed from the two and a half-dimensional training image. B) SIS generated three-dimensional reservoir model developed from the variograms taken from Tuscher Canyon dataset, Utah, USA, generated in Schlumberger Petrel v.2016 software. 199

Figure 5.16 - Summary model statistics derived from the two-dimensional summaries of the reservoir models generated using each iteration of both algorithms. A) The relative proportions of each architectural element modelled within the reservoir 201

model algorithms. The pink line highlights the model input data derived from the sedimentary analysis. B) Mean element thicknesses for each element plotted against the covariance (Cv) of each element, to highlight the thickness and dispersion in thickness across each element. C) Maximum element thickness plot for each model iteration in each algorithm to show how overestimations of vertical connectivity were affected by the choice of algorithm. Note, the depositional conditioning input means are indicated on the graph showing where the input data and training image values plot.

Figure 5.17 - Drainable volumes and vertical connectivity statistics from all thirty model iterations across the three algorithms of the generated reservoir models. A) Drainable percentage volume box-plots of the SIS- and MPS-generated models, showing the variance in results across the ten iterations of SIS-generated reservoir volumes and a narrow variance in MPS-generated iterations. B) Maximum, mean and standard deviation of the vertical thickness of net connectivity across all iterations of MPS- and SIS-generations. 203

Figure 5.18 – A) Study site location map of the Jamuna River, northern India and B) close-up of the study area (box), modified from Mitten et al. (2018). 206

Figure 5.19 – A) The Jamuna downstream accreting barform in northern India (see Figure 3 for location), annotated with width and length measurements of active and abandoned fluvial sedimentary architectures. B) Interpretive line drawing (see key and text) – note colours are the same as for the Tuscher Canyon outcrop (Figure 5.6). C) Box plots of the width, D) length and E) width:length ratio of sedimentary architectural elements within the interpreted Jamuna River barform complex (CH = Channel element, TB = Thalweg bedform complex, DA = Downstream accretion element, LA = Lateral accretion element). Note the maximum measurements of the downstream accretion element exceeds the scope of the graph. 208

Figure 5.20 – Numerical depositionally-conditioned 3D training image used in this study, created within Schlumberger™ Petrel v.2016 software, using the input parameters given in Table 5.2. The training image is 1,000 m x 1,000 m x 20 m at a cell resolution of 10 m x 10 m x 0.5 m. The datasets providing the major conditions for the planes are marked. The image provides the basis for the MPS model generation (see text). 211

Figure 5.21 - Comparison of (A) Multi-point statistics (MPS)-, (B) sequential indicator simulation (SIS)-generated and (C) Object-based (OBM) reservoir models as whole models and in cross-sections. Models were generated using the same input parameters derived from the outcrop and modern studies (see text for details). A) MPS model generated from the training image shown in figure 5.20. This evidences thin and laterally restricted baffles, individual plan-view downstream accretion elements that showed some recognisable geometries and thin and fragmented net connectivity in cross section. B) SIS model generated from the variograms (see text). Model shows large and connected net reservoir and thick laterally extensive amalgamations of non-net baffle heterogeneity. C) OBM models generated from the quantitative statistics extracted to make the depositional conditioning rules. Model shows an over-connected net reservoir and thicker preserved channel elements. Note, all models have a 20x vertical exaggeration. 215

Figure 5.22 – Summary model statistics derived from the three-dimensional summaries of the reservoir models generated using each iteration of the three algorithms. A) The relative proportions of each architectural element modelled 216

within the reservoir model algorithms. The pink line highlights the model input data derived from the sedimentary analysis. B) Mean element thicknesses for each element plotted against the covariance (Cv) of each element, to highlight the thickness and dispersion in thickness across each element. C) Maximum element thickness plot for each model iteration in each algorithm to show how overestimations of vertical connectivity were affected by the choice of algorithm. Note, the depositional conditioning input means are indicated on the graph showing where the input data and training image values plot.

Figure 5.23 – Drainable volumes and vertical connectivity statistics from all thirty model iterations across the three algorithms. A) Drainable percentage volume box-plots of the SIS-, MPS- and OBM-generated models, showing the variance in results across the ten iterations of SIS-generated reservoir volumes and a narrow variance in MPS-generated and OBM-generated iterations. B) Maximum, mean and standard deviation of the vertical thickness of net connectivity across all iterations of MPS-, SIS- and OBM-generations. OBM and SIS show a maximum thickness equal to that of the entire model, whereas MPS shows a maximum connectivity thickness of 18. The standard deviations of the SIS and OBM models also showed a high variance, whereas the MPS showed less of a variation away from the mean. 222

Figure 5.24 – Generalised workflow of this study to generate the reservoir models. Note, SIS = Sequential Indicator Simulation, MPS = Multi-Point Statistics, OBM = Object-based Modelling. 224

Figure 5.25 – The B1 Face of the Spireslack Sandstone, as interpreted in Figure 4.8 and associated multi-zonal MPS model. Note model is 400 m wide with a cell resolution of 10 m, complete model shown on the right and intersection model at the bottom (20 x vertical exaggeration).

Figure 6.1 – Examples of modern fluvial systems that show both distributary and tributary morphologies, at differing scales. A) The Rio Senguerr fluvial system, Argentina. The system shows a distinct distributive pattern from the eastern Andean margin; however, stream capture is evident on three occasions, at the fan margin, with drainage from either side of the fan, and finally, with the large basin feeding north-south fluvial system. The Rio Senguerr fluvial system may then be considered both distributive and tributary. B) The Jamuna River, Bhutan and northern India, on the southern Himalayan margin. Note the yellow box location for C. C) Smaller scale view of the Jamuna River in B. This portion of the Jamuna River shows a much larger fluvial system than in A, presenting similar traits in a vastly different climatic regime. Mountain elongate run-off fans are intersected at their toes by the major axial system, fitting to the DFS model well. However, as is clear in B, the larger scale plan-view of the Jamuna is tributary. 234

Figure 6.2 – A) Northern Quilian Mountains DFS, China from Hartley et al. (2010) and figure 2.15. Showing the locations of higher resolution channel belt images from B, C, and D. The transect of elevation profile in E is shown. Topographic transects of proximal, medial and distal fan zones are also shown. This shows steeper topographic relief on the margins of the fluvial system in the proximal zone. B) High resolution image of proximal DFS zone channel belt showing channel cut-and-fill elements and unit bars. C) High resolution image of medial DFS zone channel belt showing channel cut-and-fill elements, unit bars and some compound barform deposition. D) High resolution image of distal DFS zone channel belt showing channel cut-and-fill elements, unit bars and compound bars. E) Topographic profile from proximal (left) to distal (right) of the northern Quilian Mountain DFS. F) High resolution topographic profile 237

through the proximal zone. G) High resolution topographic profile through the medial zone. H) High resolution topographic profile through the distal zone. I) Channel belt widths displaying the typical DFS profile of decreasing widths in the distal direction. J) Architectural element widths from the proximal medial and distal zones. Green indicates unit bar, blue indicates channel cut-and-fill elements, red indicates compound barforms. Note, line indicates mean and dot raw data value. K) Element proportions for proximal, medial and distal fan zones. Colours are as indicated for J.

Figure 6.3 – Jamuna River, northern India, showing a confined morphology with submerged unit bars and a large amount of sediment deposited distal of the confinement. 240

Figure 6.4 – Cross-bedding thickness data from Wang et al. (2020). A) Histogram of cross-bed thicknesses from the Spireslack Sandstone (Modified from Wang et al. 2020). B) Plot showing the coefficient of variation from cross-set thicknesses from the Spireslack Sandstone (red dot) relative to other incised valley fill successions (blue dots). The line for a variability dominated succession is also highlighted. 241

Figure 6.5 – Data from the Fell Sandstone taken from Howell et al. (2019). The logged sections show proximal (left) to distal (right) variations in sedimentation. Palaeocurrent data show the significant divergence of the fluvial system around the Cheviot High at Bowden Doors. Maximum reconstructed flow depths and channel thicknesses plotted with relative distance downstream. Finally, a small schematic example of the plan view evolution of the Fell Sandstone fluvial system (Modified from Howell et al. 2019). 244

Figure 6.5 - Total optical porosity measurements, derived using JPor (Grove and Jerram 2011), taken from samples collected from the Lower Castlegate data set. Total optical porosity is in two-dimensions and is plotted as all locations based upon the architectural element. 248

Table Contents

Table 2.1 – Facies scheme for fluvial deposits from Miall (1978; 2010), Highlighting the large number of facies and processes that make-up and deposit fluvial strata.	16
Table 2.2 – Bounding surface hierarchical scheme, showing their magnitude in time, the process that formed them, the depositional product of those processes and their order within the hierarchy (Adapted from Miall 1991a; 2010). Note, the numerical ranks in the right-hand column correspond to the surfaces indicated in Figure 2.4.	18
Table 2.3 – Architectural element scheme developed by Miall (1978; 1985; 2010), used as a framework for future studies of fluvial deposits. The classification scheme aids fast interpretation, whilst honouring the processes of deposition and allows some modification based upon observations made in the field.	22
Table 2.4 – The typical characteristics of the low- and high-accommodation systems tracts when applied to fluvial strata (After: Catuneanu 2003; Leckie & Boyd 2003; Catuneanu 2006).	45
Table 3.1 – Facies of the Lower Castlegate Sandstone, Utah. Detailed photopanel available in Appendix 1.	71
Table 3.2 – Palaeocurrent analysis results from the Lower Castlegate.	93
Table 3.3 – Formation tops and thicknesses of Cretaceous units used in the development of one-dimensional burial history plots.	97
Table 4.1 – Lithofacies table of the Spireslack Sandstone (modified from Ellen et al. 2019).	129
Table 4.2 - The major constituent architectural elements of the B1 Face. Elements are defined by their name, code, facies assemblages and description. A real interpretation example is taken directly from the outcrop interpretation (Figure 4.11).	133
Table 4.3 – Lithostratigraphical unit tops picked for the correlation of the Central Midland Valley. The base of the Spireslack Sandstone and the thickness of the Spireslack sandstone has been used to convey the variation of thickness the fluvial unit shows.	156
Table 5.1 – Architectural element summary of the Lower Castlegate at Tuscher Canyon. The table describes each element individually by: their top, bottom and internal bounding surface framework according to Miall (1996), the idealised facies succession (in the order the facies are shown), the reservoir characteristics of the element and whether they are considered net or gross when modelled in this study, and finally an internal two-dimensional schematic architectural framework.	180
Table 5.2 – Depositional conditions of mega-bar complexes for the training image construction. This details the main sedimentary architectural elements and their respective conditional requirements: distribution, dimensions, geometry, and proportions. * indicates values weighted to the data from the Tuscher Canyon outcrop due to imaging issues in the satellite images, see text for details. Note, channel sinuosity values are included, obtained from the Jamuna River satellite imagery data.	213
Table 5.3 – Output data for the architectural elements and net connectivity for the multi-point statistics, sequential indicator and object-based model iterations.	221

1 Introduction

Fluvial strata can form high net-to-gross producing hydrocarbon reservoirs (Tyler and Finley 1991; Bowman et al. 1993; Salter 1993; Laure and Hodavik 2006; Labourdette 2011) and significant aquifers (Guin et al. 2010; Ronayne et al. 2010). As a result, the stacking pattern and stratigraphic significance of high net-to-gross fluvial multi-storey sandbodies (MSBs) has received much attention (Shanley and McCabe 1994; Heller and Paola 1996; Catuneanu and Elango 2001; Miall and Arush 2001; Adams and Bhattacharya 2005; McLaurin and Steel 2007; Hajek and Heller 2012; Colombera et al. 2015; Sahoo et al. 2016), most notably, the application of distributary fluvial systems (DFS) as a model for stratigraphic and morphological architecture (Nichols and Fisher 2007; Hartley et al. 2010; Weissmann et al. 2010; Owen et al. 2015; Batezelli et al. 2019). The DFS model describes the radial deposition of a fluvial system; where the proportion of sand, the grain size and channel thickness decrease downstream (Owen et al. 2015) and sinuosities increase towards the distal zone of a fluvial system (Nichols and Fisher 2007).

Currently, little attention is given to the controls on meso-scale (typically at one- to ten-metre) architectural elements within high net-to-gross MSBs (Miall 1993, 1994; Pranter et al. 2007; Li et al. 2015), something that is fundamental in understanding the preservation potential of meso-scale heterogeneity (Tyler and Finley 1991; Horung and Ainger 1999) and the distribution of reservoir quality within fluvial reservoirs. This is despite the general acceptance that key influences upon fluid flow through sandstones are typically of such scales (Tyler and Finley 1991; Koneshloo et al. 2018), which are extremely difficult to characterise from down-hole data alone (Miall 1994; Bridge and Tye 2000; Pringle et al.

2006). In considering the confinement of an MSB, there must be a diagnostic factor at the meso-scale that can be identified. The identification of such a diagnostic feature may be critical in the evaluation of basin palaeogeography and sandbody distribution.

This thesis examines outcrop analogues of MSBs and the controls upon the distribution of architectural elements within them. Using outcrops from the Cretaceous Lower Castlegate Sandstone of the Mesaverde Group, Utah, and the newly defined Bashkirian to Serpukovian Spireslack Sandstone from the open cast mine works of the Carboniferous of the Midland Valley, Scotland, this study examines the modes and degrees of confinement on fluvial systems and their effects on the deposition and preservation of meso-scale architectural elements within MSBs. The Castlegate and Spireslack sandstones provide a comparison because they represent unconfined and confined systems respectively. Further allo- and autogenic controls, and their MSB architectural element products and impact on preservation are also analysed along with approaches to the numerical representation of architectures of such deposits in stochastic fluvial reservoir modelling.

1.1 Multi-storey fluvial sandbodies

MSBs are defined as “a sand body of one cycle [that] is superimposed upon one or more earlier sand bodies” (Bridge and McKay 1993; Gibling 2006, pg. 732). As highlighted by Chamberlain and Hajek (2015, and references therein), there are three fundamental methods in which MSBs form (Figure 1.1), these are: intra-channel belt process development such as gradual point bar migration coupled with system aggradation (not considered within this thesis), avulsion and reoccupation such as low aggradation rate of a braidplain and highly avulsive channels (an unconfined fluvial system) and an incised valley lateral confinement, where local avulsions are not possible (a confined fluvial system). This work considers the

controls upon, and products of, deposition and preservation in confined compared to unconfined fluvial systems

Confined fluvial systems are those that are affected in their development, sediment transport and deposition by lateral confinement, typically as a result of active localised faulting or from local to regional scale incision as a result of base-level fall. These systems commonly produce erosionally dominated, macro- to giga-scale architectures with channel belts that erode one another as the fluvial system aggrades but lateral avulsions on a regional scale are impeded because of confinement (Gibling 2006; Chamberlain and Hajek 2015).

Unconfined fluvial systems, such as braidplains, are those without topographical confinement. Such systems are dominated by aggradation or avulsion, and therefore their preserved architectures are dependent dominantly upon the rate of aggradation within the fluvial system (Figure 2.12) (Chamberlain and Hajek 2015).

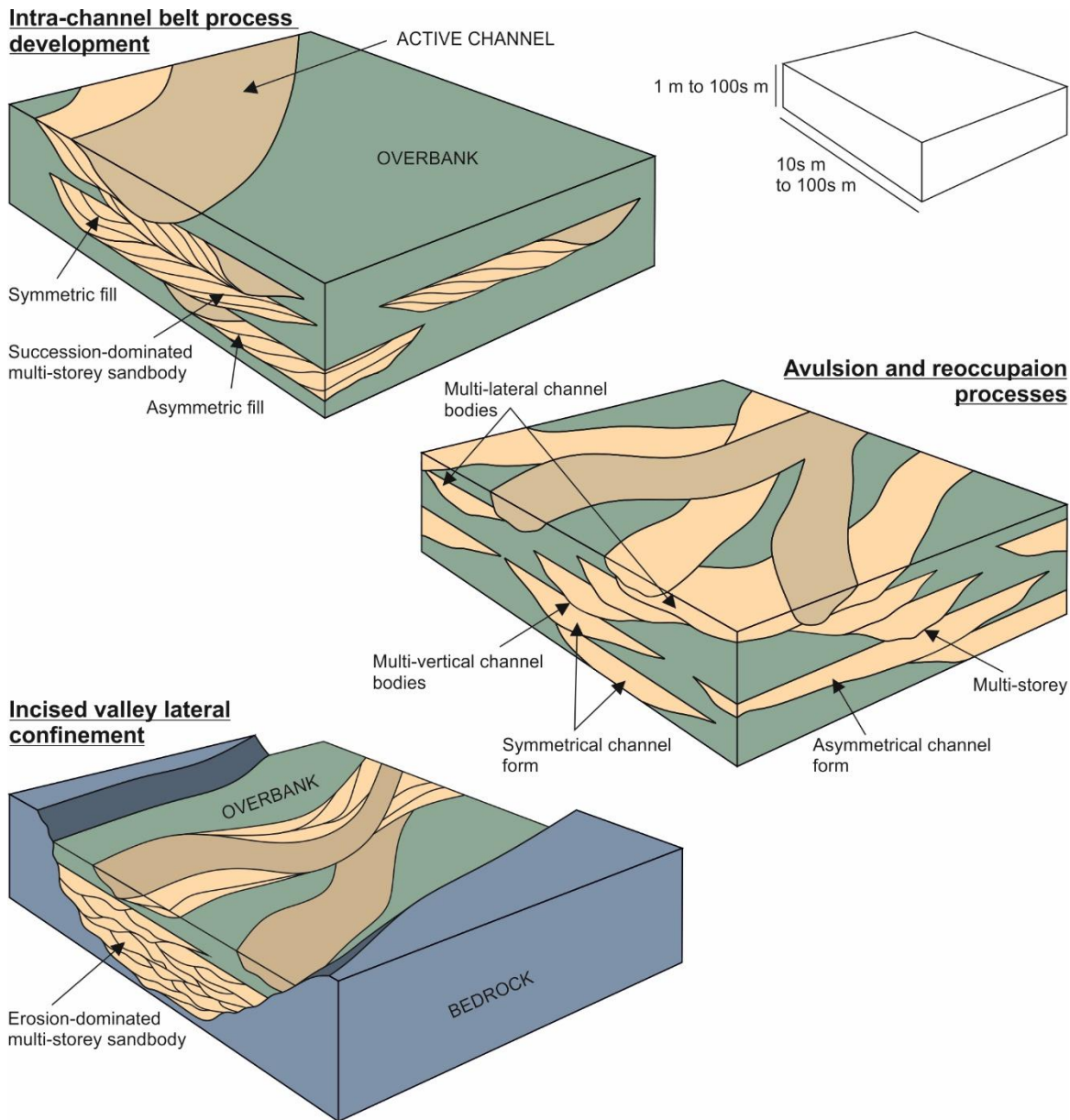


Figure 1.1 – Methods of multi-storey sandbody formation (modified from Chamberlin and Hajek 2015). Annotation and formal nomenclature has been taken from Gibling (2006) and Miall (2014). Intra-channel belt processes form MSBs through such mechanisms as aggradation and meandering. Avulsion and reoccupaion of topographical lows, compensational avulsion (Bridge and Leeder 1979; Straub et al. 2009), can generate MSBs; finally, lateral confinement, such as topographical confinements like incised valleys, can generate MSBs. Note, nomenclature labels do not suggest that their occurrence is limited to the mechanism of MSB generation they are depicted in.

1.2 Research aims and objectives

The overall aim of this work is to understand the deposition and preservation of sedimentary architectural elements within unconfined and confined high net-to-gross fluvial MSBs and how they can best be represented in numerical modelling workflows. This is achieved through three core aims:

The first aim of this work is to characterise the architectural elements in an unconfined MSB, and to determine the controls affecting their deposition and preservation. The Upper Cretaceous Lower Castlegate Sandstone, Utah, USA, is used as an example. The objectives are to:

- To establish the architectural element framework that comprises the Lower Castlegate.
- To analyse multiple outcrops along a downstream profile and determine architectural element trends.
- To determine the controls on the downstream distribution of architectural elements.
- To determine the possible identifiers for an unconfined fluvial system.
- To discuss the findings of the chapter in the context of reservoir quality and sequence stratigraphy

The second aim of this work is to characterise the architectural elements in a confined MSB, and to determine the controls affecting their deposition and preservation. The middle Carboniferous Spireslack Sandstone, Midland Valley, Scotland is used as an example. The objectives are to:

- To produce a facies analysis for the SS; to establish the architectural element and bounding surface framework that comprise the Spirelack Sandstone.
- To establish the confined nature of the deposits and the mode of confinement.
- To determine the affect confinement has had upon the architectural and bounding surface framework within the deposits.
- To determine possible identifiers for a confined fluvial system.

The third aim is to develop stochastic reservoir models that represent the preservation of architectural elements in these systems and that provide insight into modelling comparable systems in the subsurface. The objectives are to:

- To construct a populated reservoir model using quantified architectural measurements and traditional object-based models and sequential indicator simulations.
- To build a reservoir model based upon traditional two-dimensional outcrop data as a training image for multi-point statistics simulations.
- To develop a geologically conceptual three-dimensional training image to be used in the development of more modern multi-point statistics populations.
- To test the constructed models tested using static connectivity tests to determine the advantages of each modelling algorithm.
- To discuss best practice methodologies for the replication of architectural elements in MSBs for stochastic workflows.

1.3 Thesis sign-posting

In this section the content of thesis chapters, their relevance in context, and their contribution to the broad aims of the thesis are outlined.

1.3.1 Chapter 2: Literature Review and Scientific Background

This chapter provides a comprehensive literature review surrounding deposition, preservation and controls of architectural elements in fluvial systems. The chapter will detail: 1) a brief introduction into the facies that comprise fluvial systems, 2) the classification and genesis of architectural elements within fluvial systems and their bounding surface hierarchy, 3) the mechanisms that control the deposition fluvial architecture, 4) the basin scale allogenic controls that impact fluvial strata.

1.3.2 Chapter 3: The sedimentary architecture of an unconfined fluvial system: example from the Lower Castlegate Sandstone, Utah

In this chapter, a facies and architectural and bounding surface analysis is conducted on the Upper Cretaceous Lower Castlegate Sandstone, Utah, unconfined MSB. A 150 km, down-dip transect is produced from eight logs, three photogrammetric panels and ten borehole locations. Quantitative geometric data of architectural elements and set thicknesses derived from these datasets are supplemented by burial history analysis, to determine the idealised down-dip profile for architectural preservation. The effects of allogenic controls such as differential subsidence rates and autogenic controls such as discharge variation and avulsion are discussed. Finally, the chapter identifies the potential diagnostic features of unconfined MSBs.

1.3.3 Chapter 4: The sedimentary architecture of a confined fluvial system: example from the Spireslack Sandstone, Scotland

In this chapter a facies and architectural element and bounding surface analysis are conducted for the newly described Serpukovian-Bashkirian Spireslack Sandstone, Scotland. The distribution, size, geometric and juxtaposing relationships of architectural elements are presented and the potential controls of the deposits are explored. Coal-board borehole data from the Midland Valley are presented as correlations of the lateral extent of the succession described, justifying its confinement, and the degree of it. Finally, the potential products of such confinement, at the meso-scale are identified.

1.3.4 Chapter 5: Geologically realistic representation of fluvial sedimentary architecture in stochastic reservoir models.

The chapter begins with a short literature review of stochastic reservoir modelling and the algorithms used in this study. The products of architectural analysis (Chapter 3 and 4) are used to constrain populations of deterministic frameworks for the more distal Lower Castlegate Sandstone. The analysis of the ancient deposits are supplemented with modern analogues to provide plan view constraints to models. The newly defined depositional conditioning method is used to construct training images for multi-point statistics based simulations. These results are complemented by two traditional methods, sequential indicator simulations and object-based model approaches. The resulting models are then compared using static connectivity statistics.

1.3.5 Chapter 6: Discussion

The similarities and differences of unconfined and confined fluvial MSB architectures are considered and examined by discussion in the context of modern and ancient examples. to

identify the key diagnostic characteristics of confinement in ancient fluvial systems. The reservoir quality of such depositional systems is discussed and the appropriate stochastic workflows to replicate the heterogeneity in these systems are considered.

1.3.6 Chapter 7: Conclusions

This section covers the general conclusions derived from the thesis and presents a section on further work that can be conducted in the field of study. A short summary is provided with the main points the thesis has made.

1.4 List of Publications

Chapter 3:

Mitten, A.J., Howell, L., Clarke, S.M., Pringle, J.K., **2020**. Controls on the deposition and preservation of architectural elements within a fluvial multi-storey sandbody. *Sedimentary Geology*, 401, 105629.

Chapter 4:

Ellen, R., Browne, M.A.E., **Mitten, A.J.**, Clarke, S.M., Leslie, A.G. and Callaghan, E., **2019**. Sedimentology, architecture and depositional setting of the fluvial Spireslack Sandstone of the Midland Valley, Scotland: insights from the Spireslack surface coal mine. *Geological Society of London Special Publications*, 488.

Chapter 5:

Mitten, A.J., Mullins, J., Pringle, J.K., Howell, J. and Clarke, S.M., **2020**. Depositional conditioning of three-dimensional training images: Improving the reproduction and representation of architectural elements in sand-dominated fluvial reservoir models. *Marine and Petroleum Geology*, 113, p.104-156.

2 Fluvial sedimentology: a review

Fluvial systems are one of the most important environments within the geological record as they are the main mode of transport for sediment, from source to sink (Leeder 1982; 2011; Bridge 1993; Shanley and McCabe 1998; Miall 2010; 2016). Consequently, the understanding of fluvial system and their complex responses to autogenic and allogenic controls has been the subject of much research by sedimentologists working in modern environments and in the geological record. A good understanding of the fluvial system could lead to a much greater understanding of a basin fill complex (Fielding *et al.* 2012).

Fluvial sediments show responses to their controls on a variety of scales; from the grain to bedform scale, and from the channel-belt to basin-fill scale (Gibling 2006; Weissmann *et al.* 2010; 2011). This review, and the thesis' main focus, is on the sedimentological architecture of fluvial systems, what controls them and how these sedimentary architectural products are deposited (Figure 2.1). This review will up-scale from a short review of grain transport mechanisms and the facies they preserve in the rock record, to intermediate scale and sedimentary architecture found within fluvial deposits. Finally, this review will summarise the controls on basin-scale fluvial architecture, or stratigraphic architecture, and their products.

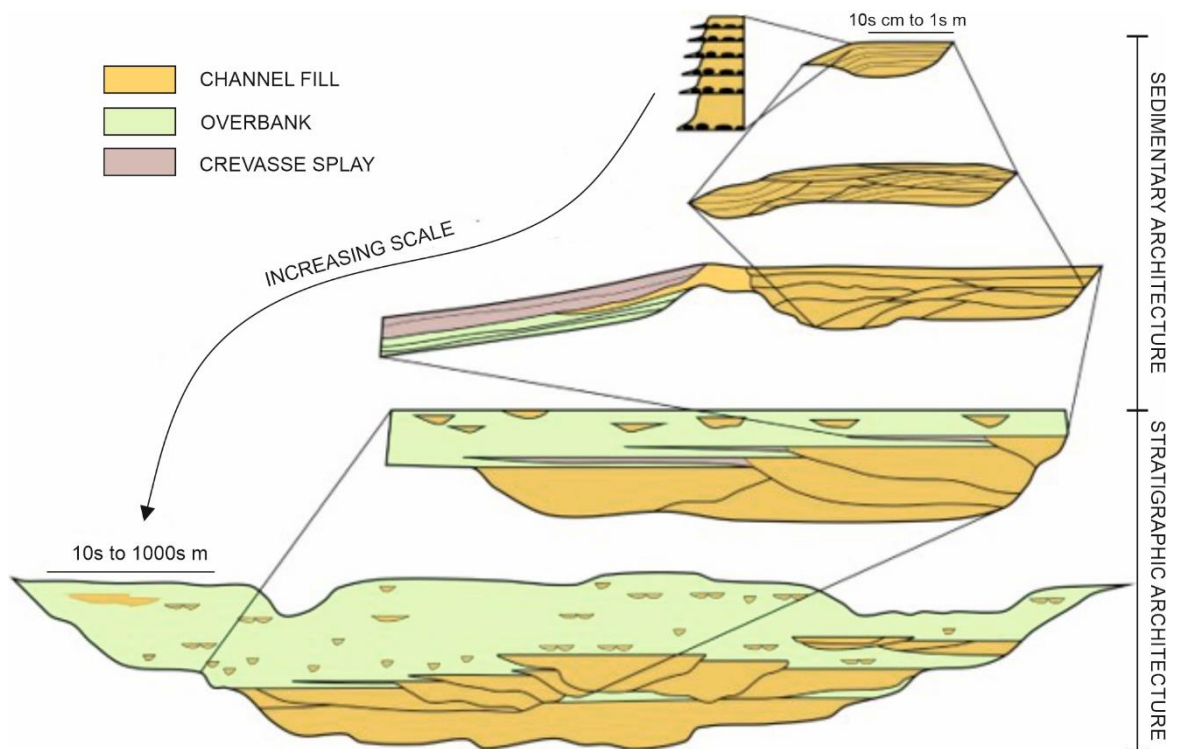


Figure 2.1 – A hierarchy of fluvial architectural elements showing the scales at which fluvial systems are studied. The diagram illustrates facies-scale interpretations through to larger scale architectural element construction and the distribution of these elements within a basin fill complex (After Miall 2014). Note the definition used herein of sedimentary and stratigraphic architecture.

2.1 Bedforms and facies in fluvial sediments

Sediment can be transported as bedload, suspended load or washload. Bedload consists of sediment that is transported along the sediment-water interface (or bed). Transport mechanisms that operate at this interface include rolling or sliding, saltation and collision interactions (Leeder 1982; 2011). A grain will cease to be transported and deposited as a result of a velocity decrease; this may be due to a change in gradient increasing friction at the sediment-water interface (Collinson *et al.* 2006; Leeder 2011). This will cause the sedimentary grain to become stationary upon the river bed. Bedforms are produced as a result of this deposition, the type and characteristics of the bedform are dictated by the mode and manner by which the sedimentary grains were transported, the grain size and the

velocity of flow (Figure 2.2). This model has been reproduced and developed numerous times by numerous authors including Guy *et al.* (1966), Williams (1970), Costello (1974), Leeder (1980; 1982; 1983; 2011), Mantz (1980), Allen (1982), Southard and Boguchwal (1990) and Ashley (1990). The model presented here (Figure 2.2) is a simplified version, to highlight bedform variations with increased velocity and grain size, at a given depth and temperature.

Sedimentologists define two general flow regimes (that consider the flow characteristics described above) for the ease of palaeoflow velocity estimations (Nichols 2009). The sedimentary structures produced in the lower flow regime include ripples, dunes and lower plane beds. Those of the upper flow regime comprise upper plane beds and antidunes (Nichols 2009).

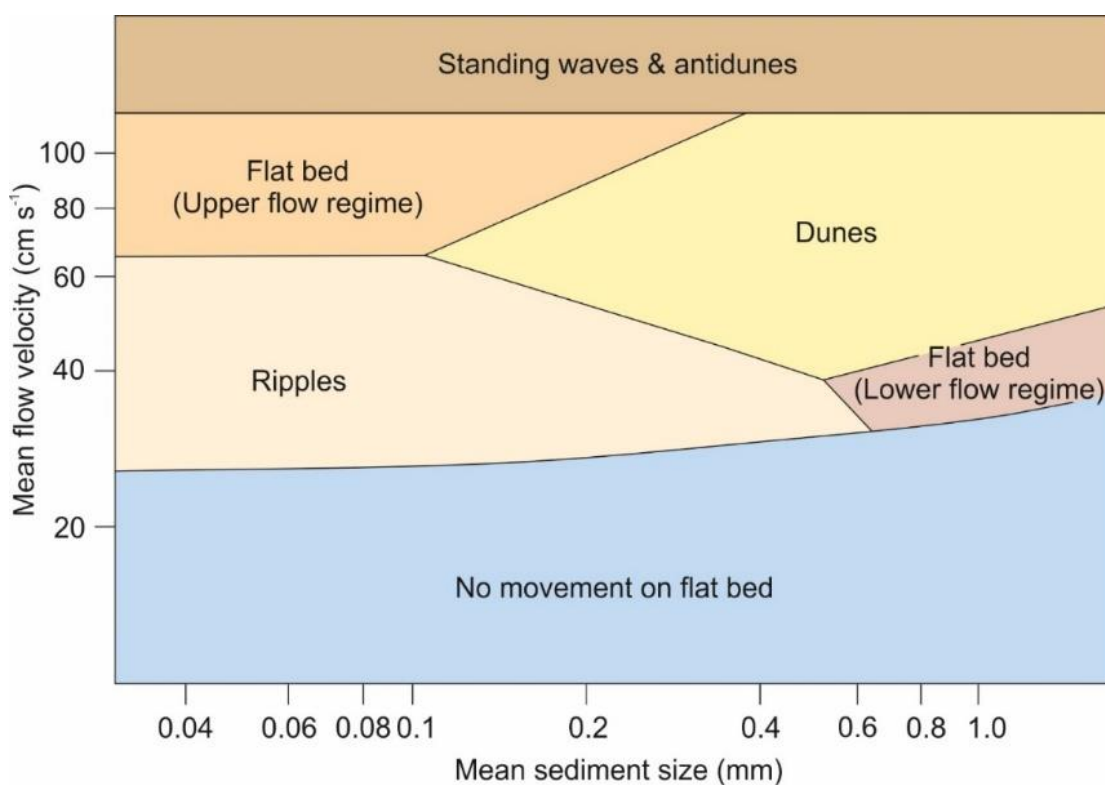


Figure 2.2 – Phase diagram for bedforms produced by various grain sizes (mm) and mean flow velocities (cm s⁻¹) within a confined flow 20cm deep and at 10°C. Diagram compiled from in-text

property ranges from Southard (1971), Ashley (1990), Leeder (1982; 2011), Hsu (2004) and Collinson et al. (2006).

Lower flow regime conditions are generated within a confined or channelised flow when Froude Number < 0.84 ; such conditions form bedforms known as plane beds, ripples and dunes (Paola and Borgman 1991).

The formation of ripples and dunes occurs due to turbulent flow passing over an irregular sediment water interface (Tucker 2001). Ripples form as a result of eddy currents close to this interface that are strong enough to entrain bedload material, but do not disturb the rest of the water column, or the surface of the confined flow (Baas *et al.* 1993; Baas 1994; 1999; Leeder 2011). Dune-scale bedforms are developed when turbulent eddies at the sediment water interface are sufficient to disturb the higher layers of the water column and material may be transported beyond the viscous layer of the confined flow (Tjerry and Fredsøe 2005; Best 2005; Leeder 2011). The migration and formation of these bedforms is demonstrated in Figure 2.3. Grains saltate up the stoss slope of the dune or ripple in a downstream direction. When the saltating grains reach the crest of the bedform, they fall down the lee slope and are deposited on or at its base forming toesets.

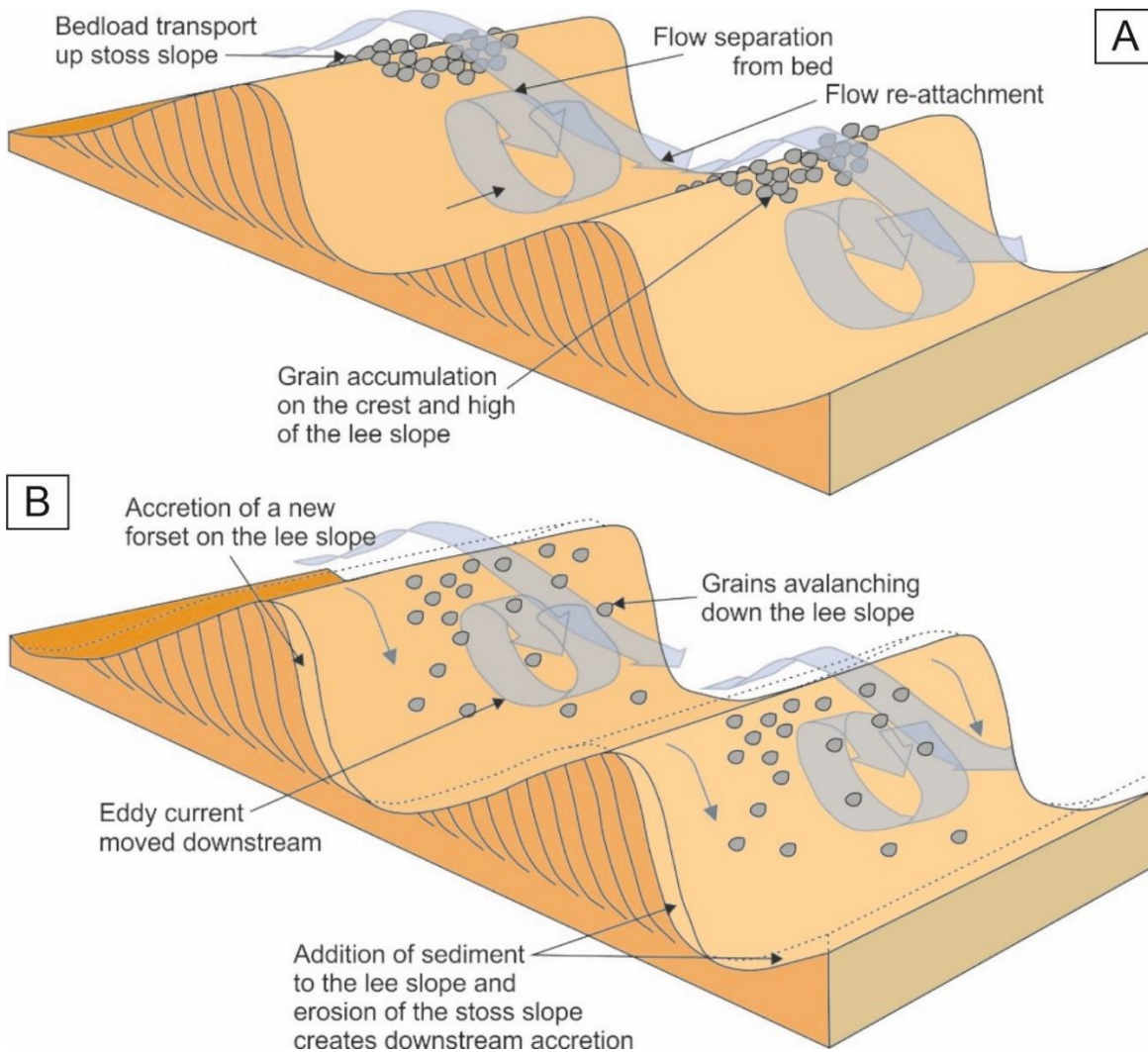


Figure 2.3 – Schematic representation of ripple formation and downstream migration. A) The formation of eddy currents within the trough between two bedforms, and the sedimentary grains in transport reaching the crest of the bedform. B) The avalanche of these grains down the lee slope of the bedforms and their subsequent downstream accretion (After Collinson et al. 2006; Nichols 2009).

Upper flow regime plane beds are produced by high flow velocities and fine grain sizes, due to high flow velocities on the lee slope of the bedform and deceleration of flow within the trough, creating low amplitude and high wavelength bed waves. When the flow exceeds a certain velocity within a confined space (or when $Fr > 1$) supercritical flow occurs (Figure 2.2), and antidunes are deposited (Alexander and Fielding 1997; Leeder 2011).

When such bedforms develop on the bed of a flow, they migrate through the continued migration of grains over their crests. If sediment supply (the number of grains) is high for the migration rate, bedforms will build-up or aggrade, climbing over one another. This preserves bedforms as sedimentary structures. These structures are used to develop a lithofacies regime that can be used to determine the hydrodynamic conditions in which fluvial sediments were deposited. Lithofacies typically consist of texture characteristics of the sediment (grainsize, sorting, rounding and sphericity), coupled with larger scale observations of colour, sedimentary structure and the addition of any non-uniform material within the sediment (organic material or out-sized clasts).

The vast majority of lithofacies within a fluvial system are clastic, with their composition dependent upon the mineralogy of the sediment source area. Typically, high velocity flows with a high sediment supply will deposit facies with upper flow regime structures. As a flow reduces in velocity and sediment supply, lithofacies structures become lower flow regime. Non-flow-related lithofacies can commonly have a biogenic component as they form on flat plains away from the major flow. Given the large amount of past work conducted on fluvial systems, Miall (1996) compiled a standardised facies scheme (Table 2.1) for use in the study of fluvial environments. From this table it is evident that fluvial deposits are a product of incredibly complex depositional processes and produce an extremely wide variety of sedimentary characteristics.

Table 2.1 – Facies scheme for fluvial deposits from Miall (1978; 2010), Highlighting the large number of facies and processes that make-up and deposit fluvial strata.

Code	Facies	Sedimentary Structures	Interpretation
Gmm	Matrix supported, structureless gravel	Weak grading	Plastic debris flow
Gmg	Matrix supported gravel	Inverse to normal grading	Pseudoplastic debris flow
Gci	Clast supported gravel	Inverse grading	Cast rich debris flow or pseudoplastic debris flow
Gcm	Clast supported structureless gravel	-	Pseudoplastic debris flow
Gh	Clast supported, crudely bedded gravel	Horizontal bedding, imbrication	Longitudinal bedforms, lag deposits, sieve deposits
Gt	Gravel stratified	Trough cross-bedding	Minor channel fills
Gp	Gravel stratified	Planar cross-bedding	Transverse barforms, deltaic growths from older remnant bars
St	Sand, fine to very coarse, may be pebbly	Solitary or grouped trough cross-bedding	Sinuuous crested and lingoid dunes
Sp	Sand, fine to very coarse, may be pebbly	Solitary or grouped planar cross-bedding	Transverse and lingoid bedforms
Sr	Sand, very fine to coarse	Ripple cross lamination	Ripples
Sh	Sand, fine to very coarse, may be pebbly	Horizontal lamination parting or streaming lamination	Plane bed flow
Sl	Sand, fine to very coarse, may be pebbly	Low angle (>15°) cross-bedding	Scour fills, humpback or wash-out dunes, antidunes
Ss	Sand, fine to very coarse, may be pebbly	Broad shallow scours	Scour fill
Sm	Sand, fine to coarse	Structureless or faint lamination	Sediment gravity flow deposits
Fl	Sand, silt, mud	Fine lamination, very fine ripples	Overbank, abandoned channel, waning flood deposits
Fsm	Silt, mud	Structureless	Backswamp, or abandoned channel
Fm	Mud, silt	Structureless, desiccation cracks	Overbank, abandoned channel, or drape deposits
Fr	Mud, silt	Structureless, roots, bioturbation	Root bed, incipient soil
C	Coal, carbonaceous mud	Plant, mud films	Vegetated swamp deposits
P	Palaeosol carbonate	Pedogenic features: nodules, filaments	Soil with chemical precipitation

2.2 Bounding surfaces

Bounding surfaces are surfaces within the sedimentary succession, which are scale independent of one another and have a specific genetic definition dependent upon the manner in which they interact with other surfaces. The scales of bounding surface can range from small-scale foresets all the way to large-scale sequence boundaries (Table 2.2). Bounding surfaces are an incredibly effective tool in the analysis of fluvial deposits as complex lateral and temporal changes in allo- and autogenic controls yield diverse lithofacies juxtapositions, making their interpretation from one-dimensional sedimentary logging and facies analysis ineffective. Establishing a bounding surface framework and hierarchy can help to group fluvial processes into meso- or intermediate-scale architectures and provide insight into their formation.

The order of this hierarchy is dictated by the concordance and discordance of bounding surfaces relative to one another, the time scale they represent, and the lithofacies they bound. The following descriptions have been compiled from Allen (1983a), Miall (1988a; 1999; 2010; 2016) and Bridge (1993).

First- and second-order bounding surfaces record microforms and mesoform deposits. First-order surfaces represent set-bounding surfaces, whereas, second-order surfaces are coset-bounding surfaces or equivalent that representing variations in flow conditions or palaeocurrent direction.

Third- and fourth-order surfaces are defined by the preservation of intermediate-scale macroforms, known as architectural elements (Table 2.3; Section 3.7). Third-order surfaces are defined as clinoformal accretionary surfaces and erosional flow reactivation surfaces.

Reactivation surfaces are formed by perturbations in stable flow that produce discordant truncation into the underlying meso- and microforms at $\sim 15^\circ$ surfaces.

Table 2.2 – Bounding surface hierarchical scheme, showing their magnitude in time, the process that formed them, the depositional product of those processes and their order within the hierarchy (Adapted from Miall 1991a; 2010). Note, the numerical ranks in the right-hand column correspond to the surfaces indicated in Figure 2.4.

Rank and characteristics of bounding surfaces	Examples of process	Fluvial deltaic depositional units	Time scale of process (years)
0 th	Burst-sweep cycle	Lamina	10^{-6}
1 st	Bedform migration	Ripple (microform)	10^{-5} - 10^{-4}
1 st	Bedform migration	Reactivation surface	10^{-3}
2 nd	Bedform migration	Dune	10^{-2} - 10^{-1}
3 rd	Seasonal flooding (10yr flood)	Macroform growth increment	10^{-1} - 10^1
4 th	Channel and bar migration	Point bar	10^1 - 10^3
5 th	Channel avulsion	Channel	10^3 - 10^4
6 th	5 th order Milankovitch cycle	Channel belt	10^4 - 10^5
7 th	4 th order Milankovitch cycle	Major depositional system	10^5 - 10^6
8 th	3 rd order Milankovitch cycle	Basin fill complex	10^6 - 10^7

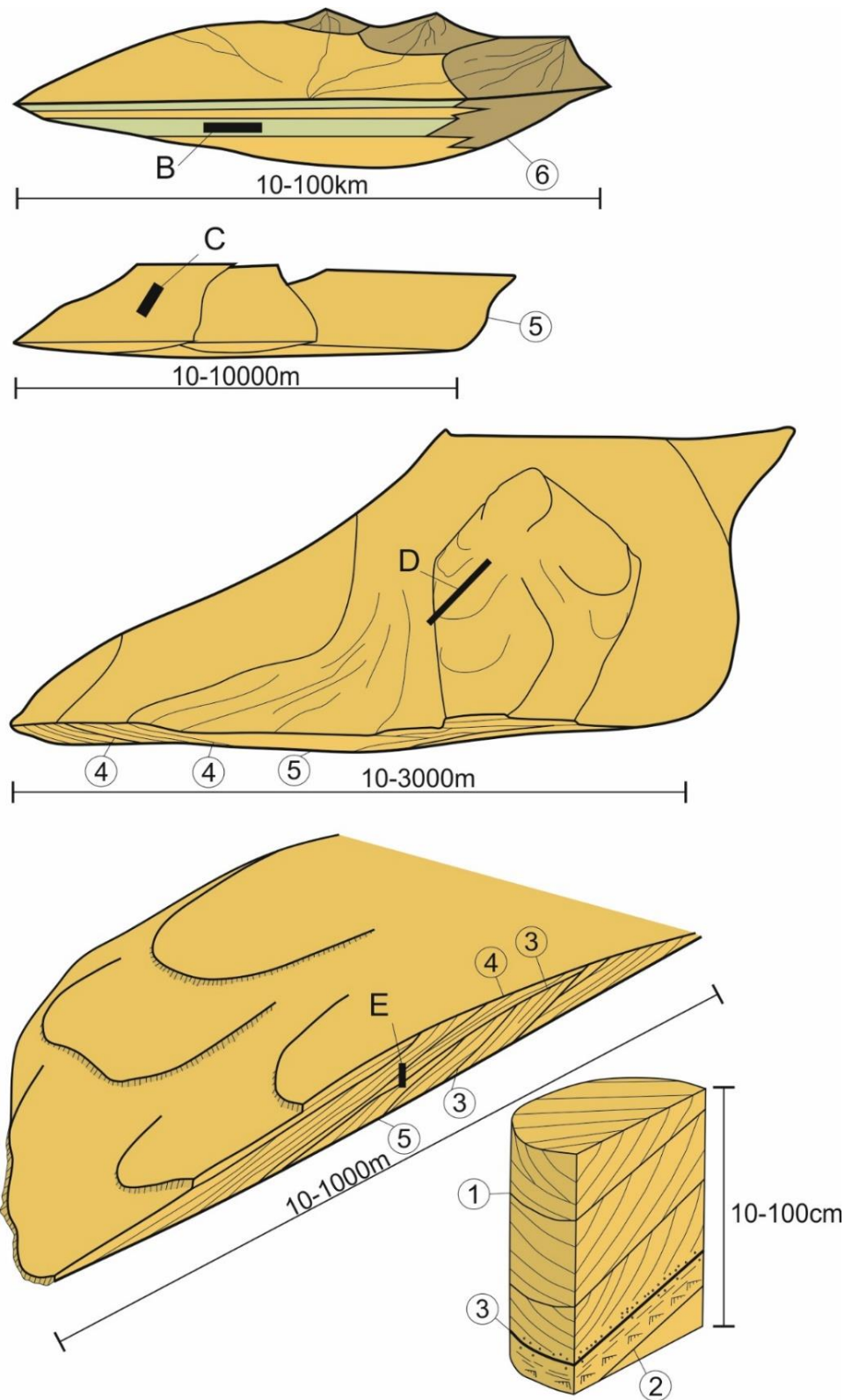


Figure 2.4 – Bounding surface hierarchy within a fluvial system, numbers correlate to the bounding surface hierarchy shown in Table 2.2 and in the text below (modified from Miall 2010).

Migratory unit bars (macroforms) are extremely common in rivers (Section 2.4) and display third-order clinoform accretionary surfaces with a sigmoidal geometry (Miall 1994; Hajek and Heller 2012). The topsets of bar clinoforms are commonly flat to shallowly dipping and are composed of packages of bar-top facies (horizontally-laminated sandstones and siltstones and ripple laminated sandstones; Miall 1994; Chamberlain and Hajek 2015, 2019). The presence of such bar tops can give an indication of flow depths and their completeness can show preservation (Hajek and Heller 2012). Their occurrence can therefore give insight into palaeoflow depths, avulsion mechanisms (Chamberlain and Hajek 2015) (Section 2.6) and the aggradational profile of an ancient fluvial system (Heller and Paola 1996; Mohrig et al. 2000; Hajek and Heller 2012) (Section 2.7.1).

The bounding surface hierarchy begins to break down at the scale of fourth-order surfaces. These surfaces define minor channel scours in the top of barforms, element tops and flat floodplain bounding surfaces, but all represent a time span of $10^1 - 10^3$ years (Miall 1988a; b).

Fifth-order bounding surfaces typically confine sandbodies; for example, channel fill elements. These surfaces are commonly horizontal, undulose or concave upward (dependent upon the direction of observation relative to that of the palaeocurrent). Palaeosol horizons may be considered as fifth-order surfaces within the floodplain section of a fluvial complex, as they represent the contemporaneous horizon equivalent to major channel erosion.

Sixth-order surfaces are mappable stratigraphic units, lithostratigraphic members or sub-members, which may represent palaeovalleys. Seventh-order surfaces, bound major lithosomes ("a discrete depositional unit bounded by a distinct bounding surface, of any rank" (Miall 2010, pg. 89)) produced by allogenic processes of high magnitude, most high-

resolution sequence stratigraphical boundaries (Section 2.7.2) are seventh-order surfaces. Eighth-order surfaces are products of regional unconformities developed by continental or global scale allogenic events, therefore large-scale sequence stratigraphical boundaries may also constitute eighth-order bounding surfaces.

2.3 Sedimentary architecture

Architectural elements are defined as “a component of a depositional system equivalent in size to, or smaller than, a channel fill, and larger than an individual facies unit, that is characterised by a distinctive facies assemblage, internal geometry and external form” (Miall 2010 pg. 91). Bounding surfaces (Section 2.2) provide an internal framework and bound the internal and external geometries of architectural elements. There are eight recognised and standardised architectural elements within the fluvial system (Miall 1996) (Table 2.3). These elements represent the major geomorphological building blocks of any modern or ancient fluvial system and vary in quantity, distribution and size with regards to fluvial style (Section 2.5) and discharge regime. To describe and classify an architectural element, six features should be noted: the lower and upper bounding surface characteristics, the external geometry, scale, lithology, internal geometry and palaeocurrent patterns.

There are various forms of nomenclature used in the description and classification of fluvial barform strata, based upon their interpretation in geomorphology and geology. This thesis considers a unit bar to be a macroform developed by a single accretionary process, and a compound barform to be one developed by multiple accretionary processes and unit bars. For example, downstream or lateral accretion bars (Table 2.3) are considered as single unit bars.

Element	Symbol	Facies assemblage	Geometry and relationships
Channels	CH	Any combination	Finger, lens or sheet; concave-up erosional base; scale and shape highly variable; internal concave 3rd order erosion surfaces common
Gravel bars and bedforms	GB	Gm, Gp, Gt	Lens, blanket; usually tabular bodies; commonly interbedded with SB
Sandy bedforms	SB	St, Sp, Sh, Sl, Sr, Se, Ss	Lens, sheet, blanket, wedge, occurs as channel fills, crevasse splays, minor bars
Downstream-accretion macroforms	DA	St, Sp, Sh, Sl, Sr, Se, Ss	Lens resting on flat or channelled base, with convex up 3rd order internal erosion surfaces and upper 4th order bounding surfaces
Lateral-accretion macroforms	LA	St, Sp, Sh, Sl, Sr, Se, Ss, less commonly Gm, Gt, Gp	Wedge shaped, sheet, lobe; characterized by internal lateral accretion 3rd order surfaces
Scour hollows	HO	Gh, Gt, St, Sl	Scoop shaped hollow with asymmetric fill
Sediment gravity flows	SG	Gmm, Gmg, Gci, Gcm	Lobe, sheet, typically interbedded with GB
Laminated sand sheets	LS	Sh, Sl, minor Sp, Sr	Sheet, blanket
Overbank fines	FF	Fm, Fl	Thin to thick blankets commonly interbedded with SB; may fill abandoned channels

Table 2.3 – Architectural element scheme developed by Miall (1978; 1985; 2010), used as a framework for future studies of fluvial deposits. The classification scheme aids fast interpretation, whilst honouring the processes of deposition and allows some modification based upon observations made in the field.

2.3.1 Unit bars

Unit bars are macroform deposits that form in rivers over a wide range of tectonic and climatic settings, and have been extensively studied in both modern and ancient fluvial systems (Herbert et al. 2020). These macroforms are usually lobate in plan-view and can be hundreds of metres long and tens-to hundreds of metres wide (Sambrook Smith et al. 2006). The barforms typically consist of climbing cross bedded facies, representing dune-scale bedforms that climb up a stoss slope to an avalanche lee slope (Collinson 1970; Cant and

Walker 1978; Herbert et al. 2020) (Figures 2.5A, 2.5BI, 2.5BII). Some researchers have concluded that the height of a unit bar is controlled by river depth (Sambrook Smith et al. 2006; Lunt et al. 2013). However, this is still equivocal, with some researchers contesting the observation or giving a very broad relationship between the two by stating that unit bar height is between six and ten times the height of maximum bank-full depth (Bridge and Tye 2000; McLaurin and Steel 2007).

Unit bar formation is initiated through non-uniform flow (Smith 1971) and a topographic non-conformity on the base of a channel (Cant and Walker 1978). Such non-conformities cause the traction of sediment and the aggradational development of bedforms that begin to stack during their migration. However, some unit bars have been termed free unit bars, as they appear to grow spontaneously on the base of channels (Tubino et al. 1999; Herbert et al. 2020).

Unit bars generally comprise a single growth event, and are broadly uni-directional in their migration. Migration can produce downstream accretion, lateral accretion or simple aggradational sandy barforms (Miall 1996). Cross strata palaeocurrent azimuths being within 50 or 60° of the mean bar migration direction (Miall 1994; McLaurin and Steel 2007), such a range is produced by local flow variations that are inherent with bar growth. Fluctuations in discharge rates and water depth often form erosional (Hajek and Heller 2012) (Figures 2.5BIII, 2.5BIV) and aggradation profiles within the otherwise continuous cross-bedded facies that make up the bar (Figure 2.5BI). This can be used to provide an indication of the hydrodynamic conditions in which the barform was deposited (Hajek and Heller 2012).

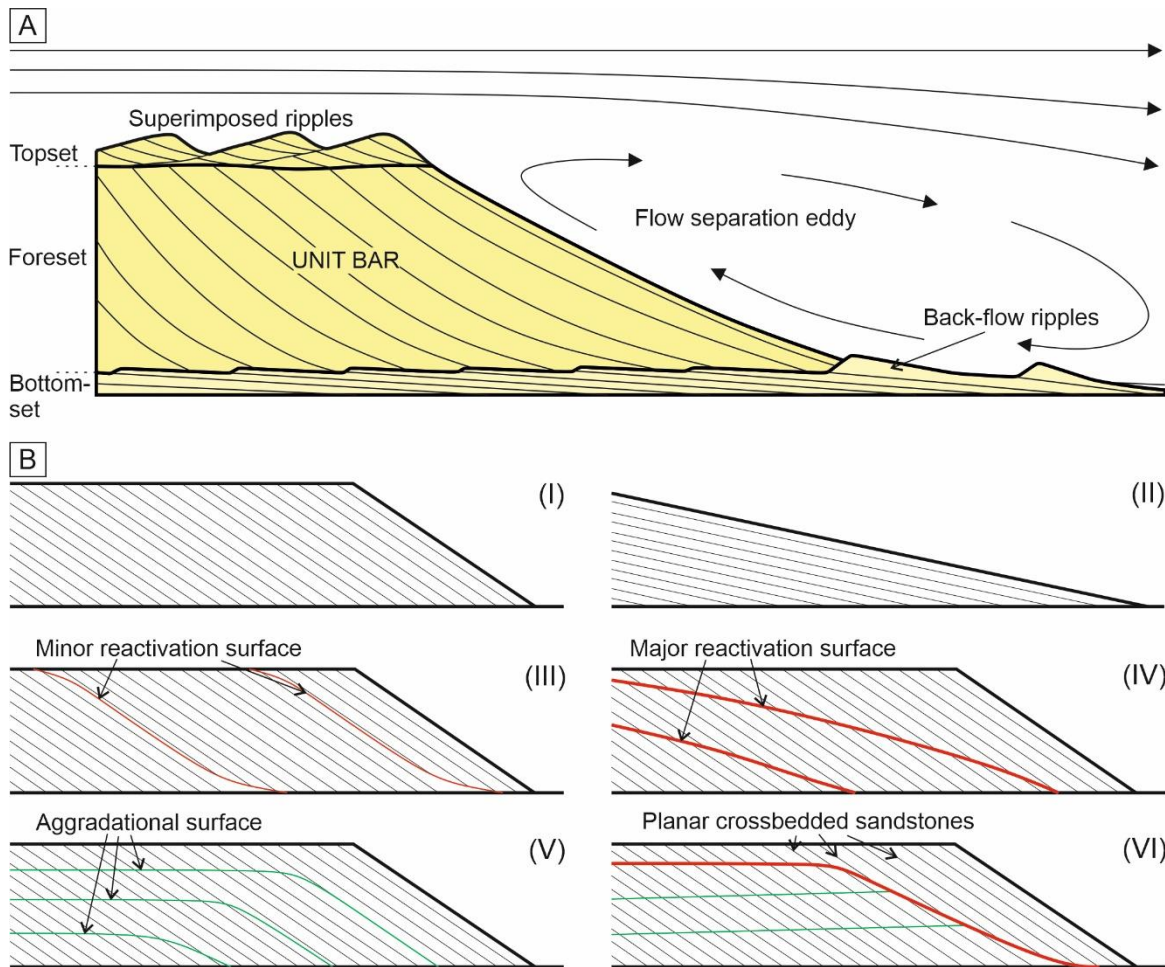


Figure 2.5 – Unit bar development and their internal structure (After Herbert et al. 2020). A) The migration of dune scale bedforms creating forests (shown here in light grey), with back-flow ripples from eddy currents forming toeset strata. Topset preserved strata are superimposed ripples and dune forms carrying material onto the lee slope. B) I) Plane foreset development in consistent flow; II) Low angle accretionary development within a unit bar; III) Minor reactivation scours

2.3.2 *Downstream accretion elements*

Downstream accretion elements are common place in the middle of channel reaches, where sediment supply and topographic variation is large enough to encourage unit bar development (Bristow 1993; Miall 1996). Downstream accretion elements represent the downstream growth of barforms. The elements are dominated by the downstream migration of dune forms over one another (Figure 2.6A). The growth or accretion of a barform is procued by the sporadic variations in discharge common in most rivers (Cant and Walker 1978; Miall 1996; Sambrook Smith et al. 2006). The downstream accreting nature of these deposits means that the clinothem accretionary deposits are most notable on the lee-slope margin of the element (Figure 2.6B) (Miall 1993; 1994; Li et al. 2015). When there is not slope failure on the lee side (Best et al. 2003), and accretionary clinorform surfaces are below the angle of failure, dune forms can migrate down the lee slope of the bar producing downward-dipping, but climbing, sets of cross strata (Hazeldine 1983; Miall 1985; Best et al. 2003) (Figure 2.6A).

The elements consist of cosets of cross bedded strata. These cross-bedded strata show second- and third-order bounding surfaces that bound planar and trough cross-bedded sandstones (Sp, St) facies. The top of the elements are usually defined by bar-top facies (horizontally laminated, low-angle cross-bedded and ripple laminated sandstones; Sh, Sl and Sr) (Miall 1985, 1996; Best et al. 2003; Ghinassi and Ieppli 2018). Palaeocurrents show that dune-scale bedforms migrate over the core of the barform and down the lee slope (Figure 2.6C) of the barform or oblique to the margins of the element (Hazeldine 1983; Miall 1996). Such barforms have been characterised in the modern South Saskatchewan River, Canada (Cant and Walker 1978; Sambrook-Smith et al. 2011), the Jamuna River, northern India (Best

et al. 2003), the River Tay, Scotland (Gilvear 1993), Niobrara River, USA (Skelly et al. 2003) and many more examples, and in the ancient geological record, from the Cretaceous Castlegate Sandstone, USA (Miall 1993, 1994; Yoshida 2000, McLaurin and Steel 2007), the Torredonian Applecross Formation, Scotland (Ghinassi and Ielpi 2018) and the Triassic Hawkesbury Sandstone, Australia (Miall and Jones 2003; Almeida et al. 2016).

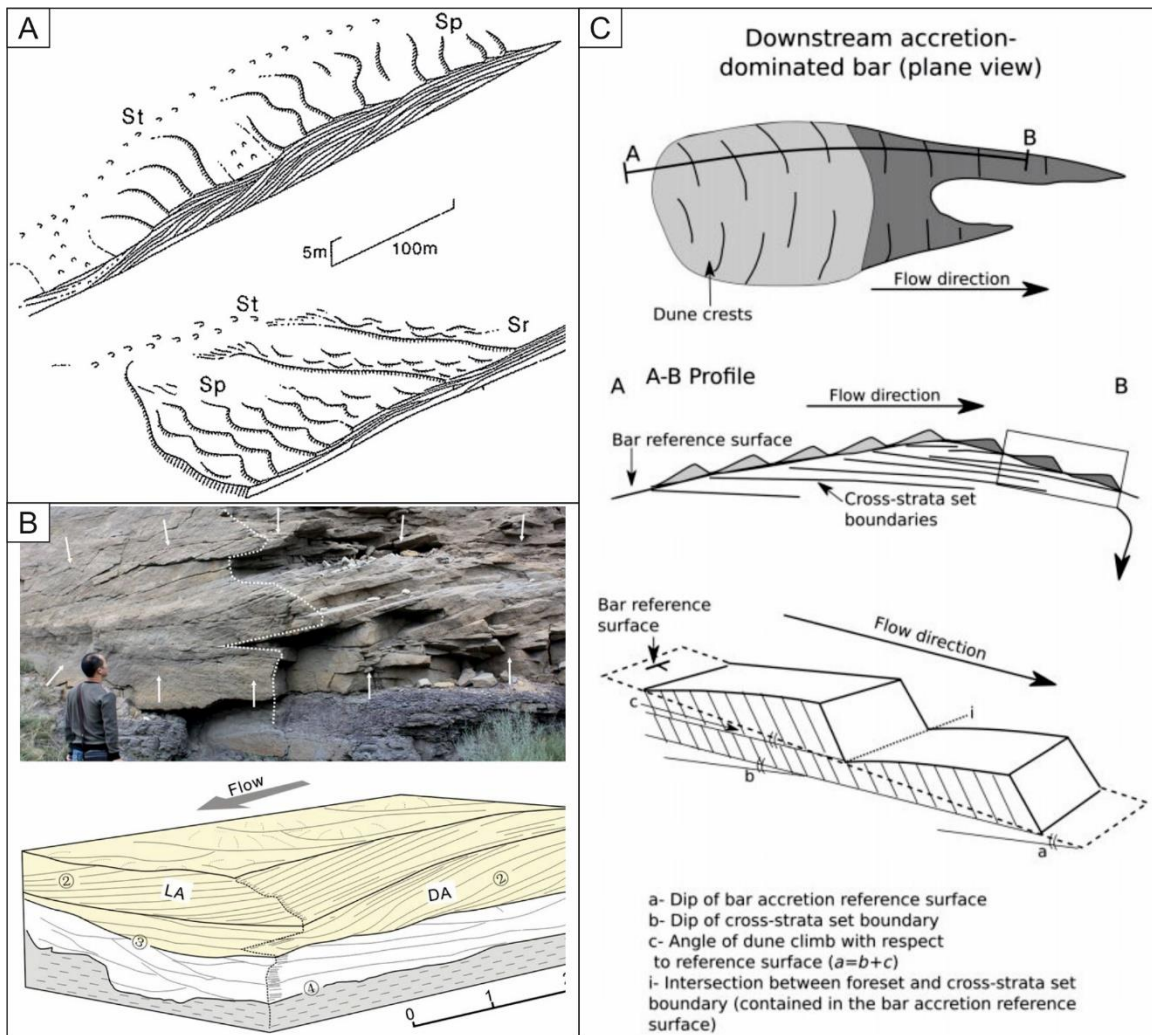


Figure 2.6 – Examples of schematic representations of downstream accretion elements. A) A generalised schematic of internal architecture and build-up of downstream accretion elements (Miall 1985). B) An example of a preserved downstream accretion element from the Rockcave Member, Yungang Formation, China (Li et al. 2015), possibly also representing a compound barform in the rock record. C) Schematic representation of downstream accretion in Almeida et al. (2016).

2.3.3 *Lateral accretion elements*

Lateral accretion elements are common at channel margins and barform margins (Figure 2.6B). They can either be a product of sinuous migration of a fluvial system or the mature lateral growth of a compound barform (Bristow 1995; Miall 1996; Best et al. 2003). The elements consist of cross bedded strata that show coset development. The facies composition of these elements is highly variable (Figure 2.6A) and is dependent upon sediment load, discharge variability channel geometry (Miall 1996). The element is produced by the migration of dune forms up and over the flanks of channel or barform margins (Bristow 1995; Miall 1996; Ghinassi et al. 2016) (Figure 2.6B). Bedforms climb obliquely over the surface of the underlying macroform and build up to form sets and cosets that dip normally to the palaeoflow direction. Lateral accretion elements represent the outward marginal growth of barforms.

The element typically comprises trough and planar cross-bedded sandstones and planar laminated mudstones and siltstones (St, Sp and Fl) facies (Table 2.1). Intermittent variations in discharge and flooding events, where material is washed in from the flood plain (Nanson and Croke 1992), can provide fine-grained deposits lining coset boundaries. The top of the elements are usually defined by bar-top facies (Figure 2.6A; Sh, Sr, Fl) (Miall 1996). Palaeocurrent show that dune-scale bedforms migrate up or obliquely over the lateral accretion element producing palaeocurrents readings approximately normal to the local channel flow direction, and opposite to the coset clinoform surface generated by accretionary events. Such barforms have been characterised in the modern the Wabash River, USA (Jackson 1976), Jamuna River, northern India (Best et al. 2003), the Powder River, USA (Ghinassi et al. 2016), the Usri River, India (Purkait 2002) and many more examples, and

in the ancient geological record, from the Cretaceous Balckhawk Formation, USA (Miall 1993, 1994; Yoshida 2000, Willis 2000) and the Ferron Sandstone, USA (Li and White 2003), the Tertiary Eureka Formation, Canada (Miall 1979) and the the Jurassic Scalby Formation, UK (Ielpi and Ghinassi 2014).

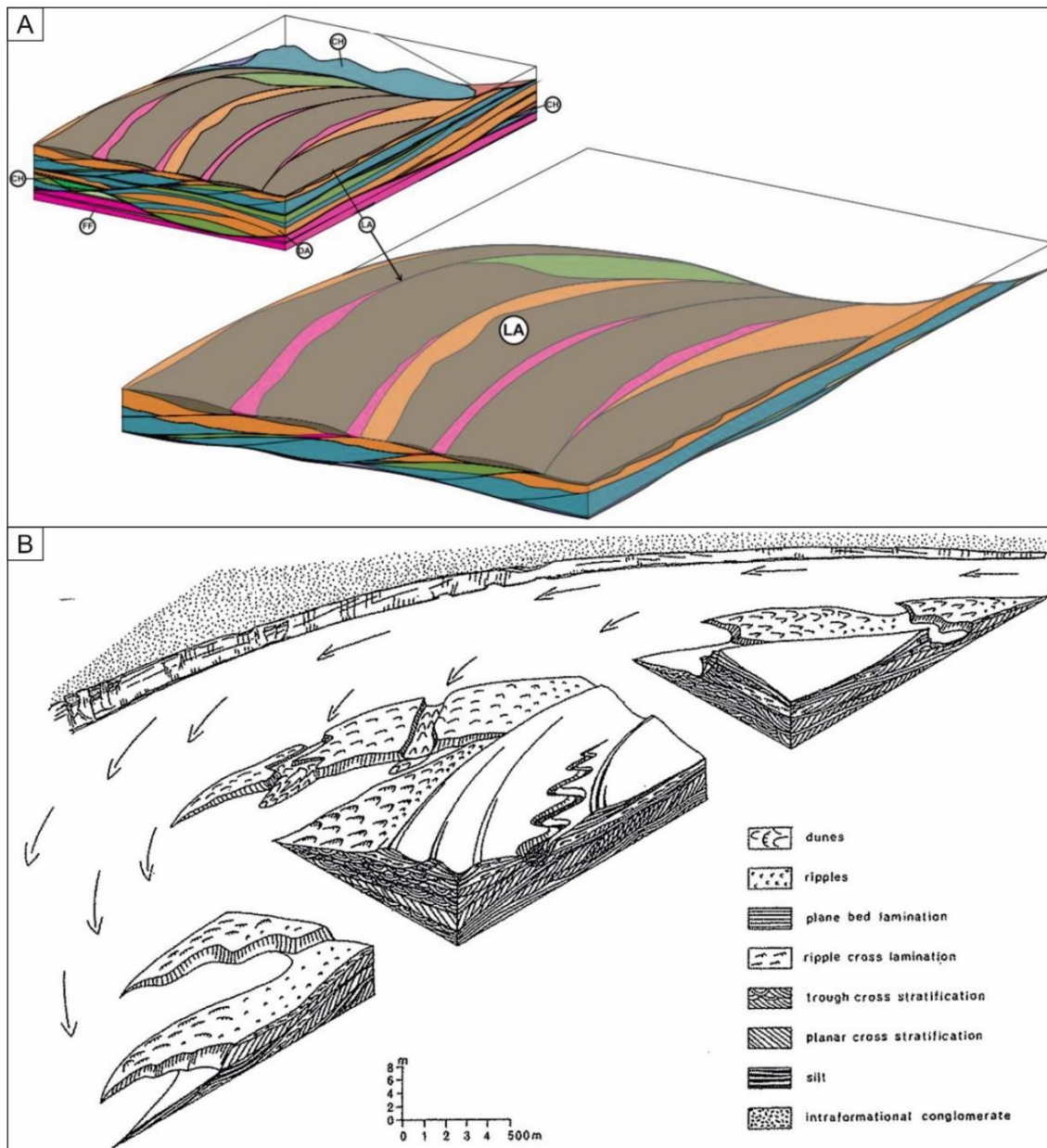


Figure 2.7 – A) Schematic representation of lateral accretion elements and their formation. A) An example of the facies distribution within a lateral accretion element. The notable facies here are blues showing cross-bedded sands, pinks fine-grained silts and browns represent ripple laminated

sandstone facies (After Colombera et al. 2013). B) Lateral accretion element from the Brahmaputra River. Note the oblique migration of dune-scale bedforms on the margin of the element and the upstream accretion present on the upstream portion of the bar (Bristow 1995).

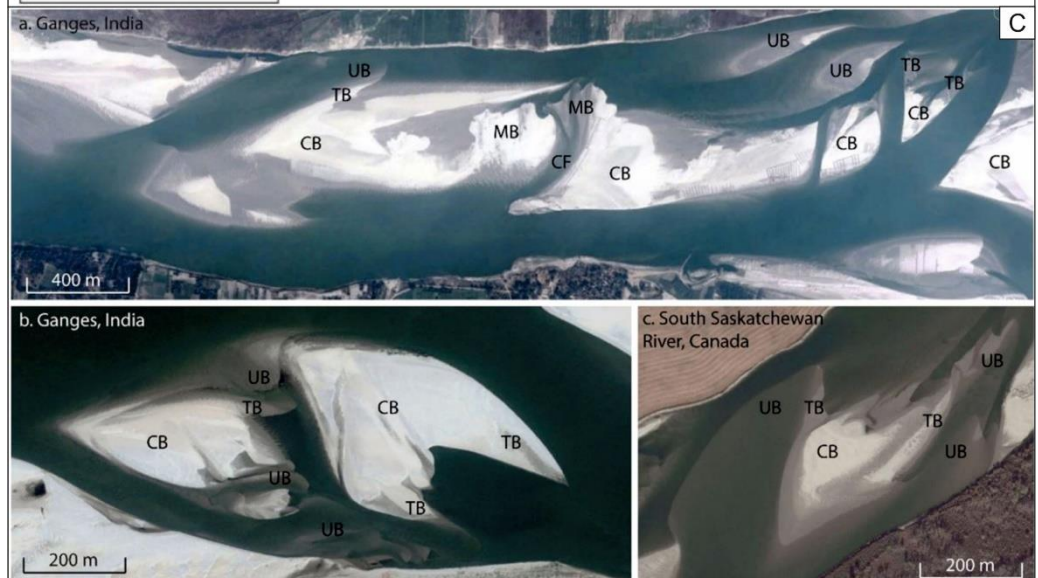
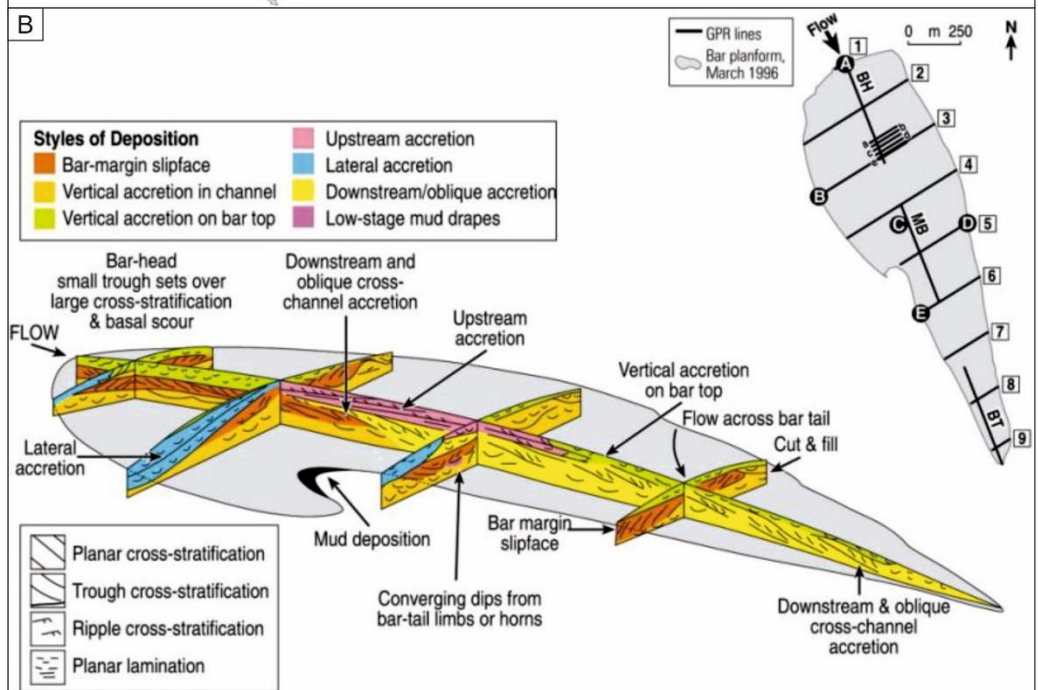
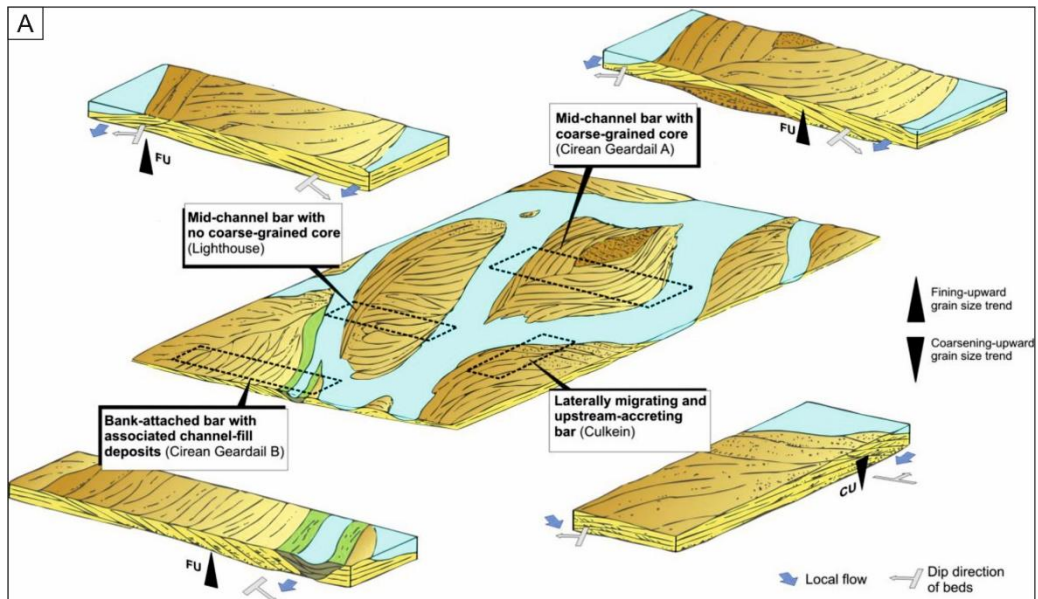
2.3.4 Compound bars

Compound bars comprise two or more-unit bars and represent multiple growth events. Central to growth of compound bar strata is a core or parent unit bar (Figure 2.8A). These complex, large-scale macroforms evolve over several growth and erosion phases, and often show no change in over thirty years or more of development (Sambrook Smith et al. 2006). Their plan view geometry is varied, however, most compound barforms will produce horn-like geometries (Cant and Walker 1978) (Figures 2.8B, 2.8C). These barforms have been previously been classified as sand flats (Cant and Walker 1978), megaforms (Bristow 1987) or braid bars (Best et al. 2003; Skelly et al. 2003). Whilst these classifications have previously been separated by slightly different morphologies, they still represent the formation of multiple growth phases surrounding a core unit bar.

Due to their inherently complex multi-process growth, compound barforms exhibit vastly different facies distributions in cross section and from lee to stoss slope (Best et al. 2003) (Figure 2.8B). Although comprising primarily cross bedded strata, some fines, upper flow regime plane beds (at bar tops) and structureless sandstones are present (Best et al. 2003; Ghinassi and Ielpi 2018). Modes of growth for compound barforms are simple aggradation, downstream accretion, lateral accretion and upstream accretion (Figures 2.8A, 2.8B). The presence of upstream accreting elements can be used to identify the early stages of compound bar growth (Bristow 1995; Skelly et al. 2003). Compound bars have been characterised in modern systems such as the Rio Parana, South America (Sambrook Smith et

al. 2009), the Jamuna River, northern India (Best et al. 2003), the South Saskatchewan, Canada (Sambrook Smith et al. 2006; Ashworth et al. 2011; Lunt et al. 2013) (Figure 2.8C). However, such barforms are still poorly defined within the ancient geological record, with only a few studies characterising complex macroform growth, most notably, the Torredonian Applecross Formation, Scotland (Ghinassi and Ielpi 2018) and the Jurassic Rockcave Member of the Yungang Formation, China (Li et al. 2015).

Figure 2.8 (next page) – A) Schematic representation of compound barform growth from the Torredonian Applecross Formation, Scotland (Ghinassi and Ielpi 2018), showing the complex interaction of lateral accretion elements and downstream accretion elements (much like in Figure 2.5B) around a central parent core unit bar. The image also provides evidence of upstream accretion on the upstream margin of the southernmost barform, similar to that shown in Figure 2.6B. B) Fence diagram of a GPR survey taken from the Jamuna River (Best et al. 2003). The barform is dominated (on the downstream section by downstream accreting cosets of cross-bedding. The flanks of the element are dominated by lateral accretion and the tops by upstream and vertical accretion strata. C) Examples of compound and unit bar development from the South Saskatchewan River (Ashworth et al. 2011).



Upstream accretion elements

One proposed indicator of primitive compound barform formation is the presence of upstream accretion architectures (Bristow 1993; Skelly et al. 2003). Upstream accretion elements have been extremely poorly characterised in literature. From the limited studies conducted, they occur as a result of bank-low discharge when planar and sinuous bedforms amalgamate on the upstream margin, or stoss slope, of compound bars and stack to the water depth (Bristow 1993; Skelly et al. 2003; Wang and Plink-Björklund 2019b). This stacking causes back-stepping of bedform migration and the development of low-angle accretionary surfaces that dip upstream (Bristow 1995; Skelly et al. 2003) (Figure 2.6B). Small-scale scour surfaces are produced by scour pits generated by eddies as dunes migrate (Hadjek and Heller 2012). Such barforms have been found within the modern Niobrara River, Nebraska (Skelly et al. 2003) and the Jamuna River (Ashworth et al. 2000) along with the Cretaceous Castlegate Sandstone (McLaurin and Steel 2007).

2.3.5 Channel fill elements

Channel fills in this thesis are described as units that represent a cut-and-fill event where a channel flow erodes down into the underlying sediment creating a concave-up erosional base (Miall 1985; Hornung and Aigner 1999) (Figure 2.9A). As the flow wanes the element backfills with a fining upwards facies succession. In this context the channel shows no distinct macroform growth and the element has been defined separate from the higher order scale channel (Miall 1985; Ghazi and Mountney 2009) (Figure 2.9B). Channels are bound by erosively based fifth-order bounding surfaces and typically show channel-lag facies overlying the basal erosional surface in the topographically lowest portion of the channel (Miall 1993; Li et al. 2015). The top of a channel is either gradational, grading from waning flow deposits

of the channel into floodplain sedimentation, or is erosional, due to a subsequent channel cut-event (Miall 1993; McLaurin and Steel 2007) (Figure 2.9C). The geometry and size of a channel fill is defined by its width to depth ratio (Gibling 2006). These elements are typically filled by single dunes or minor trains of dunes that stack and aggrade, filling the channel as the flow wanes (Ghazi and Mountney 2009) (Figure 2.9B). These elements typically show very poor preservation of sedimentary structure. If a channel is abandoned this may cause it to fill with fine grained material from the surrounding area in flood events (Nanson and Crooke 1992) to form a channel plug. These elements are recognised in every fluvial environment.

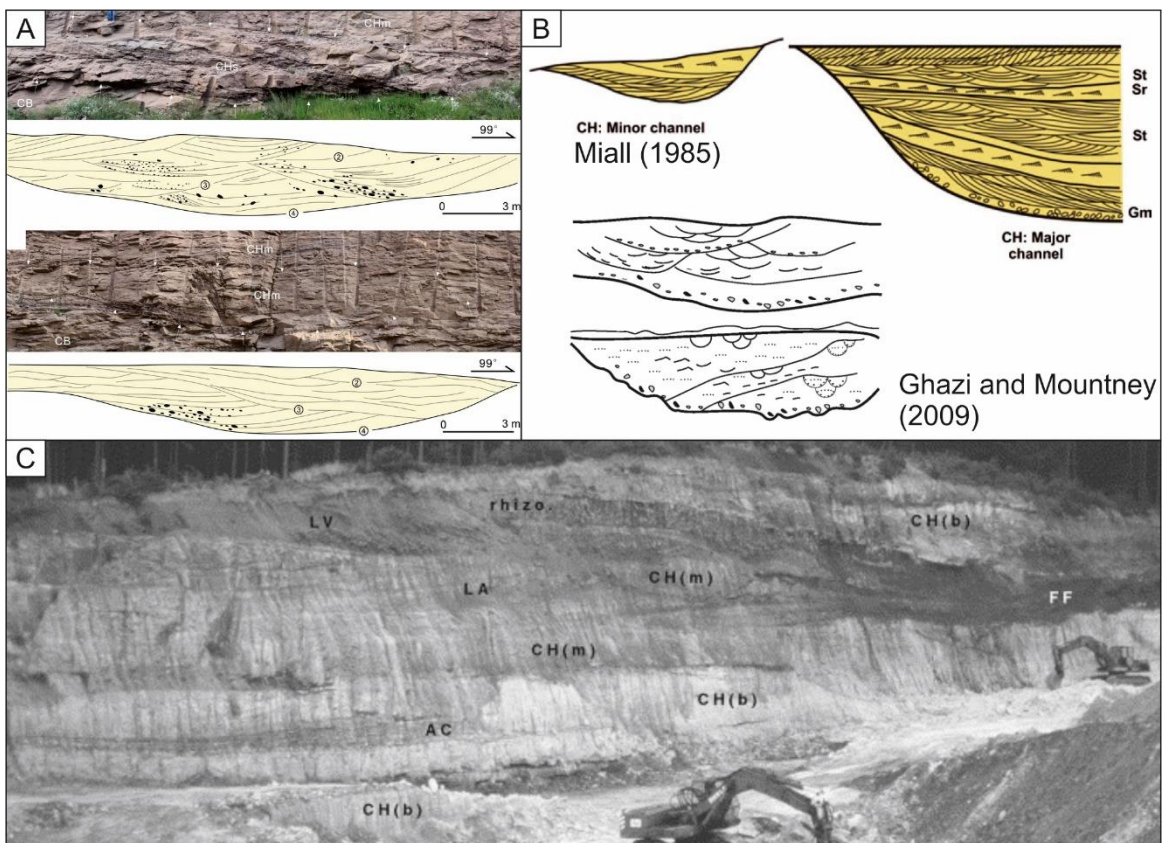


Figure 2.9 – A) Channel fill deposits from the Yungang Formation (Li et al. 2015). B) Schematic representations of channel fills in fluvial deposits (Miall 1985; Ghazi and Mountney 2009). C) Quarry face showing channel fill elements with both gradational and erosional tops, example from the Upper Triassic Stubensanstein, Germany (Honrung and Aigner 1999).

2.4 Plan-view fluvial styles

Fluvial style is governed by a wide variety of autogenic and allogenic controls, these controls dictate the formation of architectural elements and transport mode. Architectural elements are used to understand the nature of a fluvial system in three-dimensions, and the style of its deposition. Below is description of the two most dominant end members of sandy fluvial systems as they appear in plan view. Miall (1996) recognised sixteen types of fluvial system, six gravel dominated, two ephemeral systems and eight perennial sandy styles of fluvial deposition. This review concentrates on Miall's (1996) "sand-bed meandering", "shallow, perennial, sand-bed braided" and "deep, perennial, sand-bed braided" rivers, combining the latter two to create two simple end members, due to their basinal position.

Perennial sand-bed braided fluvial systems (Figure 2.10) have a relatively consistent flow, despite mild seasonal fluctuations in discharge. The main mode of transport for sediment is as bedload. Braided systems typically have multiple active channels acting in a single channel reach (Figures 2.8A, 2.10B), where avulsion and local in-channel hydrodynamic changes are commonplace. These systems are found most commonly in the more proximal reaches of the fluvial environment. These systems are likely to show multiple channel abandonments, and minimal vegetation (Figure 2.10B). As the system evolves, channels stack and amalgamate in an aggradation fashion, showing frequent small-scale avulsions within the channel complexes (Bridge 1993) (Figure 2.10C). Channel avulsions can stretch across channel reaches and limit the development and preservation of overbank facies.

The typical architectures associated with these systems are downstream accreting unit bars and compound barforms. These macroforms show a complex arrangement of internal bounding surfaces and the presence of fourth-order element tops is extremely rare due to

superimposed small- and large-scale channel scours. The dominant facies in an idealised succession of perennial sand-bed braided fluvial systems are trough and planar cross bedded sandstone, these are either confined and isolated to channel fills or to element accretion forms. These braided systems can be found over a wide variety of tectonic settings and have been extensively studied. Examples of these systems have been reported in the modern environment, such as the South Saskatchewan (Cant and Walker 1978; Ashworth et al. 2011) and the Jamuna rivers (Bristow 1995; Best et al. 2003) (Figure 2.9B); and in the geological record in the Campanian Castlegate Sandstone of the Western Interior Sea Way Basin, Utah (Miall 1993, 1994; Yoshida 2000) the Yungang Formation, China (Li et al. 2015) (Figure 2.9C), the Sherwood Sandstone of the UK Midlands (Wakefield et al. 2015) (Figure 2.9A) and the Salt Wash Member of the Morrison Formation, of the Paradox Basin, Utah (Robinson and McCabe 1997).

Perennial sand-bed meandering fluvial systems (Figure 2.10) have a relatively consistent flow, despite mild-seasonal fluctuations in discharge. The main mode of transport for sediment is as bedload. Meandering systems typically have a single active channel acting in a single channel reach, where sinuous migration of the fluvial system is common (Figure 2.11A). These systems are likely to show point bar deposits (large-scale lateral accretion deposits), and large amounts of overbank facies that commonly show vegetation. As the system evolves, channels migrate laterally (Figure 2.11B) until a meander becomes too tight and it eventually joins at its hinges, this is called neck cut-off, the most common mode of local avulsion in meandering systems.

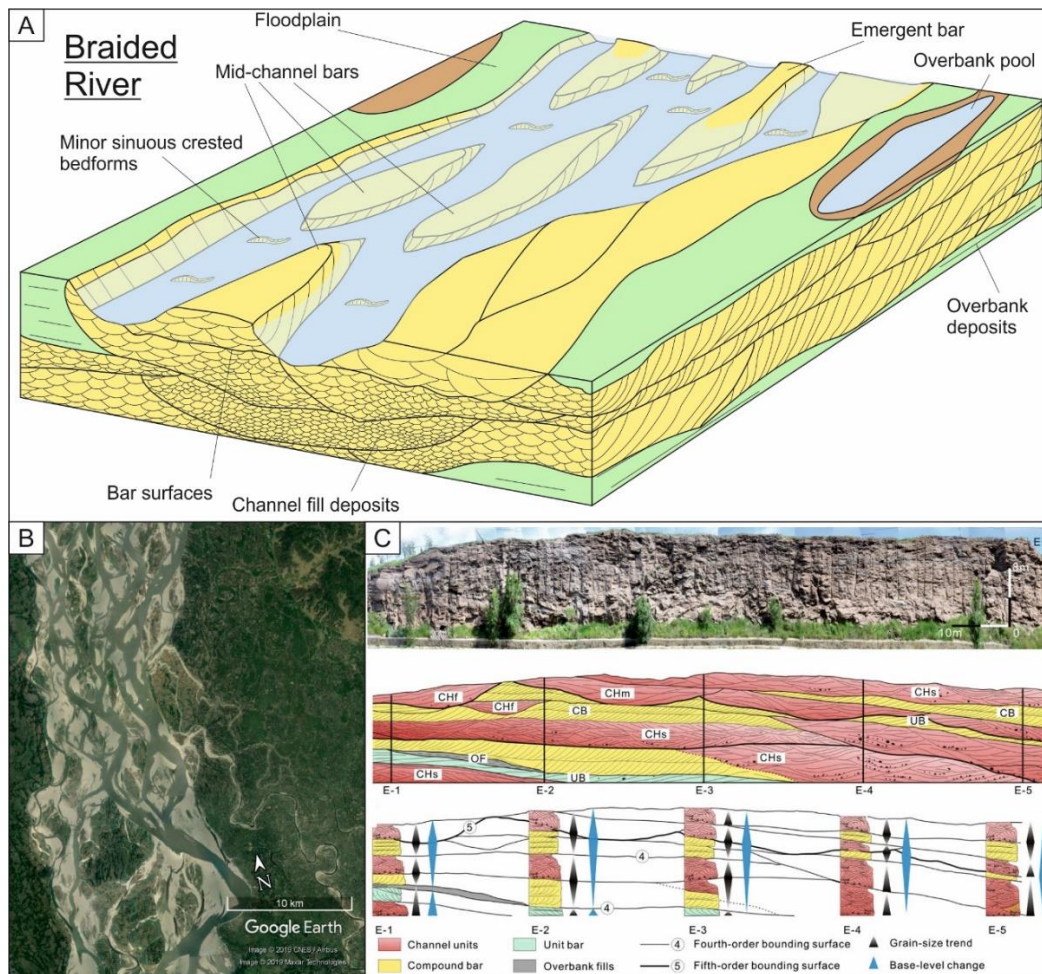
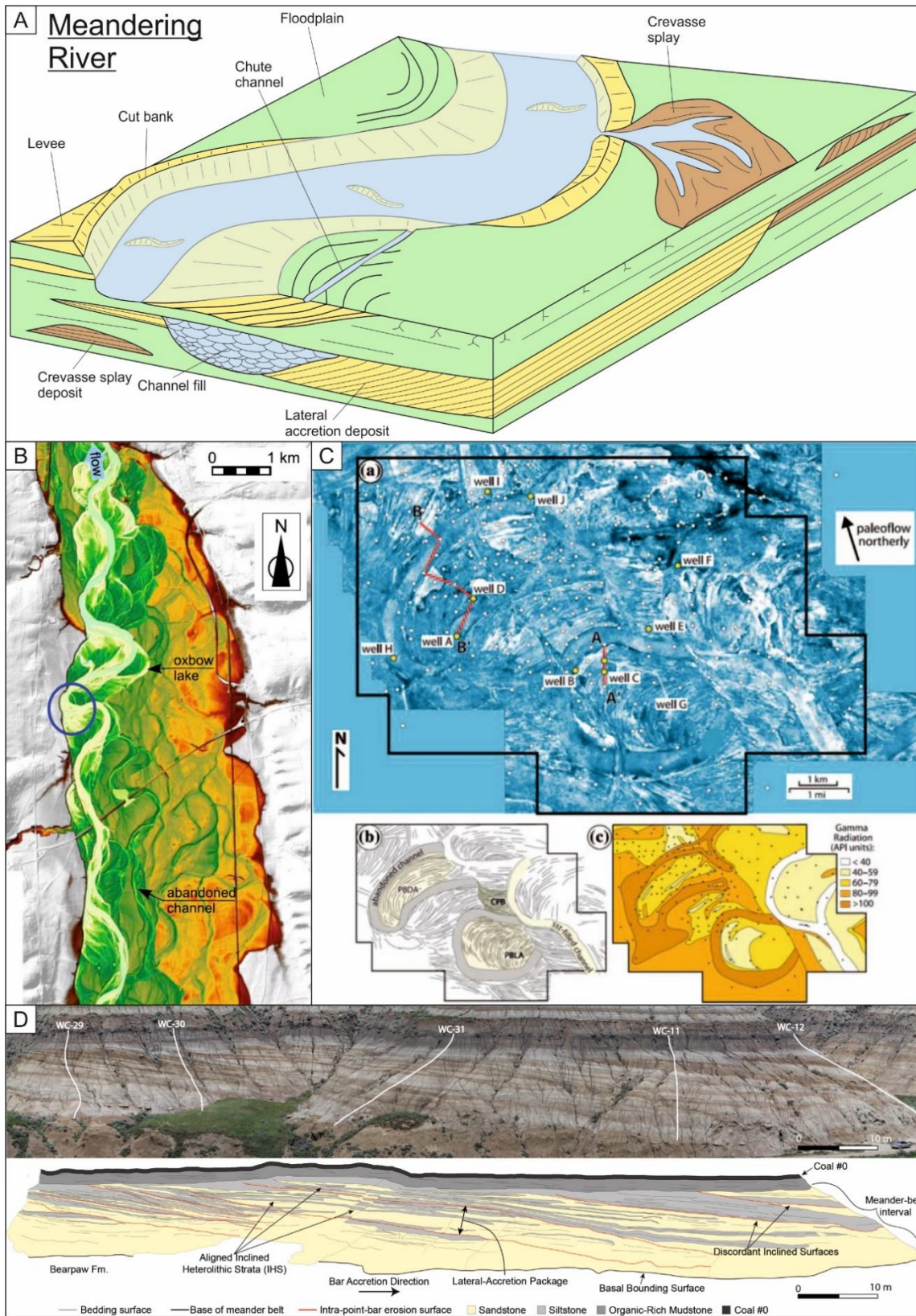


Figure 2.10 – A) Schematic representation of a braided river, example from the Sherwood Sandstone of the UK midlands (After Wakefield et al. 2015). B) Aerial image of the Jamuna River, northern India taken from Google Earth showing the multiple active channels and complex compound architecture formation associated with braided fluvial deposits. C) Panel section of an outcrop from the Yungang Formation, China, showing complex channel stacking and avulsions, with the presence of compound and unit barforms (Li et al. 2015).

The architectures associated with these systems are lateral accreting point bar elements and channel fill deposits (Figure 2.11C). These systems are found typically in the more medial or distal reaches of the fluvial environment. The macroforms preserved in this system show an inclined internal bounding surfaces and heterolithic facies assemblages (Figure 2.11D). The presence of fourth-order element tops is common due to the lateral migration of channels

being the dominant process operating in this environment. The dominant facies in an idealised succession of perennial sand-bed meandering fluvial systems is trough and planar cross bedded sandstone with bar top facies. These systems can be found over a wide variety of tectonic settings and are currently being extensively studied. Examples of these systems have been reported in the modern environment, such as the Allier River, France (Viero et al. 2018) (Figure 2.11B) and the South Esk River, Scotland (Bridge and Jarvis 1976); and in the geological record in the McMurray Formation, Canada (Durkin et al. 2017) (Figure 2.10C) and the Dinosaur Park Formation, Canada (Durkin et al. 2018) (Figure 2.10D).

Figure 2.11 next page – A) Schematic representation of perennial meandering fluvial system (After Miall 1996). B) Digital elevation model from the Allier River, France (Viero et al. 2018). Image shows multiple meanders and point bar deposits and how the fluvial system has migrated across its channel reach. C) A seismic amplitude stratal slice through the McMurray Formation (Hubbard et al. 2011). Image highlights the complex nature of meander belts and shows the dominance of lateral accretion point bar elements. D) Outcrop panel interpretation of the Dinosaur Park Formation (Durkin et al. 2017). Image highlights the inclined internal bounding surface framework of point bar deposits and the heterolithic nature of their facies assemblages.



2.5 Allogenic controls and products on fluvial strata

Base level is the most important concept to define in allogenic controlled models of fluvial stratigraphy. Base level is, when applied to the marine realm, is just below sea level due to wave action, and continues through the subsurface of the continent along the line of maximum continental denudation, this point is controlled by aggradational and erosional processes within the fluvial system and therefore the graded fluvial profile, which terminates at the shoreline base level.

2.5.1 *The graded fluvial profile*

The theory of a graded fluvial profile dictates the aggradation or incision of fluvial systems depending on discharge and sediment input rates. If a system has greater sediment supply than the discharge of a fluvial system is capable of carrying, the system will aggrade. Conversely, if the system has a lesser sediment supply than discharge, then a system will incise. The principle concept behind graded profiles is that a river will always try to return to its equilibrium profile (Holbrook *et al.* 2006; Bhattacharya 2011; Miall 2014). The graded fluvial profile is a representation of a river's stable gradient, when erosion and deposition are balanced (Mackin 1948; Sloss 1962; Miall 1987; 1992b; Emery & Myers 2009). The profile can be heavily controlled by uplift or subsidence rate and the erodibility of the underlying strata (Merritts *et al.* 1994; Howard *et al.* 1994). The graded profile of a fluvial system is pinned to a distal control beyond which fluvial deposits cannot significantly aggrade or channels cannot significantly erode. This distal control is commonly base-level, known as a "buttress" (Figure 2.12). Second to buttress control is the buffer zone. The buffer zone controls the preservation space (accommodation space) of a fluvial system and its ability to aggrade and incise.

The graded profile buttress is controlled by changes in eustatic sea-level, accommodation space and climate. These long-term allocyclic variations produce stratigraphic boundaries within the deposited sediments and can provide a framework for sequence stratigraphical analysis (Posamentier 1988). The upstream controls on the graded fluvial profile consist of climate, bedrock and tectonics (Figure 2.12) (Cant 1978; Miall 1981; Westcott 1993). Midstream controls intrabasinal tectonics; for instance, tectonic tilting can produce asymmetric subsidence and the creation of a new topography on the previously established slope (Miall 1981; Alexander & Leeder 1987; Kraus & Middleton 1987; Wells & Dorr 1987; Emery & Myers 2009). Downstream changes to the fluvial system are mainly dictated by fluctuations in relative sea-level (Figure 2.12); for example, a relative sea level drop can produce a steepening of the gradient, leading to a river system to adapt so that it may return to its equilibrium profile (Shanley & McCabe 1994; Catuneanu 2006). To return to its equilibrium profile, a river will not simply incise or aggrade, these are end results of internal variations within the fluvial system. These internal variations may include the changing of load characteristics, in channel architectural (bar) morphologies and sinuosity profiles (Schumm & Ethridge 1991; Miall 1991a; Schumm 1993; Emery & Myers 2009).

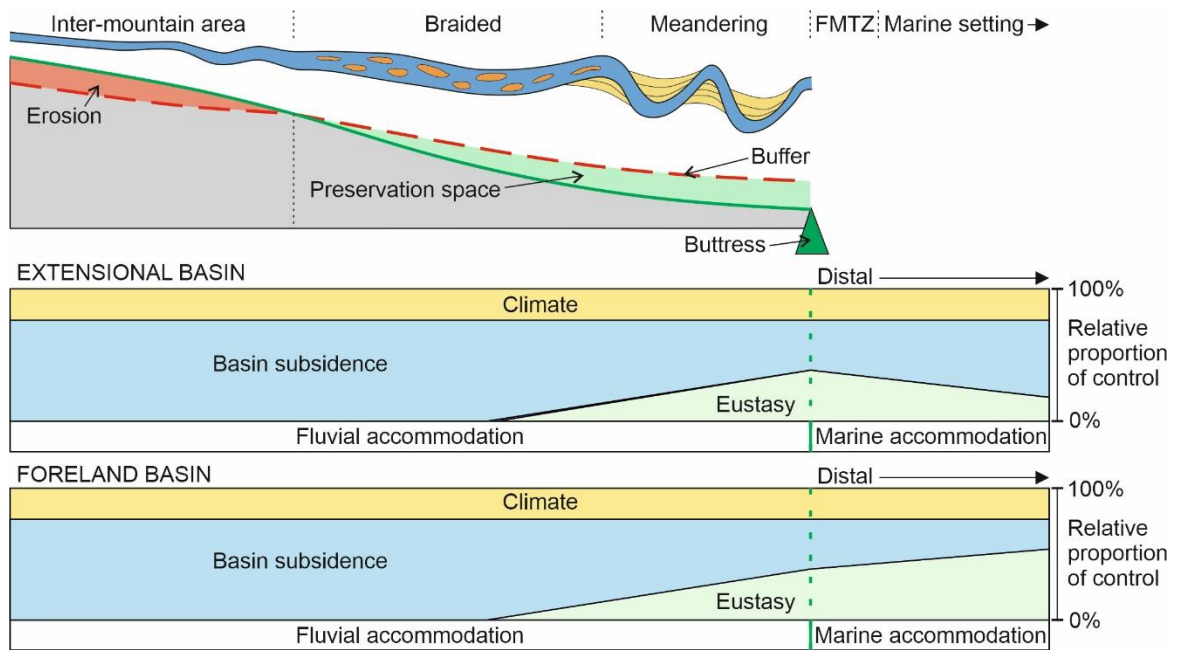


Figure 2.12 – Simplified model of downstream variations in plan-view fluvial style proximal of the fluvial marine transition zone (FMTZ), where marine base-level becomes the dominant allogenic control upon deposition (After Li et al. 2015). This margin is known as the buttress of the fluvial system. The gradient associated with fluvial systems and the graded profile is highlighted in red showing the buffer and preservation space associated with fluvial deposition (After Holbrook et al. 2006, Li et al. 2015). Basin-scale allogenic controls in extensional and foreland basins, showing controls on accommodation space and their spatial distribution through a basin. Note the “y-axis” indicates the relative proportion of a controls influence at a point in the basin (After Catuneanu 2006).

2.5.2 Sequence stratigraphy in fluvial deposits

The first principles of fluvial sequence stratigraphy as described by Miall (2002) are: (1) fluvial incision occurs when base-level falls, which produces an increase in flow discharge and reduced sediment load; (2) vertical accretion facies (Miall 1992b) dominate during base-level rise with an increased sediment load and reduced discharge; (3) fluvial evolutions induced by base-level and climate are controlled by tectonic and eustatic fluctuations and climate respectively; (4) low sinuosity fluvial systems dominate periods of low accommodation; (5)

anastomosing systems are usually confined to transgressional systems; (6) high sinuosity systems dominate stages of low to medial rates of base-level rise; (7) incised valley fill sequences may be produced by any one or multiple types of fluvial system; (8) marine influence fluvial strata (tidal features) indicate flooding and a period where the rate of increasing accommodation space is greater than the rate of sediment input. This guide has been used in previous studies such as: Murray and Dorobek (2004); Boyd *et al.* (2006); Catuneanu (2006); Ethridge and Schumm (2007); Fanti and Catuneanu (2010); Gibling *et al.* (2011).

The recognition of a sequence boundary in fluvial strata is extremely difficult. This is primarily due to rapid lateral facies variations, downstream variation and migration of facies and localised channel incision (Posamentier *et al.* 1988; Van Wagoner *et al.* 1990; Posamentier & Weimer 1993; Westcott 1993; Richards 1996). The most commonly identified sequence boundaries within the fluvial realm (in the more distal reaches of the fluvial system) are incised valleys and their associated fill, which construct the subsequent systems tract (Boyd *et al.* 2006; Miall 2010; 2016). These are often recognised as a juxtaposition of environmentally distinct facies, for example, marine shales against pedogenic overbank deposits (Van Wagoner 1990; Van Wagoner *et al.* 1990). More proximally, sequence boundaries must be identified by variations in channel stacking patterns and vertical diversities in fluvial style (Shanley & McCabe 1994), on the channel set scale.

The more proximal areas of the fluvial system are highly affected by source tectonics, climate and basin subsidence (Figure 2.12). These controls are independent of marine base level variations within the distal portion of the fluvial system and operate by varying the graded fluvial profile of the system to affect depositional or erosional architectures to accommodate

such variations in the profile. These proximal areas are therefore characterised by low- and high-accommodation systems tracts.

Climatically driven cycles often operate on a Milankovich-scale of cyclicity, with changes producing cycles of glaciation in the sediment record. Such cyclicity is evident in the phases of incision and aggradation within the proximal fluvial system. Periods of deglaciation induce an increase in stream discharge relative to sediment supply creating an erosional phase. The opposite is produced during a stage of glaciation; where discharge decreases relative to sediment supply producing an aggradation phase (Blum 1993, 2001; Catuneanu 2006). Tectonic controls change the topographic gradient acting upon the fluvial system, for example an uplift event in the hinterland will increase the discharge of the fluvial system (Catuneanu & Sweet 1999; Catuneanu & Elango 2001; Catuneanu 2006) and therefore create a period of incision (this may occur only in the hinterland, followed by a large increase in the sedimentation rate of the distal portion of the fluvial system). Subsidence will tend to produce the opposite, by shallowing the slope gradient and creating a period of deposition due to decreased discharge. Subsidence will produce the same effects and depositional products as a base level rise and a stage of climatic cooling (Catuneanu 2006). These two processes occur as a result of the climate cyclicity affecting the fluvial graded profile and the fluvial system attempting to re-equilibrate to it (Holbrook et al. 2006).

2.5.3 Systems tracts of fluvial sequence stratigraphy

Complex allogenic controls on the fluvial system make it difficult or impossible to constrain syn-depositional shoreline migrations in non-marine or overfilled basins. Therefore, the application of *traditional* systems tracts and sequence stratigraphy is extremely problematic (Figure 2.13). Dahle *et al.* (1997) considered sequence stratigraphical constraints for non-

marine/non-lacustrine influenced successions and proposed the newly defined *low-* and *high-accommodation* systems tracts. This was as result of early fluvial sequence stratigraphical models, using traditional relative sea-level based systems tracts, being argued by authors such as Blum (1990; 1993), Miall (1991b), Schumm (1993), Wright and Marriot (1993) and Shanley and McCabe (1994).

The two models may be used contemporaneously to cover the spatial extent of a marine influenced basin, the traditional model of lowstand, transgressive, highstand and falling stage systems tracts can be applied to the marine influenced extent of a basin and the distal proportion of the fluvial system (Figure 2.13). These systems are both influenced by a controlling eustatic sea level curve. However, as shown in Figure 2.13, no such control acts upon the proximal portion of a fluvial system (Catuneanu 2006). This is where the low- and high-accommodation systems tracts may be applied and used to correlate to the more distally applied traditional sequence stratigraphical model.

Low- and high-accommodation systems tracts (Table 2.4, Figure 2.13) refer to the packages of fluvial sediment that are analysed separately from their coeval marine deposits. These are defined (in large part) by fluvial architecture, channel fill and overbank deposition and their relation to the space available to accommodate the fluvial system (Dahle *et al.* 1997; Catuneanu 2006). These systems tracts are not to be confused with low- and high-accommodation settings, which indicate the points in the basin that have high and low amounts of available accommodation (Catuneanu 2006) (normally created by local tectonics). It should be noted that the model is not as simple as positive accommodation deposition in a high-accommodation setting, and vice versa. A low- or high-accommodation

systems tract may be deposited within a high-accommodation setting due to differential subsidence during the positive accommodation cycle (Olsen *et al.* 1995; Arnott *et al.* 2002).

The low-accommodation system tract (Table 2.4) typically overlies a subaerial unconformity and begins with a progradational (with limited aggradation) coarsening upwards phase in the fluvial strata produced by rejuvenated headwater expansion and hinterland erosion; therefore, the finer material tends to be bypassed (Leckie *et al.* 2004). When marine influences are considered, these are commonly confined to the incised valley (Boyd *et al.* 1999), created by a relative sea level fall. Hence, this portion of deposition may be correlated to the lowstand systems tract (Catuneanu 2006) of the traditional sequence stratigraphical model. This basal phase of the systems tract thickens downstream due to rejuvenation in the sediment source areas and higher discharges due to topographic steepening in the distal portion of the system. Heller *et al.* (1988), Sweet *et al.* (2003; 2005), Ramaekers and Catuneanu (2004) and Catuneanu and Sweet (2005) have recognised these progradational phases.

Systems Tract Features	Low-accommodation systems tract	High-accommodation systems tract
Depositional trend	early progradational	aggradational
Depositional energy	increasing at first, followed by decrease through time	decrease through time
Grading	coarsening upwards at the base	fining upwards
Grain size	coarser	finer
Geometry	irregular and discontinuous	tabular to wedge-shaped
Sand:mud ratio	high	low
Reservoir architecture	amalgamated channel fill	isolated ribbons of sandstone
Floodplain	sparse	abundant
Thickness	thinner	thicker
Coal seams	minor if not absent	well developed
Palaeosols	well developed	poorly developed

Table 2.4 – *The typical characteristics of the low- and high-accommodation systems tracts when applied to fluvial strata (After: Catuneanu 2003; Leckie & Boyd 2003; Catuneanu 2006).*

This basal progradational proportion of the low-accommodation systems tract signifies an increase in energy within the fluvial system. Basal progradation of coarse-grained terrigenous sediments is diachronous and youngs in the direction of the source material, this is due to the lag time (Catuneanu 2006) associated with the re-establishment of the fluvial equilibrium profile. Following the basal progradational facies, the energy of the fluvial system wanes as the positive accommodation cycle ends (Sweet *et al.* 2003, 2005; Catuneanu & Sweet 2005). The low-accommodation systems tract is often a multi-storey sandbody, confined to an erosional topographic feature (much like an incised valley fill) that was created during the previous negative accommodation phase (Catuneanu 2006).

The high-accommodation systems tract (Table 2.4) represents a period in which fluvial accommodation is created. The systems tract consists of a greater amount of finer material than the low-accommodation systems tract, and are positionally similar to the transgressive and highstand systems tract of the traditional system. The overall depositional model is aggradational (Boyd *et al.* 1999) with a large amount of what Allen (1970) called vertical accretion deposits (overbank material). This is due to a high-water table in relation to the palaeotopography. Flow energy wanes throughout the systems tract and produces a fining upwards succession (Catuneanu & Sweet 1999, 2005; Catuneanu & Elango 2001; Sweet *et al.* 2003, 2005; Ramaekers and Catuneanu 2004; Catuneanu 2006). The high-accommodation systems tract is also characterised by frequent and well-developed coals; however, palaeosols are rare and poorly developed (Catuneanu 2003; Leckie & Boyd 2003; Catuneanu 2006). This is a product of a high-water table in a subsiding basin (Catuneanu 2006) and the continual aggradation of the fluvial system, respectively.

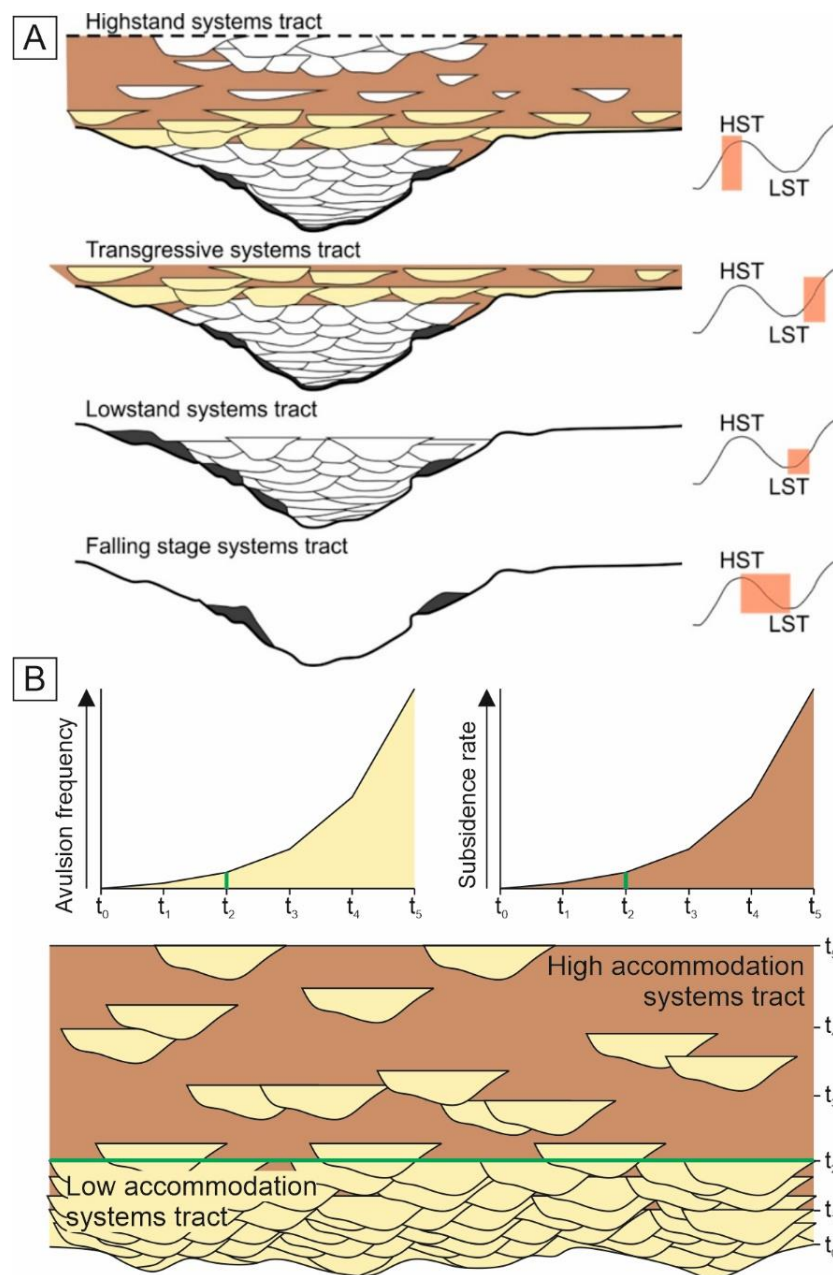


Figure 2.13 – Fluvial stratigraphic architectures across the four traditional systems tracts. The falling stage systems tract creates erosional down-cutting forming valley fill; lowstand systems tract material shows incised valley fill of stacked channels; the transgressive systems tract consists of overbank deposition (brown) and tidally influenced isolated channels (yellow); finally, the highstand systems tract showing stacked channel complexes over a wider spatial distribution. Note: the main black line at the base of each image is the incised valley and sequence boundary, to the right of each image is the position of the systems tract superimposed in red upon a eustatic sea level curve, HST – highstand systems tract, LST – lowstand systems tract (After Shanley & McCabe 1993; Cantuneanu 2006).

2.6 Stratigraphic architecture

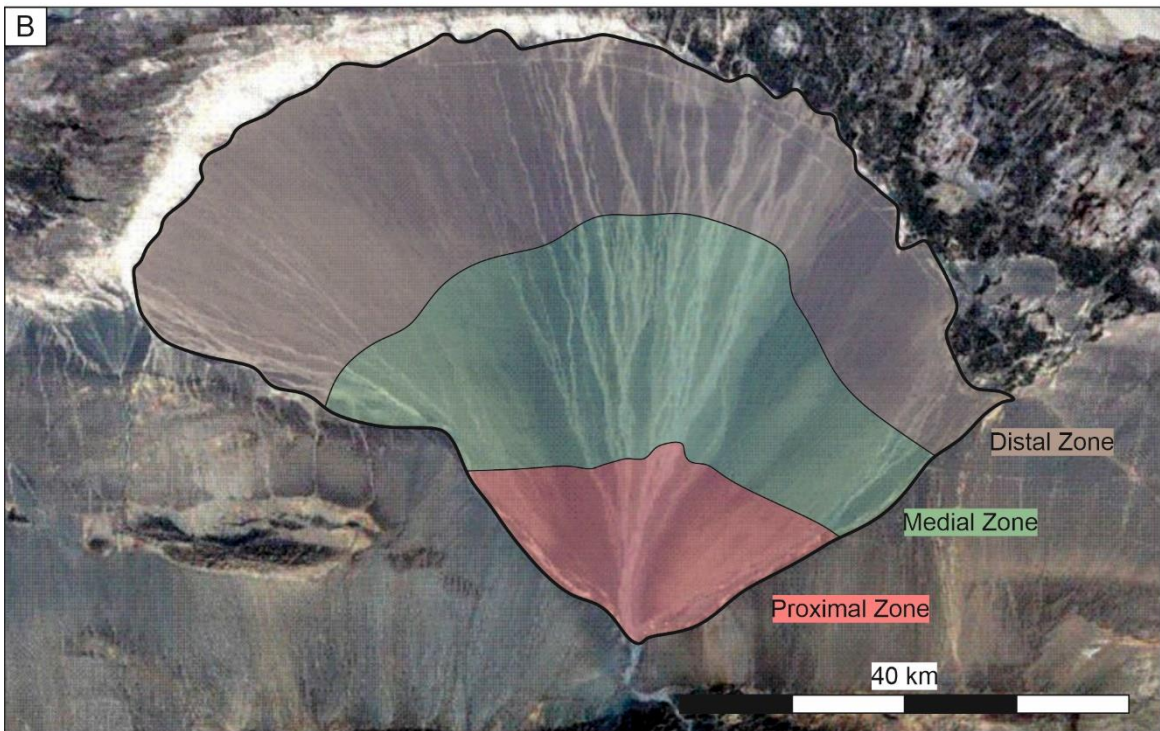
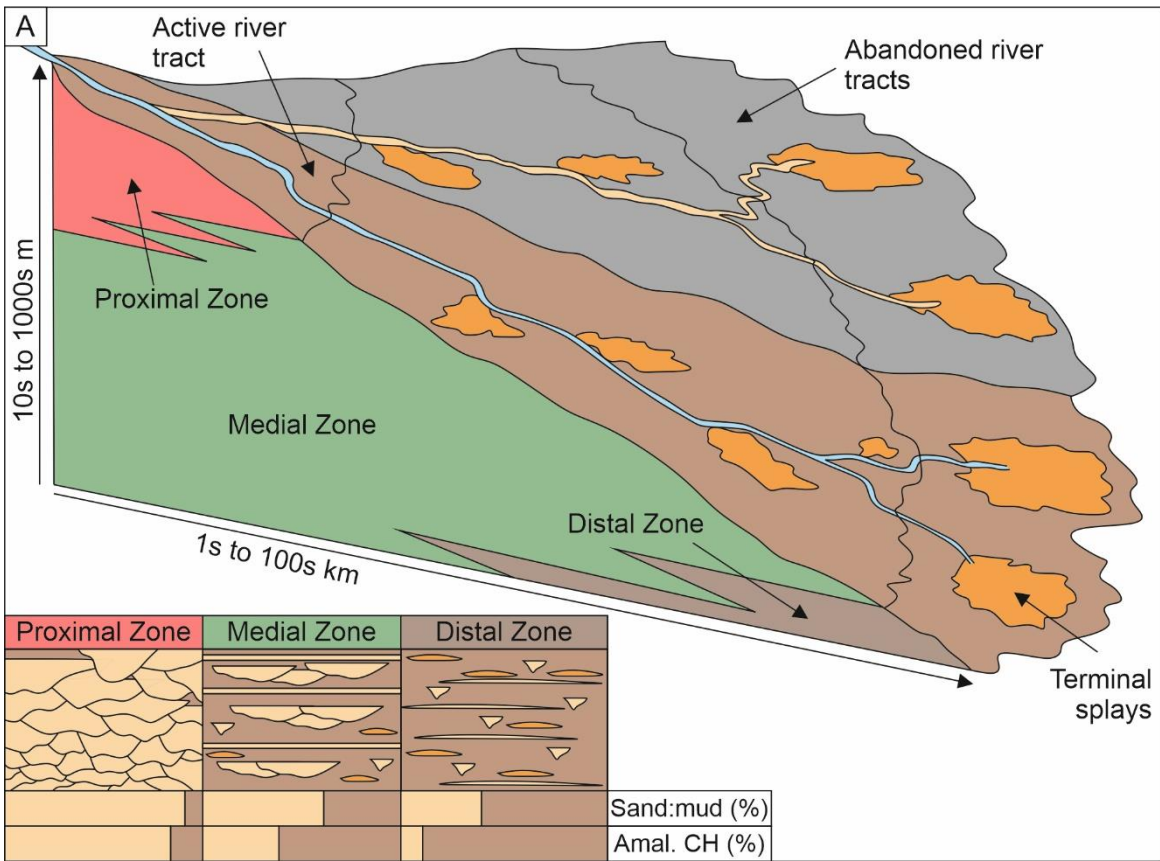
Stratigraphic architecture operates at the tens to thousands of metres scale and is bound by seventh- and eighth-order bounding surfaces. There are many models for stratigraphic architecture and palaeomorphological style in fluvial systems, considered here is the most rigorously tested of these in modern literature, the distributive fluvial system (DFS) model.

The DFS model describes the radial deposition of a fluvial system; where the proportion of sand, the grain size and channel thicknesses decrease downstream (Owen et al. 2015), and channel sinuosities increase towards the distal zone (Nichols and Fisher 2007). Deposition and transport of alluvium radiates from a proximal apex (Weismann et al. 2010), such as a headwater valley (Mikesell et al. 2010) in the inter-mountain region (Li et al. 2015). When the fluvial system leaves the highland confined area it becomes unconfined laterally, radiating fluvial deposition over the sedimentary basin as a wedge. A DFS can range from 1 - 100s km in length (Figure 2.13), depending upon the basin and river size. DFS deposits typically terminate at a large body of water (be it an axial fluvial system or a lake), however, in endorheic basins they simply grade distally onto the alluvial plain.

The proximal zone of a DFS exhibits the coarsest deposition and the deepest channels within the system. These channels are often amalgamated (>70% of deposits in the proximal portion) and very little overbank is preserved, typically accounting for less than 20% of the proximal succession. Fluvial facies in the proximal zone are usually representative of braided to straight fluvial systems, with bedload transport dominating (Nichols and Fisher 2007; Owen et al. 2015). The medial zone of the DFS can be identified by a decrease in the grain size, typically very few extraformational conglomerates (Nichols and Fisher 2007), and a decrease in the amalgamation and depth of channel fill deposits. The proportion of overbank

preserved increases to approximately 40% and sheet-like deposition following bank full flood events can be observed. Amalgamated channel-fills are typically much lower at approximately 40% of the medial zone succession (Owen et al. 2015), lowering channel connectivity. The distal zone of the DFS is easily identified by large preservation of overbank material (>60%) and the presence of extremely isolated (<20% of amalgamated channels comprises this succession) and small distributary channel deposits (Nichols and Fisher 2007; Owen et al 2015). The distal zone shows the lowest grainsize as the discharge rates in the area are low comparative to that of upstream areas. Sheet-like deposits are more typical than in the medial zone with unconfined and unlimited lateral deposition dominating the succession.

Figure 2.14 next page – *The distributary fluvial system (DFS). A) Schematic representation of a DFS running from an apex down onto the alluvial plain within the basin. The schematic highlights the radial abandonment and activation of channel reaches (or tracts) across the fan-like system. Proximal medial and distal zones are highlighted and progradation of these is shown. Approximate architectural make-ups of the DFS are shown in the table, representing channel stacking and overbank preservation for each zone. Estimations of the proportion of architectures found within each zone are also included (modified from Nichols and Fisher 2007; Owen et al. 2015, 2017). B) The northern Quilian Mountains DFS from China is shown and annotated according to its zonations shown in A (modified from Hartley et al. 2010).*



2.7 Summary

Fluvial systems and their associated deposits are controlled by a complex mix of auto- and allogenic controls. The controls on the deposition of architecture within a fluvial system depend upon the scale of observation. Sedimentary architectural elements are dominantly controlled by local hydrodynamic and bed-plane topographic fluctuations, whereas stratigraphic architecture is more commonly controlled by large-scale regional avulsion mechanisms and basin-scale allogenic controls.

Sedimentary architectural elements are comprised of facies indicative of the flow regime. They are deposited in and an internal and external bounding surface framework. These elements allow fluvial style to be commented on and make-up the constituent parts of a fluvial system. Fluvial style, for perennial sand-bed fluvial systems, have two end members: braided and meandering. Systems often show both down their reach from proximal to distal, and the style shown at a particular locality is controlled, in principal, by gradient and the graded fluvial profile.

The graded fluvial profile is a surface at which a fluvial system will attempt to re-equilibrate to. This surface is controlled by a distal buttress, marine base-level, and a buffer zone that dictates the preservation space of fluvial systems. The graded fluvial system is controlled by allogenic controls, and its fluctuation produces sequence stratigraphic scale architectures that can be combined into systems tracts. Low- and high-accommodation systems tracts are commonly defined in upstream areas away from marine base-level due to the complexities in the identification of stratigraphic surfaces in fluvial strata. Finally, these effects of downstream evolution and graded profile on the fluvial system create stratigraphic architecture that is most commonly that of a distributive fluvial system.

3 The sedimentary architecture of an unconfined fluvial system: example from the Lower Castlegate Sandstone, Utah.

Based upon: Mitten, A.J., Howell, L., Clarke, S.M., Pringle, J.K. (2020). Controls on the deposition and preservation of architectural elements within a fluvial multi-storey sandbody. *Sedimentary Geology*, 401, 105629.

At the time of this thesis submission this article has been **accepted** and **published in** *Sedimentary Geology*.

This chapter describes and interprets the depositional architecture of the Lower Castlegate Sandstone: a Campanian fluvial system that was unconfined and drained a mountain front into the Cretaceous Western Interior Seaway, USA. The chapter does not present rigorous descriptions of the facies present within the Lower Castlegate Sandstone, as these have been published previously by others and are generally accepted. Original field-collected sedimentary logs and terrestrial photogrammetric data enable a detailed interpretation of the sedimentary architecture comprising the Lower Castlegate and how these architectures are preserved along a down depositional-dip profile. This is complemented by published down-hole well data along the same profile, enabling a burial history analysis. The results of this analysis are discussed in terms of allogenic controls and the potential these findings have for sequence stratigraphic interpretation.

3.1 Introduction

Fluvial systems can preserve as multi-storey sandbodies that are formed during one cycle of deposition, by the superimposition of one or more sandbodies upon each another (Bridge and McKay, 1992; Gibling, 2006). This chapter considers the controls on deposition and preservation of an unconfined multi-storey sandbody (in this case, a fluvial sheet-like sandstone). Unconfined fluvial systems, such as braidplains, are those without significant topographical confinement (Gibling, 2006; Chamberlin and Hajek, 2015) and they are dominated generally by aggradation or avulsion (Mohrig et al., 2000). Consequently, their preserved architecture is dependent upon the graded profile of the fluvial system and the aggradation rate (Holbrook et al., 2006). The aggradation rate is most commonly dictated by a complex interplay of autogenic and large, basin-scale, allogenic controls (Holbrook et al., 2006). While autogenic controls on sedimentation can generate highly amalgamated successions (McLaurin and Steel, 2007; Hajek and Heller, 2012; Chamberlin and Hajek 2015), it is more common for large-scale allogenic controls to produce accommodation-based systems tracts in upstream areas (Section 2.7.3) (Catuneanu and Elango, 2001; Leckie and Boyd, 2003; Catuneanu, 2006). These controls include subsidence rate (Leeder, 1993; Heller and Paola, 1996; Bridge et al., 2000; López-Gómez et al., 2010), sediment input rate and climate (Fielding and Paola, 2013).

3.2 Geological setting of the Castlegate Sandstone

The Western Interior Seaway Basin (WIS) (Figure 3.1B) was a retroarc foreland basin that extended north-south from present-day Texas to the Canadian Northern Territories (Dickinson et al., 1986; Lawton, 1986; Miall and Arush, 2001). The basin formed as a result of the late Jurassic to Palaeocene loading of the North American Plate during the Cordilleran Orogeny (Lawton 1986; Kauffman and Caldwell 1993; DeCelles 2004; Miall 2008). The loading occurred in pulses as thrust terranes accreted eastward onto the Laurentian margin. The western orogenic highs supplied sediment to the basin depocentre in the east, with eastward migration of the thrust terranes shifting the basin depocentre to the east along with its sediment sources (Cross 1986; Miall 2008). The Cordilleran migration ceased during the Late Campanian to Maastrichtian Stage with the shallow subduction of the Farallon Plate that led to the Laramide Orogeny (Dickinson and Snyder 1978; Cross 1986; DeCelles 2004; Miall 2008). The Laramide Orogeny produced a more northern migration pattern to uplift, that led to the subsequent north-easterly retreat of the WIS. The result of this normal regression was extensive terrestrial deposition during the end Cretaceous and Palaeogene periods.

3.2.1 *Palaeogeography*

The Aptian Stage was dominated by gravel-bearing fluvial systems that shed sediment from their western provenance and transported it perpendicularly to orogenic strike. These Aptian sediments overlie the Late Jurassic regional unconformity and are sourced from mid-Cretaceous magmatic rocks produced during syn-depositional magmatism during a phase of tectonic quiescence (Stott 1984; Miall 2008). The sediments mark the first deposition of a new constructive phase in the Cordilleran Orogeny - known as the Sevier Orogeny - that was coeval with increased rates of subduction for the Farallon Plate. Increasing subsidence rates

and uncharacteristically high sea levels during the Early Cretaceous Period produced a transgression of the WIS (Heller et al. 1986; 1988; Heller and Paola 1989; Lawton 1994; Cant 1996; Ross et al. 2005).

During the late Cretaceous Period, major transgressions flooded the WIS producing extensive marine deposition. However, regressive phases to sea level cycles caused exposure and extensive erosion. The erosive phases produced huge time gaps within the WIS stratigraphy, some of which span millions of years (Molenaar and Rice 1988; Leckie and Smith 1992). A major transgression occurred at the end Early Cretaceous and deposited marine sands and mudstones of the Mowry Shale, Greenhorn Formation and Ashville Shale.

The Cenomanian transgression continued through until the Turonian, when sea level was at its highest in Earth's history. Such a transgression is thought to be produced by the excessive rates of sea-floor spreading and the rapid break-up of the Pangean supercontinent (Pitman 1978; McDonough and Cross 1991; Heller *et al.* 1996). The Mancos and Niobrara (northern equivalent of the Mancos Shale) Shale formations were deposited during the Coniacian to Palaeogene from Saskatchewan to Texas. These shale deposits are contemporaneous with the progradation of clastic wedges from the Sevier Orogeny. The Sevier tectonic activity was at its maximum during the Campanian due to increased subduction rates of the Farallon Plate. The subsequent flexural loading, produced by orogenesis created rapid rates of accommodation space creation for the deposition of clastic wedge deposits dispersed across the strike of the foreland (Kauffman and Caldwell 1993; Liu and Nummedal 2004; Liu *et al.* 2011). The Mesaverde Group of the Book Cliffs, Utah is one such clastic wedge. During the Maastrichtian the Laramide Orogeny had become the dominant tectonic force and controlled deposition (Lawton 1986; DeCelles 2004; Miall 2008). The orogeny uplifted the southern and

central portions of the WIS Basin and the WIS normally regressed. Post-Maastrichtian sea levels underwent a period of large-scale forced regression until the Eocene, producing large scale terrestrial sedimentation in the WIS Basin (Dickinson et al. 1988; Miall 2008)

3.2.2 *Lithostratigraphy*

The Book Cliffs succession is composed of the Mesaverde Group (Figure 3.1A): a clastic wedge that prograded eastwards (Aschoff and Steel, 2011a, 2011b) from the Sevier Fold and Thrust Belt into the WIS of the North American Cordilleran retro-foreland basin (Dickinson et al., 1986; Lawton, 1986; Robinson and Slingerland, 1998) (Figure 3.1B). The Group grades eastwards from proximal non-marine facies to distal shoreface facies that spatially grade into the contemporaneous offshore sediments of the Mancos Shale (Lawton, 1986; Olsen et al., 1995; Hampson et al., 2005). Broadly, the Group comprises the Star Point Sandstone, the Blackhawk Formation, the Castlegate Sandstone and the Price River Formation (Fouch et al., 1983; Olsen et al., 1995; Seymour and Fielding, 2013). However, the lithostratigraphical nomenclature of the Group changes to the east beyond the town of Green River (Figure 3.1C).

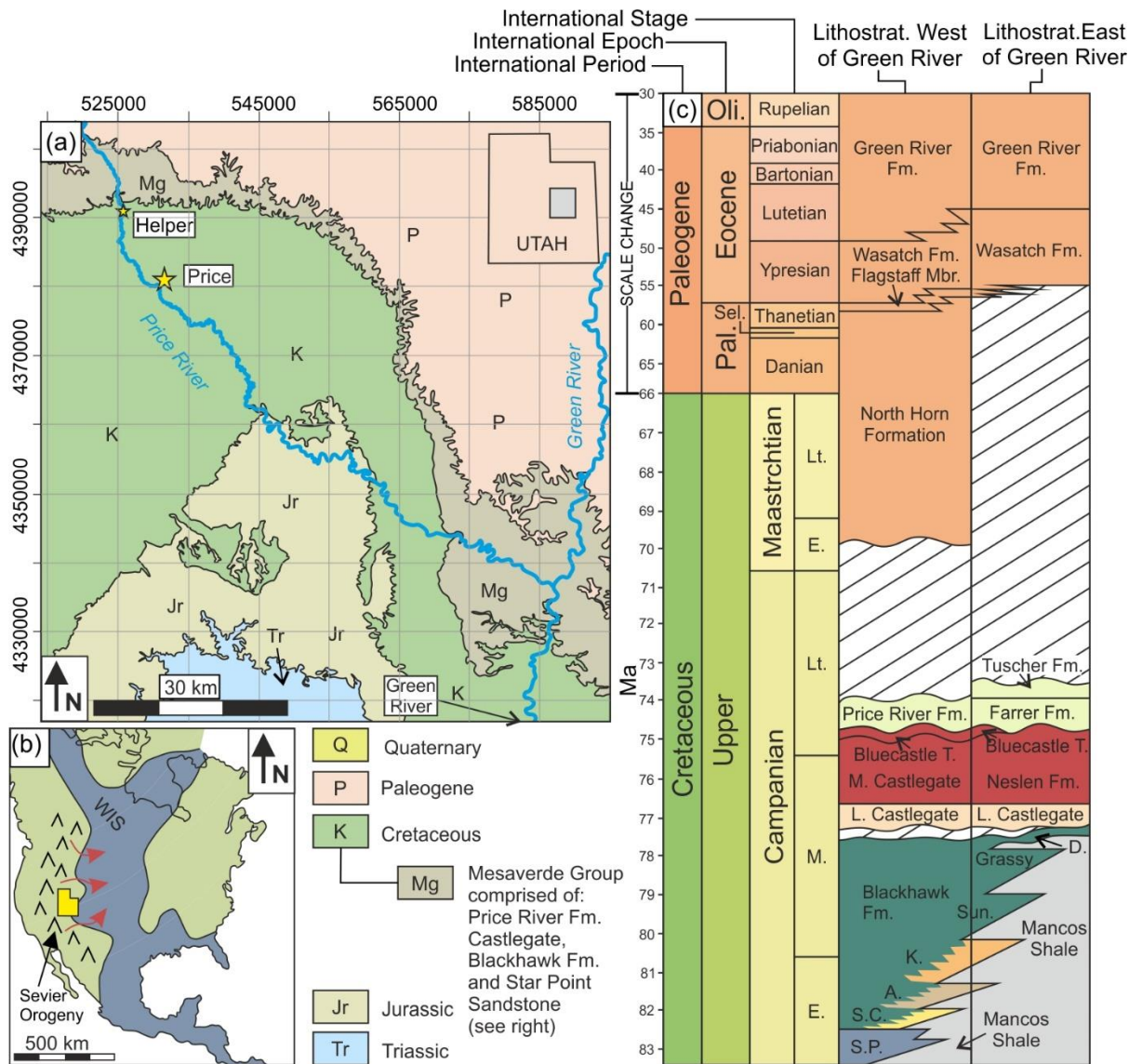


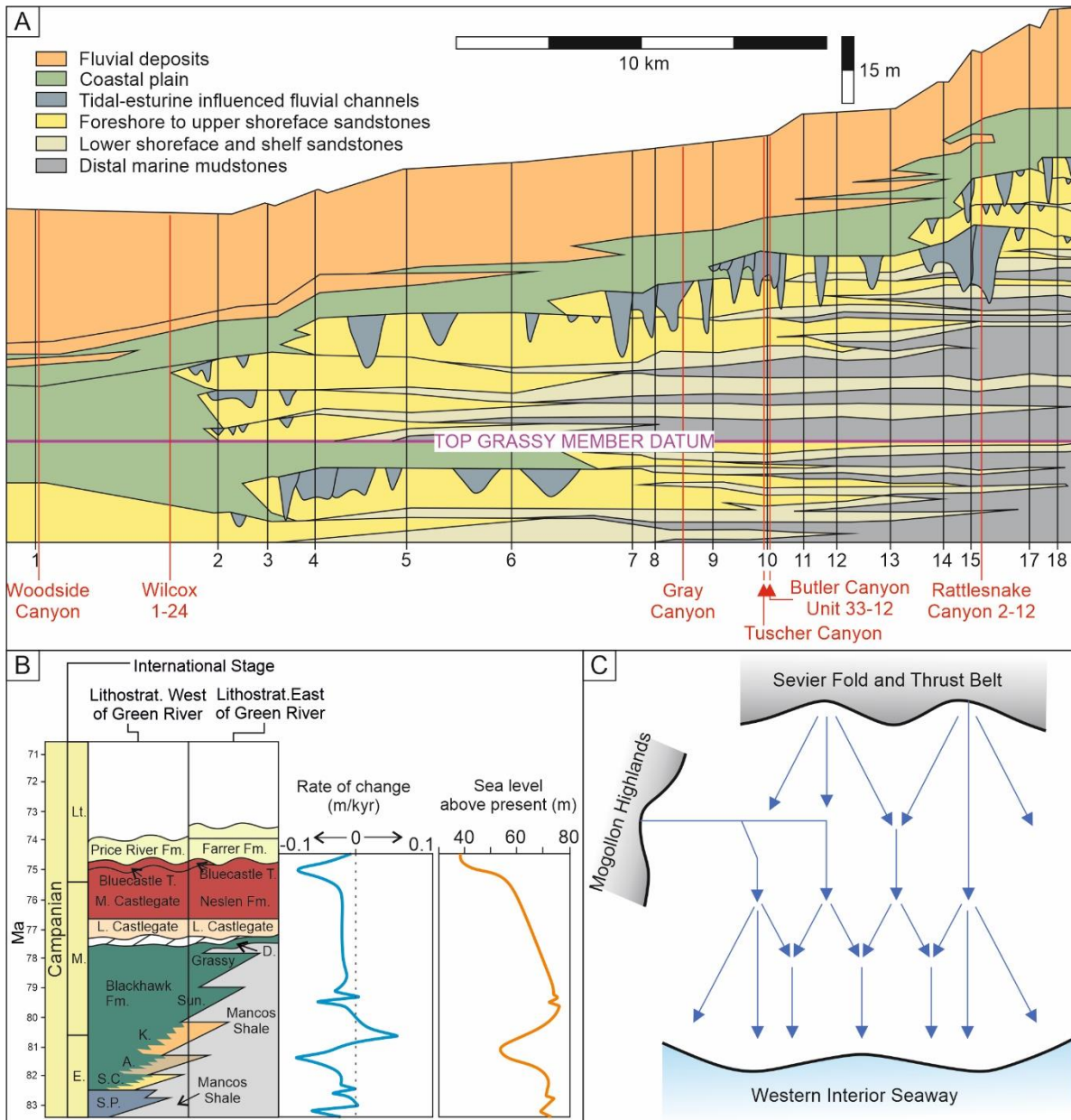
Figure 3.1 - Lithostratigraphic and chronostratigraphic context of the Campanian Lower Castlegate Sandstone MSB, Utah. (A) A geological map of the Book Cliffs in the area between Price and Green River (modified from Watkind 1995), showing the distribution of the Mesaverde Group outcrops. (B) A palaeogeographic reconstruction of the Sevier Orogeny and sediment supply pathway (red arrows), feeding the Western Interior Seaway (WIS) that spanned across North America (modified from Van de Graff, 1972; Chan and Pfaff, 1991). (C) Generalised vertical section detailing the lithostratigraphic make-up of the Upper Cretaceous and Lower Paleogene of the study area, west and east of Green River (modified from Pitman et al., 1987; Seymour and Fielding, 2013; Burns et al., 2017).

Seymour and Fielding (2013) correlated the Book Cliffs succession to time-equivalent strata of the western Henry Mountains, to the south, based upon four distinct lithostratigraphic units: The Star Point Sandstone, the lower Blackhawk Formation, the middle and upper Blackhawk Formation, and the Lower Castlegate Sandstone MSB. The lower Blackhawk Formation (as defined by Seymour and Fielding, 2013) consists of prograding and aggrading, shoreface and coastal plain parasequence sets (Figure 1C). The Blackhawk is unconformably overlain by the Lower Castlegate Sandstone MSB (Olsen et al., 1995; Yoshida et al., 1996; McLaurin and Steel, 2000; Miall and Arush, 2001), deposited in a humid climate (Miall, 1994).

The Castlegate Sandstone is a structurally and topographically unconfined fluvial system that drained the Sevier Mountain Belt (Miall 1994). The Castlegate is informally sub-divided into three units (Chan and Pfaff, 1991; Olsen et al., 1995; McLaurin and Steel, 2007): the Lower and Middle Castlegate Sandstones, and the Bluecastle Tongue. The Lower Castlegate Sandstone is the subject of this chapter. West of Green River it comprises a 40-80 m thick, highly amalgamated, high net-to-gross fluvial MSB (Yoshida, 2000). Palaeocurrent analysis indicates a south-east to east palaeoflow from the Sevier Fold and Thrust Belt (Willis, 2000; Yoshida, 2000; McLaurin and Steel, 2007). The more distal deposits to the east of Green River, at Tuscher Canyon (Figure 3.1A, C), show a thinner, approximately 25 m succession of the Lower Castlegate Sandstone (Fouch et al., 1983; McLaurin and Steel, 2000). The Castlegate MSB extends 140 km downslope from the proximal portion of the basin, covering an area of over 20,000 km² (Gibling, 2006) but it is an extremely complex unit and no one continuous stratigraphic surface can be traced through it (Miall and Arush, 2001; Hajek and Heller, 2012; Pattinson, 2018).

The Blackhawk – Lower Castlegate boundary has long been considered a sequence boundary (Van Wagoner, 1995, Olsen et al., 1995; Yoshida et al., 1996; McLaurin and Steel, 2000; Miall and Arush, 2001). However, more recent correlations of shoreface incising channels (Pattison, 2018, 2019a), correlations to eustatic events (Howell et al., 2018) and provenance analysis (Pettit et al., 2019) have suggested a far more complex Lower Castlegate deposition (Figure 3.2), in which two source areas feed a prograding fluvial system. The progradation of the fluvial system and its associated autogenic scouring (Trower et al., 2018) have persevered as a sequence boundary-like surface at the Blackhawk – Lower Castlegate boundary (Howell et al., 2018; Pattinson, 2018, 2019a,b).

Figure 3.2 (next page) – A) Correlation of the study area (modified from Pattinson 2018). Showing the parasequence stacking of the Blackhawk Formation and its intertonging with the distal marine shales of the Mancos Shale. The fluvial deposits highlighted on the correlation comprise the Castlegate Sandstone. The top Grassy Member of the Blackhawk Formation is used as a datum. Locations on the correlation are from Pattinson (2018; Figure 4), localities used in this study are highlighted in red. B) Correlation of sea-level variation to the sediments of the Mesaverde Group (modified from Howell et al. 2018), correlations of the lithostratigraphy presented in Figure 3.1C matched to the rate of sea-level change and the height of Campanian sea-level above the present day sea-level. C) Fluvial channel mixing and flow contamination pathways based upon provenance analysis (modified from Pettit et al. 2019). Note, not to scale and locations in A are shown in Figure 3.3.



3.3 Methodology

The study uses sedimentological data from eight field sites selected to form a broadly west to east palaeoflow-parallel transect along the Book Cliffs. Sedimentary logs were collected from field sites at a centimetre resolution to permit accurate measurements of set thicknesses. These data were supplemented with ten down-hole well logs and used to construct burial history and calculate subsidence rates (Figure 3.3A). Three large, well exposed, outcrops were chosen for terrestrial photogrammetric data collection: the Castle

Gate type locality (Figure 3.3B) in the proximal region of the Lower Castlegate fluvial system, Sunnyside (Figure 3.3C) in the medial region, and Tuscher Canyon in the distal region (Figure 3.3D).

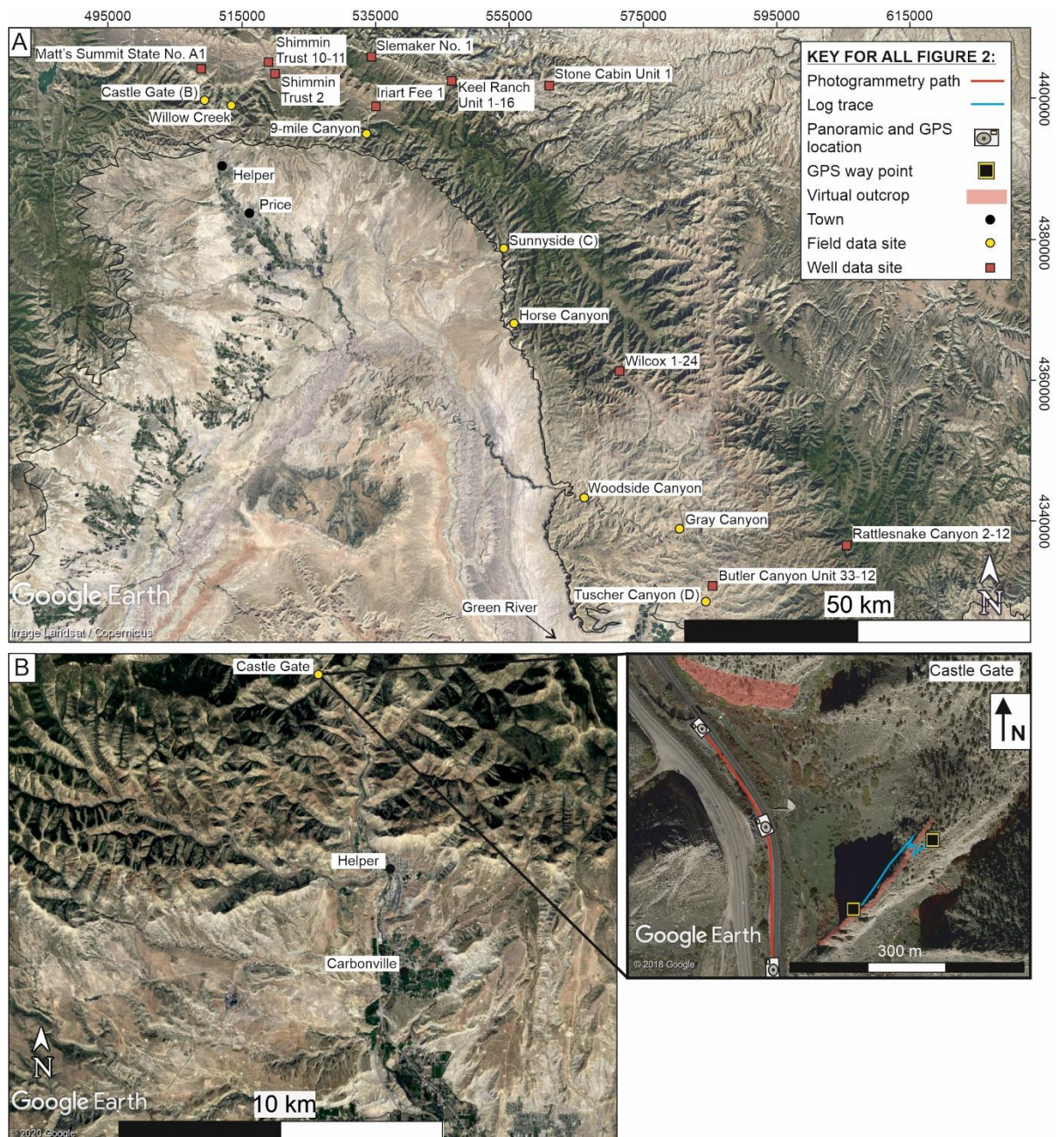


Figure 3.3 - (A) Location of the wells (red) and outcrops (yellow) (GoogleEarth image acquired on 12/31/2016) (B) Data collection map from the proximal Castle Gate study site (GoogleEarth image acquired on 10/16/2013).

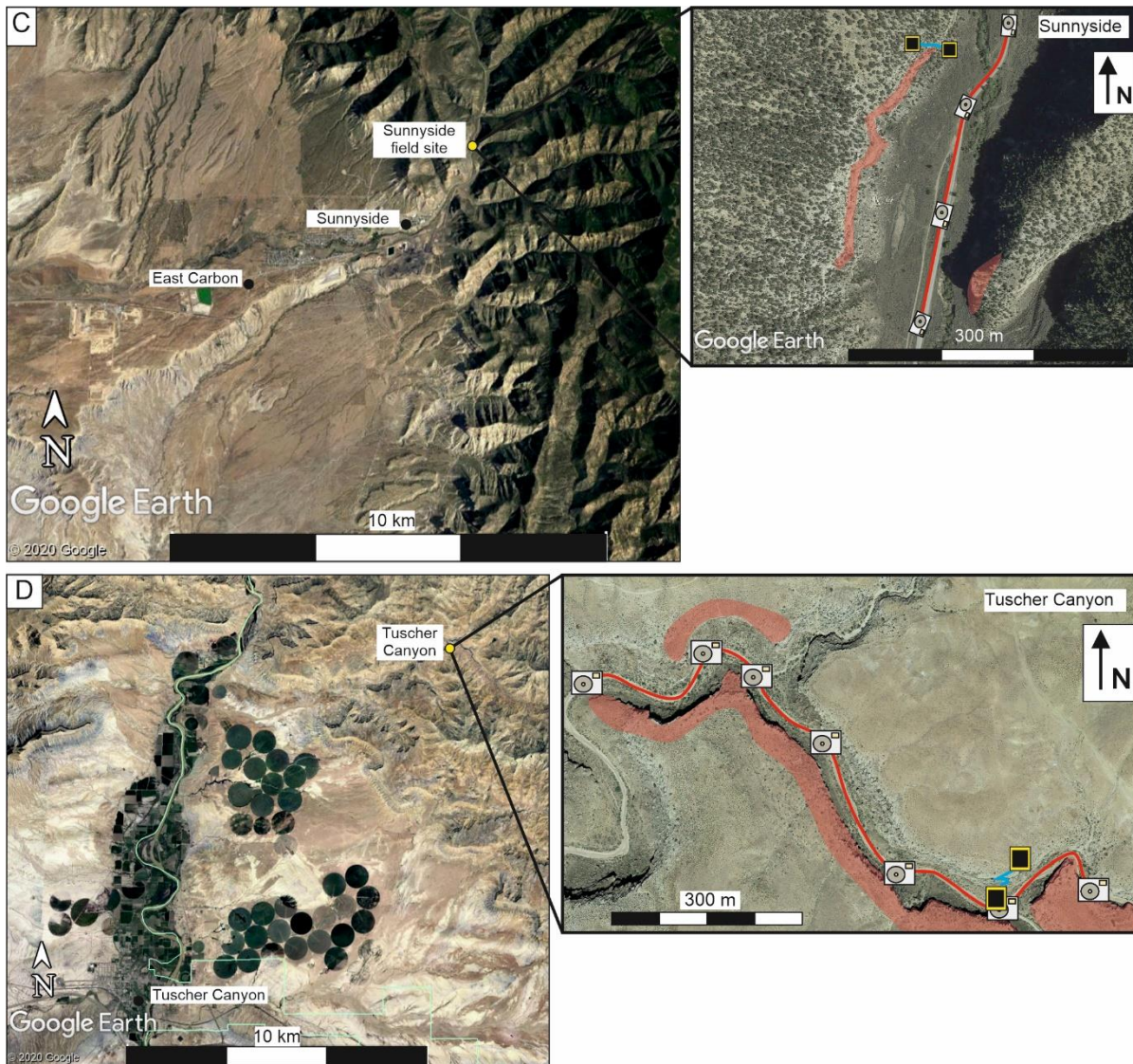


Figure 3.3 (continued) - (C) Data collection map from the medial Sunnyside study site (GoogleEarth image acquired on 08/08/2015). (D) Data collection map from the distal Tuscher Canyon study site (GoogleEarth image acquired on 07/28/2015). Note, key in Figure 3.3A applies to all.

In addition to photogrammetry, a total 306 m of high-resolution sedimentary logs, measuring 21-77 m vertically was collected from the eight field localities (Figure 3.3). The sedimentary logs were used to ground-truth the interpretations made from photogrammetric datasets, to make facies-scale observations, and to determine the relative abundance of each facies within a field site. Facies proportions are based upon thickness in log data and are therefore one-dimensional (Miall, 1973; Priddy and Clarke, 2020).

3.3.1 *Terrestrial photogrammetry*

Photogrammetry is the compilation of images to reproduce an imaged target in three-dimensions. Photogrammetry works by using overlapping photographs to calculate three-dimensional points relative to the camera. The 'structure from motion' algorithm is the most commonly employed in the development of photogrammetric models (Westoby et al. 2012). The algorithm first finds common mid-points in the overlapping images and aligns them relatively with respect to the position of the camera in order to create a sparse point cloud (Figure 3.4A). Once the images and camera positions are spatially orientated relative to one-another, the algorithm searches over the sparse point cloud to identify best match points between sparse points and the overlapping images, to generate a dense point cloud. This process gives greater precision than the initial analysis (Barazzetti et al. 2010; Bemis et al. 2014). The next phase of model generation produces a triangulated mesh over the dense point cloud. This is done by taking given amount of dense point cloud points and applying a triangular shape over them, this is done repeatedly over the spatial extent of the model, at any resolution the user requires (dependent upon detail required and computational time). The product of this is a wireframe mesh (Favalli et al. 2012). The final stage is to produce a textured model, this overlays RGB and features from the images onto the triangulated mesh, relative to its position in the orientated space.

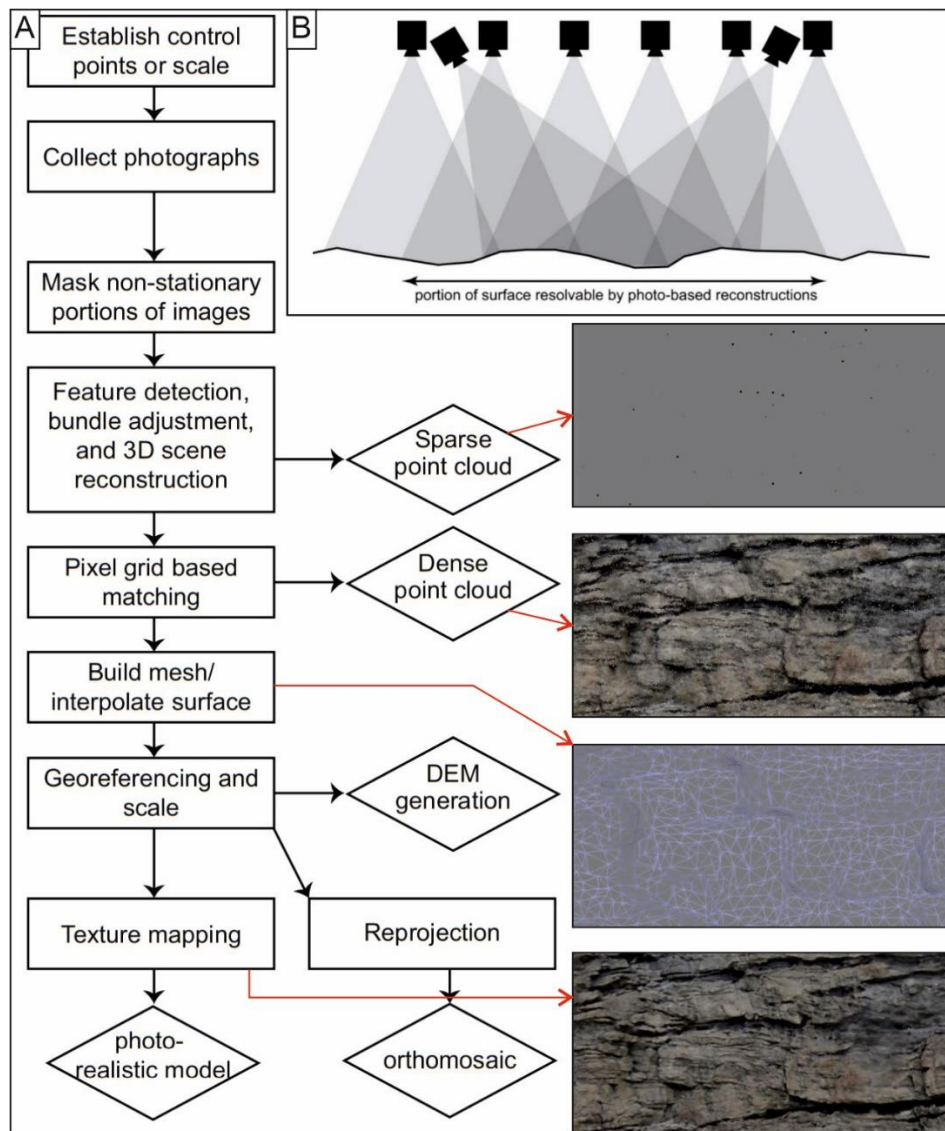


Figure 3.4 – The photogrammetry method. A) Workflow for implementing structure from motion from field photos (modified from Bemis et al. 2014). Black arrows indicate workflow pathways, red arrows indicate the position of the created model relative to the workflow. Images on the right show the Castle Gate north outcrop model created using structure from motion algorithm, and demonstrates stages in the process. B) Schematic of the overlap required for generating photogrammetric models (modified from Bemis et al. 2014), showing the ideal overlap required to construct photogrammetric models and how it enables the rugosity of the outcrop to be imaged.

3.3.2 *Photogrammetric data acquisition and processing*

Outcrop photographs, with approximately 85% overlap (Figure 3.4B), were processed using structure-from-motion digital photogrammetry software (Agisoft Photoscan Pro.; see Buckley et al., 2006; Pringle et al., 2006; Bemis et al., 2014; Ellen et al., 2019; Priddy et al., 2019; Bilmes et al., 2019) to create virtual outcrop models (VOMs) for each location. Each photogrammetric dataset collected has an outcrop-to-area ratio (Enge et al., 2007) of approximately 0.75 and the total area covered by the photogrammetric models is approximately 280,000 m². VOMs were spatially referenced to ground control points, using hand-held GPS (Ellen et al., 2019; Priddy et al., 2019) (Figure 3.3).

Analysis of the VOMs was performed using Virtual Reality Geoscience Studio (VRGS, v. 2.39, Hodgetts et al., 2015), to provide interpretations of bounding surface hierarchy (Miall, 1985), sedimentary architectural elements, sedimentary geometry (width and thickness measurements), vertical set thicknesses and measured palaeocurrent directions (following the approach of Burnham and Hodgetts, 2018). Geometric measurements of elements are corrected, for the relationship between the orientation of the outcrop to compared to their palaeoflow direction, within VRGS to give measurements in a section perpendicular to palaeoflow in all cases (Burnham and Hodgetts, 2018). The geometric width data of architectural elements are uncorrected for partial and complete elements, due to the lack of complete elements preserved within outcrops and the abundance of elements that are unlimited in lateral extent (Visser and Chessa, 2000). This is as a result of the highly erosional nature of the Lower Castlegate Sandstone. It should, therefore be considered that the values presented here are minimum values (Visser and Chessa, 2000). This may also influence and underestimate true width to thickness ratios. Two-dimensional architectural element

proportions where obtained from orthorectified images of the VOM interpretations. This was done using an equal surface area measurement tool (e.g., Grove and Jerram, 2011; Mitten et al., 2020) in Image J (v. 1.51; Rasband, 2009).

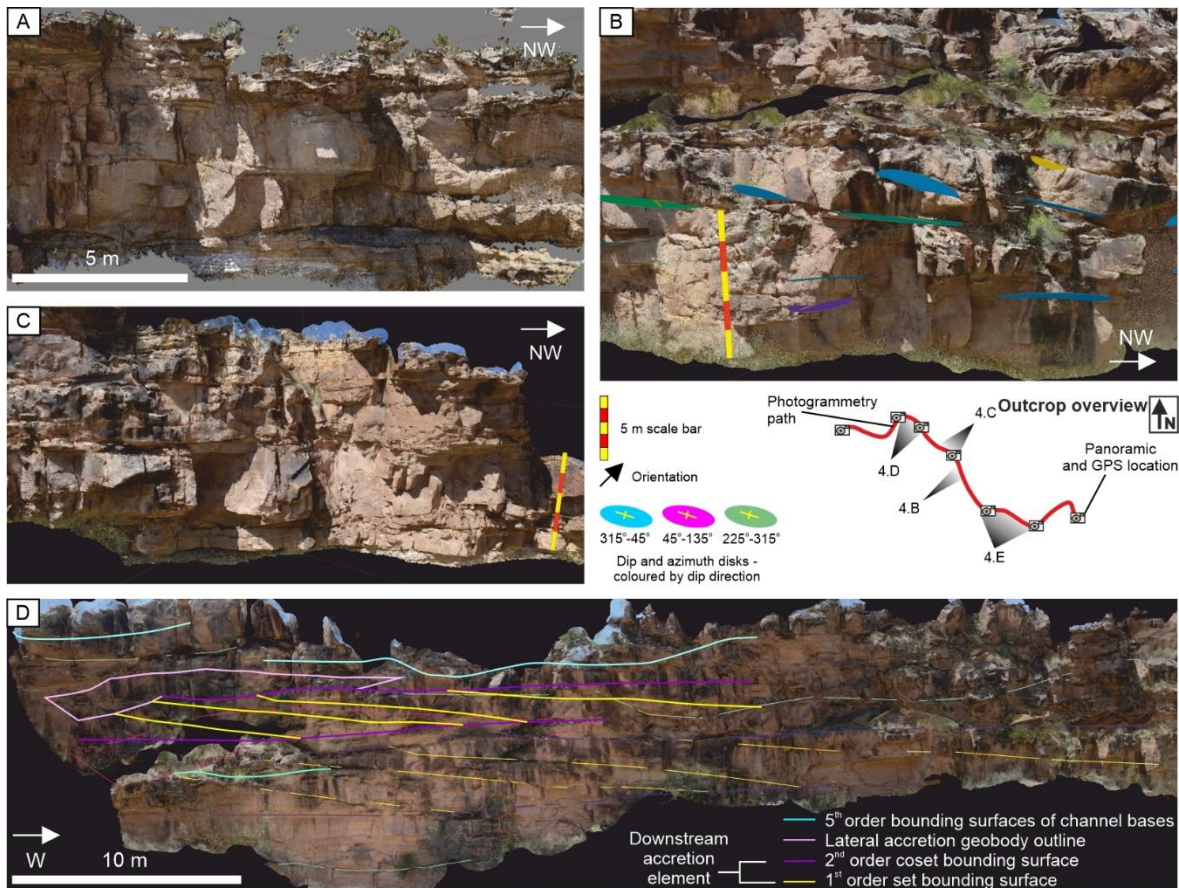


Figure 3.5 - A) Digital dense point cloud data from the outcrop dataset. Note: the outcrop overview shows the study location Tuscher Canyon. B) and C) show sedimentary dip and azimuth measurements (coloured surfaces) on the digital surface within the VRGS software (see text). D) Bounding surface analysis on the digitally-textured mesh surface.

3.3.3 Barform analysis from photogrammetric data

The occurrences of preserved barform topsets provides insight into palaeoflow depths, avulsion mechanisms (Chamberlin and Hajek, 2015) and aggradational profiles of ancient fluvial systems (Section 2.5.1) (Heller and Paola, 1996; Mohrig et al., 2000; Hajek and Heller,

2012; Chamberlin and Hajek, 2019). Erosion of topset strata (Section 2.4.1) can be produced from element scour (Hajek and Heller, 2012) and discharge reactivation (Herbert et al., 2020). Therefore, each preserved topset and erosional surface found within an accretionary element was counted in the VOMs. The ratio of topset occurrences to erosional surfaces within individual elements is used as a rough proxy for aggradation rate and discharge variability. This is done with the assumption that the more prevalent are erosional surfaces within a succession, the lower the preservation. Conversely, preservation of a clinoform top indicates that, at that time, aggradation was dominant (Hajek and Heller, 2012; Chamberlin and Hajek, 2019). The ratio of these two types of surface is considered as an indication of preservation. The higher the ratio the more aggradational and stable the flow is during deposition of the element; the lower the ratio the greater the amount of erosion or denudation that is taking place during deposition of the element.

3.3.4 Palaeoflow reconstructions

A standard analysis using circular statistics (Allen, 1967; Petit and Beauchamp, 1986) of palaeocurrent measurements taken from crossbed foresets was employed in this study to give the vector mean direction (v_m) and dispersion (r) of the flow and the sinuosity of the system. Equal area, 15° bin, rose diagrams were plotted using GeoRose (v.0.4.3; Y.O.N.G., 2015).

Maximum channel sinuosity estimations were calculated using three widely used techniques. However, each individual technique has its limitations. Therefore, for a rigorous attempt at deriving empirical relationships of sinuosity from one VOM to another, all three have been used to demonstrate a range of plausible sinuosities and reducing the error in assumptions from individual techniques. The first is the sine-generated curve method (Bridge et al., 2000;

Equation 1) using half the maximum palaeocurrent range in radians (φ) and the assumption that meanders are generated as sine-curves (Figure 3.6A) (Bridge et al., 2000). This method adopts the approach that the maximum range in radians is the equivalent to the amplitude of a sine-curve. However, the method poorly accounts for wavelength. In this method, sinuosity (P) is given by:

$$P = 4.84 / (4.84 - \varphi^2)$$

[1]

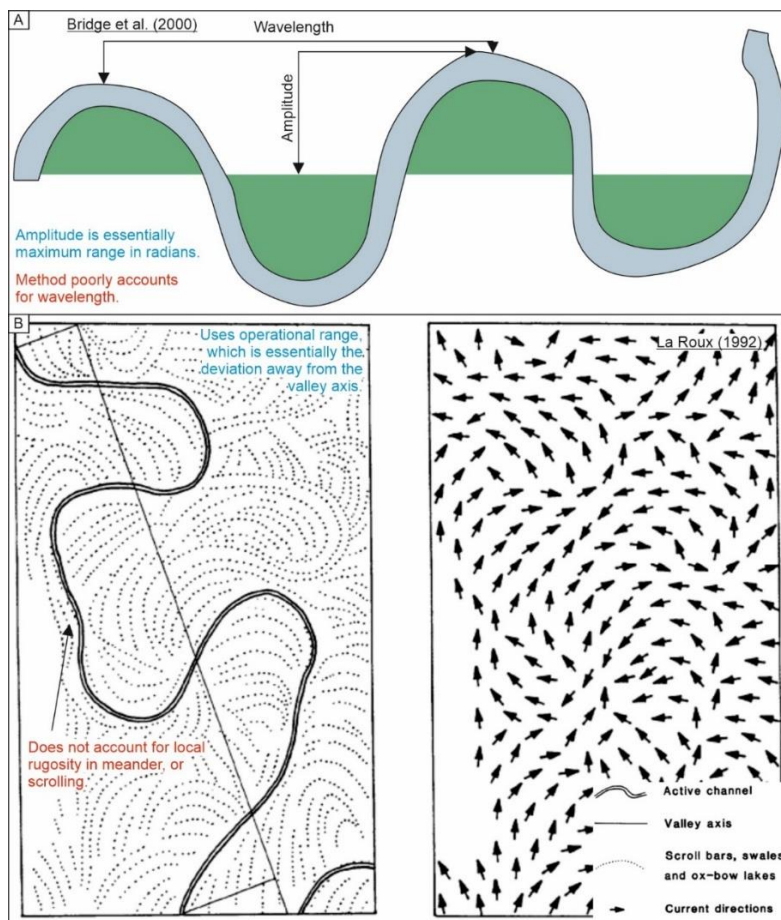


Figure 3.6 – Plan form examples of sinuosity reconstruction. A) Schematic of Bridge et al. (2000) reconstruction method of a sine-generated meander. See text for details. B) La Roux (1992; Figure 3) Showing the assumption of sinuosity as a function of the deviation of individual palaeocurrents from a local mean or valley axis. See text for details.

The second method of La Roux (1992, 1994) uses the operation range (Figure 3.6B) (ϕ ; 3.2 times Curray's (1956) circular standard deviation; La Roux, 1994). This method assumes that the operational range is the deviation away from a valley axis (or vector magnitude), hence its reliance upon circular standard deviation. However, the method fails to account for local rugosity in meander morphology. In this method, Equation 2 should be used when ϕ is less than 180° and Equation 3 when ϕ is greater than 180° .

$$P = \pi(\phi/360)/\{\sin(\phi/2)\} \quad [2]$$

$$P = \pi(\phi/360)/\{\sin(360 - \phi/2)\} \quad [3]$$

The final method (Equation 4) used to determine maximum channel sinuosity uses the vector magnitude as a percentage (L; Ghosh, 2000). In a similar manner to the technique above (La Roux 1992, 1994), the Ghosh (2000) method looks at the strength of the mean data and the deviation away from it. It however, rather than determining deviation away from a valley axis, uses fractals to segment the river course into fractions of an overall trend. In a study such as this, where outcrops provide fractal segmentation along a course of a river, the application of the Ghosh (2000) is easily applied.

$$\ln P = 3.68 - 0.0684L + 0.00032L^2 \quad [4]$$

Sinuosity was calculated for channel fill elements to account for single channel thalweg sinuosity (independent of barform accretion), and also for total palaeocurrent data, to account for total channel-form sinuosity (including barform accretion). The results of the sinuosity analysis allow downstream variations in local palaeocurrent, changes in dispersions and sinuosity to be observed. The sine-generated curve method (Equation 1) may be biased towards larger sinuosity values, these have therefore been treated as maximum values. However, the trends represented within the Bridge et al. (2000) reconstructions are

complemented by the results of other reconstruction methods (La Roux, 1994; Ghosh, 2000) and therefore can be considered representative of trends, despite the limitations imposed upon the absolute values.

Maximum flow depth reconstructions were produced from crossbed set thicknesses (Equation 5; Bridge and Tye, 2000). This approach uses the mean of measured crossbed set thicknesses (s_m) to determine the maximum depth of a flow (h_m) during the time of deposition of the measured set from:

$$h_m = 5.3\beta + 0.001\beta^2 \text{ where } \beta \approx s_m/1.8$$

[5]

3.4 Architectural elements identified

Seven facies are recognised within the Lower Castlegate MSB (Table 3.1). The facies are dominantly comprised of trough and planar crossbedded sandstones that represent simple cut and fill channel facies. Stacking of crossbeds into sets and cosets in barform is common throughout barforms facies. For a detailed facies-scale analysis of the Lower Castlegate the reader is referred to Van de Graff (1972), Chan and Pfaff (1991), Miall (1993, 1994), Adams and Bhattacharya (2005) and McLaurin and Steel (2007). Channel and barforms facies have been identified by the previous authors, however, barform specific facies were interpreted by Miall (1993) and McLaurin and Steel (2007). Figure 3.7 shows a detailed field log of the Castle Gate type locality, highlighting the distribution of these facies through the Lower Castlegate, further details of the facies identified can be found in Appendix A.

Five distinct architectural elements are recognised in the lower Castlegate: (1) erosionally based, lensoid to sheet sandstones representing channel fill elements; (2) low-angle, cross stratified sandstones representing upstream accretion elements; (3) large-scale, inclined

heterolithics representing lateral accretion elements; (4) large-scale, cross-stratified tabular to lentic sandstones representing downstream accretion elements; and (5) tabular, fine-grained sandstone to mudstones elements interpreted as overbank elements. Each element is described and interpreted below.

Table 3.1 – Facies of the Lower Castlegate Sandstone, Utah. Detailed photopanels available in

Appendix 1.

<i>Facies</i>	<i>Lithological Description</i>	<i>Interpretation</i>
<i>Clast-supported conglomerate (Cc)</i>	<i>Boulder-sized clasts, little matrix, clast supported. Matrix (where present) comprises fine- to very coarse-grained sandstone, moderate to poorly sorted. Structureless, normally graded, with rip-up clasts and coal clasts.</i>	<i>Subaqueous, pseudo-plastic, high sediment load, non-Newtonian deposits (Miall, 1988).</i>
<i>Trough-crossbedded sandstone (St)</i>	<i>Fine- to very coarse-grained, grey-brown sandstone, sub- to well-rounded, moderate sorting and sphericity. Trough-cross-bedding, some pebble-sized material lining basal surface of the facies, soft sediment deformation.</i>	<i>High-energy lower-flow regime sinuous-crested dune-scale sub-aqueous bedforms (Collinson et al., 2006) (Figure 3.7B, C).</i>
<i>Planar-crossbedded sandstone (Sp)</i>	<i>Fine- to coarse-grained, grey-brown sandstone, sub- to well-rounded, moderate sorting and sphericity. Planar cross-bedding, foresets occasionally lined with darker clasts, sometimes granule- to pebble-sized clast material, rare asymmetrical ripples.</i>	<i>Lower- flow regime straight crested dune-scale bedforms (Miall 1996) (Figure 3.7E, I).</i>
<i>Structureless sandstone (Sm)</i>	<i>Medium-grained, black-grey sandstone, sub-rounded, very poor to poor sorting and sphericity. Structureless, normally graded, large wood fragments at the base of the facies.</i>	<i>High sediment load during rapid deposition (Miall, 1996; Leeder, 1999) (Figure 3.7F, G, H).</i>
<i>Horizontally laminated sandstones (Sh)</i>	<i>Medium- to coarse-grained, grey-brown sandstone, sub- to well-rounded, poorly sorted, moderately spherical. Planar horizontal lamination, normally graded with wood fragments at the base of the facies.</i>	<i>Upper-flow regime plane bed deposits (Miall, 1996; Collinson et al., 2006).</i>
<i>Ripple laminated sandstone (Sr)</i>	<i>Very fine- to fine-grained, grey-brown sandstone, sub-rounded, moderate sorting and sphericity. Asymmetrical ripple lamination, some finer black material on ripple laminae.</i>	<i>Lower-flow regime small-scale sub-aqueous bedform migration (Miall, 1985) (Figure 3.7A)</i>
<i>Planar laminated fines (Fl)</i>	<i>Grey, well-sorted mudstone to siltstone, very fine- grained sandstone interbeds. Planar horizontal lamination, some symmetrical ripple lamination. Soft sediment deformation, pedogenic nodules, organic enrichment of laminae.</i>	<i>Suspension settling, with mild flow fluctuations, some sub-aerial exposure (Figure 3.7G), some evidence of standing water (Miall, 1996; Bridge, 2003).</i>

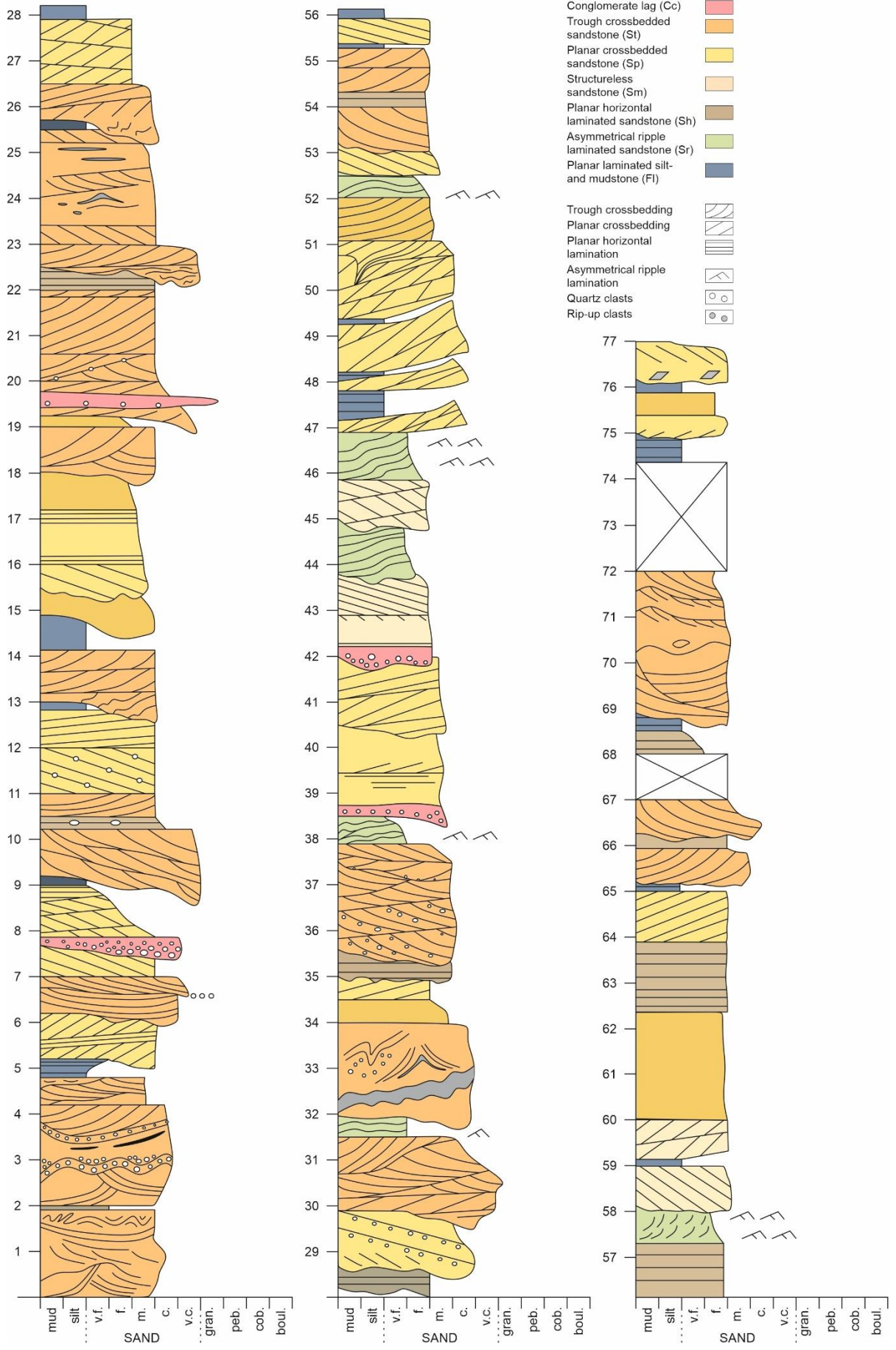


Figure 3.7 – *Field collected sedimentary log through the Lower Castle Gate, collected from the Castle Gate type locality.*

3.4.1 Channel fill elements

Description - Occurrences of these elements are typically 2-10 m thick and 20-180 m wide, with a width to depth ratio of 10:1 to 30:1. The sand bodies are confined within fifth-order, concave-up, basal scour bounding surfaces. The elements (when fully preserved) are capped by fourth-order bounding surfaces. However, in the majority of cases across the Lower Castlegate, the full succession is truncated by a fifth-order erosional surface. The elements typically show a succession of conglomerate pebble-lag material (Cc), fining upwards from coarse- to fine-grained crossbedded facies (St, Sp; Figures 3.8B, C, E, F; Table 1) to, fine- to very fine-grained horizontally laminated sandstone facies. Some coarse- to medium-grained structureless sandstones are also found within the succession (Sm; Figures 3.8G, H). At the base of the element, wood fragments and imprints can be found along with mud- to siltstone rip-up clasts. Convolute to wavy soft sediment deformation structures are also abundant within the lower portion of the element. Measured thicknesses of crossbed sets within the element vary from 0.23 m to 0.88 m. The sets within the major sandstone facies do not often form cosets. Fourth-order, small-scale scour surfaces are also common and punctuate the development of sets within the element. The mean palaeocurrent of the elements measured (n = 476) is 92° with a dispersion of 45% across the study area.

Interpretation - The confining erosional nature of the concave-up basal scour surface and waning flow deposits suggest channel fill deposits (Figures 3.8D). The progression from pebble-lag material through upper flow regime to lower flow regime deposits indicates the preservation of a complete channel cut-and-fill succession (Miall, 1985; Bridge, 1993). The

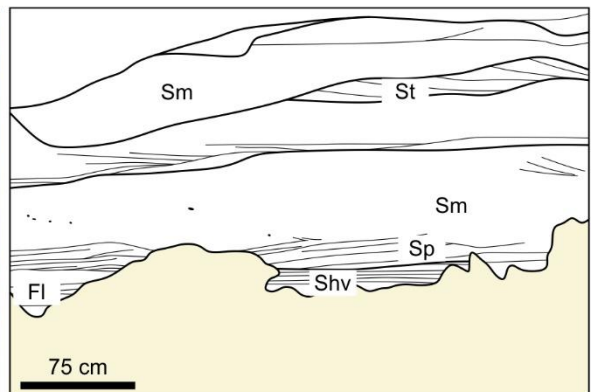
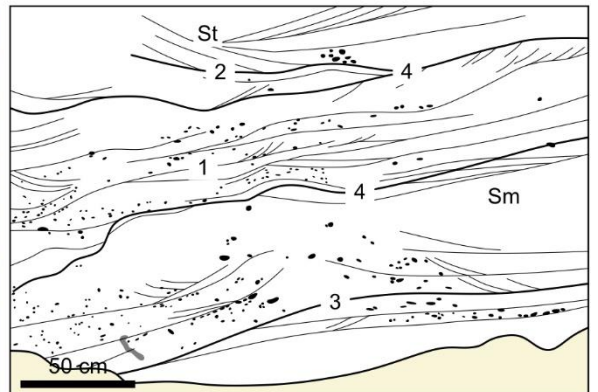
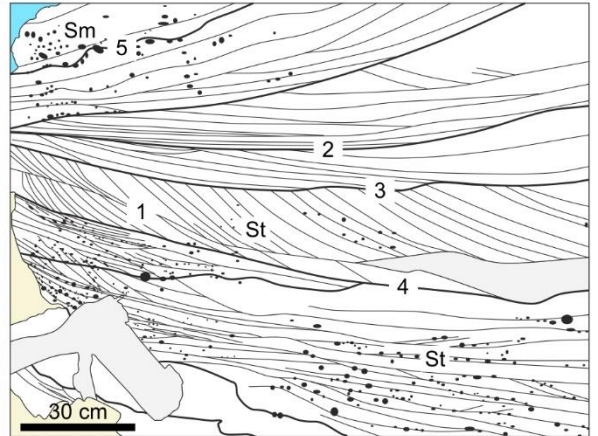
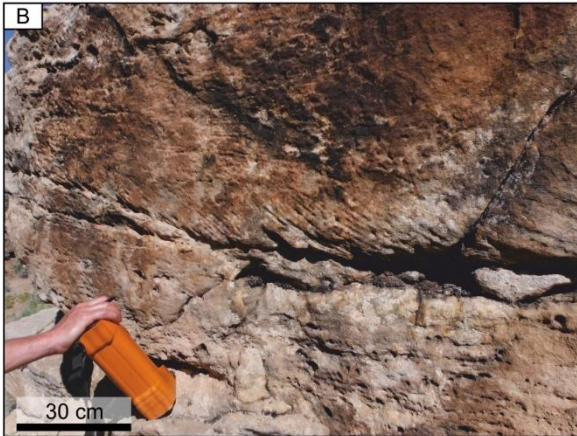
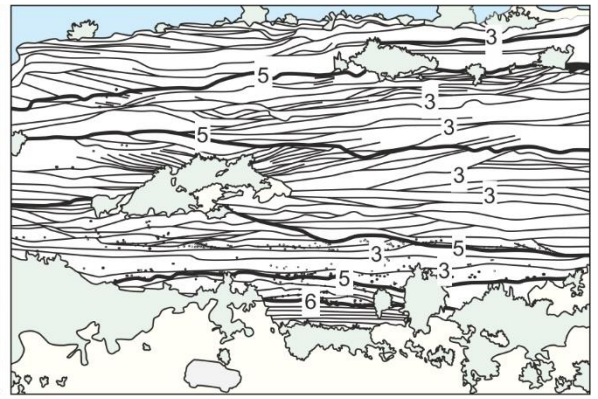
presence of rip-up and wood clasts indicates the transport, and therefore presence of overbank material, which was re-worked by channel elements. Variations in set thickness indicate variable flow depths (Bridge and Tye, 2000; Bridge et al., 2000; Adams and Bhattacharya, 2005; McLaurin and Steel, 2007; Lunt et al., 2013). This is further evidenced by the abundant nature of fourth-order scour surfaces and the lack of coset development, and indicates either immature unit bar formation (Hubert et al., 2020) or the simple migration of single bedforms. The mean palaeocurrent direction of elements measured across the Lower Castlegate is 92°, indicating a generally eastward flow to the channels, and agrees with that found in previous studies (Miall, 1993, 1994; Miall and Arush 2001). The lateral and vertical amalgamation of channel elements within the Lower Castlegate has been attributed to the local avulsion events (Miall, 1994; Miall and Arush, 2001; Gibling, 2006; McLaurin and Steel, 2007; Hajek and Heller, 2012).

Figure 3.8 (next page) - *Facies photoplate from the Lower Castlegate, Utah. (A) Two sets of asymmetrical ripple laminated sandstone from the Castle Gate log at approximately 52 m, pen for scale. (B) Large trough crossbedded sandstone sets showing downlapping onto basal channel surface, highlighted is a pencil for scale. Clast moulds can be seen along the set surfaces. Image is taken from the Castle Gate log at approximately 33 m. (C) Smaller scale trough cross-bedded sets from Horse Canyon log at approximately 31 m. (D) Asymmetrical channel fill from the Castle Gate log at approximately 36 m. (E) Planar cross-bedded sandstone from 9-Mile Canyon log at approximately 28 m. At the base of the cross bedded facies an erosional base has been interpreted overlying fine-grained material, this erosive surface is overlain by a minor channel lag consisting of small extra- and intra-formational clast material. (F) Horizontally laminated sandstone erosionally overlain by trough crossbedded sandstone from Tuscher Canyon log, at approximately 5 m. (G) Structureless sandstone with some rip-up clasts, comprised of siltstone that have been deformed due to compaction. Photo is from the Castle Gate log at approximately 18 m. (H) Fine grained siltstones*

and structureless sandstones in the overbank succession of the Castle Gate log, from approximately 15 m.



Figure 3.9 (next page) - The genetic units of the most common sedimentary facies found within the Castlegate Sandstone. The numbers indicate bounding surfaces hierarchy (Miall, 1985). A) Representative section of the bounding surface framework within the Lower Castlegate at Tuscher Canyon, and bounding surface hierarchy interpreted from that framework. B) Sandstone (St) facies showing pebble-lined foreset and set surfaces stacking below and above a third-order erosional scour surface. C) Third-order erosional surfaces bounding conformable packages of St and Sm facies. D) Sm facies within third-order scours (see Table 3.1 for facies codes).



3.4.2 *Downstream accretion elements*

Description - Elements of this type are typically 4-12 m thick and are 20-160 m wide. Their lensoid geometries are confined within fourth- to fifth-order bounding surfaces at the tops of the elements and fourth-order scour surfaces beneath. Tabular to lensoid geometries are usually much greater in lateral extent relative to preserved thickness. Such elements are typically the largest of the elements seen within the Lower Castlegate Sandstone. They consist of trough to planar crossbedded medium-grained sandstone facies (St, Sp) with minor occurrences of structureless medium- to fine-grained sandstones (Sm). When fully preserved, the succession grades normally to horizontal and ripple laminated fine- to very fine-grained sandstone facies (Sh, Sr). The internal bounding surface framework of these elements is dominated by climbing sets forming cosets and large, high-angle (12° - 20°) accretionary surfaces, forming clinof orm geometries. The framework is punctuated by small-scale, fourth-order scour surfaces. The mean palaeocurrent of these elements, derived from data from all localities (n=344), is 107° but shows a higher dispersion (over 50%) than that of the channel elements.

Interpretation - The presence of accretionary surfaces, a lensoidal to tabular geometry, and a mean palaeocurrent direction (107°), sub-parallel to parallel with that of local channel fill elements, suggest these are downstream accretion elements (Miall, 1985; Hornung and Aigner, 1999; Best et al., 2003; Miall and Jones, 2003; Ghinassi and Ielpi, 2018). They represent the largest dimension architectural elements within the Lower Castlegate Sandstone (Figure 3.9B). Any packages of sediment extending up to 50° away from the mean channel thalweg palaeocurrent direction have been attributed to oblique barform migration or slip-face failure (Best et al., 2003). The normally graded, sand dominated, succession

suggests a waning flow, until low flow depths cause the deposition of bar top facies (Cant and Walker, 1978; Hajek and Heller, 2012; Chamberlin and Hajek, 2019). Fourth-order local scour surfaces have been interpreted as forming through reactivation of flow in variable discharge. Scour marks potentially form as a result of variable discharge rates (Hajek and Heller, 2012; Chamberlin and Hajek, 2019).

3.4.3 Lateral accretion elements

Description - Elements of this type are heterolithic and exhibit alternating inclined units of sandstones and planar-laminated siltstones (Fl). The interbeds have an asymptotic nature, are not laterally extensive, and are inclined at moderate- to high-angles. The elements are typically 2 - 4 m thick and are 15 - 110 m wide, and is found mainly on the margins of other accretionary elements. The elements are lensoid and confined within fourth- or fifth-order bounding surfaces at their tops, and fourth- or fifth-order scour surfaces at their bases. Trough and planar cross-bedded sandstone facies (St and Sp) are abundant within medium to fine grained sandstone strata. Minor sporadic occurrences of structureless sandstones (Sm) are also observed. Towards the top of the succession (when preserved) planar horizontal (Sh) and ripple (Sr) lamination are present within fine- to very fine-grained sandstone. The top of the element may also be gradational into finer grained sediments (Fl). Crossbeds form sets that are typically 0.10-0.30 m thick. Accretionary surfaces and internal set surfaces are commonly punctuated by small-scale scour surfaces. The elements show palaeocurrent directions that are normal to that of the local channel fill element.

Interpretation - The inclined heterolithic and lensoidal nature of the elements, and the mean palaeocurrent directions approximately normal to those recorded in channel elements, indicate that these elements are lateral accretion elements (Jordan and Pryor, 1992; Best et

al., 2003). The high angle of the asymptotic interbeds suggests steep accretionary surfaces between the sandstones and siltstones that indicate local discharge rate variation and sporadic bedform migration at the margins of lateral accretion elements (Miall, 1985; Ielpi and Ghinassi, 2014). Internal small-scale scour punctuations to the inclined heterolithic strata further indicate variable discharge rates. The preservation of horizontally laminated sandstones at the tops of the barform and ripple lamination are evidence of very shallow water depths and therefore probably represent bar top facies (McLaurin and Steel, 2007; Hajek and Heller, 2012; Chamberlin and Hajek, 2019). A dominant occurrence of these elements on the margins of other accretionary elements suggests that they are not to the scale of large point-bar elements, but probably represent lateral growth strata of small intra-channel belt channels and barforms.

3.4.4 Upstream accretion elements

Description - Sandstone elements that are typically 3 m thick and 20 m-80 m wide. The elongate lensoid geometries of the elements (width-to-depth ratio of approximately 25:1) are confined within fourth- or fifth-order bounding surfaces at the tops of elements and fourth-order scour surfaces at the bases. These elements always form on the more upstream side of other architectural elements. The succession comprises trough and planar cross-bedded facies. No grain size trend can be determined, as no sedimentary log records an example of the element. The element shows prominent low-angle accretionary third-order and small-scale fourth-order scour bounding surfaces that bound crossbed sets. The set thicknesses within the element range from 0.20 to 0.43 m. Low-angle accretion surfaces dip at about 12° to the west and upstream from the recorded channel palaeocurrent directions.

Interpretation - The lensoidal geometries and locations of elements of this type on the upstream margins of another elements, coupled with low-angle and upstream dipping accretionary surfaces within them, indicate elements of this type are most probably deposited as upstream accretion elements (Bristow, 1993; Skelly et al., 2003). Upstream accretion occurs as a result of bank-low discharge when planar and sinuous bedforms amalgamate on the upstream margin of bars and stack to the water depth (Bristow, 1993; Skelly et al., 2003; Wang and Plink-Björklund, 2019b). This stacking causes back-stepping of bedform migration and the development of low-angle accretionary surfaces that dip upstream (Skelly et al., 2003). The erosional nature of the fourth-order, small-scale scour surfaces seen within the element are produced by scour pits generated by eddies as dunes migrate (Hajek and Heller, 2012). Such barforms have been found within modern analogues such as the Niobrara River, Nebraska (Skelly et al., 2003) and the Jamuna River (Ashworth et al., 2000). They have been attributed to early stage compound barform development (Ashworth et al., 2000).

3.4.5 Overbank elements

Description - These elements preserve as thin tabular bodies that are usually no wider than 170 m or thicker than 1.5 m and represent the least abundant of the elements within the Lower Castlegate (only 2.3% of the total Lower Castlegate in the three VOMs). The basal bounding surfaces of the elements are a gradational fourth-order top surfaces of the underlying element. The margins and tops of the elements are always fifth-order erosional bounding surfaces. The elements consist of fine-grained structureless to horizontally laminated sandstones (Sm, Sh) to planar laminated mudstone facies. Some minor plant fragments, rooting (approximately 0.5-8 cm wide) and poorly preserved pedogenic nodules

are noted within the mudstone facies, along with very minor intercalations of coal and millimetre- scale siderite concretions.

Interpretation - The fine-grained nature, minor palaeosol nodules, minor coal intercalations and the presence of rooting indicate sediment deposited as a moderately wet and vegetated sub-strate. Consequently, occurrences of this element are interpreted as overbank or floodplain material (Nanson and Croke, 1992; Törnqvist and Bridge, 2002). Planar lamination develops from suspension settling within the flow when discharge breaches channel banks. The limited extent of the element suggests that regular avulsion of channels eroded the overbank material, and that overbank elements have occupied previously abandoned channels (Reinfields and Nanson, 1993).

3.5 Downstream variations Lower Castlegate

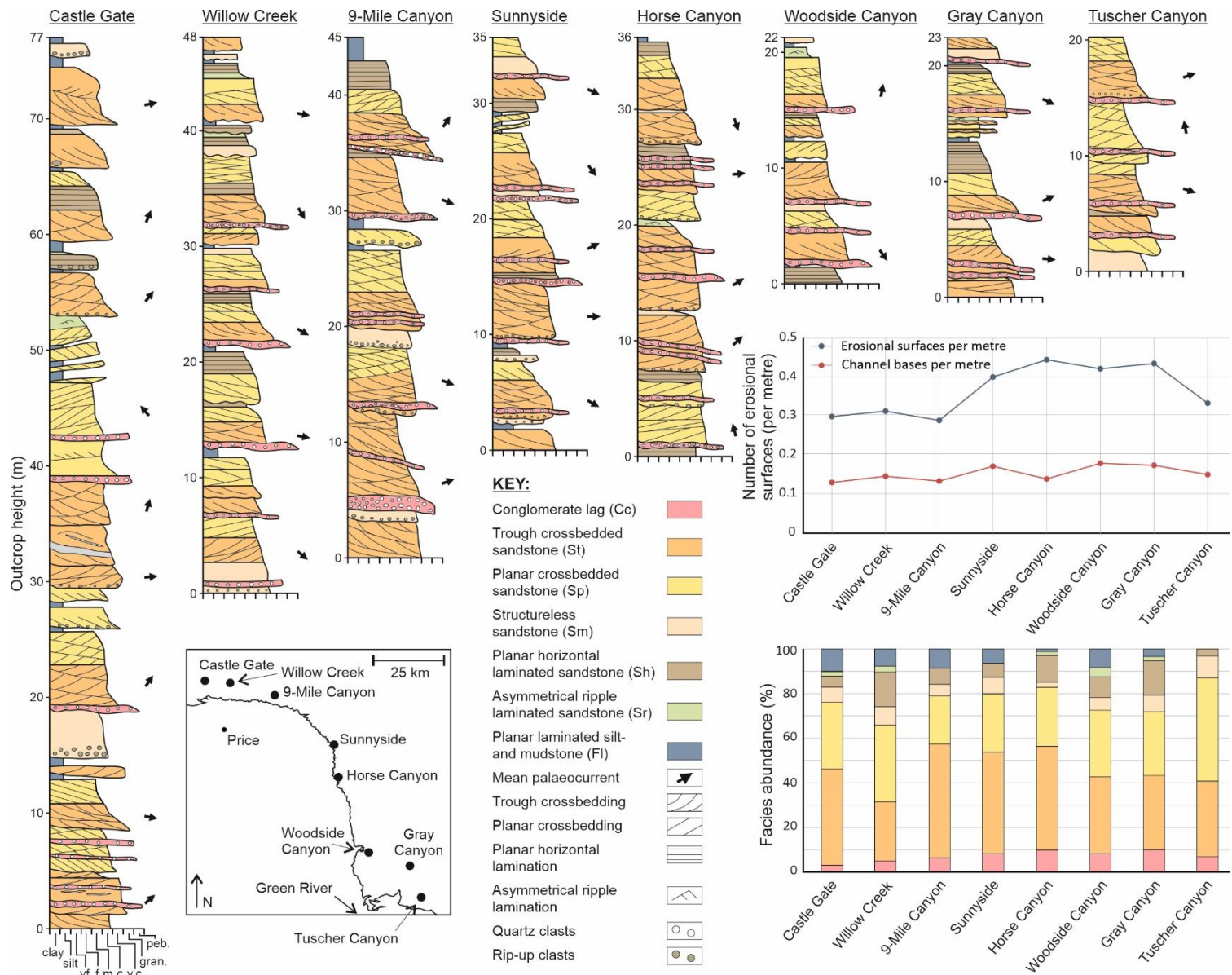
This section will look at regional trends and variations in the facies and architecture described above, across a downstream profile.

3.5.1 *Downstream distribution of facies*

The Lower Castlegate MSB comprises mainly trough and planar crossbedded sandstone, with little notable downstream trend apparent for either facies. Trough cross-bedded sandstone proportions range from 33% to 50% (Figure 3.10). The relative proportion of planar crossbedded sandstone facies remains largely similar downstream (22 % to 35%), with an exception at the more distal Tuscher Canyon section (44%). The amount of preserved channel-lag increases downstream to a medial setting (Horse Canyon), before remaining relatively constant, at approximately 10%, towards the more distal portion of the fluvial system. Conversely, preservation of planar laminated mudstones decreases downstream

towards the distal Tuscher Canyon section, where they are not preserved (Figures 3.10), with the exception of Horse Canyon to Woodside Canyon where an increase of 9% in mudstone content is noted. The proportion of bar-top facies (horizontally laminated and ripple laminated sandstones; Hajek and Heller, 2012) (Figure 3.9) shows a very general decrease downstream.

Figure 3.10 (next page) - *Field-obtained sedimentary logs and mean palaeocurrent directions of architectures collected in the field for each study locality. Logs are ordered (left to right) from west to east, highlighting the thickness variations observed across the Lower Castlegate Sandstone. A stacked bar graph of facies proportions is shown, proportions are obtained from the vertical thickness of the facies in the logs shown. A graph of erosional surfaces shows the number of erosional surfaces per metre, for each logged locality, and the number of channel bases per metre preserved across the Castlegate. This highlights the lack of preservation of in channel material towards the more distal portion of the basin.*



3.5.2 *Downstream variations in architecture*

This section highlights the varying proportions of elements and their preserved architectural element dimensions.

Proportions of architectural elements

The architecture of the proximal Lower Castlegate MSB, in its type locality area (Figure 3.2), is dominated by channel fill elements (64%; Figure 3.11). It shows notable preservation of overbank elements (6%) but shows a relatively low preservation of downstream accretion elements (17%). A similar distribution of channel elements is noted in the medial Sunnyside outcrop, in which the elements form the dominant portion of the succession. However, in the medial section overbank preservation is negligible (<1%; Figure 3.11). The Sunnyside and Castle Gate outcrops show similar proportions of upstream accretion (approximately 4%) and lateral accretion elements (approximately 8-9%). The distal Tuscher Canyon section exhibits a markedly different distribution in the relative proportions of architectural elements than the more proximal sections, with over 50% of the succession comprising downstream accretion elements and 11% comprising lateral accretion elements. The succession has a reduced channel proportion (34%) and has no upstream accretion or overbank elements preserved (Figure 3.11), when compared to upstream sections.

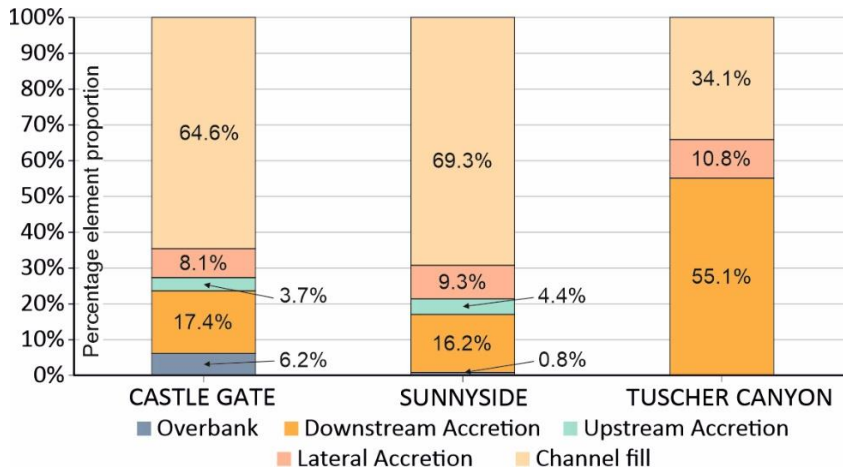


Figure 3.11 - The abundance of architectural elements across the three photogrammetric datasets across the Book Cliffs derived from the photogrammetric analysis of the proximal (Castle Gate), medial (Sunnyside) and distal (Tuscher Canyon) sections.

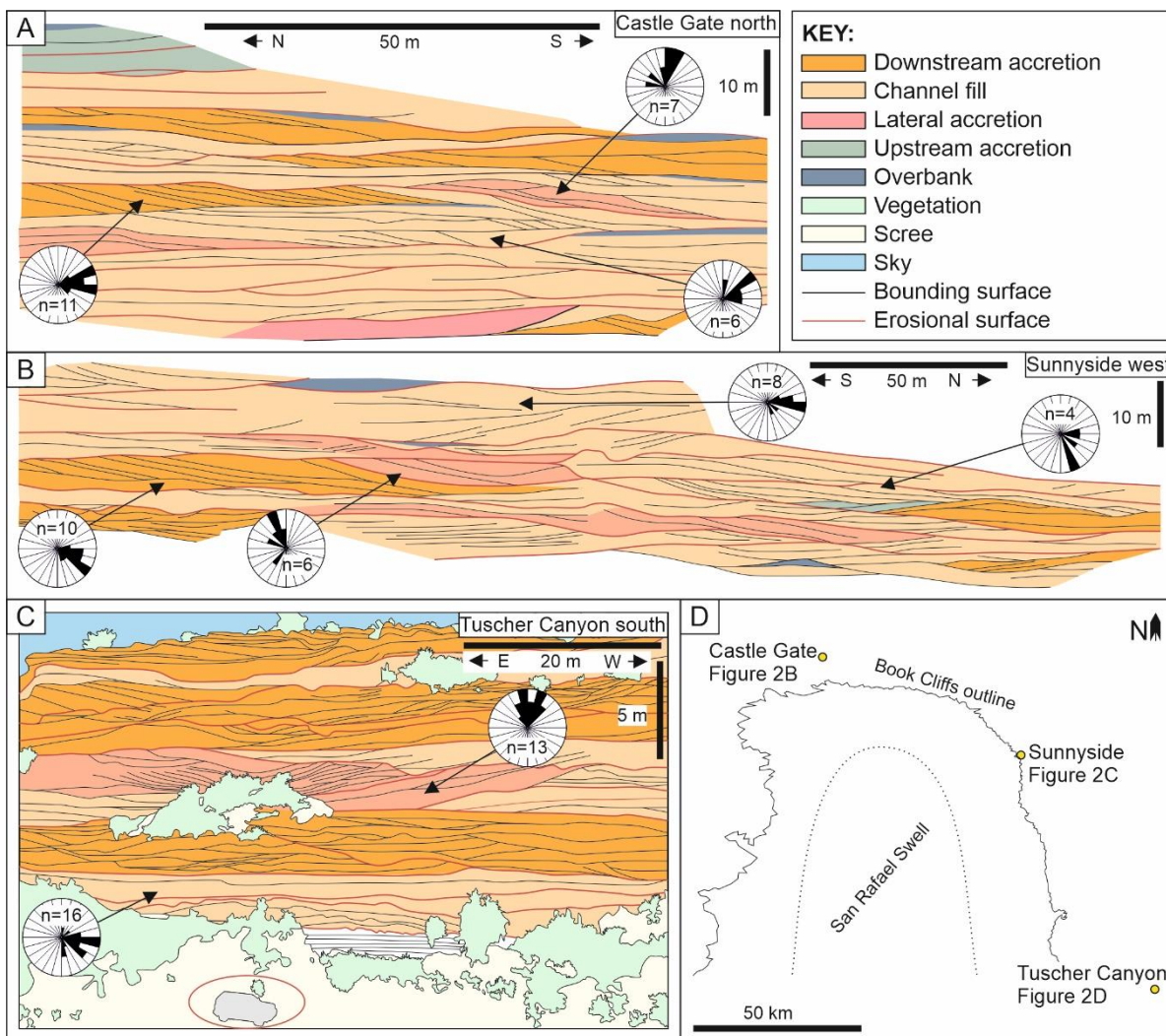


Figure 3.12 - Outcrop interpretation images with (inset) location map, with palaeocurrent data and n values of individual elements (15° bins). (A) Castle Gate north outcrop (509831, 4400284) from McLaurin and Steel (2007) showing the proximal section of the Castlegate MSB. (B) Sunnyside west outcrop (553925, 4379887) for the medial section. (C) Tuscher Canyon south (584290, 4327974), note mid-sized SUV for scale (highlighted). (D) Inset map showing the locations of the outcrops and the Book Cliffs classic outcrop outline in Figure 3.3. For more detailed analysis of photogrammetry please refer to Appendix B and C.

Architectural element dimensions

Channel fill elements in the proximal Castle Gate are approximately 40 m wide (Figure 3.12, 3.13) and generally 3.5 m thick. The channel elements become progressively wider and deeper through Sunnyside (150 m wide and 6 m thick) and Tuscher Canyon (208 m wide and 6.6 m thick). The width to thickness ratio of channel elements increases from 11:1 in the proximal region to 31:1 in the distal Tuscher Canyon section (Figure 3.13). An increasing width to thickness ratio is also shown in downstream accretion elements (Figure 8), where it progressively changes from 5:1 to 42:1 between the Castle Gate and Tuscher Canyon sections, respectively. Lateral accretion elements, however, do not experience the same trends. Whilst displaying the same width to thickness ratio trend downstream (14:1-35:1; Figure 3.13) they do not show any major increase in thickness from proximal and distal settings (ranging from approximately 2.2 m to 3.2 m). The trends of lateral accretion are only defined by partial element exposure in Sunnyside, it is therefore likely that a further increase in size of lateral accretion elements downstream has been suppressed.

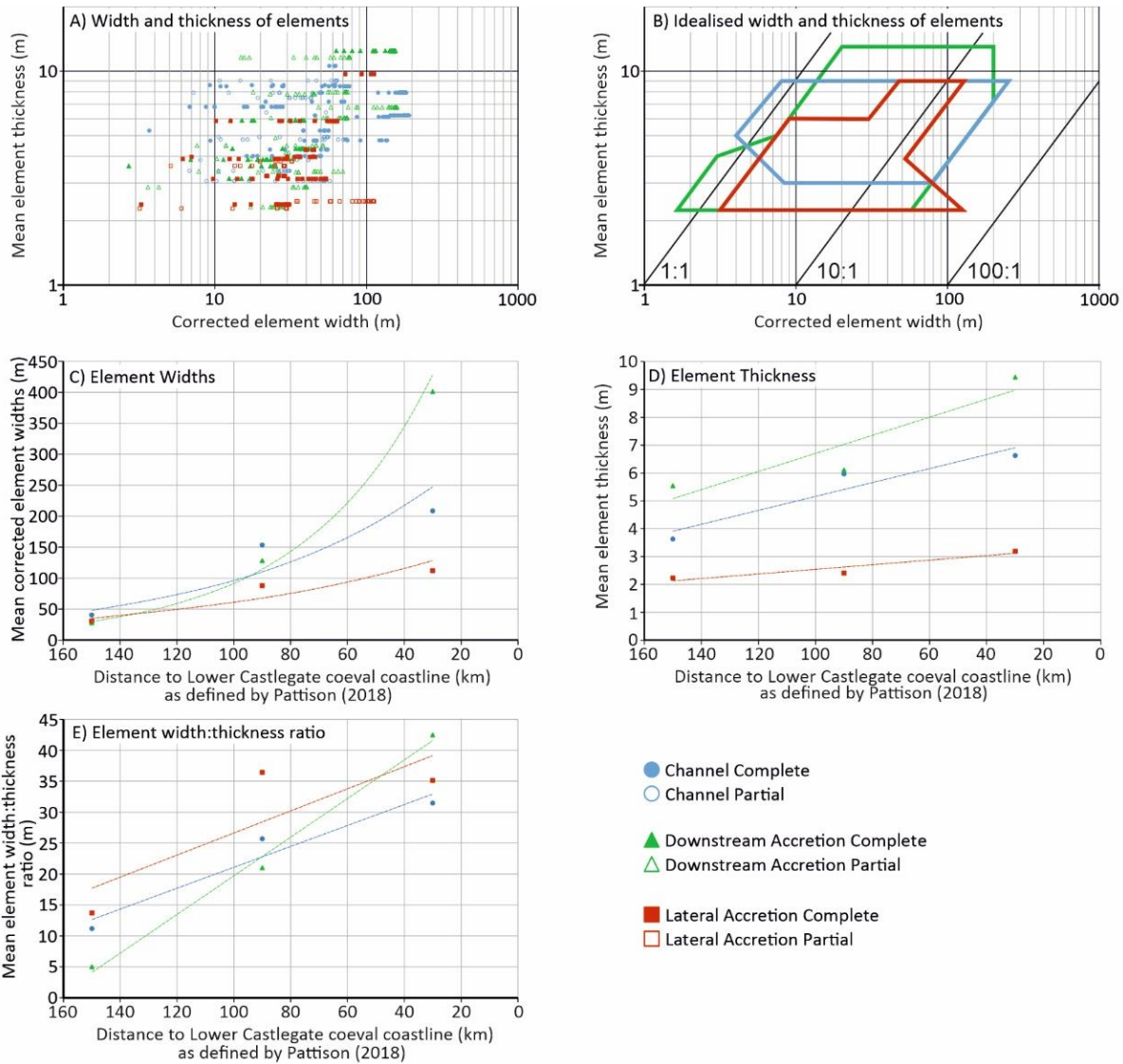


Figure 3.13 - (A) Scatter log-log plot showing the relationship of corrected width to thickness for each of the major constituent architectural elements within the Lower Castlegate Sandstone. (B) The corrected width against thickness for each of the major constituent architectural elements of the Lower Castlegate, shown as data envelopes (Gibling, 2006) highlighting the area in which corrected widths and thicknesses will occur. (C) Mean complete and partial element thickness for each field site relative to the palaeo-coastline. (D) Mean complete and partial element widths for each field site relative to the palaeo-coastline. (E) Mean complete and partial element width:thickness ratio for each field site relative to the palaeo-coastline.

3.5.3 *Downstream variations in accretionary element preservation*

There are at least two-types of erosional surfaces within the Lower Castlegate MSB: reactivation scours, element scours and channel bases (Hajek and Heller, 2012) (Figure 3.12). Concave-up listric reactivation surfaces scour crossbed sets and cosets of accretionary elements, and form when channel discharge increases from bank-low conditions to bank-full conditions and accompanying increased flow rates promote erosion into in-channel elements (Herbert et al., 2020). Undulatory horizontal to shallowly dipping element scour surfaces are formed from autogenically induced changes of in-channel hydrodynamics that can partially or completely erode bar top facies (Miall, 1994; Hajek and Heller, 2012). The depth of such scours can depend upon subsidence rate, discharge and aggradation rate (Hajek and Heller, 2012). Erosional concave-up (in flow perpendicular orientation) and undulatory planar to shallowly dipping channel bases that incise much deeper than element scour surfaces and typically show a large grain size increase across the erosional surface. Such scours formed from local avulsion of a channel belt (Lynds and Hajek, 2006; McLaurin and Steel, 2007; Hajek and Heller, 2012; Chamberlin and Hajek, 2015), whereby a fluvial channel will avulse to a topographically lower area (Bridge and Leeder, 1979; Straub et al., 2009).

The number of channel bases per metre, vertically, does not change downstream and remains between 0.12 and 0.18 (Figure 3.10) across the Lower Castlegate MSB. The number of erosional surfaces per metre within the sedimentary logs increases downstream towards the distal Tuscher Canyon section. There is an increase from 0.3 in the proximal Castle Gate, Willow Creek and 9-Mile Canyon region, to 0.42 in the more distal Horse Canyon to Gray Canyon sections. There is a markedly lower number of erosional surfaces per metre (0.33), vertically, in the most distal Tuscher Canyon section.

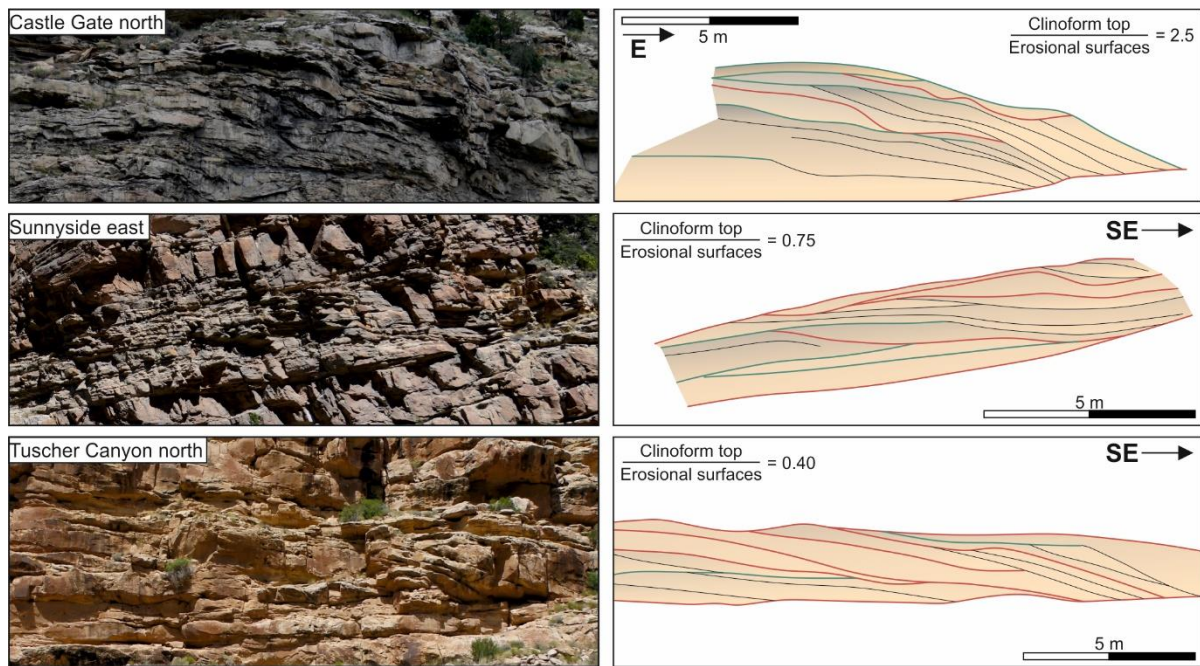


Figure 3.14 - Three preserved barforms from the Lower Castlegate Sandstone in the studied log sections. The images show a downstream accretion barform and to the right there is an interpretation of the bounding surface nature for each barform, along with a rough quantification of erosional surfaces against clinoform top (Hajek and Heller, 2012) to highlight the degree of barform preservation.

This increase in erosional pattern is also seen further downstream where accretionary element clinoforms rarely preserve their topset (Hajek and Heller, 2012) (Figure 3.14). In-channel accretionary element topsets preserve well within the proximal Castle Gate section (2.5 topset surfaces to erosional surfaces); whereas downstream in the distal Tuscher Canyon section, erosional surfaces dominate (0.4 topset surfaces to erosive surfaces; Figure 3.14), preserving only the basal to mid-portions of the accretionary elements.

3.5.4 Downstream variations in palaeoflow reconstructions

Maximum flow depths reconstructed from crossbed set thicknesses in the Castle Gate proximal locality suggest depths of 3.8-11.6 m (Figure 3.15A) with a general deepening up

section. These results concur with those of McLaurin and Steel (2007), who recorded estimated flow depths of approximately 4.6-7.7 m and a maximum depth of 14.7 m. The general deepening upwards through the succession is also recorded by previous studies (McLaurin and Steel, 2007; Hajek and Heller, 2012). The reconstructed maximum flow depths within the type locality area show a mean of 6.9 m and a variance of 0.32 indicating variable discharge (Figure 3.15), and confirming the interpretation presented from the reactivation surfaces within the accretionary element bounding surface framework.

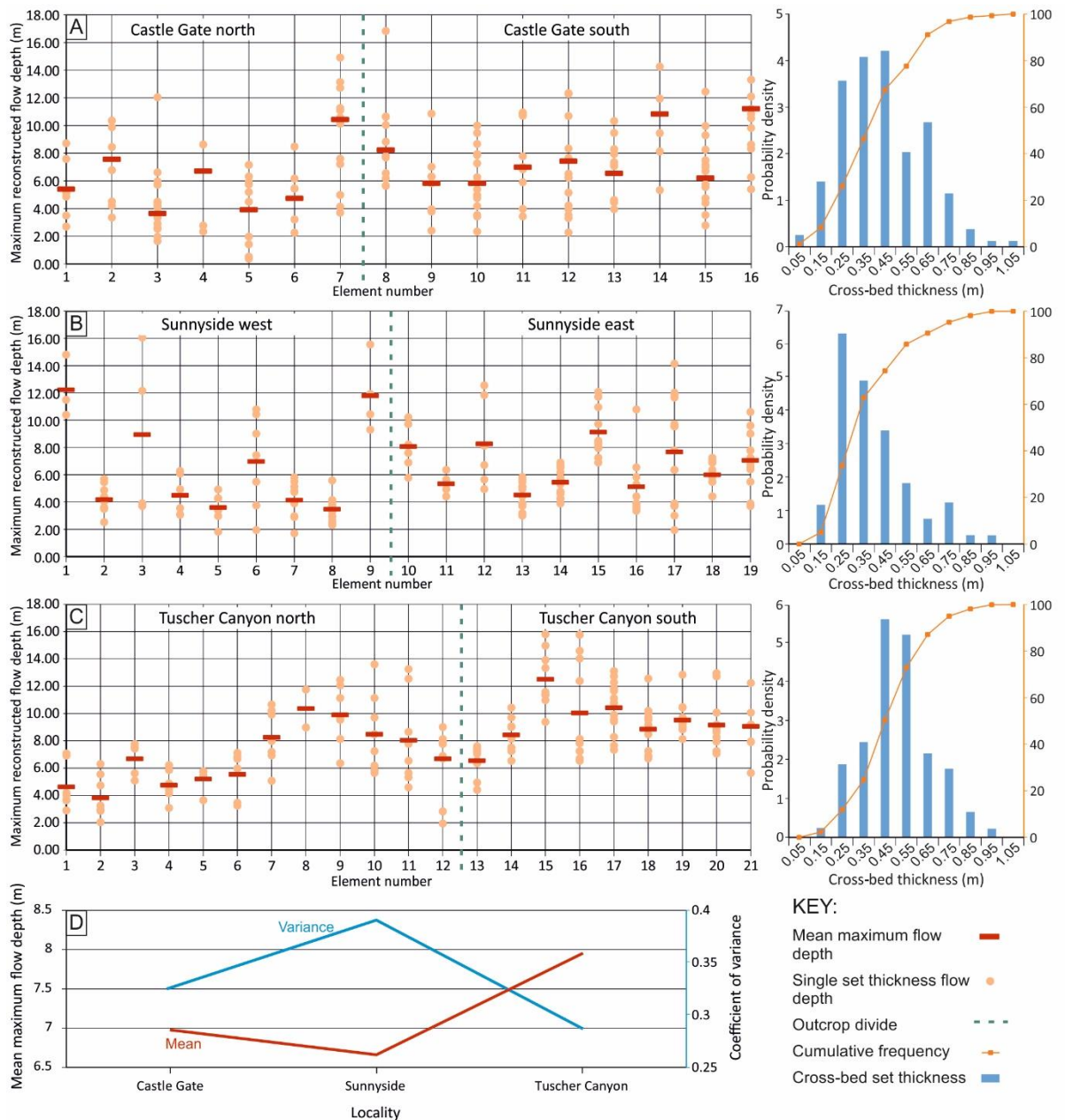


Figure 3.15 - Reconstructed flow depths from set thicknesses in each VOM locality. (A) The Castle Gate locality, showing mean maximum flow depth of each element relative to a single set thickness measurement. The green dashed line represents where data from one outcrop ends and another begins. Each element has been assigned a number; the numbers assigned to elements increase upsection (elements 1-7 make up the northern outcrop, 8-16 make up the type locality). Histograms based on the probability density of set thicknesses are provided with the cumulative frequency (%), orange). (B) The Sunnyside locality (elements 1-9 make up the western outcrop, 10-19 make up the eastern), showing mean maximum flow depth of each element relative to a single set thickness measurement. (C) The Tuscher Canyon locality (elements 1-12 make up the northern outcrop, 13-21 make up the southern), showing mean maximum flow depth of each element relative to a single set thickness measurement. (D) The mean maximum reconstructed flow depths of each locality plotted with the coefficient of variance (secondary y-axis) of those means as a proxy of variable maximum flow depths.

Reconstructed maximum flow depths in the Sunnyside locality are between 3.7-12.1 m (Figure 3.15B) with a mean of 6.7 m and a variance of 0.38. The Sunnyside locality shows a similar depth of flow to the type locality. However, there is an increase in discharge variability shown in the variance, and no obvious increasing in flow depth is indicated up-section. Reconstructions from Tuscher Canyon indicate flow depths of 4-12.3 m (Figure 3.15C) that are similar to those indicated for the more proximal areas. However, mean maximum flow depth is much greater (8 m) and shows a much lower variance of 0.28 (Figure 3.15D). Consequently, a deepening of flow with a more consistent discharge rate may be implied for the distal portion of the study area.

The sinuosity of the Lower Castlegate MSB shows a progressive increase downstream. The proximal Castle Gate section shows low sinuosity (1.11; Table 3.2) in channel fill elements

and intermediate sinuosity (1.54) when incorporating accretionary element data. The distal Tuscher Canyon section gives values of sinuosity of 1.83 and 2.03 (Table 3.2), with and without accretionary element data respectively, that indicate intermediate to high sinuosity. These trends are consistent for all three methods of sinuosity reconstruction (Table 3.2).

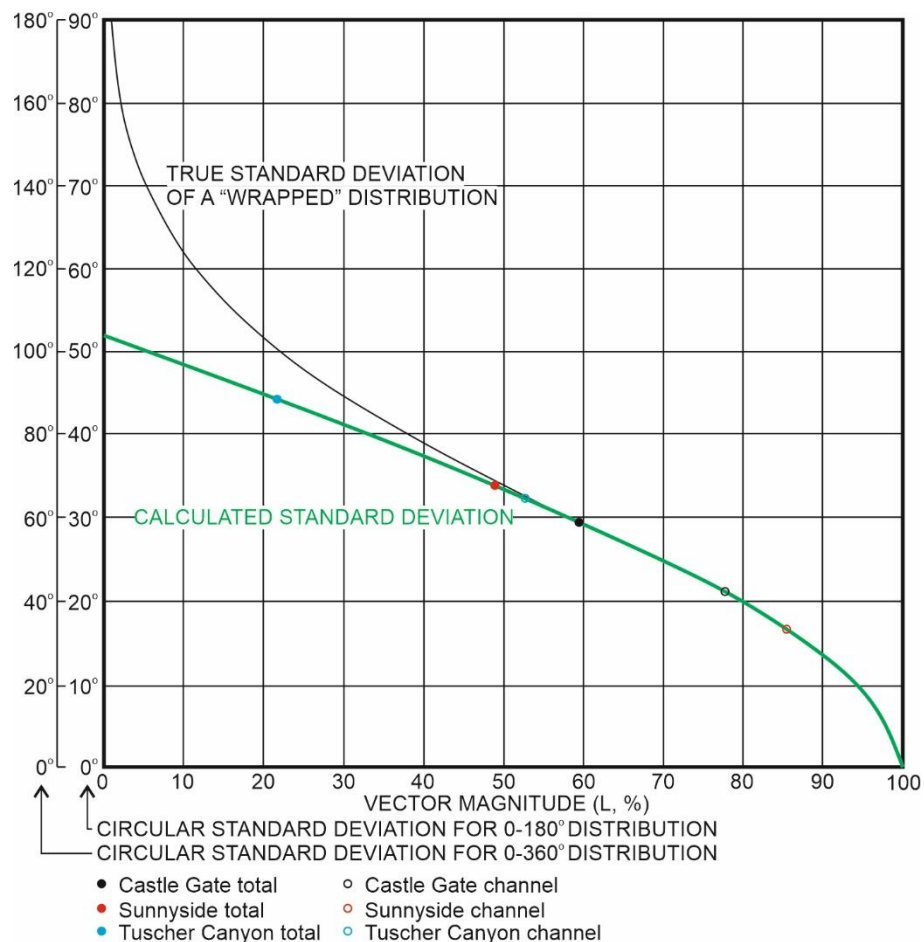


Figure 3.16 – Plots of palaeocurrent vector magnitude and circular standard deviation (modified from Curray 1956). Plot shows channel only and total palaeocurrent data results from each locality.

The channel fill elements show a greater dispersion of palaeocurrent data towards the distal portion of the Lower Castlegate Sandstone (Figure 3.16) implying a downstream increase in sinuosity. Downstream accretion elements show a greater dispersion of palaeocurrent data towards the distal portion of the Lower Castlegate MSB, which may reflect different directions to accretionary element palaeoflow in the distal section, or more probably an

increase in oblique growth of the elements due to their more mature development. Palaeocurrent trends for lateral accretion elements, that are normal to local thalweg flow, become more prominent downstream towards Tuscher Canyon, implying further evidence of sinuosity increase. These results concur with those previously published (Miall, 1993, 1994) and indicate sinuosity and lateral accretion trends increasing downstream.

Method	Castle Gate		Sunnyside		Tuscher Canyon	
	Channel	Total	Channel	Total	Channel	Total
La Roux (1994)	1.24	1.75	1.31	1.73	2.21	2.51
Ghosh (2000)	1.21	1.83	1.28	1.88	1.82	2.98
Bridge et al. (2000)	1.11	1.54	1.21	1.4	1.83	2.03

Table 3.2 – Palaeocurrent analysis results from the Lower Castlegate.

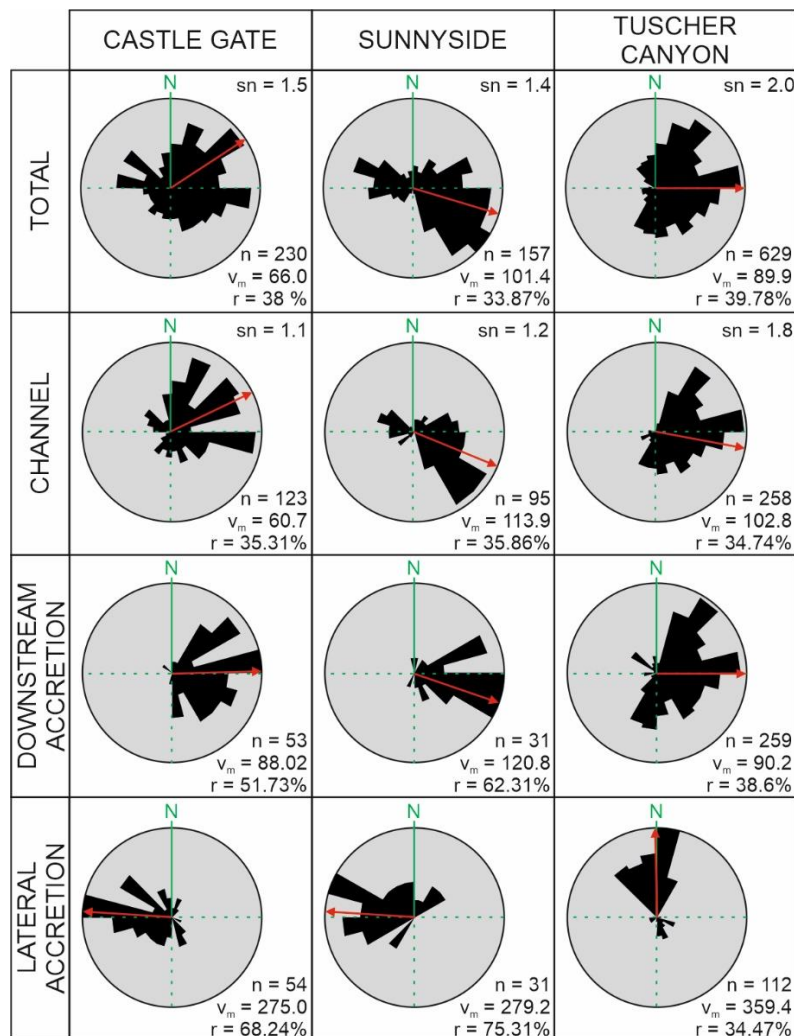


Figure 3.16 - Palaeocurrent summary of the Lower Castlegate MSB, divided by architectural elements at each location. Note, n = number of measured forests, v_m = mean azimuth, r = dispersion as a percent, sn = sinuosity value. Note, 15° bin size.

3.6 Subsidence rates across the Lower Castlegate Sandstone

This section highlights the geometric trends in stratigraphic architecture and uses published well log interpretations to produce an original burial history. This enables basin scale controls upon deposition to be understood and their influence upon potential architectures to be identified.

3.6.1 Burial history methodology

Subsidence rates provide primary controls upon fluvial depositional architecture and preservation potential (Catuneanu and Elango, 2001; Leckie and Boyd, 2003; Catuneanu, 2006). In order to determine basin-scale variations in subsidence rate, decompacted one-dimensional burial history curves were constructed in the basin modelling software Genesis (Zetaware) software for ten borehole sections penetrating the Mesaverde Group along a ~150 km WNW-orientated transect, parallel to depositional dip. Calculation of the decompacted rock unit thickness was performed in Genesis and is lithology specific (c.f., Perrier and Quiblier, 1974).

The gamma ray responses of the ten borehole sections (from Hampson et al., 2005) were used to determine depths to unit tops (identified in Hampson et al., 2005; Seymour and Fielding, 2013), unit thicknesses and lithology (Figure 3.18, 3.19; Table 3.3). Values for depth to top and unit thickness and were obtained for the Star Point, Lower Blackhawk, Upper Blackhawk and the Lower Castlegate Sandstone (Seymour and Fielding, 2013), based on similar interpretations made by Hampson et al. (2005) (Figure 3.19). The biostratigraphic

zonation schemes of Obradovich (1993) and Seymour and Fielding (2013; and references therein) (Figure 3.18) are used to provide timing constraints. The estimates of Pitman et al. (1987), Olsen et al. (1995) and Aschoff and Steel (2011b) provided control upon eroded overburden thicknesses (Figure 3.18). Deposition is assumed to have occurred at or close to sea level so the effects of bathymetry are not accounted for in our models.

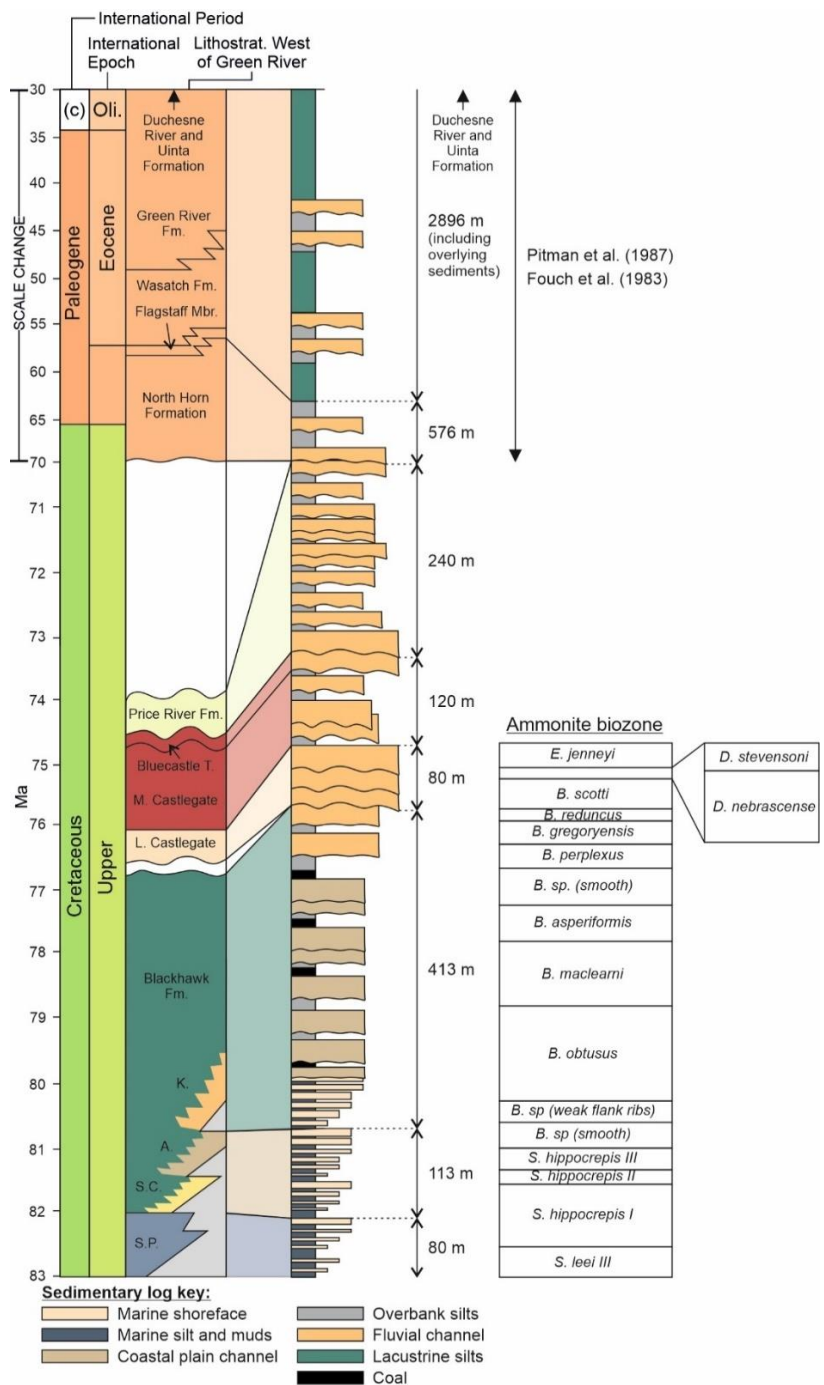


Figure 3.18 - Information used in the creation of the burial history plots. Thicknesses of the overburden and environment of deposition have been taken from Pitman et al. (1987), Olsen et al. (1995), Miall and Arush (2001), Aschoff and Steel, 2011a,b) and Seymour and Fielding (2013).

3.6.2 Burial history results

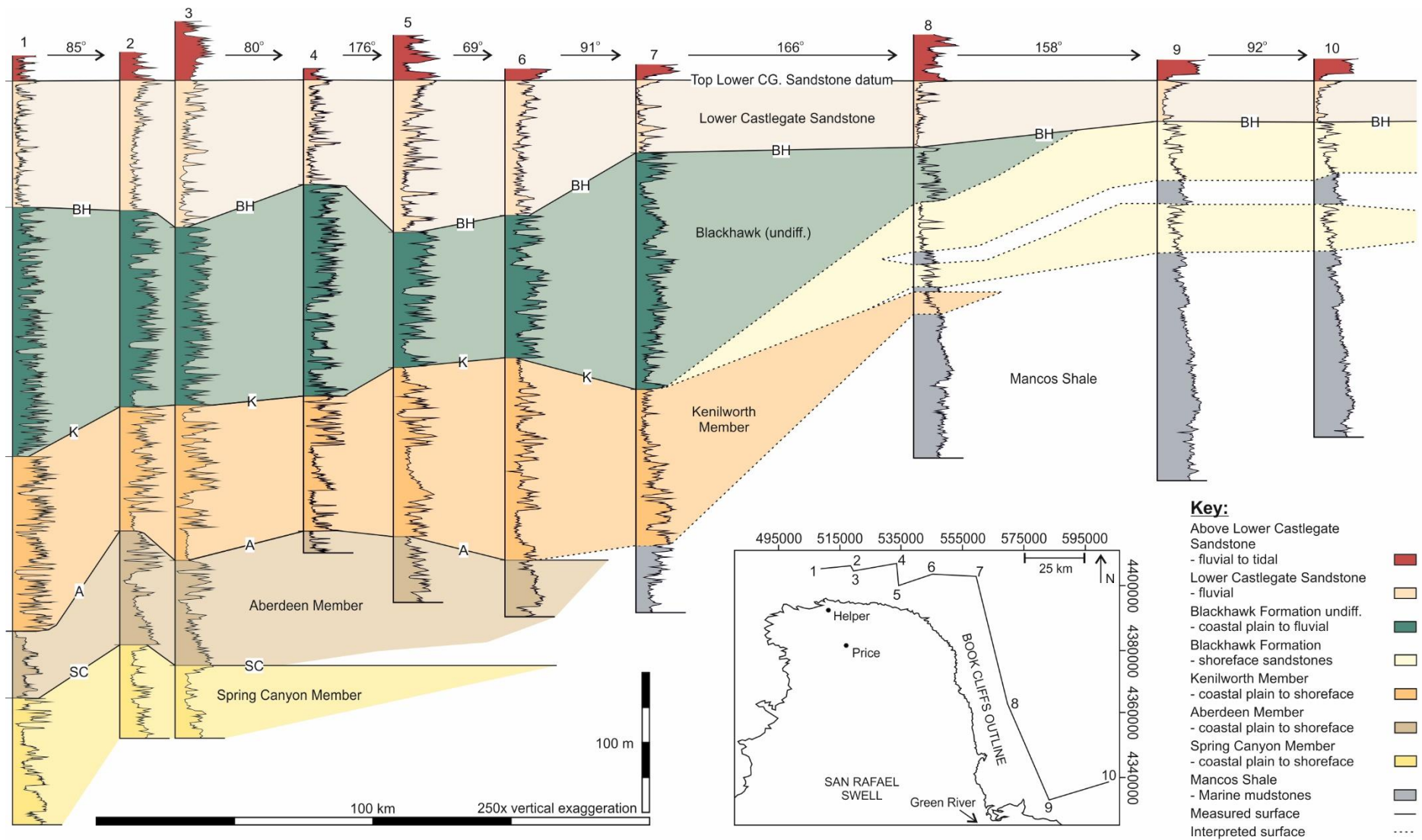
Results of the burial history analysis (Figure 3.19) show that in the more proximal foreland (e.g., Matt's Summit State; Figure 13B), the Upper Cretaceous succession is interrupted by two breaks in deposition at 77 Ma and 70 Ma respectively (Seymour and Fielding, 2013) (Figure 3.4). The earliest of these is associated with the unconformity at the base of the Lower Castlegate Sandstone (Olsen et al., 1995; Yoshida et al., 1996; McLaurin and Steel, 2000; Miall and Arush, 2001). The latest of these unconformities is the regional pre-North Horn unconformity (Lawton, 1986; Guiseppe and Heller, 1998; Olsen et al., 1995). The Lower Castlegate Sandstone is at its thickest in the eastern part of the Cordilleran retro-foreland basin system and pinches out towards the west (Figures 3.18, 3.19), reflecting syn-depositional downwards flexure of the foreland due to the easterly migration of the Sevier Fold and Thrust Belt (Lawton, 1986; Hampson et al., 2005; Aschoff and Steel, 2011a, 2011b). In the more distal foreland, only the latest of these breaks in deposition is apparent (Figure 3.19B). Although this may be attributed to the poorer stratigraphic constraints within the condensed succession of the distal foreland region.

Formation Tops	Matts Summit State A1		Shimmin Trust 10-11		Shimmin Trust 2		Slemaker A1	
	Thickness [m]	Formation Top [m]	Thickness [m]	Formation Top [m]	Thickness [m]	Formation Top [m]	Thickness [m]	Formation Top [m]
Lower Castlegate	91.44	1038.1488	95.0976	1026.8712	97.536	926.592	75.5904	1745.5896
Blackhawk Fm.	181.0512	1129.5888	142.9512	1121.9688	135.636	1024.128	153.3144	1821.18
Kenilworth Mbr.	140.8176	1310.64	89.0016	1264.92	141.732	1159.764	95.4024	1974.4944
Aberdeen Mbr.	63.3984	1451.4576	82.296	1353.9216	45.72	1301.496	-	2069.8968
Spring Canyon Mbr.	-	1514.856	-	1436.2176	-	1347.216	-	-
Formation Tops	Iriart fee 1		Keel Ranch 1-16		Stone Cabin 1		Wilcox 1-24	
	Thickness [m]	Formation Top [m]	Thickness [m]	Formation Top [m]	Thickness [m]	Formation Top [m]	Thickness [m]	Formation Top [m]
Lower Castlegate	110.3376	672.9984	89.916	1775.46	52.4256	2053.1328	47.728	882.816
Blackhawk Fm.	97.8408	783.336	95.0976	1865.376	112.1664	2105.5584	-	930.544
Kenilworth Mbr.	122.2248	881.1768	135.0264	1960.4736	117.6528	2217.7248	-	-
Aberdeen Mbr.	-	1003.4016	-	2095.5	215.7984	2335.3776	-	-
Spring Canyon Mbr.	-	-	-	-	-	2551.176	-	-
Formation Tops	Butler Canyon Unit USA 33-12		Rattlesnake State 2-12					
	Thickness [m]	Formation Top [m]	Thickness [m]	Formation Top [m]				
Lower Castlegate	28.956	194.1576	34.7472	194.4624				
Blackhawk Fm.	-	223.1136	-	229.2096				
Kenilworth Mbr.	-	-	-	-				
Aberdeen Mbr.	-	-	-	-				
Spring Canyon Mbr.	-	-	-	-				

Table 3.3 – Formation tops and thicknesses of Cretaceous units used in the development of one-dimensional burial history plots.

Subsidence curves for each of the ten borehole successions (Figure 3.20) display a convex upwards profile, indicating exponentially increasing subsidence rates due to the basinward convergence of a thrust belt or orogenic load (cf., DeCelles and Giles, 1996; Littke et al., 2000; Burgess and Gayer, 2000). There are significant (less than 150%) lateral variations in the subsidence rates during deposition of the Lower Castlegate Sandstone, perpendicular to the thrust-belt (Pang and Nummedal, 1995). In the more proximal region of the foreland (e.g., the Matt's Summit State A1 and Shimmin Trust boreholes; Figure 3.20) average subsidence rates are approximately 0.2 mm yr^{-1} (Figure 3.20C). This decreases towards the more distal region of the foreland (e.g., the Butler Canyon Unit USA 33-12 and Rattlesnake Canyon 2-12 boreholes; Figure 3.20), where average subsidence rates are 0.08 mm yr^{-1} , which reflects the proximity of the succession to the orogenic load (Pang and Nummedal, 1995) (Figures 3.20B).

Figure 3.19 (next page) - *Gamma ray correlations of the Mesaverde Group to the top of the Lower Castlegate (correlation datum; (based upon Hampson et al. 2005). Inset map shows the outline of the Book Cliffs and the profile of the log transect represented in the correlation. Correlation plot shows the thinning of the Lower Castlegate moving distally in the basin (eastwards from Green River). Numbers of well locations are: 1 = Matt's Summit State A1, 2 = Shimmin Trust 10-11, 3 = Shimmin Trust 2, 4 = Slemaker A1, 5 = Iriart Fee 1, 6 = Keel Ranch 1-16, 7 = Stone Cabin 1, 8 = Wilcox 1-24, 9 = Butler Canyon Unit USA 33-12 and 10 = Rattlesnake Canyon 2-12 respectively. Note, abbreviations of formation tops are as follows: SC = Spring Canyon, A = Aberdeen Member, K = Kenilworth Member, and BH = Blackhawk Formation undivided.*



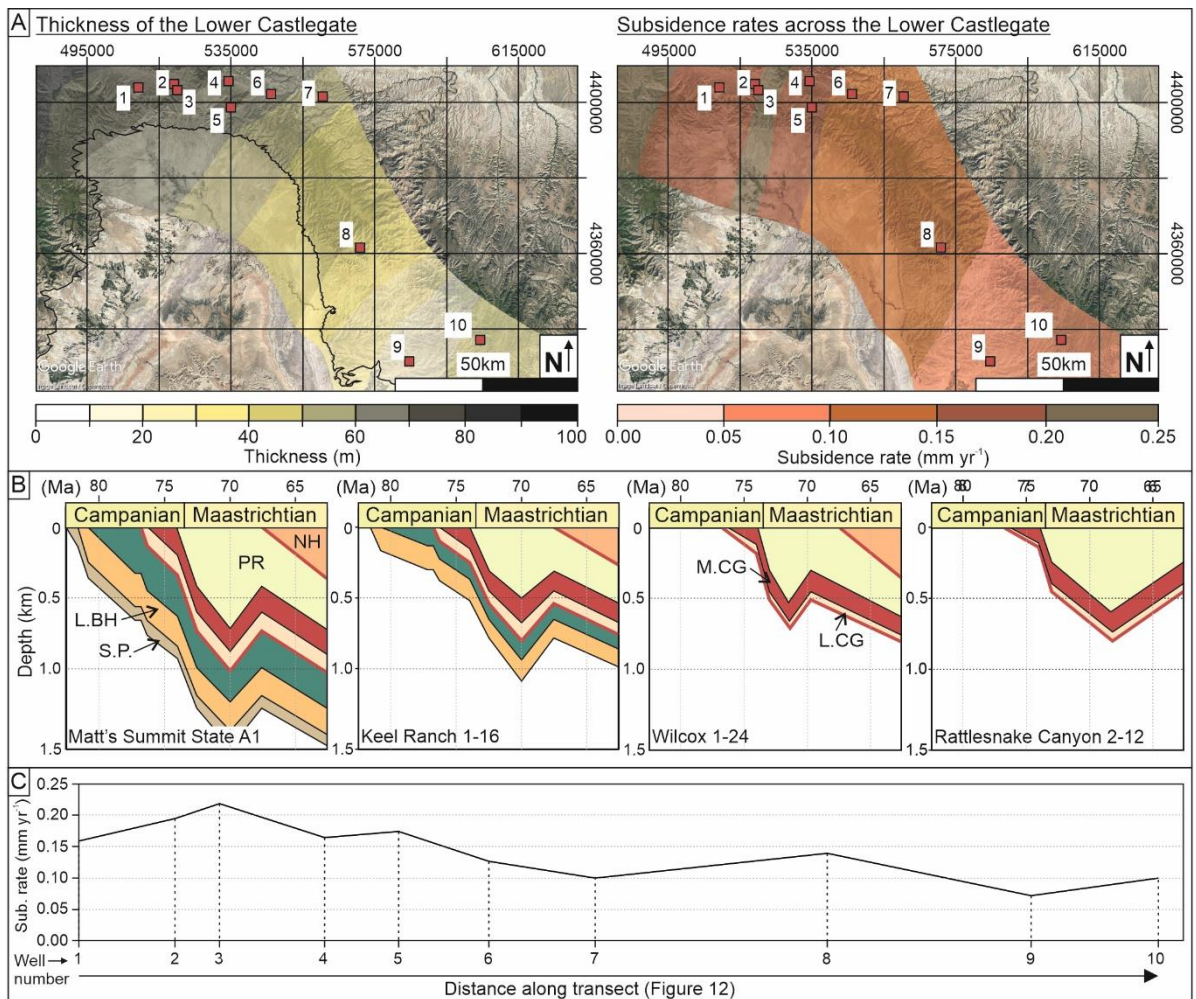


Figure 3.20 - Burial history analysis of the Lower Castlegate Sandstone, Utah. (A) Thickness map from the down-hole logs from Figure 11. Subsidence rate map based upon burial history from down-hole formation thicknesses. (B) One dimensional burial history curves for four of the wells. (C) Subsidence rate for each down-hole log based upon their respective burial history analysis, plotted relative to the well positions across the basin (Figure 12). Numbers of well locations are: 1 = Matt's Summit State A1, 2 = Shimmin Trust 10-11, 3 = Shimmin Trust 2, 4 = Slemaker A1, 5 = Iriart Fee 1, 6 = Keel Ranch 1-16, 7 = Stone Cabin 1, 8 = Wilcox 1-24, 9 = Butler Canyon Unit USA 33-12 and 10 = Rattlesnake Canyon 2-12.

3.7 The influence of subsidence rates on fluvial architecture preservation

The small, low-sinuosity channel-fill elements of the proximal Lower Castlegate (Miall and Arush, 2001; McLaurin and Steel, 2007) contain small accretionary elements that preserve a large number of clinoform topsets (Hajek and Heller, 2012) (Figure 3.14). The succession also exhibits overbank preservation. This overbank and clinoform topset preservation is perhaps indicative of high subsidence rates (Heller and Hajek 2012). The preservation of fluvial systems is dominated, principally, by the aggradation rate, which is controlled in upstream areas by subsidence rates and a buffer zone of the graded fluvial profile (Holbrook et al., 2006). The buffer zone is controlled by the sediment supply and stream power. If sediment supply exceeds stream power then an aggradational profile is established. Such a profile may be visible within the proximal type locality of the Lower Castlegate strata. The combination of buffer zone aggradation and high local subsidence rates in the type locality area may explain the dramatically thicker succession (Holbrook et al., 2006). These arguments are supported in this study by burial history analysis that indicates that subsidence rates were approximately 0.19 mm yr^{-1} at the time that the Lower Castlegate MSB was deposited. The minor presence of upstream accretion elements suggests some primitive compound architecture (Skelly et al., 2003; Ashworth et al., 2011; Lunt et al., 2013) and the presence of reactivation surfaces in accretionary elements, along with evidence presented in the reconstruction of maximum flow depths (Figure 3.15A), indicate variable discharge (Lunt et al., 2013; Almeida et al., 2016) within the channel flow.

The same pattern of upstream accretion and reactivation is present within the Sunnyside succession (Figures 3.11, 3.14), however, greater channel sinuosity is noted (Figure 6a, Table 2). Intermediate-sinuosity channel-fill elements (Figure 3.16) again dominate the succession

and accretionary elements comprise the remaining proportion of the outcrop (Figure 3.11). Poor overbank preservation within the succession can be attributed to reduced subsidence rates (approximately 0.11 mm yr^{-1} ; Figure 3.19, 3.20). The channel dominance and increased sinuosity is interpreted to be a product of downstream evolution in the fluvial system (Holbrook et al., 2006; Li et al., 2015), as it reaches a more stable medial portion of its reach. An increased discharge variability (Figure 3.15D) may also play a factor in the dominance for channel forms, with accretionary barform element formation being suppressed.

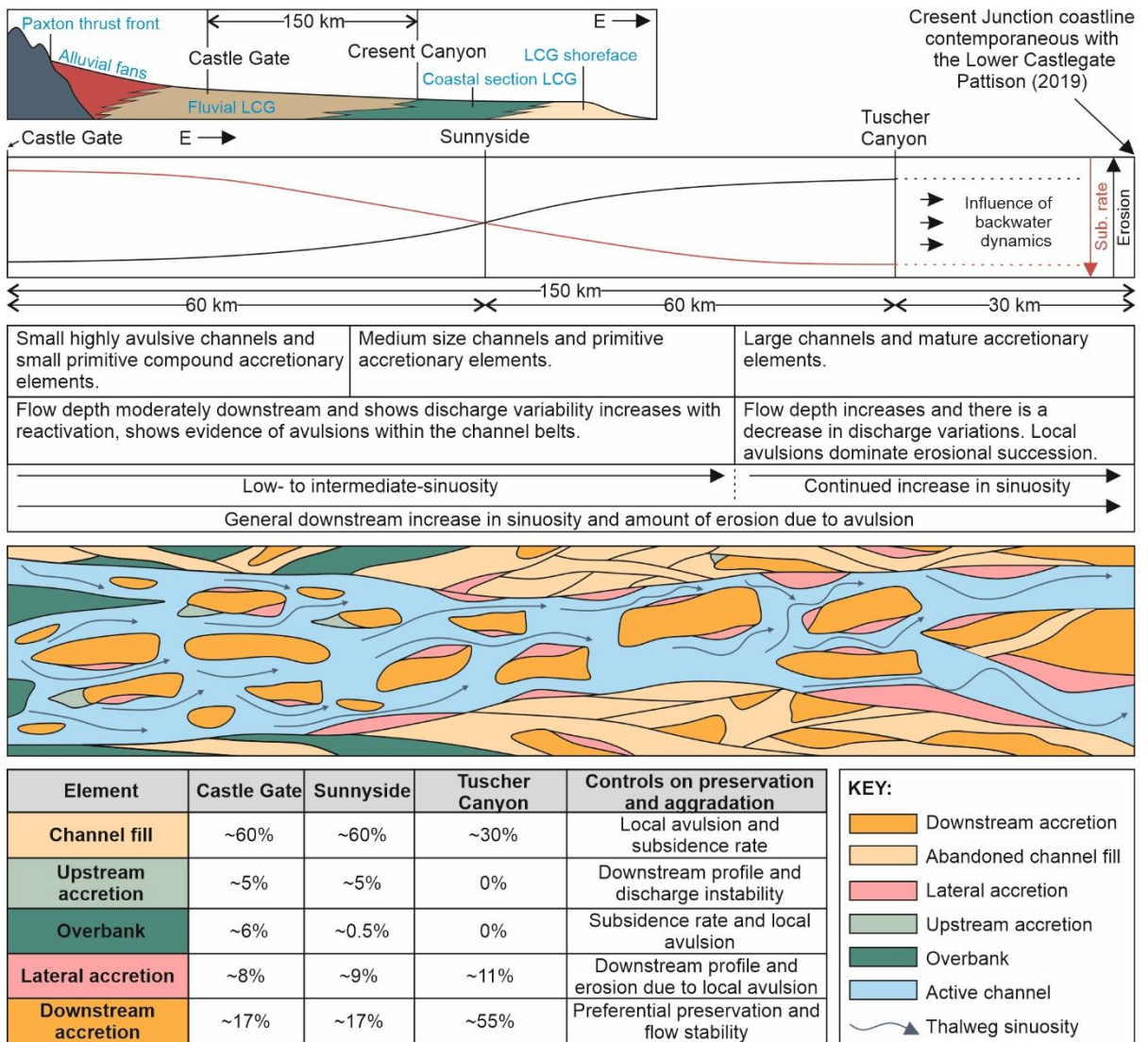


Figure 3.21 - Summary figure of the Lower Castlegate Sandstone MSB. Image is comprised of a cross-sectional view of the Western Interior Seaway during the Lower Castlegate deposition and higher resolution view of the profile within the fluvial profile. Descriptive interpretations of the fluvial strata and architectural elements making the idealised profile are highlighted, relative to their position downstream. This assumes constant avulsion frequency. A top-down view is also given showing the relative size and complexity of the channel and barform architecture within the Castlegate MSB. Finally, a brief summary of the critical changes observed downstream are highlighted and their controls stated.

Finally, the distal Tuscher Canyon section shows a markedly different architectural assemblage than the two more proximal locations (Figure 3.11). Lateral accretion and downstream accretion elements occur without upstream accretion elements being preserved, and suggest a more mature compound architecture formation. The channels, although much larger and more sinuous (Figures 3.13, 3.16, 3.21), form the subordinate proportion of the outcrop. Maximum flow depth reconstructions show less variability (Figure 3.15) and infer that flow depths were more consistent in the area. No overbank elements are preserved in the area. This may be due to a minimal subsidence rate of 0.08 mm yr^{-1} that the burial history analysis indicates. However, despite the presence of high-sinuosity channel deposits with large width to thickness ratio, and indicators of a relatively stable flow, little lateral accretion is preserved.

These interpretations highlight the preferential preservation of compound downstream accretion elements instead of lateral accretion elements within a fluvial unconfined MSB preserved in the distal portion of a retro-foreland basin (Figure 3.21). The increased sinuosity within a fluvial system downstream will generate and deposit lateral accretion elements (not necessarily at the large point bar scale), but the preservation of such elements is dependent

upon aggradation rates, that are here dominantly controlled by subsidence rate. Preserved lateral accretion elements occupy the margins of channels and downstream accreting elements (Miall, 1993; Best et al., 2003). The location of such elements makes them susceptible to erosion, when local avulsion, during periods of low subsidence, encourages the reoccupation of old channel courses (Mohrig et al., 2000). Subsequent flows will most likely occupy previous channel reaches and erode their internal architecture (Chamberlin and Hajek, 2015). This will erode the lateral accretion elements, given their location, preferentially preserving the downstream accretion elements.

3.8 Palaeogeography of the unconfined Lower Castlegate

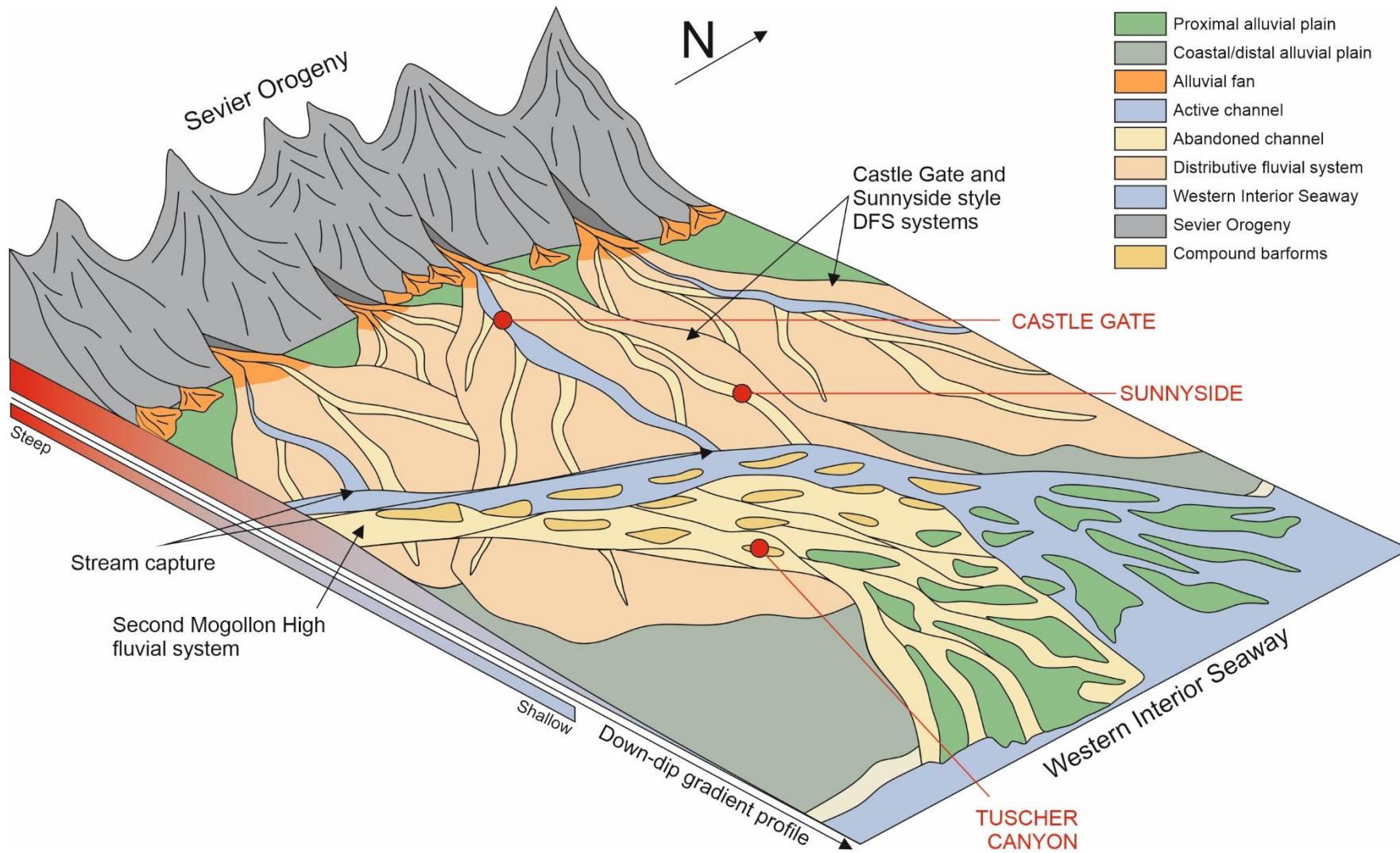
The analysis of the preservation of the architecture within the proximal Castle Gate and medial Sunnyside localities presented here yields similar results to previously published studies on other fluvial strata. For example, Li et al. (2015) studied the fluvial architecture of the Middle Jurassic Rockcave Member of the Yungang Formation, China. The results of their study indicate channel thickness decreasing from proximal to more distal areas (Li et al., 2015 their Table 3) in direct comparison with this study presented here. Further to this Li et al. (2015) evidence a 49-65% increase in channel architecture and a 10% decrease in barform preservation. These results also compare to the data presented herein between the proximal Castle Gate and medial Sunnyside localities. It is proposed that these proximal systems operate as a result of downstream evolution of an unconfined mountain run off (DFS-like) system (Owen et al., 2015; Weismann et al., 2015) in an active foreland setting (Li et al., 2015), further highlighting that these are not location unique trends in fluvial architecture across a basin. However, the Tuscher Canyon section remains anomalous.

The sedimentary architecture preserved in the distal Tuscher Canyon location challenges conventional fluvial profile evolution. The increased sinuosity and lack of variation in discharge may be typical of downstream trends within a fluvial graded profile (Schumm et al., 2002; Holbrook et al., 2006; Li et al., 2015). However, the high proportion of barforms present and the lack of an observable decrease in sediment calibre, show anomalous results that do not conform to the standard DFS model, and those like it (Nichols and Fisher, 2007; Hartley et al., 2010; Weissmann et al., 2010; Owen et al., 2015). Such contrasting fluvial architecture is most simply explained by stream capture (Mikesell et al., 2010), and this may imply that there is more than one fluvial system operating within the study area. Such an argument is further evidenced by the discharge variation (as reported previously by Miall, 1993) indicated by the sedimentology of the proximal (Castle Gate; Figure 10A) and medial (Sunnyside; Figure 10B) portions of the Lower Castlegate, compared to indications of a more consistent flow in the distal Tuscher Canyon section (Figure 3.15C, D). Flow stability may also explain the more mature compound architecture of accretionary elements, and the absence of upstream accretion elements, in Tuscher Canyon (Wang and Plink-Björklund, 2019b) (Figures 3.11, 3.20). Where more proximal and medial deposits have shown small channels with immature compound element development and variable discharge rates (a coefficient of variance for the maximum reconstructed flow depths of approximately 0.35; Figure 3.15D), the distal region shows larger-scale more stable characteristics (coefficient of variance for the maximum reconstructed flow depths of 0.27; Figure 3.15D). It is therefore proposed that a smaller more immature fluvial system, such as a proximal mountain run off DFS, was active in the Castlegate and Sunnyside areas, feeding a larger more sustained fluvial system forming the deposits of Tuscher Canyon (Figure 3.22). The confluence of the two fluvial systems created a significant hydrodynamic change downstream, when compared to

more proximal area. Indicating that stream capture can have a dramatic effect on the sedimentary architecture and interpretation of unconfined fluvial systems.

The interpretation of stream capture has been suggested previously (Pettit et al., 2019), where detrital-zircon data have suggested a river confluence upstream of Tuscher Canyon, around Horse Canyon (Figure 3.2; Figure 3.22), and the presence of an axial fluvial system draining a secondary sediment source area to the south-west, typically referred to as the Mogollon Highland Source Area (Pettit et al., 2019). It is therefore proposed that the proximal (the Castle Gate) and medial (Sunnyside) regions of the study area operated within a typical small DFS-type system (Nichols and Fisher, 2007), whereas the distal Tuscher Canyon section represents a stable and more mature fluvial system. Further evidencing intrabasinal stream capture between Sunnyside and Tuscher Canyon.

Figure 3.22 (next page) – *Palaeogeographic plan view reconstruction of the Lower Castlegate Formation. Showing stream capture of DFS-like run-off systems from the Sevier Orogeny and the more mature Mogollon Highlands fluvial system. Note, not to scale.*



3.9 Discussion

The understanding of architectural preservation down depositional dip is fundamental to the interpretation of reservoir quality and heterogeneity in the subsurface. The results of potential overbank preservation and palaeodischarge reconstruction, presented herein, agree with previously published works (Miall, 1985, 1993, 1994; Wright and Marriott, 1993; Leeder, 1993; Shanley and McCabe, 1994; Bridge and Tye, 2000; Weismann et al., 2010; Owen et al., 2015; Li et al., 2015). When subsidence rates are higher, overbank preservation is more likely (Catuneanu, 2006; McLaurin and Steel, 2007; Hajek and Heller, 2012). In the more downstream reaches of a fluvial system, sinuosity and barform preservation increases (Wright and Marriott, 1993; Shanley and McCabe, 1994; Holbrook et al., 2006; Nichols and Fisher, 2007), showing the downstream evolution of a fluvial system.

This study, whilst providing interpretations for the impact of subsidence on in-channel fluvial architecture, recognises that this is not the only controlling factor. Avulsion scale (regional or local) and avulsion frequency are major controls on fluvial architecture (Mackey and Bridge, 1995; Heller and Paola, 1996; Colombera et al., 2015). Here, variations in avulsion frequency have not been considered specifically, and are therefore assumed to be relatively constant along the down-dip profile, despite the fact that, in this tectonic setting, avulsion is likely to be more frequent in the proximal region of the basin (Heller and Paola, 1996). Indeed, the presence of upstream accretion elements (Figure 3.11), the small size of accretionary elements (Figure 3.13) and preservation of overbank (Figure 3.11) within the proximal region of the study area indicate a lack of barform maturity that may indicate a higher avulsion frequency compared to downstream. Equally, sedimentation rate can significantly affect fluvial architecture and may contribute to the sedimentology observed in

this study. However, whilst sedimentation rates have been reported to decrease toward the distal portion of retro-foreland (Heller and Paola 1996), no such evidence is found within the Lower Castlegate. Aggradation rates of fluvial deposits can be linked to both subsidence rate and sedimentation rate. The proximal Castle Gate and medial Sunnyside locations show vastly different aggradation rates which are attributed, predominantly, here to differences in subsidence rate.

3.9.1 Implications for reservoir quality

Reservoir meso-scale (typically at one- to ten-metre) heterogeneity is primarily controlled by the distribution of architectural elements (Tyler and Finley 1991; Horung and Aigner 1991; Koneshloo 2018). This study has provided insight into the downstream distribution and effects of subsidence rate on the preservation potential of sedimentary architectural elements and therefore meso-scale heterogeneity. In the more distal reaches of a foreland fluvial MSB, lateral accretion elements would have been deposited in abundance. However, architectural analysis of the Lower Castlegate MSB has shown the limited lateral accretion element preservation in such distal reaches of low subsidence rates.

Lateral accretion elements have been shown, to become more heterogeneous downstream (Horung and Aigner 1999). Proximal lateral accretion elements typically exhibit higher porosity and permeability values than distal equivalents. This is due to a downstream change in sediment calibre (Armitage et al. 2011; Whittaker et al. 2011; Colombera et al. 2015) where bedload transport may become less dominant. In this study, the erosion of these elements by compensationally avulsing channels therefore refines the reservoir quality preserved in the distal portion of foreland fluvial MSBs, despite the downstream profile.

Further refining distal reservoir quality, bar-top facies become less prevalent downstream; rarely being preserved in the distal portions where low subsidence rates occur. This erosive pattern further reduces meso-scale heterogeneity within the distal reaches of a foreland fluvial system. The lack of bar-top facies increases the relative sand content within each individual barform and removes potential baffle-heterogeneities from within fluvial strata that may impede meso-scale vertical communication of architectural elements.

3.9.2 Implications for sequence stratigraphy

This study shows, through the analysis of in-channel fluvial architecture and palaeoflow dynamics, that the Lower Castlegate Formation has a progressive downstream change from a low-sinuosity system to a more intermediate- to moderately high-sinuosity fluvial system towards the coastal plain and the backwater reach (Figure 3.21). This supports recent interpretations of a non-sequence boundary between the Lower Castlegate MSB and the underlying coastal plain Desert Member of the Blackhawk Formation (Howell et al., 2018; Pattison, 2018, 2019a,b; Trower et al., 2018). The visually, but not genetically, different strata were interpreted to be unconformable (Olsen et al., 1995; Yoshida et al., 1996; McLaurin and Steel, 2000; Miall and Arush, 2001), when in reality they display a simple progradational regime (Howell et al., 2018; Pattinson, 2018; 2019a,b).

Pattison (2019b) used the Tuscher Canyon outcrop to show how miscorrelation of shoreface elements and distributive channels in the Blackhawk and Castlegate, to those in Thompson Canyon (farther east), had major implications for the genetic temporal and spatial linkage of coastal plain and fluvial strata. The Desert Member of the Blackhawk Formation is well recognised as a moderate to high-sinuosity fluvial system deposited within a coastal plain environment (Olsen et al., 1995; Adams and Bhattacharya, 2005). However, the Castlegate

was previously interpreted to be a more braided proximal fluvial system (Olsen et al., 1995; Yoshida et al., 1996; McLaurin and Steel, 2000), when in fact, as demonstrated here, there is sinuosity within the Lower Castlegate fluvial system at Tuscher Canyon. This study demonstrates that no major facies dislocation occurs across the Blackhawk-Castlegate boundary. Although its simple visual recognition is difficult to see from basic palaeocurrent and facies analysis alone.

Further evidence of sequence stratigraphic significance can be found in the increasing reconstructed flow depths up-section in the proximal region of the study area, this same observation was noted by McLaurin and Steel (2007). This is most probably due to headwater expansion and erosion of the uplifted hinterland as a consequence of active Sevier-aged thrusting and the subsequent incision of the fluvial system as it re-equilibrated to a graded fluvial profile (Holbrook et al., 2006). The product of such uplift and erosion is increased discharge and sedimentation rates (Yoshida, 2000; Holbrook et al., 2006; Fielding and Paola, 2013). However, given the aggradational profile and buffer zone effects interpreted from evidence in the proximal Castle Gate, it is suggested that discharge rates do not exceed sedimentation rate in that locality. The base of the Lower Castlegate is relatively flat, which may indicate that the boundary has been produced by increased discharge (Fielding and Paola 2013), or that increased discharge has played a role in its formation.

3.9.3 Implications for architectural elements in unconfined multi-storey sandbodies

This chapter demonstrates the complex nature of unconfined multi-storey sandbodies and their genesis. Whilst presenting in outcrop as a large and seemingly simple braided fluvial system, their genesis and mode of preservation can be initially mis-interpreted without significant understanding of the palaeohydraulic characteristics and the sedimentary

architecture of the depositing fluvial system. The unconfined Lower Castlegate presents a good example of this. Stream capture and the associated stabilisation of flow led to a drastically sedimentary architecture, but maintained a down-stream grain size, showing little fluctuation. The presence of upstream accretion elements, immature or absent compound barform growth, and the nature of inconsistent palaeohydraulics highlight and characterise a traditional DFS-like unconfined mountain run-off system. Stream capture from the Mogollon Highland fluvial system (Figure 3.22) then breaks down the traditional model, removing distal DFS-like sedimentology and even refines reservoir quality towards the distal portion of the fluvial system.

3.10 Summary

The Lower Castlegate MSB shows a complex sedimentary architecture that formed as a product of variable discharge rates, the fluvial graded profile and spatially variable aggradation rates produced by subsidence rate variation across the basin. Furthermore, stream capture has played a role in the anomalous architecture shown in the more distal region of the Lower Castlegate, providing hydrodynamic changes and flow stabilisation.

Using multiple approaches to analyse the controls on deposition and preservation of architectural elements within unconfined MSBs deposited in foreland basins. This study demonstrates that downstream profiles, discharge variations, avulsion scales and subsidence rates play a key role in the preservation of fluvial architectural elements. Discharge variability and position along the fluvial profile provide control over the upstream accretion of barforms, whereas subsidence rates control the preservation of lateral accretion and overbank elements. Such an understanding may prove critical as a diagnostic feature of the lateral confinement on a fluvial system and therefore provide insight into sandbody location

and palaeogeographic interpretation in basin analysis and basin-scale interpretations of sequence stratigraphy. Finally, in unconfined fluvial systems stream capture can play a pivotal role in the preservation and deposition of architectural elements. The palaeohydraulic nature of unconfined MSBs is a key indicator of this, with limited understanding of the hydrodynamics of a system little reliable interpretation can be taken from architectural analysis, unless upstream accretion elements are recognised. These architectures are found to be indicative of variable discharge, as seen in unconfined MSBs such as the Lower Castlegate.

4 The sedimentary architecture of a confined fluvial system: example from the Spireslack Sandstone, Scotland.

Based upon: Ellen, R., Browne, M.A.E., Mitten, A.J., Clarke, S.M., Leslie, A.G. and Callaghan, E., 2019. Sedimentology, architecture and depositional setting of the fluvial Spireslack Sandstone of the Midland Valley, Scotland: insights from the Spireslack surface coal mine. Geological Society, London, Special Publications, 488.

This article has been **accepted and published** in the Geological Society of London Special Publication Series.

This chapter describes and interprets the depositional architecture of the Spireslack Sandstone: a Carboniferous fluvial system confined within an incised valley. The analysis utilises the published facies scheme of Ellen et al. (2019) along with an original architectural analysis conducted by the author of this thesis (which was this author's contribution to that paper). The chapter also describes a regional correlation of the area based on borehole data, allowing the degree of lateral palaeo-topographic confinement to be determined. The preservation of sedimentary architecture as a result of large- and small-scale avulsion events, in a confined fluvial system, are then discussed.

4.1 Introduction

This chapter will highlight the sedimentology and architectural distribution of a confined, multi-storey sandbody. The succession analysed is the Serpukhovian Spireslack Sandstone of the Midland Valley of Scotland. The Spireslack Sandstone is exposed by opencast surface mine workings in Ayrshire, and provides an excellent analogue for confined high net-to-gross fluvial sandstones within the Carboniferous strata of the UK.

The succession at Spireslack was produced by a bedload-dominated fluvial system that deposited abundant conglomerate lenses and cross-bedded sandstone facies (Ellen et al. 2019). The architecture of the sandstone is limited, in outcrop, to a section approximately twenty metres in vertical extent but the unit is recognised over a lateral distance of over twenty kilometres. This high net-to-gross sandbody shows multiple erosional surfaces within its make-up which have been interpreted to form as a result of channel avulsion and variable discharge. The avulsion pattern and lack of overbank preserved within the succession suggest a cannibalistic nature to the sedimentary system in which deposited sediment is subsequently reworked. This typically indicates deposition during a period of low subsidence (Hajek et al. 2010; Hajek and Wollinski 2012; Hajek and Heller 2012) or deposition confined within a palaeovalley that limits avulsion (Aslan and Blum 1999; Blum and Aslan 2006; Hajek et al. 2010).

Here, digital photogrammetry of multiple large quarried faces is obtained in conjunction with sedimentary log data in order to conduct a full facies analysis including bounding surface and subsequent architectural analysis of the Spireslack Sandstone. This enables a depositional model for a confined fluvial system to be generated, allowing quantified architectural data to be incorporated into reservoir models (Chapter 5).

4.2 Geological Setting of the Spireslack Sandstone

The Spireslack, Grasshill and Ponesk site (SGP) is a series of opencast surface mine workings within the Midland Valley, Ayrshire, Scotland (Figure 4.1). The SGP exposes strata of the Lawmuir to Upper Limestone formations (Brigantian to Arnsbergian, or end-Viséan to end-Serpukovian, respectively; Leslie et al. 2016). There are numerous open-cast pits within the SGP (further to those that lend it its name), the largest of which is the Main Void: an approximately one kilometre long and one-hundred and thirty-metre-tall ‘high wall’ exposure that shows the almost the entirety of the SGP succession (Figure 4.2).

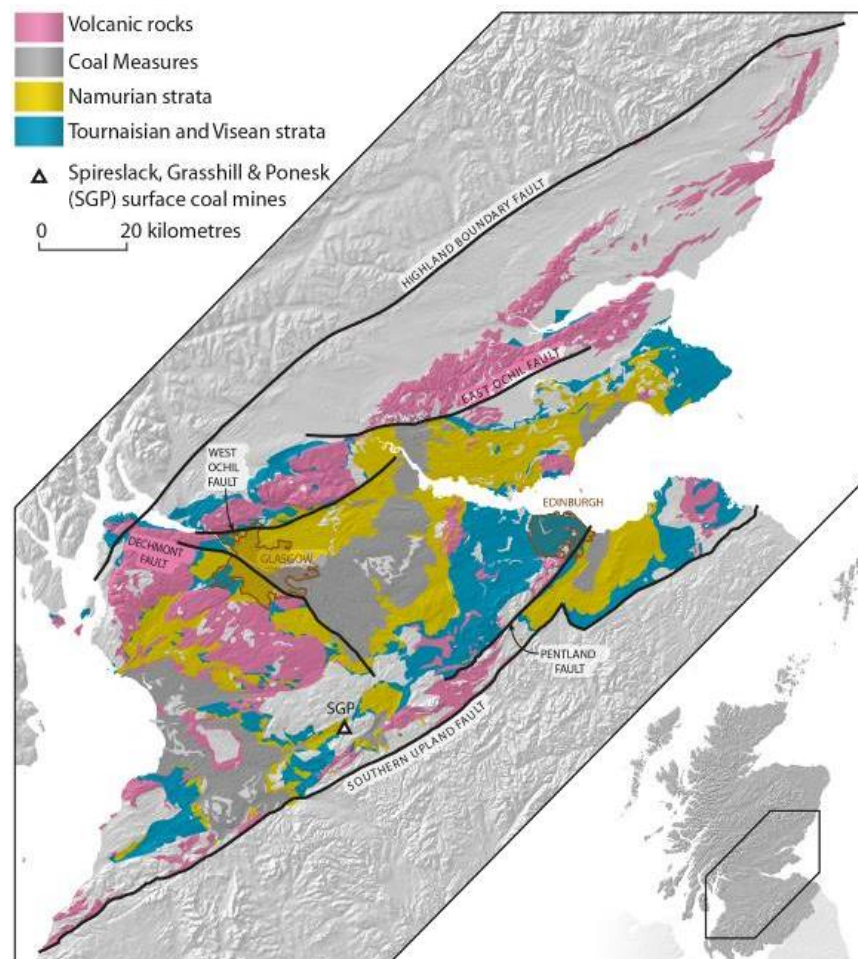


Figure 4.1 - The ENE-WSW striking Midland Valley Graben, Scotland (after Ellen et al. 2019). Bound to the north by the Highlands Boundary Fault and to the south by the Southern Uplands Fault. The location of the SGP coal mine is indicated by the labelled triangle.

4.2.1 *The Midland Valley, Ayrshire, Scotland*

The Midland Valley of Scotland is a large ENE-WSW striking, approximately 90 km wide graben bound by the Highland Boundary Fault to the north west and the Southern Upland Fault system (Figure 4.1) to the south east (Browne and Munro 1989; Floyd 1994; Read et al. 2002). The boundary faults originally formed as structural lineaments during the Caledonian Orogeny. These faults bound the basin in a back-arc setting, thermal relaxation and back-arc extension subsequently provide principal controls upon Tournasian sinistral strike-slip and later ?post-Westphalian dextral strike-slip faulting (Browne and Munro 1989; Ritchie et al. 2003; Underhill et al. 2008). This faulting had extensive control upon the sediment thickness within the basin (Read et al. 2002; Underhill et al. 2008). The basins of the Midland Valley were separated from contemporaneous Carboniferous basins to the south by the lower Palaeozoic Southern Uplands Block (Cameron and Stephenson 1985; Figure 4.1).

Extensive syn-sedimentary northwest-trending sinistral oblique-slip faulting is evident within the Visean to Bashkirian succession of the Midland Valley. This faulting and the development of NNE-SSW striking growth folds (Underhill et al. 2008), such as the Muirkirk Syncline (Figure 4.3A; Ellen et al. 2019), form in a brittle-ductile stress regime. Such faulting is consistent with the pattern of sinistral transpression during the early Carboniferous Period (Caldwell and Young 2013; Leslie et al. 2016) as part of post-Caledonian relaxation.

During the Pennsylvanian Stage, a regional dextral regime dominated, tightening or locally significantly refolding pre-existing fold structures and developing steeply inclined reverse faults (Underhill et al. 2008). This dextral stress is associated with transpressional deformation that occurred across the Variscan Foreland (Underhill et al. 1988; Corfield et al. 1996; Glennie and Underhill 1998), the effects of which are believed to reach as far north as

the Inner Moray Firth (Underhill and Brodie 1993). During the Latest Carboniferous and Permian periods, dextral transpressional deformation had been replaced by north-south compression, itself a product of extensional Permian Basin development in the North Sea region (Glennie and Underhill 1998; Underhill et al. 2008). Following Permian extensional basin formation, Palaeocene uplift caused large-scale erosion of the Carboniferous succession and the emplacement of basaltic dykes through pre-existing fault structures (Browne et al. 1999; Underhill et al. 2008).

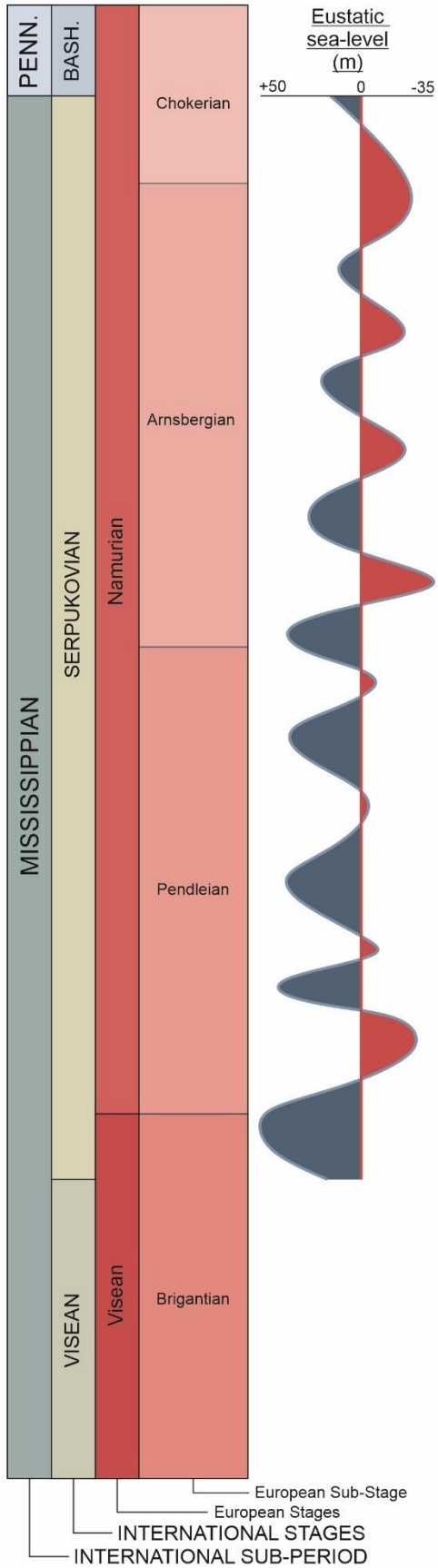
The Midland Valley was separated from the northern Pennine basins of Northern England by the Southern Uplands Block, the latter bound to its north against the Midland Valley by the Southern Uplands Fault. However, minor northwest-trending basins breach this block creating a moderately open basin (Browne et al. 1999). During the late Devonian Period and Tournasian Stage of the Carboniferous Period, the deposition of the fluvially-dominated Inverclyde Group was sourced from the north east and east of the Midland Valley Basin, with rivers draining parallel to the Highland Boundary Fault (Read and Johnson 1967). Drainage switched to a predominantly southwest trend, with rivers draining from the topographic high lying to the north of the Highland Boundary Fault, providing sediment for the Strathclyde (Visean) and Clackmannan (Serpukovian) groups and Westphalian Coal Measures, along with some minor sediment incursions from the Southern Uplands Block (Muir 1963; Greensmith 1965; Browne et al. 1999). The major marine influence to the basin at this time was restricted to the south; its occurrence is limited during the Tournasian. Marine sedimentation became more prevalent through the Visean, reaching its peak during the Serpukovian (Veevers and Powell 1987; Browne and Monro 1989; Cope 1992; Browne et al. 1999). Glacio-eustatic sea-level fluctuations produce mixed carbonate and siliciclastic parasequence architectures, with highstands producing regionally correlatable limestones (Browne et al. 1999).

4.2.2 *The Carboniferous succession of the SGP*

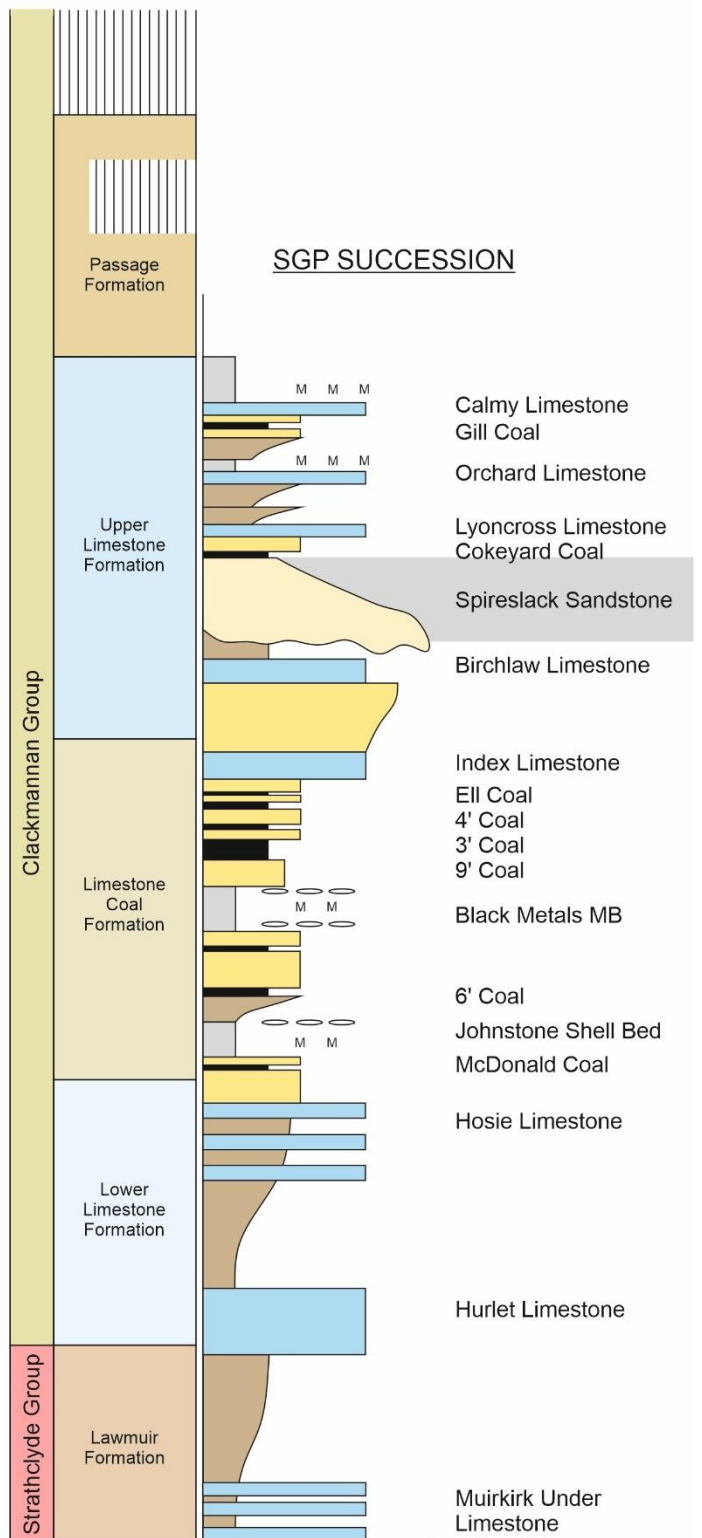
The Carboniferous succession of the SGP is composed, predominately, of sediments of the Serpukovian Clackmannan Group. The succession, best exposed in the Main Void High Wall (Figure 4.3B), comprises the upper portion of the Visean Lawmuir Formation of the Strathclyde Group to the late-Serpukovian (Arnsbergian) Upper Limestone Formation of the Clackmannan Group (Figure 4.2).

Figure 4.2 (next page) - *The Carboniferous stratigraphic framework for the Midland Valley of Scotland, showing the International and British chronostratigraphic subdivisions. The lithostratigraphic subdivisions of the Clackmannan Group and their associated informal unit subdivisions of the SGP succession (Modified from Ellen et al. 2019; Howell et al. 2019) are shown on the right of the Midland Valley lithostratigraphic column. The GVS also shows a eustatic sea-level curve for the Serpukovian (Haq et al. 2008), referenced to the present day sea-level.*

CHRONOSTRATIGRAPHY



LITHOSTRATIGRAPHY OF THE MIDLAND VALLEY



Lawmuir Formation

The upper 20 m of the Lawmuir Formation (approximately 100 m thick regionally) are exposed at the SGP. The Lawmuir Formation consists of minor sandstones, along with interbedded limestone, siltstone, and mudstone with ironstone concretions. The base of the formation is marked by the first appearance of the Muirkirk Under Limestone: a ~60cm grey bioclastic limestone that is abundant in corals and *Gigantoproductus* (Browne et al. 1999). The Limestone occurs as three bands interbedded with grey mudstones, that are not laterally extensive. The top of the Muirkirk Under Limestone marks a regional interglacial flooding surface (Read et al. 2002). Conformably overlaying the Muirkirk Under Limestone are units of mudstone, siltstone and sandstone arranged into a general coarsening upwards succession synonymous with cyclic Carboniferous sedimentation. This limestone unit is often extremely weathered at outcrop and may be strongly fractured in response to faulting (Browne et al. 1999). The formation is capped by a 10 m thick fossiliferous mudstone that is characterised by reddish-brown ironstone bands (Browne et al. 1999).

Lower Limestone Formation

The Lower Limestone Formation, approximately 80 m thick, has its base marked by the pale brown Hurler Limestone that contains abundant *Gigantoproductus* and colonial corals (Browne et al. 1999). The succession above is composed of marine and fluvio-deltaic mud and siltstone, subtle variations of which are attributed to glacio-eustatic relative sea level oscillations (Read 1994b). The top of the formation is marked by the top of the Hosie Limestone. The Hosie Limestone contains five limestone units (each 0.5-0.7 m thick), interbedded with siltstone and mudstone up to 1.2 m thick (Browne et al. 1999). The uppermost limestone unit of the Hosie Limestone forms the engineered northwest wall of the Main Void at Spireslack (Figure 4.3B); this limestone is referred to in more local coalfield

nomenclature as the McDonald Limestone. The top limestone surface is characterised by the presence of abundant trace fossils, predominately *Rhizocorallium*, *?Planolites* and *?Chondrites* (Browne et al. 1999). In addition, this limestone contains abundant *Paladin* sp., brachiopods and rare examples hybodont shark remains.

Limestone Coal Formation

The Limestone Coal Formation consists of a fluvio-deltaic upwards-coarsening succession. The formation is approximately 95 m thick and comprises the lower half of the Main Void High Wall (Ellen et al. 2019; Figure 4.3B and 4.4). The base of the formation starts at the top of the Hosie Limestone and ends at the base of the Index Limestone. There are two significant markers of marine incursion within the succession, the Johnstone Shale Bed and the Black Metals Marine Band (Browne et al. 1999). The Johnson Shale Bed is extremely fossiliferous and contain abundant *Pleuropugnoides* sp., *Productus concinnus*, *Schizophoria* cf. *resupinata* and *Pernopecten sowerbii*. Both marine bands are regionally extensive and can be mapped across the majority of the Midland Valley, Scotland (Read 1994a).

The Limestone Coal Formation can be divided up into six parasequences. These parasequences are exposed within the Main Void High Wall, where six major sandstone units can be mapped (one of which being the unnamed sandstone highlighted in Figure 4.4), these sandstones are typically 2-10 m thick (Browne et al. 1999; Bilton 2019; Ellen et al. 2019). The sandstones of the Limestone Coal Formation show planar cross-bedding and current ripples, with organic fragments and ironstone nodules. The sandstones were deposited as stacked barforms in a fluvio-deltaic succession. These sandstones are overlain by upwards-fining cycles of mudstone, siltstone, sandstone, seatearth, sideritic ironstone and coal (Read et al. 2002). There is an abundance of coal seams throughout the succession, these are the:

McDonald, Muirkirk Six Foot, Muirkirk Thirty Inch, Muirkirk Nine Foot, Muirkirk Four Foot, Muirkirk Three Foot, Muirkirk Ell and Index coal seams (Browne et al. 1999; Figure 4.2). These coals were deposited as equatorial and floral peat mires populated by heterosporous lycopod tree rainforests (Phillips & Peppers 1984; Clymo 1987).

Upper Limestone Formation

The Upper Limestone Formation is composed of cyclic sequences of sandstone, mudstone, siltstone and marine limestone, which includes the regionally significant Index Limestone (Browne et al. 1999). The base of the Index Limestone marks the base of the Upper Limestone Formation. The limestone is 1.3 m thick, in the SGP area, grey and extremely hard, with a fossiliferous assemblage showing *Gigantoproductus cf. irregularis*, *Latiproductus cf. latissimus*, *Pleuropugnoides sp.*, *Schellwienella sp.*, *Myalina sp.* and *Polidevcia attenuate* (Patterson et al. 1998). The limestone represents a regional marine transgression episode (Read et al. 2002). The Index Limestone is overlain by a 7-10 m thick black marine mudstone that is erosively down-cut into by a thick fluvial sandstone. This fluvial sandstone is the Spireslack Sandstone (Figure 4.4), first characterised and recognised by Ellen et al. (2019). The succession of the Upper Limestone Formation continues with the deposition of a generally upwards fining estuarine succession and is capped by the youngest limestone of the SGP area, the Calmy Limestone (Browne et al. 1999).

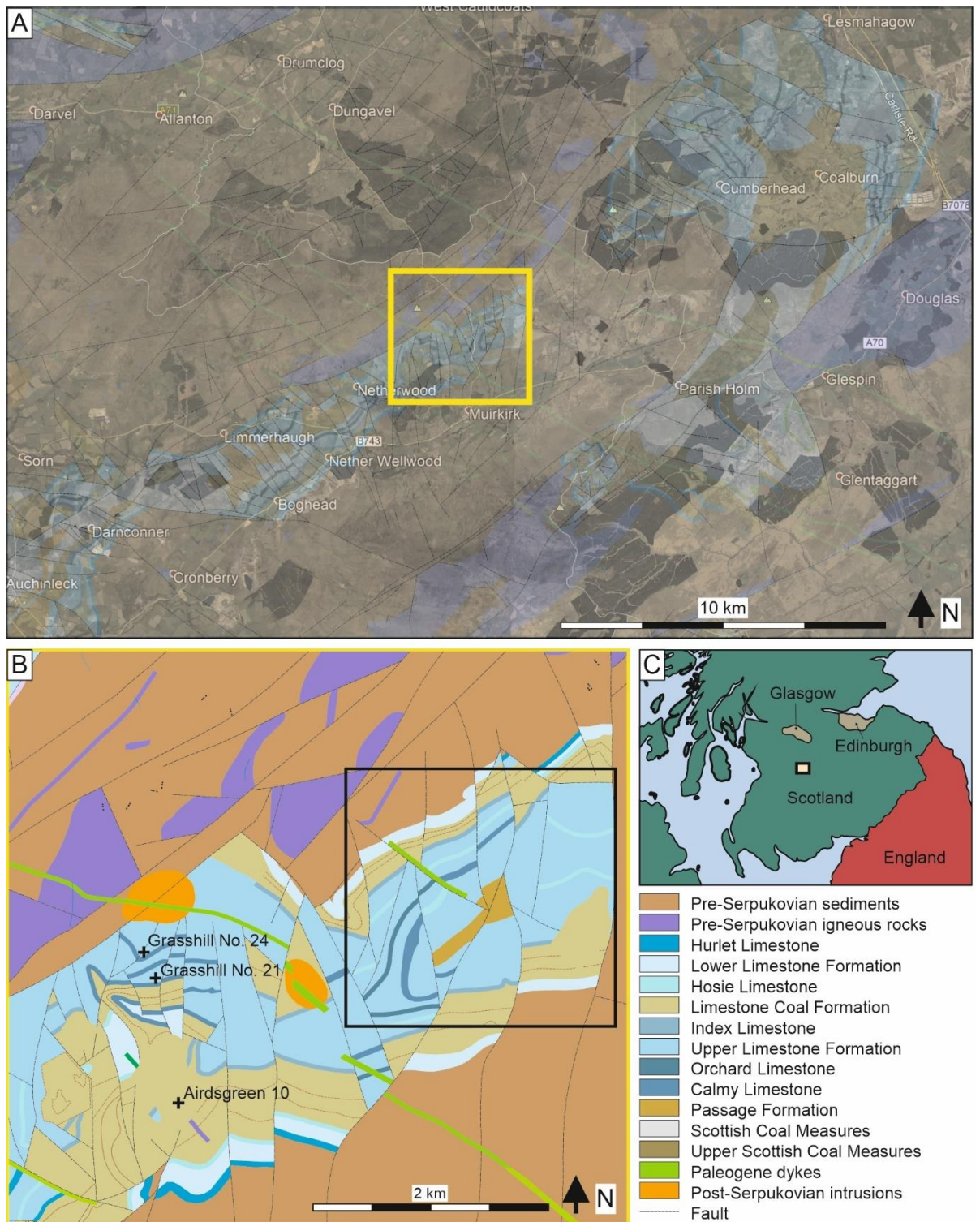


Figure 4.3 – Map of the central Midland Valley, highlighting the Serpukovian strata exposed in the region and the location of the SGP site geological map. A) Regional geological map and Google Earth Image showing the area surrounding the SGP field site. B) Geological map of the yellow boxed area

shown in (A). Black box highlights the exposure of the studied area and the location of figure 4.5. C)

Inset map showing the location of the central Midland Valley map relative to Scotland.

Spireslack Main Void Highwall

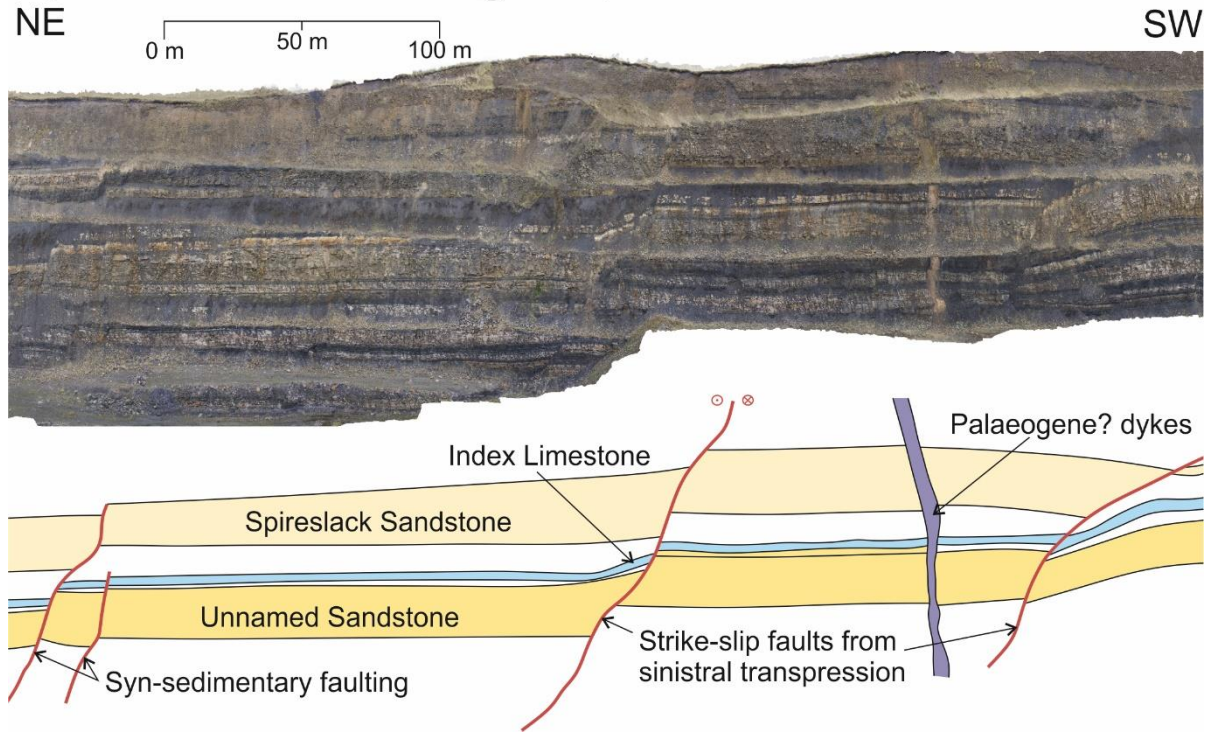


Figure 4.4 - Ortho-rectified image from a photogrammetric survey of the Main Void High Wall, with an accompanying interpretation panel (Modified from Ellen et al. 2019). The succession clearly shows several thick sandstone units and an obvious cyclic succession of mudstone, sand, limestone and coal. There are several faults that cut through the High Wall at a normal to oblique angle. These faults are mapped in Figure 4.3A, and are strike-slip in nature. Two Palaeogene? basaltic dykes cut through the succession on the south western side of the High Wall. Below the High Wall image is an interpreted image showing the pick of an unnamed sandstone that forms a major component of the Hosie Cyclothem, and is consistent with the sandstones above the 9ft Coal. Conformably overlying the mudstone? above the unnamed sandstone is the Index Limestone (2-4m). Erosionally down-cutting into the mudstones at the base of the Index Cyclothem is the Spireslack Sandstone, indicated by the pale sandy colour illustrated in Figure 4.2.

4.3 Methodology

Data were collected from two locations, the Main Void High Wall in the northeast of the SGP and the B1 Face in the southeast (Figure 4.5). The Main Void is an approximately one kilometre long, NNW-facing outcrop with a small access road to its western edge that provides a section that can be accessed safely. The B1 Face is four-hundred metres wide and is the best exposure of the Spireslack Sandstone. Unfortunately, the face is extremely unstable and access to the face was prohibited and no log data were obtainable.

Following the methodology highlighted and explained in Section 3.2. High-resolution photogrammetric data (both UAV and terrestrially based) were collected from the SGP outcrops, to produce a VOM from which architectural elements of the Spireslack Sandstone could be analysed. Individual photographs were captured with a two-metre spacing along transects approximately sixty metres from the outcrop, ensuring a minimum of approximately 85% overlap between the images. The photographs were taken using a Nikon D800E camera with a NIKKOR 24–120 mm 1:4 lens. Ground control points were collected at 25 m intervals along the data collection transects (Figure 4.5). This enables the VOM to be georeferenced to place the 3D model in space and to constrain the model scaling to within an error of 3.7 m. Images were imported into Agisoft Photoscan© (Using the same methodology outlined in Section 3.2) to create a photorealistic VOM. The outcrops were built using a low photographic alignment, a dense point cloud and a textured mesh. The VOM provides a realistic and scaled reconstruction of the outcrop from which sedimentary architectures, bounding surfaces, geometric relationships and hierarchies can be measured, described and interpreted.

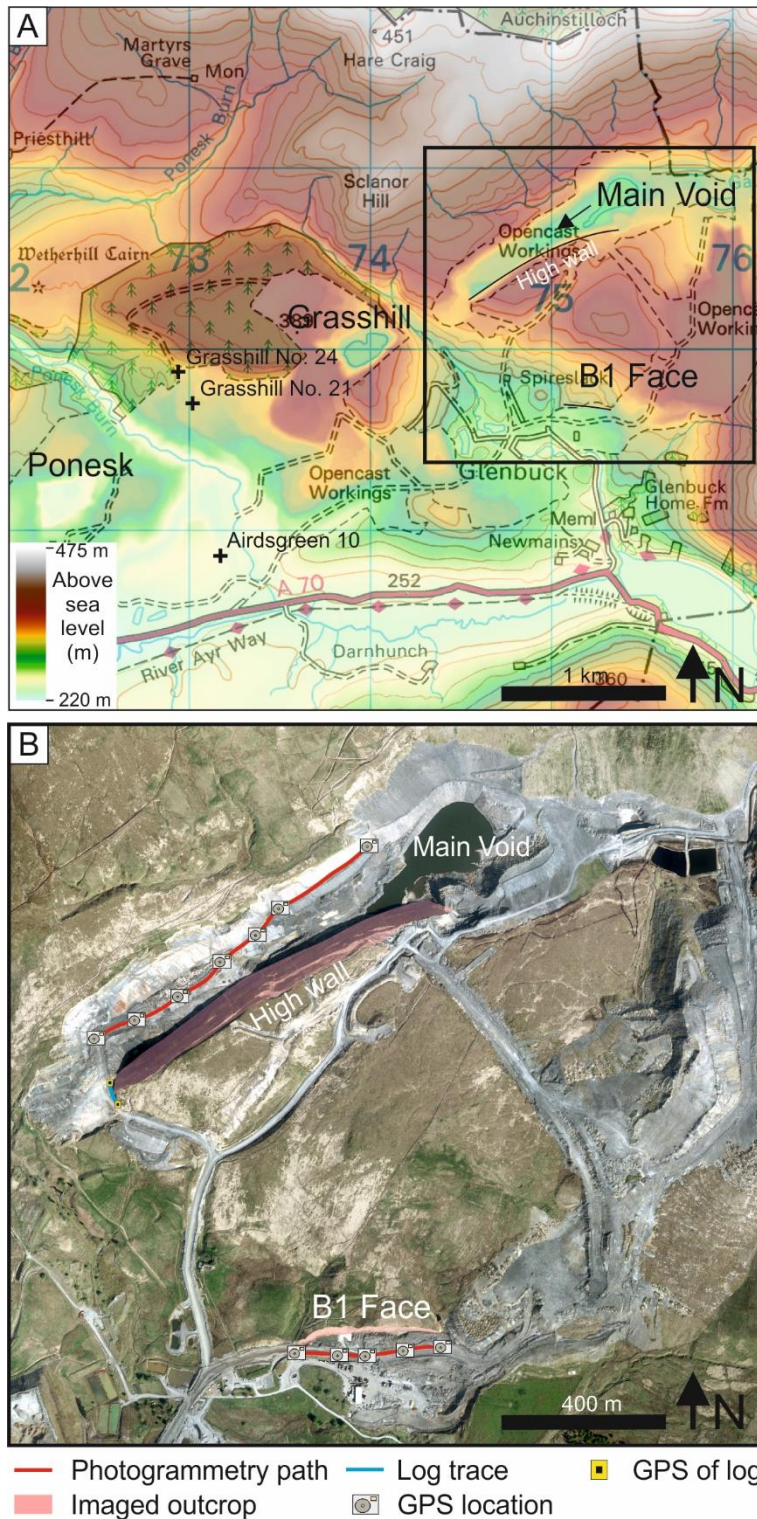


Figure 4.5 – Study location highlighting the location of the four major outcrops in the SGP area and the location of data collection. A) DEM and Ordnance Survey map (OS MasterMap 2019) with annotations of SGP mined faces and borehole locations, along with highlighted (black square) outline of aerial image. B) Aerial image of the Main Void and B1 Face, photogrammetry collection paths and GPS locations have been marked on the image (Bing Maps 2015).

Where access to the face is possible, VOMs were supplemented with the collection of high-resolution sedimentary logging and subsequent facies analysis. Sedimentary logs of the Spireslack Sandstone (Figure 4.5) and associated strata were collected from the Ponesk and Grasshill outcrops by the co-authors of Ellen et al. (2019) to provide local control over the spatial distribution of facies and architecture. The results of the facies analysis conducted over the Spireslack field area were used to develop a depositional model for the Spireslack Sandstone.

4.4 The architecture of the Spireslack Sandstone

The following sub-sections consist of a description and interpretation for the genesis of each individual architectural element interpreted from the Spireslack succession. For the sake of brevity, the reader is referred to the published facies scheme (Ellen et al., 2019) reproduced in Table 4.1. The facies scheme shows a typical example of a fluvial succession, therefore the following detail will extend beyond the scale of facies and to the architectural element composition.

Table 4.1 – Lithofacies table of the Spireslack Sandstone (modified from Ellen et al. 2019).

Facies codes	Lithological description	Sedimentary structures	Other Features	Interpretation
Cc	Clast-supported conglomerate: Granule to pebble clast-size with very little matrix, clast-supported. Matrix is composed of fine- to very coarse-grained sandstone. Clasts are angular to sub-rounded.	Occasionally minor normal grading.		Bedload transport at the base of a Newtonian flow.
Sm-c	Structureless sandstone (coarse): Coarse to very coarse, cream sub-arkosic arenite, clasts-supported rounded to well-rounded, moderately- to well-sorted.	Structureless, often in lenticular units. Rare intermittent and poorly developed trough cross-bedding at the base with load casts and scours.		High sediment load Newtonian flow.
Sm-f	Structureless sandstone (fine): Very fine- to medium-grained, white sub-arkosic arenite, well-rounded and well-sorted.	Normally graded, with some wood fragments and rip-up clasts. Intermittent and poorly developed trough cross-bedding.	Lenses of Cc are common.	High sediment load, intermittent development and migration of sinuous crested dune bedforms.
Sh-c	Planar laminated sandstone (coarse): Medium-grained, white quartz-arenite, sub-rounded and well-sorted.	Horizontal bedding with primary current lineations.		Upper flow regime plane bed deposition.
Sh-f	Planar laminated sandstone (fine): Fine- to medium-grained, cream sub-arkosic arenite, well-rounded and well-sorted.	Horizontal lamination with occasional asymmetrical ripple lamination.	Bioturbation and rooting	Lower flow regime low-energy settling from suspension with minor ripple-scale bedform migration and deposition.

<i>St</i>	Trough-crossbedded sandstone (<i>St-c</i> and <i>St-f</i>): fine- to coarse-grained sandstone, white sub-arkosic arenite, sub-rounded to rounded, well sorted.	Trough cross-bedding, sometimes poorly developed.	Lenses of <i>Cc</i> at the base.	Lower flow regime migration and deposition of sinuous crested dune-scale bedforms.
<i>Sp</i>	Planar cross-bedded sandstone: Medium-grained, white to cream sub-arkosic arenite, well-rounded, well-sorted.	Planar cross-bedding		Lower flow regime migration and deposition of straight-crested dune-scale bedforms.
<i>Sr</i>	Ripple laminated sandstone: Fine-grained, white quartz-arenite, sub-rounded to well-rounded, moderately- to well-sorted.	Ripple lamination		Lower flow regime migration and deposition of ripple-scale bedforms.
<i>Fl</i>	Planar laminated fines: Grey siltstone, well sorted.	Planar lamination	Some wood fragments	Lower flow regime extremely low-energy suspension settling.
<i>C</i>	Coal: immature with numerous plant fragments.	Poorly developed laminations and very weak cleat, occasionally structureless.		Immature coalification of plant debris

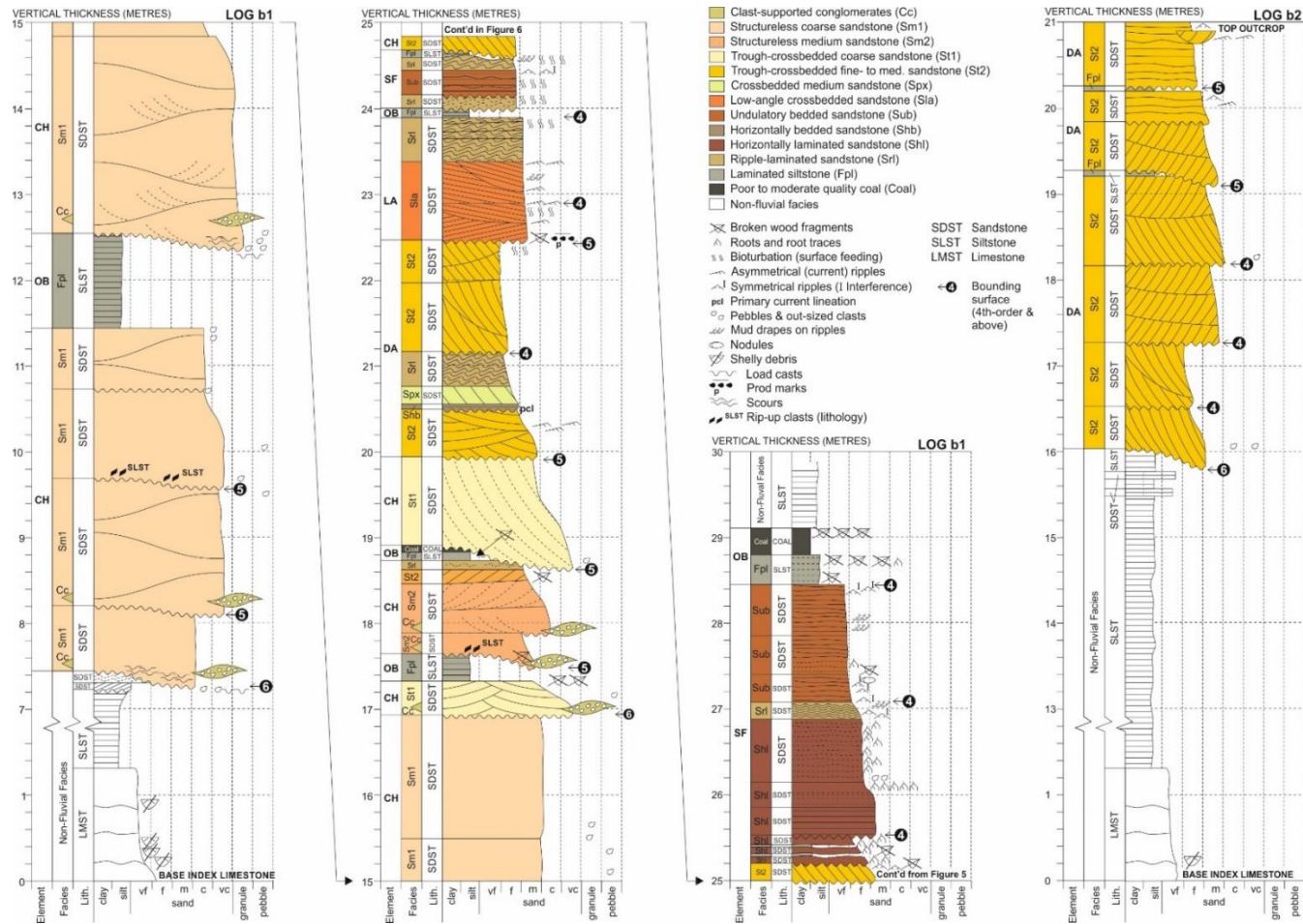


Figure 4.6 - Sedimentary log data of the Spirelack Sandstone collected from the exposure adjacent to the Main Void High Wall shown in Figure 4.5B (from Ellen et al. 2019).

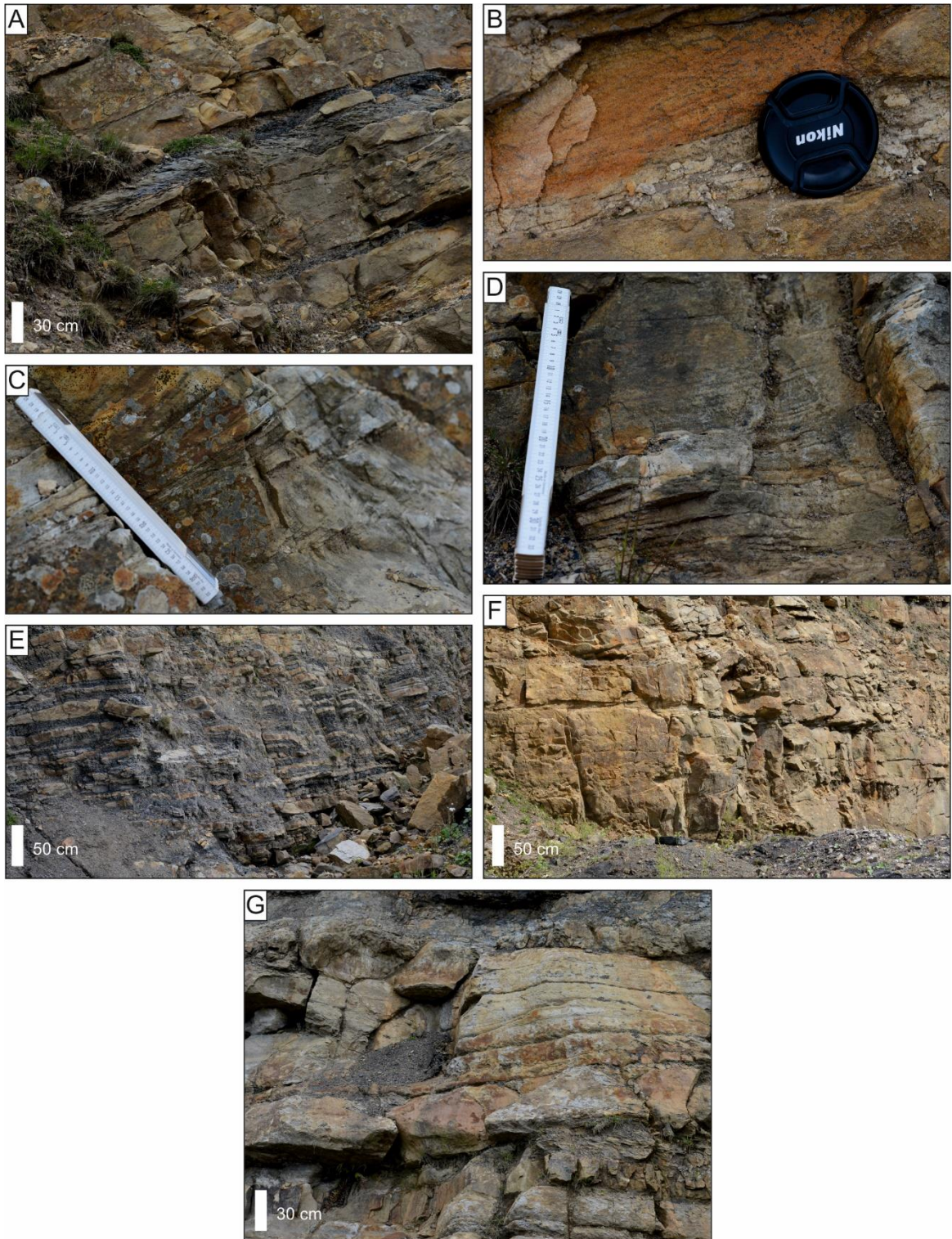


Figure 4.7 – Photoplate highlighting the various facies of the Spireslack Sandstone and overlying succession. A) Planar crossbedded sandstone with heavily cleaved siltstone and coal, cleavage is inherited from syn-sedimentary movement along sinistral faults. B) Close up of trough crossbedded sandstone facies highlighting its coarse and sub-subangular nature. Black flecks in here are intraformational coals. C) Poor preservation of trough cross bedded facies in base of image, with

overlying set showing better preservation and exposure of cross bedded sandstone facies. Scale bar is in centimetres. D) Transition from planar bedded sandstones to planar laminated to structureless sandstones over 30 cm. This is as a result of increasingly reducing water depth, transitioning through the lower flow regime towards the higher end of the lower flow regime, see text for further description. E) Inclined heterolithics of structureless bioturbated sandstone and siltstone couplets. F) Spireslack Sandstone trough cross bedded sandstone strata, typical of the unit. G) Bioturbated sandstone at the top of the inclined heterolithic section. Top of the image shows the top of the Spireslack Sandstone with a locally correlatable siltstone

The above facies scheme of Ellen et al. (2019) (Table 4.1, Figure 4.9) was used with the B1 Face photogrammetric datasets so that spatial geometry and facies distributions could be used to define the architectural elements that comprise the Spireslack Sandstone (Table 4.2).

Table 4.2 - The major constituent architectural elements of the B1 Face. Elements are defined by their name, code, facies assemblages and description. A real interpretation example is taken directly from the outcrop interpretation (Figure 4.11).

Name	Element code	Facies	Description	
Lateral accretion element	LA	Sla, Srl	Lateral extent of 60-80m and 1.5-3.2m thick, lensoidal shape, truncated in every observed occurrence.	
Downstream accretion element	DA	St2, Shb, Stx2	Lateral extent of 37-58m and 0.5-2.5m thick, lensoidal shape, truncated in the majority of observed occurrences.	
Channel	Ch	Cc, Sm1, Sm2, St2, Srl	U-shaped concave-up erosive base, lateral extent of 34-59m and 2.2-3.7m thick, truncated in every observed occurrence.	
Chute Channel	Cch	Sm2, Srl	Smaller scale channel form erosively downcutting into the top of a barform, lateral extent of 2.1-3.7m and 0.2-0.5m thick.	

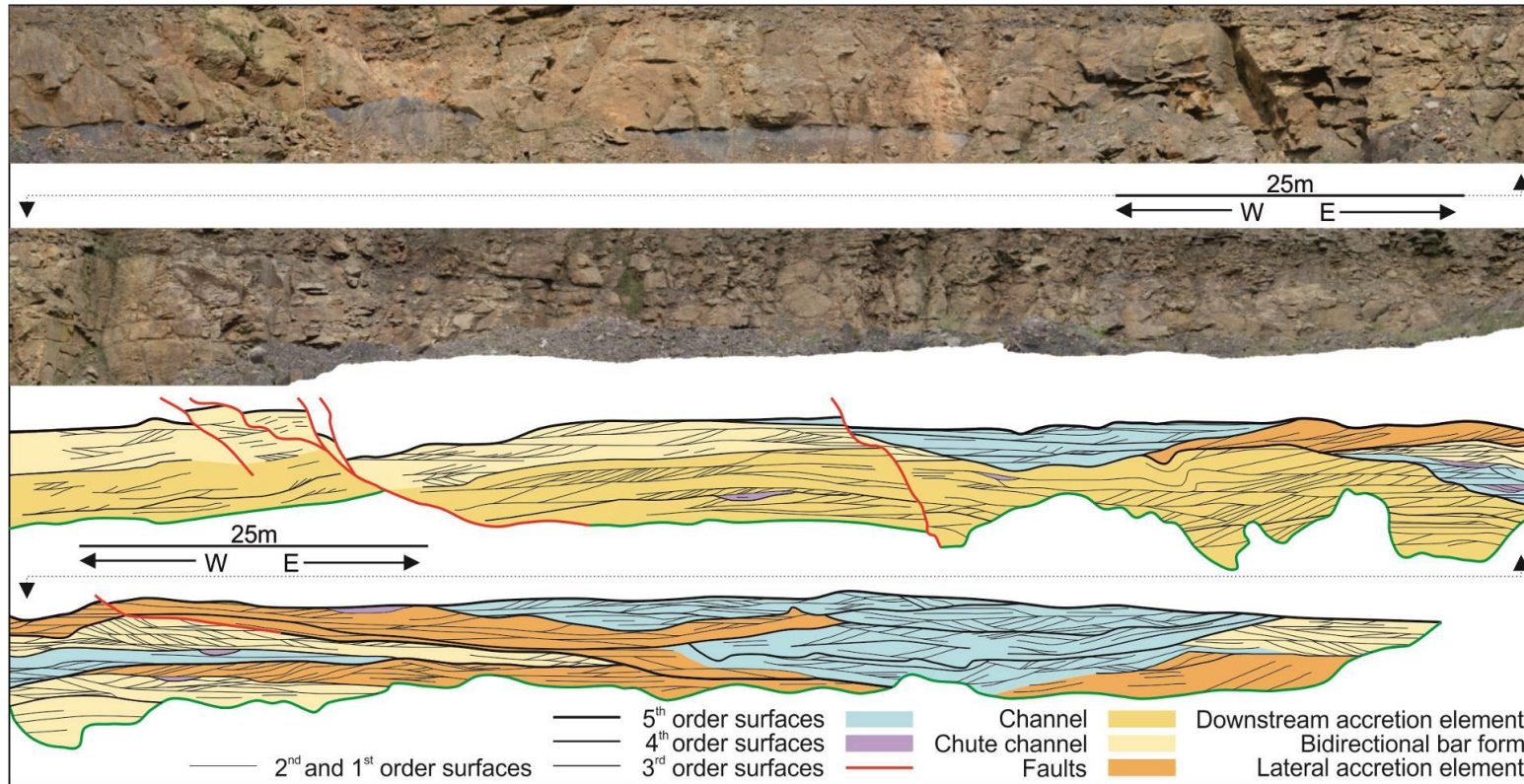


Figure 4.8 - Ortho-rectified projection of the photogrammetric dataset collected from the B1 Face. The data shown is for the fluvial portion of the Spireslack Sandstone, the top two images are interpreted below. The image shows two distinct channel sets with one eroding down into the other preserving distinctly more cut-and-fill channel elements than the previous bar-form dominated channel set (Ellen et al. 2019). Note, there is some syn-sedimentary faulting cutting obliquely through the outcrop.

4.4.1 Channel element

Description: U-shaped elements that have basal fifth-order scour bounding surfaces, and are topped by fourth-order surfaces when fully preserved. Full preservation of the element is rare due to subsequent down-cutting fifth-order bounding surfaces of elements of the same type. These elements consist of lenses of clast-supported conglomerate facies (Cc) structureless sandstones (Sm), trough cross-bedded sandstones (St-c, St-f), and some ripple-laminated sandstones (Sr). Where the element is fully preserved it has a width of 34 - 59 m and a thickness of 2.2 - 3.7 m giving an average width-to-depth ratio of approximately 18:1.

The basal fifth-order surface commonly shows scouring and loading. This basal surface is commonly overlain by trough cross-bedded sandstones (St-c) with intermittent lenses of red structureless sandstone (Sm) and mudstone. Gravel to pebble conglomerate lenses (Cc) (~15cm wide) also punctuate the trough cross-bedded strata. The basal trough cross-bedded strata are arranged into sets ~50 cm thick that climb at subcritical angles and show some outsized clasts up to pebble grade, rip-up clasts of siltstone, and wood fragments. The preservation of foresets, and the development of sets, is far more common in the centre of the element where the basal fifth-order surface down cuts furthest into the underlying sediments. Such trough cross-bedded strata are conformably overlain by planar cross-bedded sandstones (Sp). The succession wanes through the lower flow regime until the deposition of ripple laminated (Sr strata), where the element is fully preserved. Third-order scour surfaces commonly cut and truncate both cross-bedded sets and lenticular structureless sandstones.

Interpretation: These architectural elements are interpreted as cut and fill channels. The large, fifth-order bounding surface at the base of the channel is produced by the initial down-cutting phase of a channel that scours down into the underlying sediments (Bridge 1993; Gibling 2006; Wakefield et al. 2015). Upper flow regime facies (towards the base of the element) wane to the lower flow regime facies near the top of the element, when fully preserved. The vertical variation in facies shows a general fining-upwards trend, indicating a waning-flow as the channel deposits during its back-filling stage. The upward-fining strata of the channel element fill finishes with the ripple-laminated sandstone facies and the top fourth-order bounding surface (where preserved). Structureless sandstones showing some intermittent poorly developed foresets suggest a high sediment load. Such high sediment load deposits lead to rapid deposition suppressing bedform development and migration (Bridge & Best 1988; Todd 1996). This rapid deposition also generates the load casts on the basal fifth-order surface (Allen 1983; Miall 1996). Small-scale, trough cross-bedded sandstone sets climb sub-critically within the base of channels suggesting the development and migration of sinuous crested bedform trains at times of lower sediment load. Lenses of conglomerate facies and large outsized pebble clasts are attributed to bedload transport and deposition in localized high-energy eddies (Froude et al. 2017). This is most prevalent within the deeper parts of the flow towards a centre thalweg. The lack of such structures up-section, and the greater preservation of cross-bedding indicates a decrease in sediment supply as the channel backfills. The width-to-depth ratio of channel elements suggests that they may be fixed (Leeder 1973; Ethridge & Schumm 1978; Miall 1996). Further evidence for this is provided by the number of third-order scour surfaces attributed to in-channel avulsions and bedform reactivation from variable discharge.

4.4.2 *Lateral accretion element*

Description: Lensoid elements, 60–80 m in lateral extent and 1.5–3.2 m thick are bounded by basal fifth-order bounding surfaces that correspond to channel incision. These elements are found within a larger and more complex channel scour than previously described (Section 5.3.1). In some examples from the main void, the element is topped by a fourth-order surface which is overlain by parallel laminated mud and siltstone facies (FI). However, in most occurrences in the B1 Face (Fig. 4.8), the tops of the elements are truncated by fifth- or third-order scour surfaces depending upon the scale of the incision. The element is dominated by sets of trough cross-bedded and planar cross-bedded sandstone facies (St and Sp). These sets are cross cut by second-order coset bounding surfaces of a low angle.

The coset bounding surfaces of the element are often inclined normal to the local channel palaeoflow direction, these coset bounding surfaces are commonly lined with mudstone and siltstone (FI facies). The sets (of St and Sp) are separated by first-order or second-order bounding surfaces that show a sigmoidal geometry and have abundant asymmetrical ripples preserved along them. Coset surfaces show asymptotic geometries, where they terminate against the basal fifth-order bounding surface. The element often has third-order scour surfaces cutting through the set and coset bounding surfaces. The climbing sets and cosets of the element are conformably overlain by ripple laminated sandstone facies (Sr).

Interpretation: This architectural element is interpreted as a lateral accretion element. Planar and trough cross-bedded sandstones that accumulate into sets climbing normal to local flow directions indicates the deposition on the margins of a helical flow (Frothingham

and Rhoads 2003; Kolla et al. 2007), away from the thalweg of the host channel. Such sets being cross-cut by coset bounding surfaces and planar laminated siltstone, indicates intra-element variations in discharge and sediment capacity (Nanson and Page 1983; Miall 2006). Cross-bedded sandstone sets that occasionally overly the basal fifth-order scour surface indicate that in such occurrences the element was part of the initial back-filling phase of the channel. Ripple lamination and preserved asymmetrical ripples on second-order coset bounding surfaces represent wash-over across the element top (Wakefield et al. 2015). Third-order bounding surface truncation cutting down through first-order set surfaces and second-order bounding surfaces indicate reactivation to flow. A cut and fill phase has been superimposed upon the longer scale lifetime of the element, enabling incision of the element at peak discharge followed by bedform development and build-up during the subsequent backfilling phase (Bridge 1993; Bridge et al. 1995). This may also be due to a change in the migration direction of the element as a response to a variation of in-channel conditions (Leopold & Wolman 1957; Jackson 1976; Nanson 1980; Nanson & Croke 1992).

4.4.3 Downstream accretion element

Description: These architectural elements have a lateral extent of 37-58 m and a thickness of 0.5-2.5 m, and are typically basally bound by channel base fifth-order surfaces and topped by fourth-order surfaces. The elements have a tabular geometry. The element is dominantly composed of planar and trough cross-bedded sandstone facies (Sp and St), that build into sets that climb sub-critically and are typically 0.8 to 1.2 m thick. These sets stack forming cosets 2-2.5 m thick that preserve asymmetrical ripple lamination along their coset second-order bounding surfaces. There are some occurrences of third-order

scour surfaces with subsequent infilling of the set and coset build-up of cross-bedded sandstone facies. In a few cases the foresets change direction along set surfaces; otherwise, the major migration direction is parallel to that of the local channel. The lateral margins of these elements (when preserved) can show extremely steep erosional sides bounded by third-order if fully preserved and fifth-order bounding surfaces when the margins of the element have been eroded into. In some occurrences, the planar and trough cross-bedded sandstones of the element are overlain by ripple-laminated sandstone (Sr), planar laminated sandstone (Sh-c) and planar-laminated siltstone (Fl).

Interpretation: This element has been interpreted as a mid-channel downstream-accreting element. The progressive build-up of cross-bedded sandstone facies as sets and cosets within the more central areas of a larger scale fifth-order erosional bounding surface suggests a mid-channel bar development. Palaeocurrent directions that are roughly similar to those of the surrounding channel facies indicate that the element may be accreting downstream. The barforms are occasionally bound by fourth-order bounding surfaces, in these cases the deposition of the element is bounded by a conformable boundary with the element below. The build-up of elements then form compound downstream accreting barforms (Jackson 1976; Miall 1977, 1996; Almeida et al. 2016). The element is more commonly topped by another fifth-order bounding surface indicating the bar top has been eroded by the scouring of subsequent channels and other downstream accreting elements.

Planar and trough cross-bedded sandstone sets represent the downstream migration of bedform trains under relatively normal sediment loads. The preservation of ripples along second-order coset surfaces indicates ripple-scale bedforms migrating over dune-scale

bedform trains during periods of variable water depth. The variation in palaeocurrent directions given by foresets along individual set surfaces may reflect a change in accretion direction. The element may switch from a downstream-dominated migration to oblique migration (Rust 1972; Miall 1977). The downstream to oblique nature of the element's migration is shown in the steep-sided third-order faces on the margins of the element. These are slip faces where bedform migration has built up but not developed normal to the channel palaeoflow.

Horizontally laminated sandstone and their associated primary current lineation features indicate upper flow regime conditions due to extremely shallow water depths on bar tops at times of high discharge. The deposition of planar laminated siltstone facies may occur from suspension settling in standing water pools on an emergent barform top, despite this there is no observed evidence that the tops of these elements is emergent.

4.4.4 Chute channel

Description: This element is the smallest within the succession with a lateral extent of 2.1–3.7 m and a thickness of 0.2–0.5 m. The element has a U-shaped geometry and is basally bound by a third-order scour surface that cuts down into the underlying sediments of a larger element such as a downstream accretion or lateral accretion element. The element is topped by the larger fourth-order bounding surface top of the underlying or parent architectural element. The fill of the element comprises of structureless sandstone (Sm) facies.

Interpretation: The element is interpreted as a chute channel. The small-scale scour surface eroding down into a parent architectural element suggests the small channel cut through the top of a downstream accretion or lateral accretion element. This may occur

due to a rapid increase in discharge forming chute channel scours when the barform tops become submerged (Figure 4.12; Ghinassi 2011; Wakefield et al. 2015).

4.4.5 *Sheetflood*

Description: This element is laterally extensive (no preserved lateral margins are observed) with a maximum thickness of 4 m. The element is basally bound by an erosional planar third-order scour surface, which typically cuts into underlying planar laminated siltstone facies. The element is topped by a conformable fourth-order bounding surface. The element consists of horizontally laminated sandstone (Sh-c), ripple-laminated sandstone (Sr) and fine-grained trough cross-bedded sandstone (St-f). The horizontally laminated sandstone facies typically contains plant debris and overlies the basal conformable fourth-order bounding surface. This facies is overlain by single sets of trough cross-bedded sandstone facies; however, two sets are rarely observed. These sediments are overlain by asymmetrical ripple laminated sandstone facies that typically preserve with some minor mud draping of the laminae. These ripple laminated sandstones commonly exhibit undulose bedding lined with plant debris and show pervasive rooting. The succession (when fully preserved) finishes with symmetrical ripple marks and interference ripples on the top bed surfaces.

Interpretation: The element is interpreted as a sheetflood exhibiting tabular and lateral extensive geometries. Such a sheetflood may be characterised as an overbank flood deposit. The element has a basal scour surface that is planar indicating a rapid hydraulic jump and a rapid erosion of relatively unconsolidated material. Each individual fining-upwards succession of the element represents an individual flood (Miall 1996; 2014). The low sediment-calibre attributed to the element indicates that the element formed away

from the main high-energy flow. However, the flow did, contain sufficient sediment to support bedform growth and migration. The flow must have been shallow enough to encourage upper flow regime conditions to enable planar laminated sandstone facies to be deposited and overlain by single-set trough cross-bedded sandstones (Arnott & Hand 1989). Further to this, the flow must have waned quickly to preserve such strata. Symmetrical and interference ripples at the top of the element suggest wind rippling of slowly moving or stagnant water during the latter waning stages of flooding.

4.4.6 Overbank

Description: These elements have a lateral extent beyond the studied outcrops and are less than one metre thick. The conformable basal bounding surface is a fourth-order bounding surface of an underlying element such as a channel, accretionary element or sheetflood. The top of the element is eroded in every observable occurrence and marked by a fifth-order down-cutting basal bounding surface of a channel form or by a planar third-order scour of a sheetflood deposit. Only two facies comprise the element planar laminated siltstone (FI) and coal, both of which are abundant plant debris and roots.

Interpretation: The element has been interpreted as an overbank element; deposition of the element was on a wet floodplain which contained areas of sustained standing water. The laminated siltstone facies was produced by suspension settling in standing water from extremely late stages of flooding. These were subsequently vegetated during periods of quiescence. The presence of coal suggests stagnant, palustrine and anoxic conditions (Nanson & Croke 1992; Bridge 2009; Gulliford et al. 2017) during prolonged periods of no deposition. The lack of desiccation cracks within the siltstone facies also suggests persistent sub-aqueous or wet conditions.

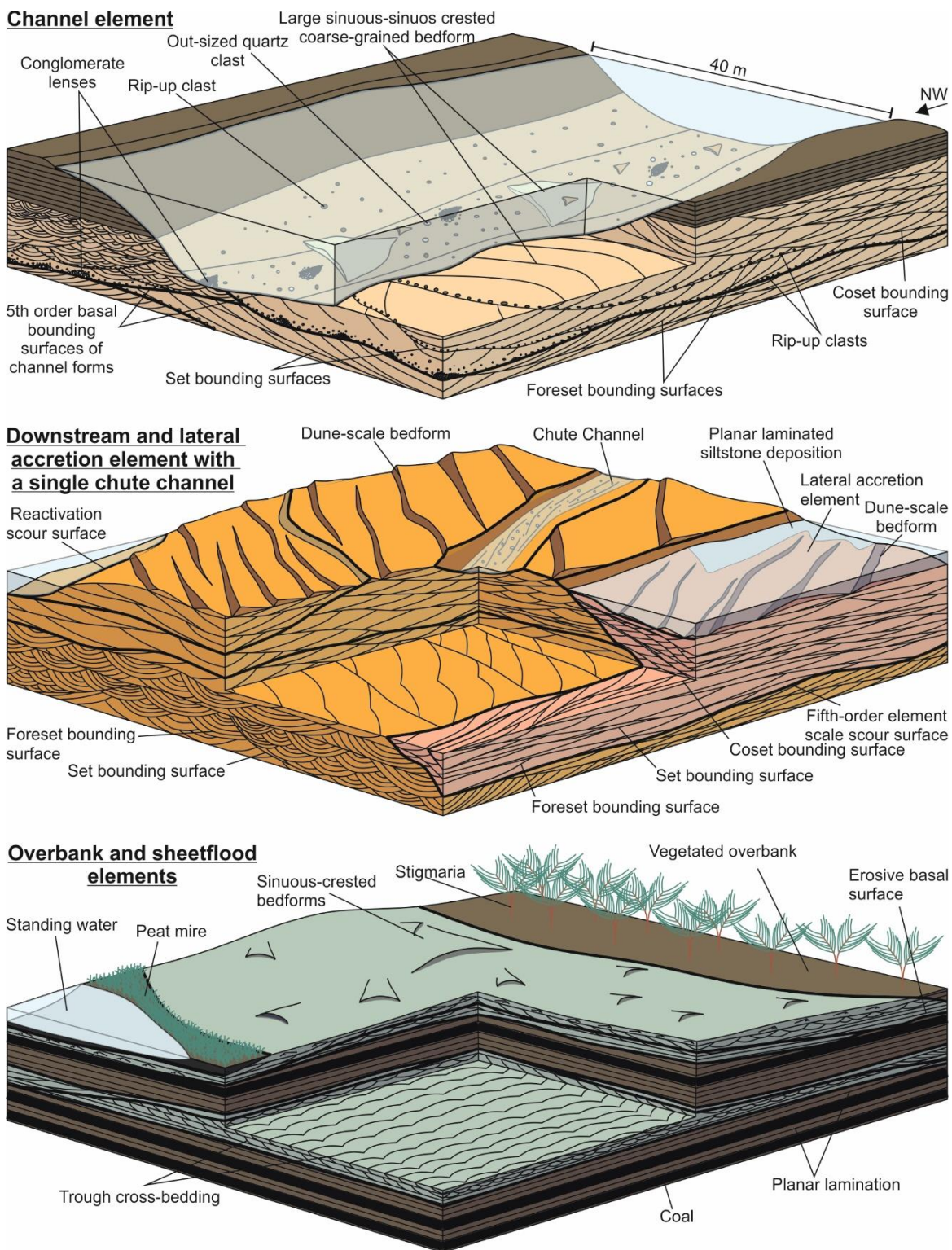


Figure 4.9 – Schematic three-dimensional representations of the six architectural elements that make-up the Spireslack Sandstone. The channel element can be seen to erode through overbank material transporting bedload dominated material downstream in a north-western direction, as dunes and gravel lag deposits. Preserving trough cross-bedding and conglomerate lenses within

erosional channel scour surfaces. Downstream accretion elements show trough cross bedded sandstones built into sets and cosets with major slip faces and reactivation surfaces punctuating. Chute channels can be seen to erode into the top of barforms at periods of peak discharge, these show little internal architecture. Lateral accretion elements are commonly developed on the flanks of such mid-channel bars and contain inclined draped sandstone strata. The final model shows the overbank hosted elements such as sheet flood and overbank elements which are composed of fine grained, clay rich sedimentation, along with abundant coal formation indicating a perennially high water table.

4.5 Depositional model

The fluvial succession of the Spireslack Sandstone is dominated by downstream accretionary and simple cut-and-fill channel elements indicating a low-sinuosity nature to the flow. The succession was deposited as a mixed load system in which gravel grade material was transported as bedload, represented as conglomeratic lensoidal facies (Cc). The typical complex channel fill succession is characterized by both lateral and downstream, simple and compound, accretionary elements. Variations in sediment load, and discharge, are evidenced throughout the succession. Common factors such as sediment grade, energy conditions and fluvial processes play an important role in the process of deposition and preservation of the facies deposited. Variable sediment load is typically due to changes in discharge rates (Schumm 1981; Syvitski et al. 2000; Bhattacharya et al. 2016) and also autogenic small scale in-channel avulsions that are commonly associated with braided low-sinuosity fluvial systems (Miall 1977; Lesemann et al. 2010; Ashmore et al. 2011; Lui et al. 2015; Storz-Peretz et al. 2016).

The Spireslack Sandstone shows abundant reactivation surfaces at a third-order bounding surface scale. These surfaces cut through crossbed set and coset surfaces, as local discharge shows a rapid increase rejuvenating the energy of the flow and scouring architectures. Where this increase in discharge is gradual, chute channels may develop and preserve on the tops of possibly emergent accretionary elements. The classic low-sinuosity braided fluvial system model (Leopold et al. 1964; Schumm 1981; Miall 1977, 2014) does not support some of the observations derived from the Spireslack Sandstone. The proportion of bedload transport (Galloway 1981; Friend 1983), the channel width-to-depth ratio (Blum 1994; Gibling 2006; Paola et al. 2009) and the maturity of the overbank (Miall 1996, 2014) are all non-characteristic of classic braided fluvial system models. Discharge variability may be the cause for such sedimentary characteristics for in-channel avulsions. However, high channel stability, associated with mature and vegetated overbank may, would increase longevity of a channel reach, which is not associated with classical braided systems.

The presence of lateral accretion within the Spireslack Sandstone suggests a degree of sinuosity to some of the flow within the channel reach. Such sinuosity is likely within the Spireslack fluvial system given the width-to-depth ratio of ~18:1, and the lack of observable hollow elements (Cowan 1991; Miall 2014) indicating a moderately fixed channel nature (Leeder 1973; Ethridge & Schumm 1978; Miall 1996; Gibling 2006). This interpretation is supported by evidence for the significant development of overbank characterized by standing water and palustrine conditions replenished by frequent flooding. Despite likely widespread development, the preservation of overbank sediment is rare throughout most of the fluvial Spireslack Sandstone (Figure 4.12).

The occurrence of small lenses of overbank material indicates the formation of overbank, possibly semi-consolidated, and its subsequent erosion and transportation in channel forms. Surviving overbank elements show the greatest preservation potential at the top of the Spireslack Sandstone. Here, a laterally extensive section of the facies is preserved marking a drastic change in the depositional regime. Given the low-sinuosity nature of flow within the Spireslack system, avulsion would have been frequent and may have been attributed to a low rate of aggradation (Wright & Marriott 1993; Blum & Törnqvist 2000; Miall 2014). Such a cannibalistic nature will have been the primary control on lack of overbank preservation (Lynds and Hajek 2006), rather than the lateral accretion of channels (the more prominent control in higher-sinuosity fluvial systems; Nanson and Crooke 1992).

As outlined above, a low-sinuosity, sand-dominated, mixed-load fluvial system has been interpreted as a likely depositional environment for the Spireslack Sandstone. However, various characteristics of the system such as: relative proportions of different elements, their sizes and their relationships up-section, do not allow the succession to be constrained to a single depositional model, but suggest variations in fluvial style through time. Consequently, the fluvial Spireslack Sandstone sub-divided into two distinct, individual channel sets with differing but defining characteristics (Figure 4.13).

The B1 Face shows the lower of these two channel sets (Figure 4.8), with an architectural composition exhibiting stacking of channel elements, each showing preserved thickness exceeding 1 metre. The section shows an amalgamated channel succession dominated by coarse-grained structureless sandstone (Sm-c), coarse-grained trough cross-bedded sandstone (St-c) facies and lenses of conglomeratic facies (Cc). The succession suggests

that there is a high sediment load within the flow but with increasing abundance of cross-bedded sandstone facies upwards, suggesting a decrease in sediment load as the channel set aggrades. The lower channel set of the B1 Face shows downstream accretionary barforms only.

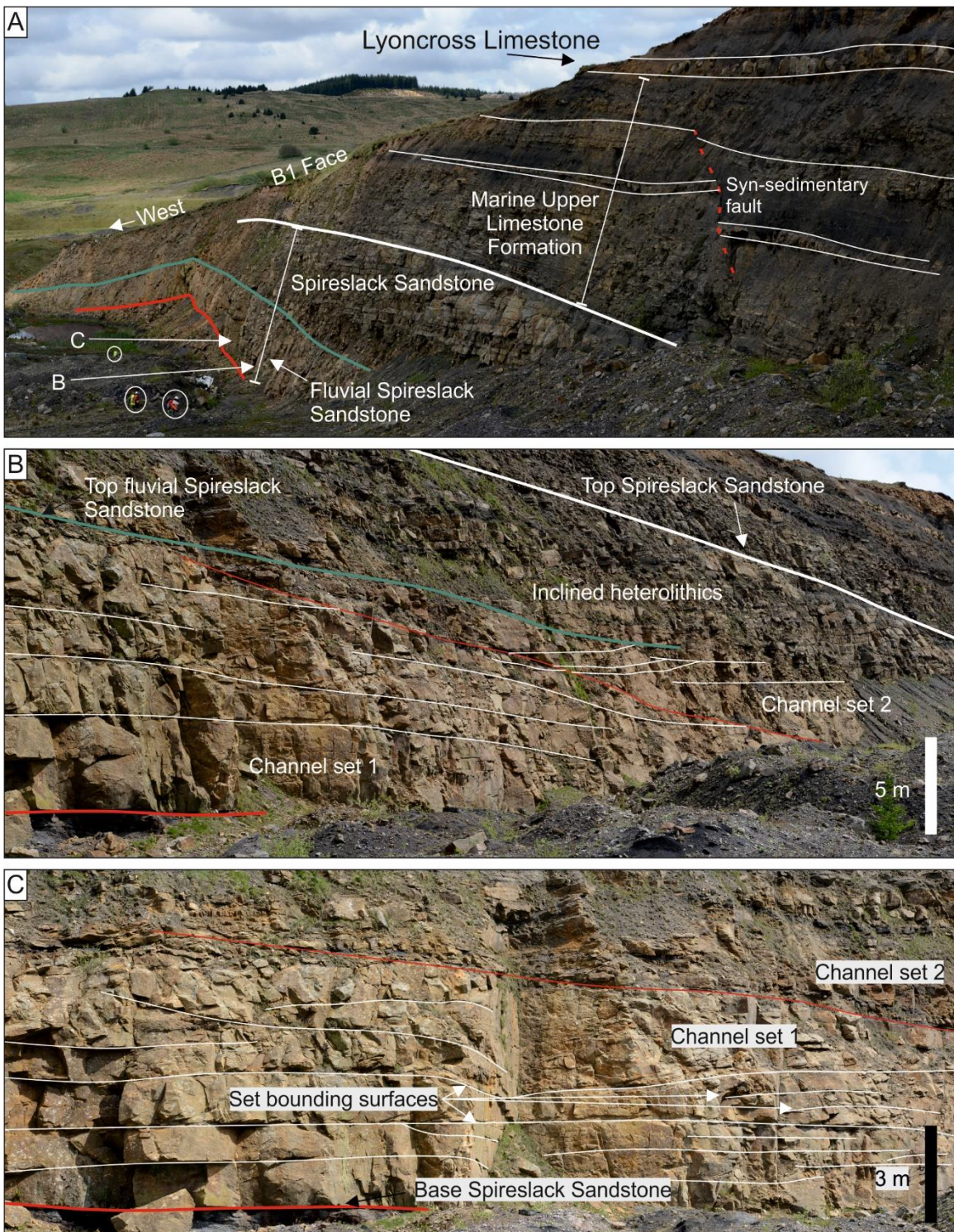
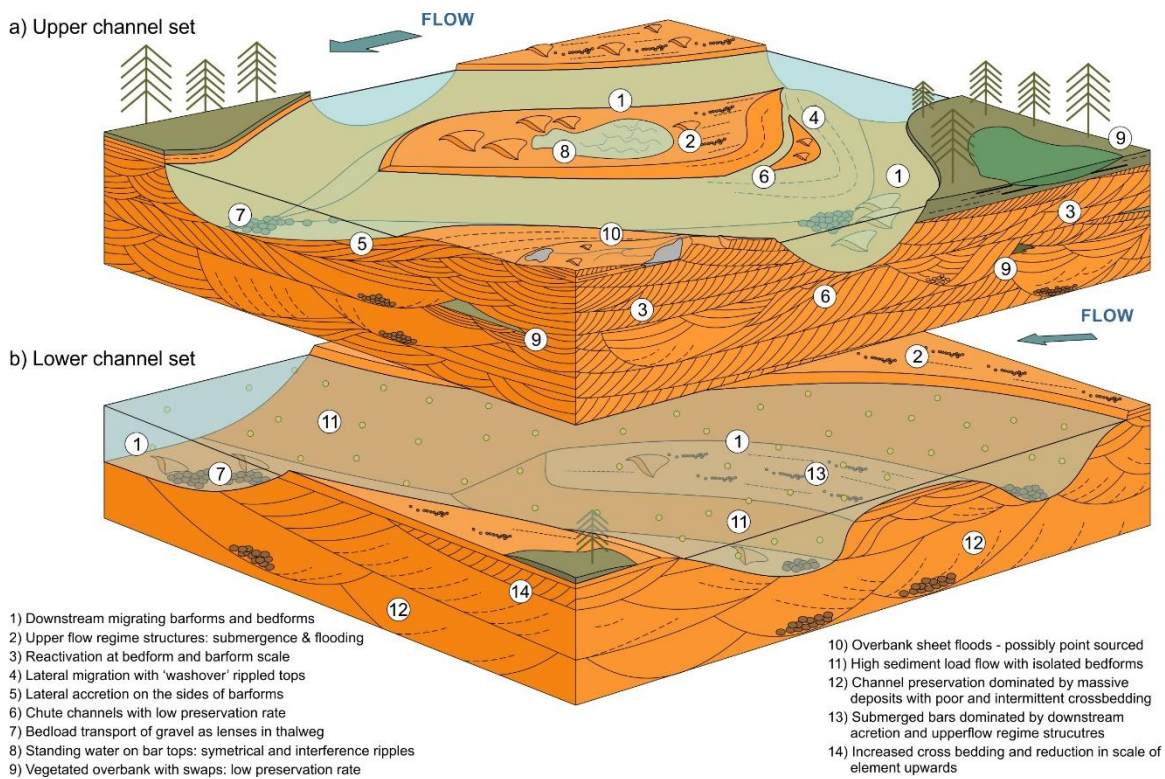


Figure 4.60 – Images from the B1 Face showing how the Spireslack Sandstone’s stratigraphic architecture lies within the context of the outcrop and the rest of the Upper Limestone Formation. A) The fluvial portion of the Spireslack Sandstone lies at the base of the outcrop, with a large inclined heterolithic architecture above it and finally the remaining outcrop overlying this is the marine portion of the Upper Limestone Formation. Note people for scale and the location of images 4.10b and c have been located with reference to the rest of the outcrop. B) Planar erosional base of the fluvial Spireslack Sandstone which is subsequently eroded by a second smaller scale erosion and the deposition of a second channel set. Channel set 2 shows onlapping set surfaces helping to pick out the second channel set. The top of the fluvial portion is picked by the downlapping of the inclined heterolithic clinoforms from the above architecture. C) Complex trough crossbedded sandstone set and coset scale architecture characterising the bar development of the homogeneous channel set 1 in the fluvial Spireslack Sandstone.

Figure 4.71 (next page)- *Schematic representation of the two channel sets of the Spireslack Sandstone. The lower channel set shows limited bedform development and a much higher energy flow, the upper channel set is characterised by bedform development and bar-form growth (Ellen et al. 2019).*



The evolution of the section is accompanied by rotation of the dominant palaeoflow direction from face-parallel to face-oblique (with respect to the B1 Face). The geometries within the upper channel set of the section show smaller channel elements than those preserved in the lower set. The log data from the Main Void section (Figure 4.9) indicates that the upper channel set consists of finer-grained and lower sediment load flows. This is indicated by an increase in bedform development and the arrangement of foresets into sets and cosets (rather than their intermittent preservation in the lower channel set). Lateral accretion elements and overbank are more prevalent than in the lower channel set. Such observations indicate that the fluvial system has become more mixed-load than bedload dominated and shows an increase in sinuosity.

4.6 Regional Correlation

In this section, a regional correlation of the Spireslack Sandstone is presented, using old coal board drilling data across the Muirkirk Syncline. The use of such sub-surface data

enable comments on the lateral extents of the Spireslack Sandstone to be made, providing insight into the nature and extent of the Spireslack Sandstone confinement.

4.6.1 Method of regional correlation

The Spireslack Sandstone was correlated across the central Midland Valley using the borehole data collected from the exploration drillings highlighted in Figure 4.12. Fourteen boreholes were used in the analysis, taken along a roughly south-west to north-east profile. This is approximately perpendicular to palaeoflow and the orientation of the proposed valley highlighted by Ellen et al. (2019) (Figure 4.13). The borehole data are extremely poor, no core or geophysical logs are present and interpretation is based upon the logs and descriptions derived from chippings (Figure 4.14).

The data show a regionally correlatable horizon in the Index Limestone that appears in all fourteen wells (Figures 4.6, 4.15 and Table 4.3), this is therefore used as a datum. The Spireslack Sandstone is identified within the logs based upon stratigraphic position. It must be above the Index Limestone and below the Lyoncross (Tibbie Pagan) Limestone. At the SGP site, the Spireslack Sandstone erodes down into a fossiliferous mudstone that is above the Index Limestone. The presence of this mudstone abruptly changing to medium- to coarse-grained sands showing “iron-staining”, roots and “clay galls” (assumed to be rip-up clasts (Browne pers. comms.)), are used as key identifiers to enable the Spireslack Sandstone to be correlated from borehole to borehole. The regional correlations shown in Figure 4.15 are tentative and limited by the data shown in Figure 4.14.

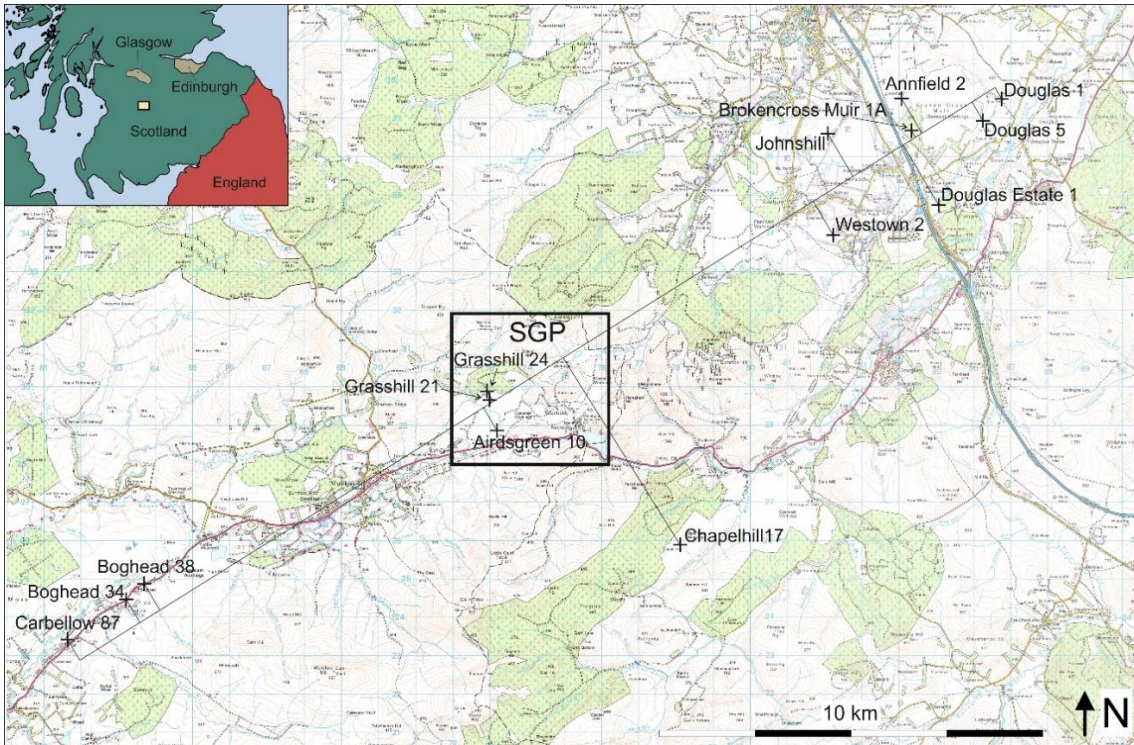
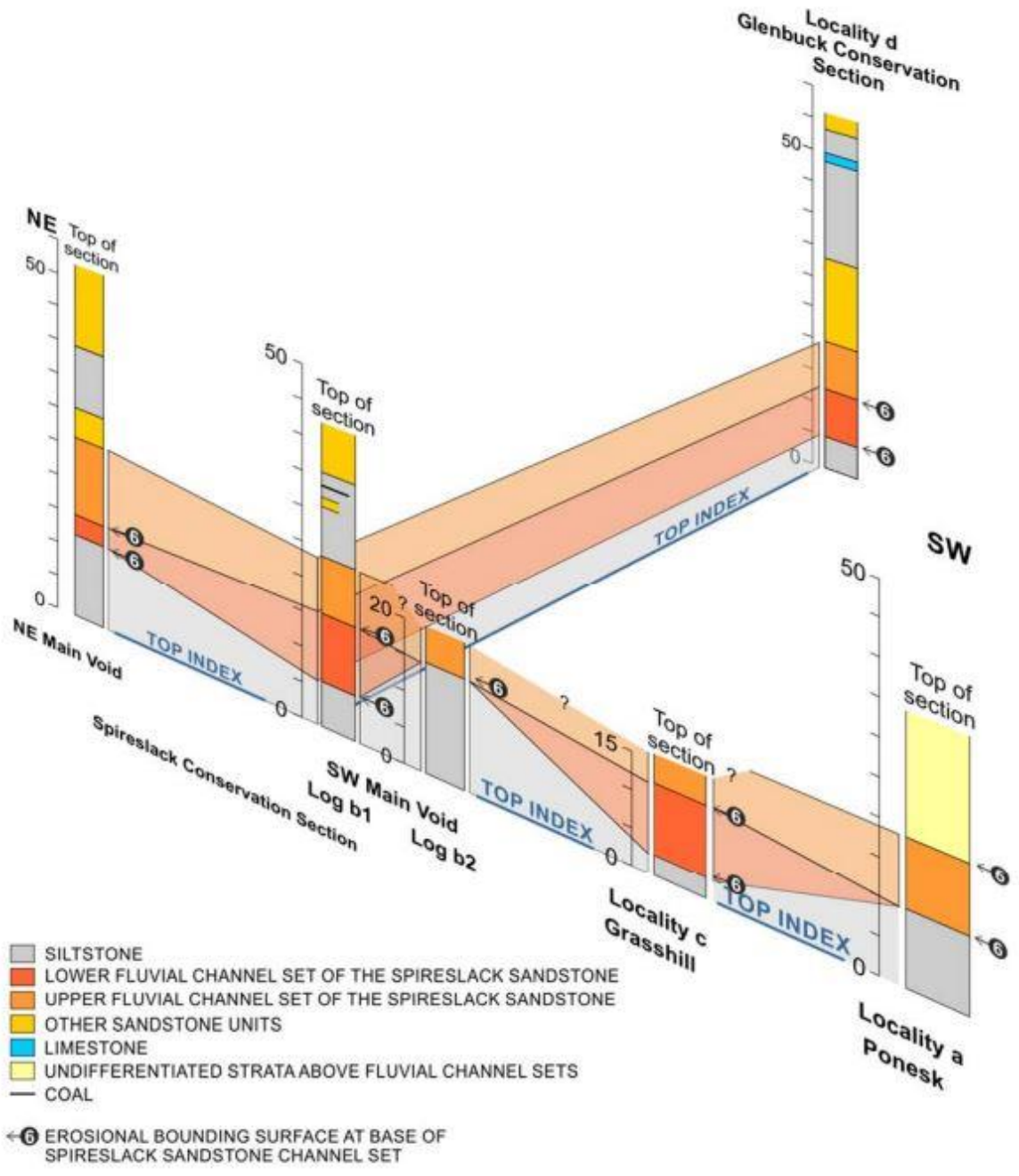


Figure 4.12 – Borehole map of the central Midland Valley with inset map showing where the outlined area lies in the Midland Valley of Scotland (Ordnance survey, 2002). All boreholes have been aligned to a correlation line. For details of each borehole see Table 4.3.

Figure 4.13 (next page)- Generalized vertical sections take from the SGP log sites (Ellen et al. 2019). All sections are aligned to the top Index Limestone datum, highlighting the differences in thickness and occurrence of the fluvial channel sets of the Spireslack Sandstone. The incision of these channels indicates that the valley is orientated north-west to south-east.



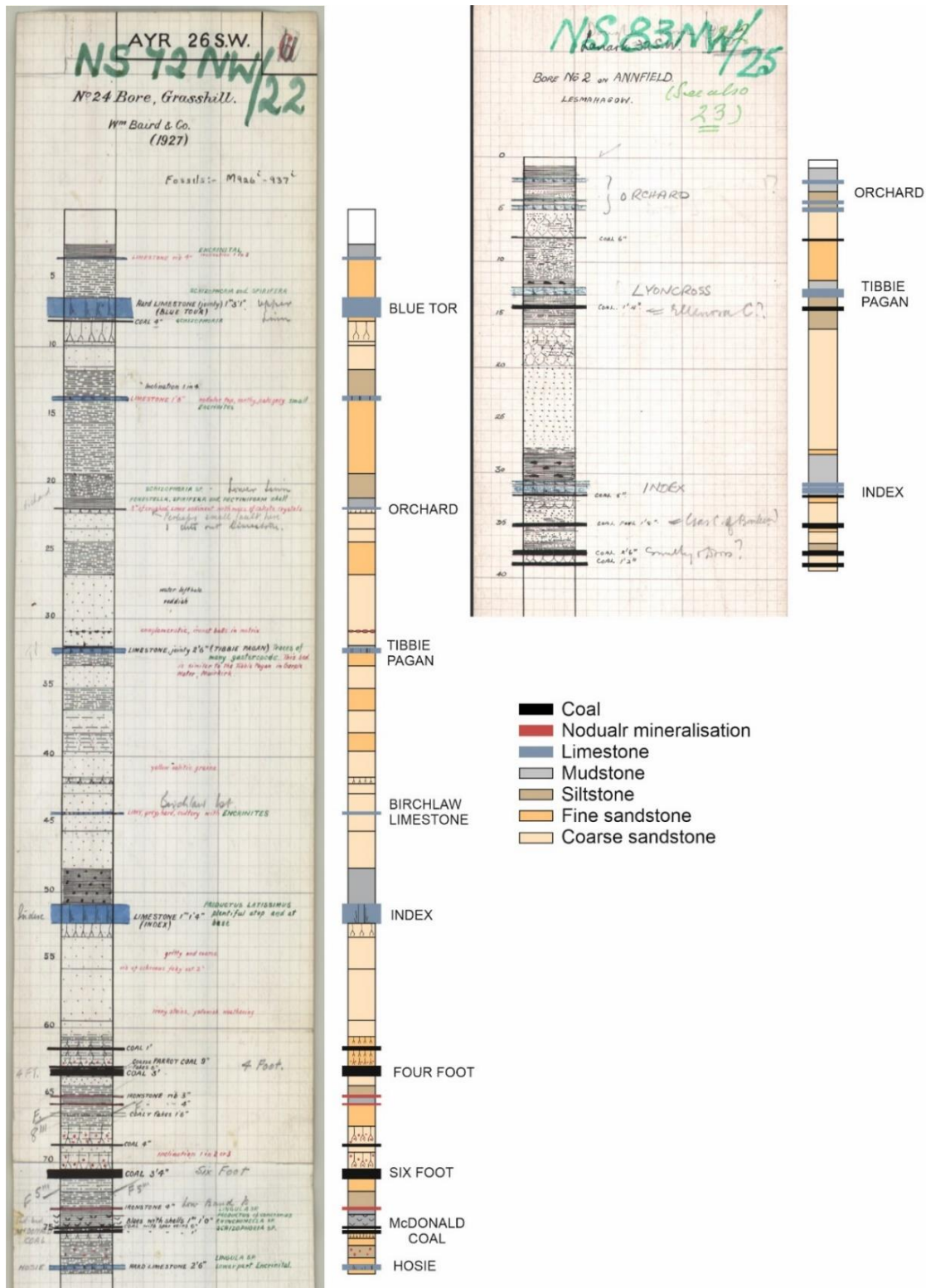


Figure 4.14 – Examples of two sets of borehole data used in the correlation of the Spireslack Sandstone, Grasshill 24 (left) and Annfield 2 (right). Logs show notes from chippings and the major correlated limestone and coal units within the area.

4.6.2 Results of regional correlation

The fourteen wells show the Spireslack Sandstone (Figure 4.14, 4.15). In the south west of the central Midland Valley, the Carbellow 87, Boghead 34, Boghead 38, and in the SGP area, the Ardsgreen 10, Grasshill 21 and 24 wells all contain the Birchlaw Limestone (Figure 4.15), another regionally correlatable marine limestone within the Upper Limestone Formation. However, all wells north east of the Grasshill 24 well do not contain this limestone but do contain the Index Limestone and the underlying Limestone Coal Formation. The absence of the Birchlaw Limestone has been interpreted as a product of the Spireslack Sandstones erosional nature. The base of the Spireslack fluvial system is shown as becoming more deeply incised towards the north east, producing erosional juxtaposition of the Spireslack Sandstone against the Birchlaw Limestone somewhere between the Grasshill 24 and Chapelhill 17 wells within the SGP area.

The thickness of the Spireslack Sandstone is also varied, with an abrupt thickness change between the Douglas Estate 1 well and the Douglas 5 well, varying from 7.9 to 16.7 m, a variation of 8.8 metres in the two and a half kilometres between the wells. Erosional incision within the Upper Limestone Formation is pervasive across the whole study area, but not to the same degree, with the thickness of the Spireslack Sandstone decreasing by five metres over another twenty kilometres to the south west.

The Cokeyard Coal is a regionally correlatable, conformable, informal lithostratigraphic unit. However, the unit is absent from the Boghead 38, Ardsgreen 10, Grasshill 21, Grasshill 24 and Chapelhill 17 wells (Figure 4.6, 4.15; Table 4.3). The coal then reappears within the Westown 2, Annfield 2, Douglas 5 and Douglas 1 wells. It is however absent from the Douglas Estate 1 and Broken Muir 1A indicating that it has been eroded in this

area, implying there has been a down-cutting. The internal architecture of the Spireslack Sandstone correlates as two or three channel sets within the thicker portion of the succession, from Boghead 38 well to the north east. This multi-scale erosional architecture is captured by the preservation of the Cokeyard Coal, indicating a second or even third erosional channel set within the larger erosional fluvial channel belt of the Spireslack Sandstone. There is no constraint on the number of erosional events within the Spireslack Sandstone. However, from these correlations and analysis of the facies that comprise them; given the high sinuosity of the second channel set, it is unlikely it is a multi-thread channel and therefore three channel sets may be suggested.

The erosional profile of the Spireslack Sandstone cannot be developed by the incision of a single distributary channel eroding down into a delta top. Incision of this spatial and temporal scale, coupled with its multi-scale erosional internal architecture, must have been produced by a large-scale allogenic control or an allo-induced autogenic control.

Table 4.3 – Lithostratigraphical unit tops picked for the correlation of the Central Midland Valley. The base of the Spireslack Sandstone and the thickness of the Spireslack sandstone has been used to convey the variation of thickness the fluvial unit shows.

Well	Lithostratigraphic top depths (m)									Spireslack Sandstone (m)	
	Ground level	Lyoncross Limestone	Cokeyard Coal	Birchlaw Limestone	Index Limestone	Ell Coal	3' Coal	9' Coal	Black Metals	BASE Spireslack	Spireslack Thickness
<i>Douglas 1</i>	189	4.56	6.08	-	11.552	-	-	15.504	20.064	8.512	9.2
<i>Douglas 5</i>	195	8.208	8.816	-	16.112	22.496	-	24.016	26.448	5.776	16.7
<i>Annfield 2</i>	240	3.952	4.256	-	9.424	-	-	-	-	8.208	10.1
<i>Broken Muir 1A</i>	247	15.808	-	-	20.368	24.016	-	25.232	26.752	19.456	8.7
<i>Douglas Estate 1</i>	190	46.512	-	-	53.808	56.848	-	58.672	60.192	52.592	7.9
<i>Johnshill</i>	221	8.208	-	-	13.68	17.328	-	19.152	20.368	12.768	6.8
<i>Westown 2</i>	262	2.736	3.648	-	8.208	11.248	-	12.464	17.328	7.296	7.8
<i>Chapelhill 17</i>	344	-	-	-	4.56	-	-	-	-	3.952	-
<i>Grasshill 24</i>	238	10.032	-	13.376	15.504	-	-	-	19.76	13.072	7.6
<i>Grasshill 21</i>	205	-	-	1.52	3.648	-	6.688	7.904	10.032	1.216	-
<i>Airdsgreen 10</i>	257	-	-	12.16	30.4	-	-	-	-	11.552	-
<i>Boghead 38</i>	193	15.504	-	20.368	22.496	22.8	24.32	25.232	-	19.152	3.6
<i>Boghead 34</i>	213	32.528	35.264	37.696	39.52	-	41.648	42.256	43.472	37.392	4.5
<i>Carbellow 87</i>	198	51.68	55.632	57.76	59.28	59.888	61.408	62.016	63.232	56.848	3.1

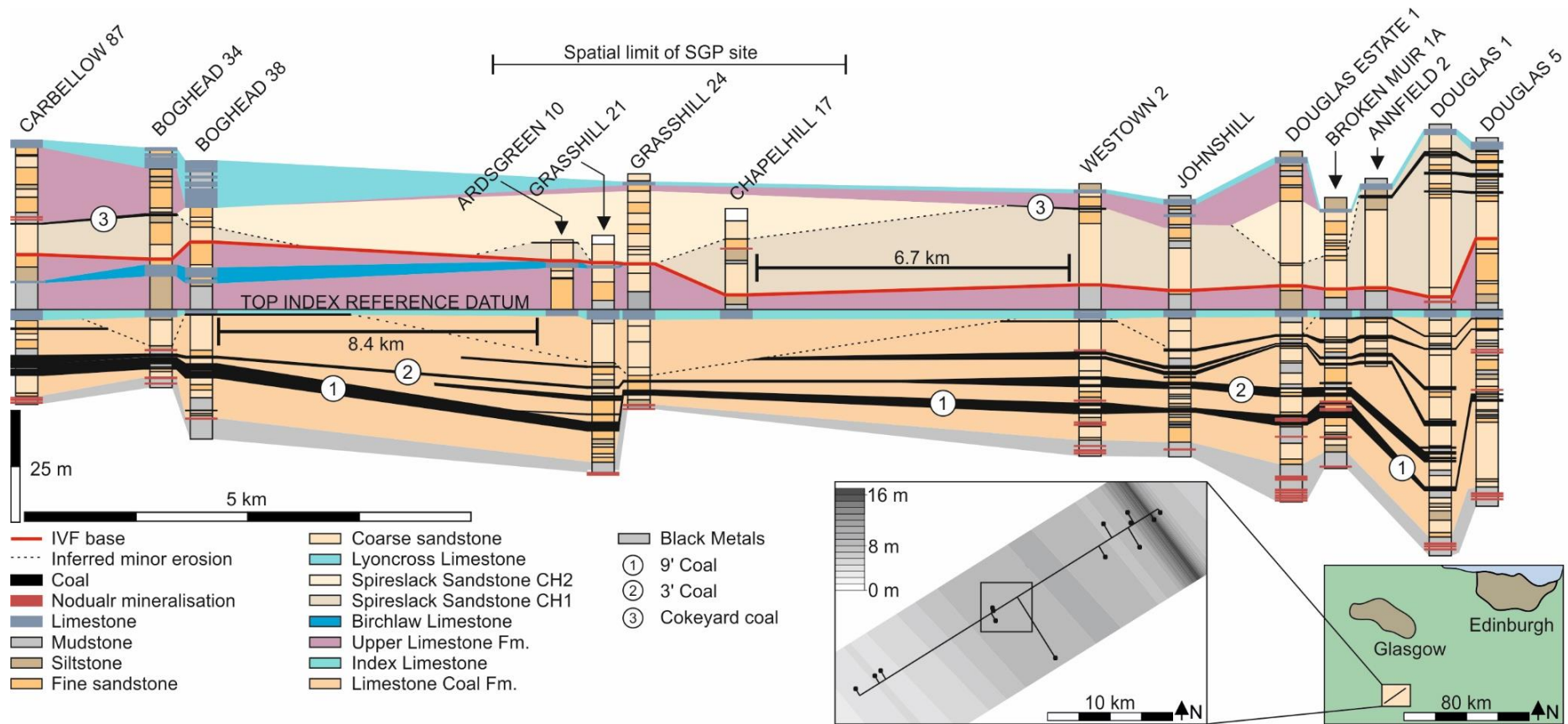


Figure 4.85 – Borehole correlation panel of the central Midland Valley. Panel has been referenced to the Index Limestone, a laterally correlatable, conformable unit across the Midland Valley Basin. Key stratigraphic units have been picked (Table 5.3) to show how the Spireslack Sandstone thins to the south west. This south east thinning trend shows the unit pinching out as the fluvial strata are juxtaposed against the paralic portion of the Upper Limestone Formation.

Figure 4.15 (continued) - Inset map shows where the correlation line lies relative to the rest of the Scotland. Thickness inset map shows the lateral variation in the thickness of the Spireslack Sandstone, and how it thickens dramatically towards the Douglas 1 well, and then thins again to the north east.

4.7 Evolution of the confined Spireslack Sandstone

The Spireslack Sandstone is laterally confined within the paralic sediments of the Upper Limestone Formation and shows a dramatic thickening within the Douglas area of the central Midland Valley of Scotland (Figure 4.15). This stratigraphic architecture is complemented by a complex erosional internal architecture indicating channel sets stacking on top of one another. This major erosional confinement of the fluvial system may have been generated by a significant base-level fall within the Serpukovian Stage. There is a significant eustatic sea-level drop within the middle to late Serpukovian Stage (Figure 4.2) that is potentially contemporaneous with the incision of the Spireslack Sandstone, providing further evidence that the erosion and the juxtaposition of paralic with proximal fluvial sediments is as a result of relative sea-level fall. However, the temporal correlation between the lithostratigraphy of the Clackmannan Group and the eustatic sea-level curve (Figure 4.2) is extremely tentative. There are no absolute date constraints imposed in the correlation as extensive biostratigraphic work has not been conducted in the area, and any palaeontological age constraints established initially in mapping yield resolutions too low to confirm or deny the correlation to the large eustatic sea-level fall within the Serpukovian Stage.

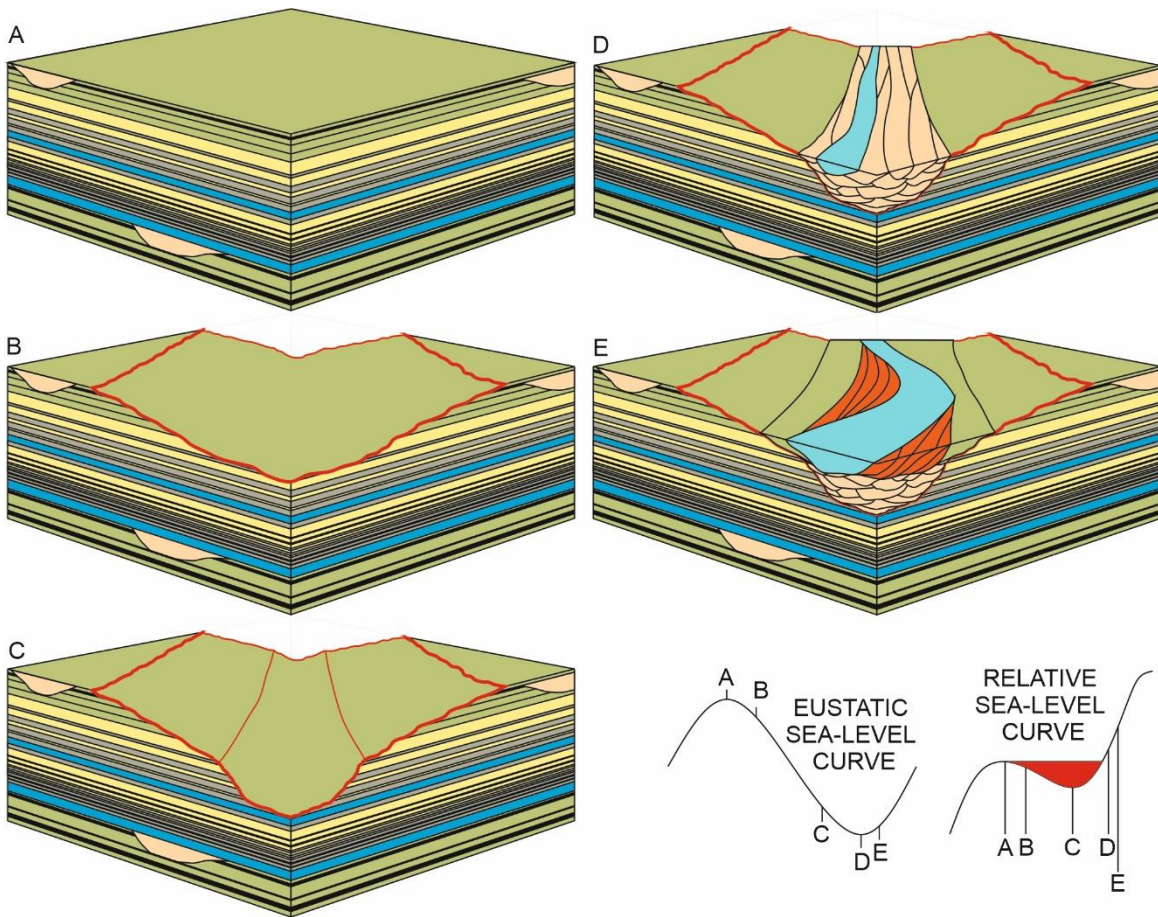


Figure 4.96 – Evolution of the Spireslack Sandstone stratigraphic architecture as a result of relative sea-level fall and the position of each schematic image relative to a eustatic and relative (assuming linear subsidence and sediment input rate) sea level curves. A) Highstand deposition of coastal plain facies and distributary channels, during normal regression. B) Initial stages of forced regression, moderate base level fall producing slowly changing fluvial gradients forming wide incision. C) Final phase of forced regression, steep fluvial gradients generated by the more rapid change in base level form concentrated incision and the formation of an incised valley. D) Initial early lowstand normal regression backfilling phase of the valley, Spireslack Sandstone channel set one and two. E) Late lowstand high sinuosity incised valley fill formed by moderate backstepping of the fluvial system as normal regression transitions into transgression.

Given the limitations within the data used, the interpretation of base level fall being the control on fluvial confinement cannot be confirmed or denied. However, given the preserved stratigraphic architecture and the speculative spatial and temporal correlations (Figures 4.15 and 4.2, respectively), an interpretation for the formation of the stratigraphic architecture seen in the SGP succession can be offered. The highstand sedimentation of the Limestone Coal Formation and lower Upper Limestone Formation provided normal regression into the Midland Valley Basin punctuated by minor transgressions highlighted by the Index and Birchlaw Limestones (Browne et al. 1999). Base level fall during the mid-Serpukovian creates a period of forced regression during which the graded fluvial profile adjusts (Holbrook et al. 2006). As forced regression is initiated, gradual rates of base level fall change the gradient of the fluvial graded profile causing it to incise slowly (Catuneanu 2006). As this forced regressive phase continues the rate of regression is increased and the gradient to the graded fluvial profile steepened (Catuneanu 2019). This creates more rapid incision and the more intense confinement of the fluvial system. As forced regression turns into normal regression at the end of base level fall, local accommodation begins to be filled with coarse, highly erosive early lowstand fluvial sediment (Catuneanu et al. 2011; Catuneanu 2019). As local accommodation is filled and normal regression continues, moderate base level rise occurs as the eustatic sea level curve starts to shallowly transgress. This base level rise forms a backstepping of the fluvial system and the development of a sinuous more mixed load fluvial system (Holbrook et al. 2006; Blum and Aslan 2006; Peeters et al. 2016), confined within the incised valley. Subsequent, more rapid transgression then forms the estuarine portion of the incised valley fill.

Another possible explanation for the confinement of the Spireslack Sandstone, is structural confinement. Where a fault may have generated syn-sedimentary local accommodation to trap and preserved the Spireslack Sandstone. There is a significant strike-slip fault through Hawksland and Douglas Water (the most north eastern fault in Figure 4.3), in the north eastern Douglas region of the correlation (Figure 4.15). This fault will have formed during sinistral transpression in the Viséan to Bashkirian. This oblique NW-SE-trending fault may have provided accommodation for the Spireslack Sandstone to be entrained in through a syn-sedimentary increase in local subsidence rates, pinning the lateral confinement of the Spireslack Sandstone to the footwall of the fault. Such a control on palaeotopography may help to explain the asymmetrical nature of the confinement to the Spireslack Sandstone. With the thickness variations being much less sharp in the south west, in contrast to the north east (Douglas area) where rapid thickness changes are seen.

Multiple erosional phases can be seen within the punctuation of the Cokeyard Coal (Figure 4.13), based upon the regional correlation of boreholes. Such erosional phases indicate avulsion at two scales, the small-scale local avulsions operating within a channel set and those on a semi-regional (within the confined Spireslack Sandstone Valley) larger scale. The small-scale scour patterns are those that erode bar tops and channel fill tops, this occurs within a channel set as a fluvial channel flow re-occupies or compensationally stacks within a large-scale channel scour. The larger scale scours occur within the limits of the palaeovalley margins. This semi-regional (not truly regional as an affect is laterally confined due to the

topography) scale avulsion scours at a channel set scale, where one channel set is superimposed upon another generating the multi-storey sandbody.

4.8 Discussion

High-resolution photogrammetric and sedimentary log data derived from the Spirelack Sandstone show that the classical models of fluvial systems (Miall 1985; 1996; 2014) do not apply to such sections. Here, a complex interplay of high sediment load deposition and avulsion patterns yield assemblages that comprise a high net-to-gross fluvial system. The rates of subsidence and local, laterally restricted avulsion are the driving controls in the development of this high net-to-gross nature and drive the connectivity of sandbodies within the succession. The understanding of these controls therefore provides greater constraint on the petrophysical properties of the strata.

Channel stacking and high sandstone body connectivity are produced by local and semi-regional scale avulsion, which is primarily controlled by low rates of accommodation space creation or confinement.

4.8.1 *Confined multi-storey sandbodies*

Presented here is a study of a single confined multi-storey sandbody. Whilst data are limited to a single system some more generic comments may be posed about the nature of the preserving architecture within these systems. The nature of the initial fill of these deposits is typically high-sediment load, impeding the development of bedforms and thus the preservation of forest bounding surfaces within preserving strata. Whilst there is no evidence

for a true increased sediment input rate, there may be an argument that the sediment input rate is higher relative to the reach of the fluvial system, confining the distribution, transportation and deposition of sediment to a limited lateral extent. Whilst this may be the case, if the eustatic model in section 4.7 is assumed, then sediment input rates dramatically increase during periods of forced regression (Catuneanu et al. 2011; Catuneanu 2019). This is due to erosional down-cutting as the fluvial system attempts to re-equilibrate to its graded fluvial profile (Holbrook et al. 2006). If the eustatic model is invalid, then the suggestion, based upon data herein, is that the increase in sediment load is a relative one.

With regards to initial channel fill, the architecture of the preserving fluvial system consists of unit bar formation at approximately four to five metre thickness. This is evidenced by the downstream accretion elements of channel set one (Figure 4.8). Wang et al. (2020) interpret the reconstructed maximum flow depths of the Spireslack Sandstone as approximately 6.1 to 10 m depth. A one to six metre difference from what may be assumed as maximum flow depth from the preserving bar top (Hajek and Heller 2012). Whilst this may be due to incorrect application of the maximum flow depth calculations of Bridge and Tye (2000) there may be a more geologically significant explanation. The maximum flow depth reconstructions of Wang et al. (2020) may be true (given they are approximate to the logged unit thickness in Figure 4.6), in this case the flow would be significantly deeper than in the unit bar thickness. This may be due to the same water discharge rate being unchanged, but flowing through an area of limited the lateral extent, confining the flow and making it deeper relative to the same amount of sediment within the system. This is further evidenced in the

lack of bar-top facies on the unit bars, as evidenced by the sedimentary log (first 11 m of the log in Figure 4.6). This provides observations that support the theory of a relative sediment load increase. There is not enough sediment to build up-to the ten-metre water depth but it is concentrated enough to develop high sediment load-type depositional products and unit bars (just not to the level required for accurate bar-top to flow depth correlation).

Wang et al. (2020) also comment on the consistency of the flow reconstructed from relatively uniform thicknesses of cross-bed sets. This consistency of cross-bed thickness may, in part, be due to consistent water depths, as further evidenced by consistent bar thicknesses and as highlighted in Section 3.9.3 the lack of upstream accretion elements preserved in the succession.

4.9 Summary

The Spireslack Sandstone of the Upper Limestone formation consists of a major high net-to-gross fluvial sandstone with two distinct channel sets. The lower channel set showing limited bedform preservation and showing a dominance of bedload transport and a low-sinuosity morphology is extremely cannibalistic. The second channel set comprises a more moderate sinuosity and higher suspended load transport system, preserving more bedforms. The evolution of the two channel sets is attributed to a retrogradation of the fluvial system. The cannibalistic character of the lower channel set is due its lateral confinement as a result of relative sea-level fall within the area, not allowing for fluvial aggradation to occur and therefore preservation of sandbodies. This relative sea-level fall is evidenced within the

eustatic sea-level curve for the Serpukovian (Figure 4.2) and in the incisional scale of the Spireslack Sandstone seen in the borehole correlation (Figure 4.13).

Evidenced provided herein suggests that confined multi-storey sandbodies may have a relatively high-sediment load and may also exhibit water depths greater than the bar tops suggest. Unit bar and high sediment load conditions dominates deposition in the basal portion of confined fluvial systems. Consistent flow depths are also highlighted as a potential diagnostic criteria for the fluvial system confinement, where any fluctuation proximal or distal of the confinement would be minimal in comparison to the larger water depths compared to the sediment available for deposition. Finally, the architecture of the confined MSB at Spireslack appears to have a simple barform arrangement, with some evidence of unit and compound bar growth, given this compound barform development it is interesting that no upstream accretion elements are present.

5 Geologically realistic representation of fluvial sedimentary architecture in stochastic reservoir models.

Based upon: Mitten, A.J., Mullins, J., Pringle, J.K., Howell, J. and Clarke, S.M., 2020. Depositional conditioning of three-dimensional training images: Improving the reproduction and representation of architectural elements in sand-dominated fluvial reservoir models. *Marine and Petroleum Geology*, 113, p.104-156.

At the time of this thesis submission this article has been **accepted and published** in *Marine and Petroleum Geology*.

This chapter provides a short literature review into stochastic reservoir modelling techniques followed by a model study of the Tuscher Canyon outcrop from section 3.3. The chapter, secondly, constructs two-point simulations and two-dimensional training images to develop a reservoir model from outcrop conditioning alone. The third portion of the chapter, which comprises the main bulk of it, uses depositional conditioning to develop three-dimensional constraints for the generation of a training image, by utilising satellite data from the Jamuna River, northern India. This newly developed training image is then used to build multi-point statistics models. These models are then qualitatively and quantitatively compared to more traditional object-based models and sequential indicator models. The geological realism and reproduction of these model sets is then discussed.

5.1 Introduction

Architectural element scale (meso-scale; Figure 5.1) heterogeneity becomes more important over longer reservoir production periods due to the increased sensitivity of fluid migration to smaller-scale heterogeneity over time (Tyler *et al.*, 1994). While research has addressed the giga- to mega-scopic sedimentary heterogeneity in fluvial systems (Figure 1), such as sandbody stacking (e.g. Laure and Hovadik, 2006, Hovadik and Laure, 2007, Villamizar *et al.*, 2015; Cabello *et al.*, 2018a) and its reproduction in reservoir models (Seifert and Jensen, 2000), relatively less attention has been given to the architectural element scale (Figure 1; Gibling, 2006; Enge *et al.*, 2007; Rittersbacher *et al.*, 2014; Colombera *et al.*, 2016; Koneshloo *et al.*, 2018). This chapter focuses on the realistic reproduction of architectural element scale heterogeneity (Figure 5.1) within an unconfined multi-storey sandbody deposited by a sand-dominated braided channel system. This work utilizes the sedimentary logs and digital photogrammetric outcrop data from Tuscher Canyon, Utah (Chapter 3), to develop two-dimensional training images conditioned to the outcrop data. Finally, it will use aerial imagery data from the Jamuna River, northern India, to develop a training image conditioned to basic depositional characteristics in three dimensions.

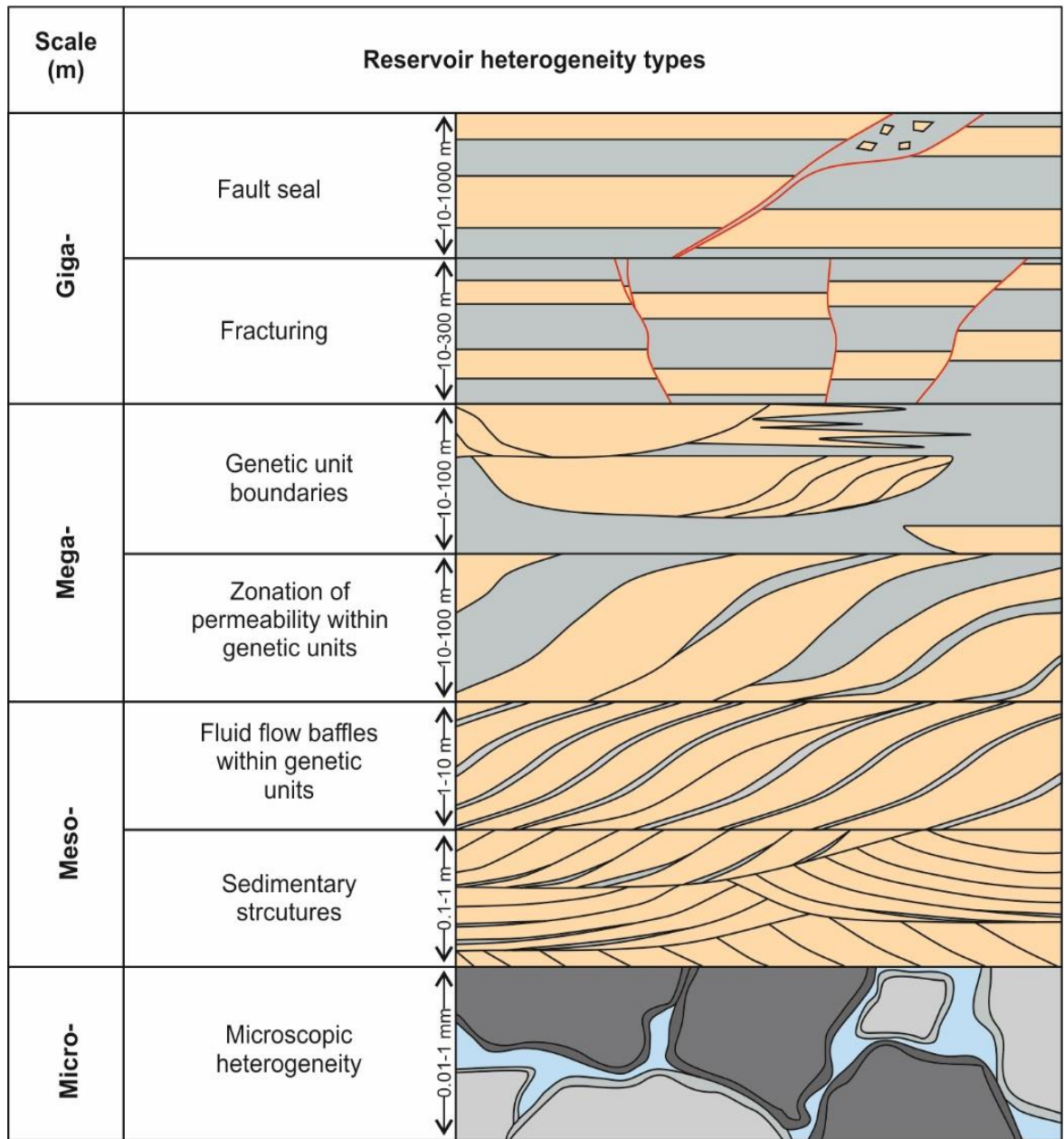


Figure 5.1 – The scales of typical fluvial reservoir heterogeneity (modified from Tyler and Finley, 1991; Morad et al., 2010). Note the 1 m - 10 m meso-scale of this study: zonation of permeability is within genetic units (Morad et al., 2010; Mitten et al., 2018). In giga- to meso-scale, the yellow indicates sandstone and the grey mud and siltstone, the red lines indicate faulting. In the micro-scale image, the black and grey represent quartz grains and the light blue indicates pore space.

5.2 Stochastic reservoir modelling

Reservoir models are used as three-dimensional representations of the sub-surface strata during exploration and production phases of hydrocarbon exploitation. The models are used to develop visualise reservoir strata, estimate resource volumes, develop risk profiles for specific plays, create frameworks for fluid flow simulations and to develop effective drilling plans. A major issue in the acquisition of sub-surface resources is the simulation of geologically realistic geometries in reservoir models (Deutsch and Journel, 1992; Seifert and Jensen, 1999; Zhou *et al.*, 2018). Geostatistical techniques attempt to solve this issue by using available input data to condition stochastic geostatistical algorithms enabling uncertainty to be quantified in a risk profile (Gooverts 1999; Pyrcz and Deutsch 2014).

Three major conventional geostatistical techniques are used currently in reservoir modelling of fluvial deposits: object-based modelling (OBM), sequential-indicator simulation (SIS) and multi-point statistics (MPS). OBMs use pre-defined geometric shapes to occupy multiple-cells (Holden *et al.*, 1998; Stephen *et al.*, 2001; Manzoocchi *et al.*, 2007), rather than using two-point or multi-point statistics, to build facies models. SIS is one of the most commonly used pixel-based methods, it uses a two-point statistical approach and populates a model volume using variograms derived from one- or two-dimensional data (Deutsch and Journel, 1992; Seifert and Jensen, 1999, 2000 and references therein; Martinius *et al.*, 2017). The SIS method is designed to apply stationarity to a model, so that any realisation should honour the input parameters. MPS techniques use a training image (TI) – a conceptual representation of the geometry and patterns of studied physical properties (Falivene *et al.*,

2006; Maharaja, 2008; Pickel *et al.*, 2015) – to dictate the stationary distributions of sedimentary heterogeneity expected within a reservoir (Strebelle and Journel, 2001; Strebelle, 2002; Caers and Zhang, 2004; Strebelle and Levy, 2008; Daly and Caers, 2010). MPS models have the potential to provide geologically realistic simulations of reservoir heterogeneity by incorporating analogous data into their workflows (Caers and Zhang, 2004, Strebelle and Levy, 2008; Le Coz *et al.*, 2011; Hu *et al.*, 2014; Zhou *et al.*, 2018).

Each modelling approach has its limitations with regards to the replication of facies and the reproducibility of the input data. OBMs are limited by the pre-defined shapes they can produce (Holden *et al.*, 1998; Stephen *et al.*, 2001; Manzocchi *et al.*, 2007). SIS commonly produces model elements with margins, geometries and distributions that are not realistic compared to the geology simulated (Seifert and Jensen, 1999; Deutsch, 2006; Ringrose and Bentley, 2015). Finally, MPS has been hampered, to-date, by the lack of appropriate libraries of TIs, the difficulty in constructing three-dimensional TIs, their re-usability, and the lack of standardized methods for their development, particularly in three dimensions (Comunian *et al.*, 2012; Ringrose and Bentley, 2015).

5.2.1 *Object-based models*

Object-based models (OBMs) require manual inputs of geometric information to constrain geobodies within a stochastic framework (Holden *et al.*, 1998; Stephen *et al.*, 2001; Manzocchi *et al.*, 2007). Individual geobodies are constrained using input data derived directly from hard (well log or outcrop) or soft (seismic) conditioning data (Haldorsen and Damsleth 1990; Dubrule 1998). Predefined inputs given to the geobodies include: size,

geometry, palaeocurrent and target fractions (the proportion of the total simulated volume the geobody should occupy). These geobodies or objects are placed stochastically within a background framework (Figure 5.2) (Holden 1998; Falivene et al. 2006). For example, channels of a given sinuosity, flowing in a given direction, are placed within a background facies of overbank. This approach can provide visually recognisable geometric trends that are visually representative of the environment they represent. Furthermore, a multi-scale approach is easily adopted within OBMs as smaller scale geobodies can be projected within larger scale predefined geobodies (Deutsch and Wang 1997).

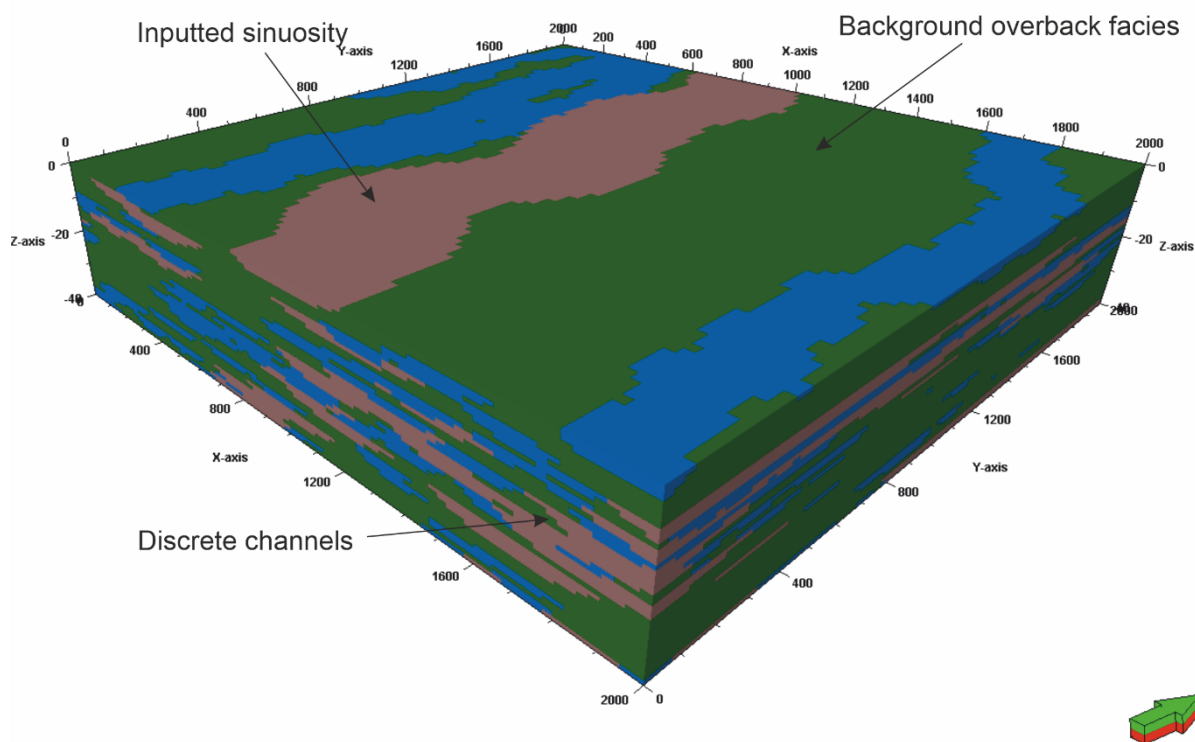


Figure 5.2 – Object-based model example generated in Schlumberger Petrel v.2016 software, illustrating discrete geobody reproduction within a background facies. The objects inputted in this example are channels with two different dimensions, the pink and the blue. These have an inputted

sinuosity to them, highlighted by the pink channels. The channels are added into a green (in this case floodplain) facies.

OBFs are a popular method to stochastically reproduce the architecture of geobodies, due to their visual results and the easily accessible input data (Deutsch and Tran 2002). Despite their popularity there is one major drawback to their use; OBFs are notoriously difficult to condition (Holden, 1998; Seifert and Jensen, 2000; Strebelle and Journel 2001; Vevle *et al.*, 2018). A further downside to the implementation of OBFs is the computational time required to use individual algorithms in the reproduction of each new type of object or geobody (Strebelle and Journel 2001; Strebelle and Payrazyan 2002).

5.2.2 Sequential indicator simulations

Sequential indicator simulation (SIS) is a pixel-based technique that enables spatial variability to be projected from hard conditioning data (Deutsch and Journel, 1992; Seifert and Jensen, 1999, 2000 and references therein). The algorithm uses variograms to project the probability of covariance (γ) away from conditioning data points. The variogram most commonly expressed is the semi-variogram (Equation 5.1), this can be calculated for all datasets regardless of how regularly spaced they are (Ringrose and Bentley 2015).

$$\gamma(h) = \frac{1}{2} \frac{\sum \{ [Z(x+h) - Z(x)]^2 \}}{N} \quad [5.1]$$

Where, the variance (γ) at a given lag distance (h), ($Z(x+h)$) is the value at a given lag distance from a given point in space ($Z(x)$).

The variogram consists of three key statistical elements: the sill, range and nugget (Figure 5.3; Gringarten and Deutsch 1999; Ringrose and Bentley 2015). The sill is representative of complete variance and expresses no correlation between data (or projected data) points. The range is the lag distance it takes to achieve complete variance, and the nugget is a discontinuity at the beginning of the variogram. This represents the geological variability below the resolution of the lag distance.

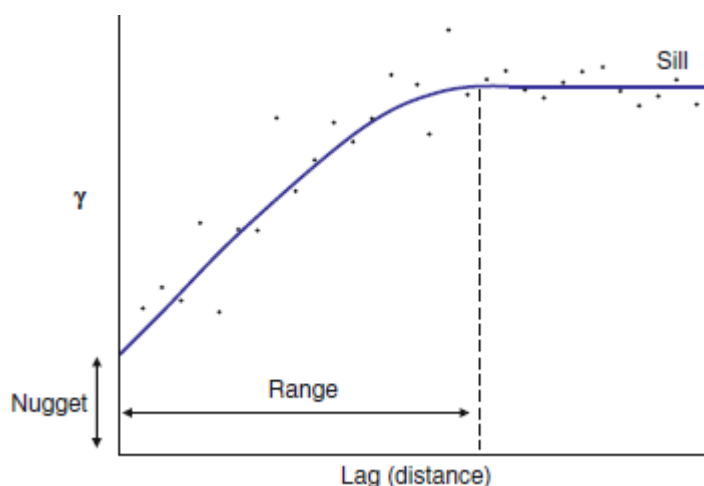


Figure 5.3 – Example of a semi-variogram showing the nugget, range and sill with associated axis (Ringrose and Bentley 2015). The sill indicates total variance, the range is the distance or lag when the sill is achieved and the nugget represents sub-lag distance variance.

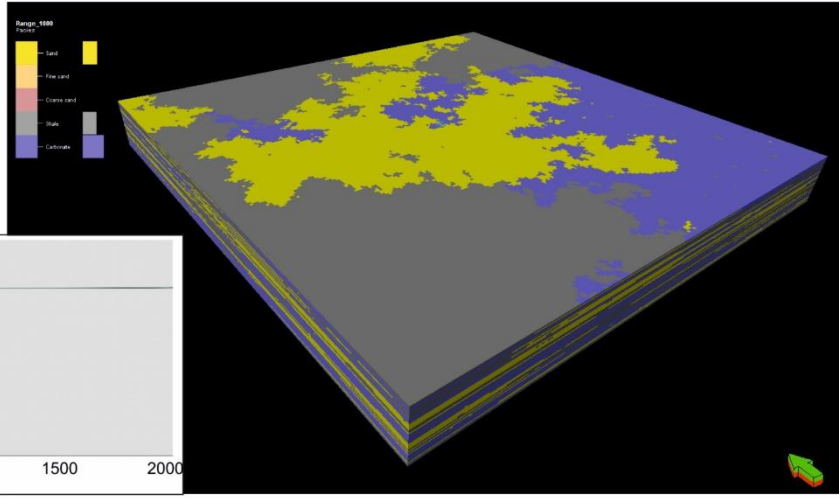
SIS (Figure 5.4) uses a sequential simulation process, in which simulated values provide local conditioning values for surrounding cells along a random route through the three-dimensional simulation volume (Gooverts 1997; Strebelle and Payrazyan 2002). The conditioning data input into the models are used to determine the value of surrounding cells, the distance from this conditioning data increases as the simulation runs, adding data points

that are later used for local conditioning (Deustch 2006). This pixel-based method provides a lot of flexibility for conditioning data to be honoured, and is therefore a popular technique in simulating sub-surface reservoirs. The major drawback to this technique, however, is that it relies upon two-point statistical inputs and therefore capturing multi-point geological problems (such as channel sinuosity) is difficult (Strebelle and Payrazyan 2002; Strebelle 2012).

Figure 5.4 (next page) – Examples of unconditional sequential indicator simulations based upon variable variogram attributes, generated in Schlumberger Petrel v.2016 software. A) A large range variogram yields large geobodies. B) A smaller range produces smaller geobodies. C) A large nugget, representing sub-model scale heterogeneity, shows non-discrete geobody boundaries, a common effect of gradational transitions between sedimentary bodies.

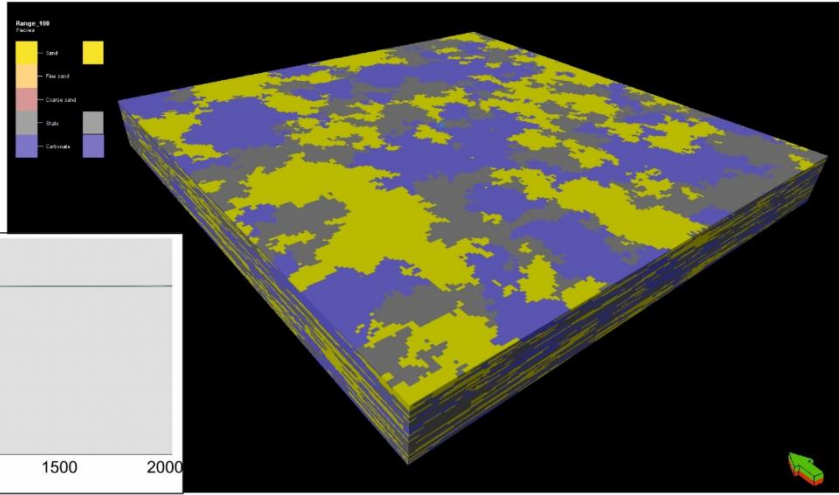
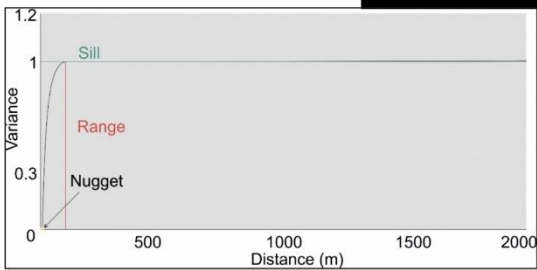
A

Semi-variogram with low nugget and range of 1000 m.



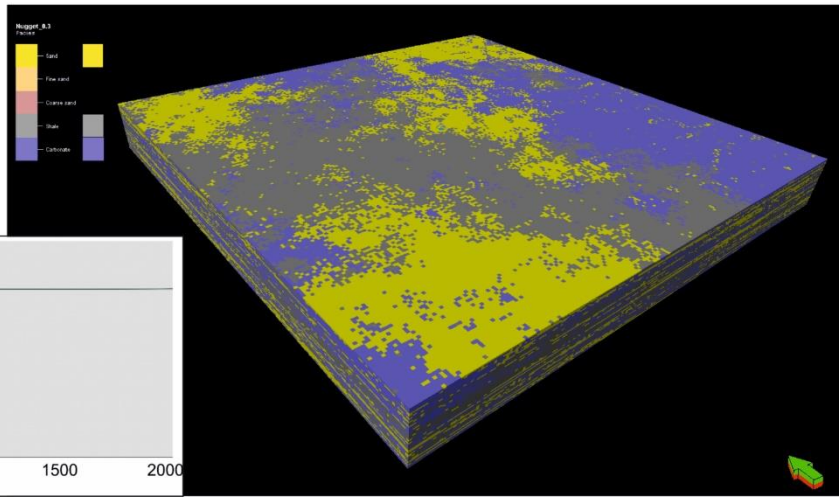
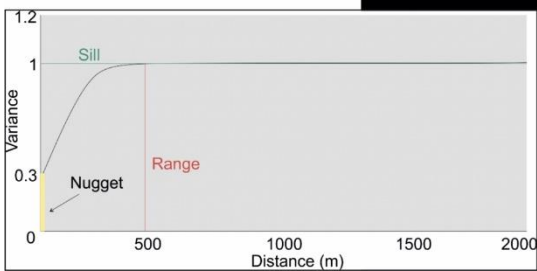
B

Semi-variogram with low nugget and range of 100 m.



C

Semi-variogram with high nugget and range of 500 m.



5.2.3 Multi-point statistics

Multi-point statistics (MPS) borrow conceptual reservoir data from training images (TIs) (Caers and Zhang, 2004, Strebelle and Levy, 2008; Le Coz *et al.*, 2011; Hu *et al.*, 2014). A TI is a three-dimensional or two-dimensional numerical concept or rendering of the heterogeneity within the reservoir (Figure 5.5). Training images (TIs) are created from either conceptual representations of the reservoir, object-based models, analogous data (outcrop or areal imagery) or from geophysical data. The type of TI and how a TI is created is a matter of the modeller's preference, scale and available data.

The MPS algorithm discussed below and used in this thesis is called the Single Normal Equation SIMulation (SNESIM) (Strebelle *et al.*, 2002). The SNESIM algorithm (Figure 5.5) searches for data events within the TI, data events are a representation of a geometrical configuration of attributes in cells surrounding the one being searched. This is then stored in a search tree, prior to simulation. Previous algorithms (Guardino and Srivastava 1993) searched TIs and populated the reservoir model iteratively taking up more computational time. The data events recorded in the TI are then translated into the reservoir volume, being simulated by starting with conditional data and populating a logical path away from the conditioned node, similar to the SIS.

MPS is difficult to develop effectively, three-dimensional TIs are difficult to produce from outcrop data alone. Communian (2012) used compound probability to project two-dimensional TIs across a three-dimensional space. This is done by calculating the probability for a given number of data events across the two-dimensional TI and projecting it through

the third dimension. This was successfully done by Pickel et al. (2015), where they projected two-and-a-half dimensional data into three.

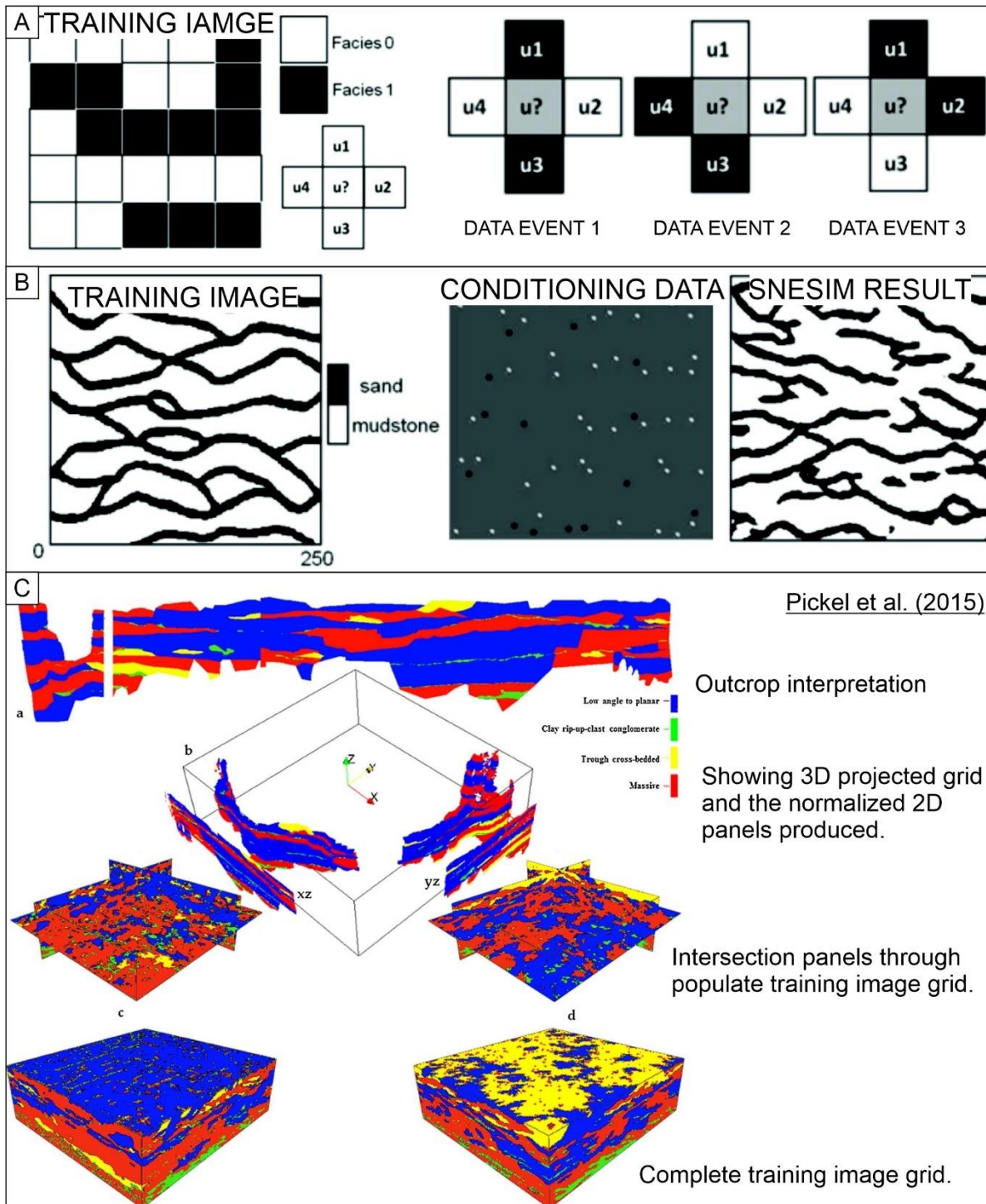
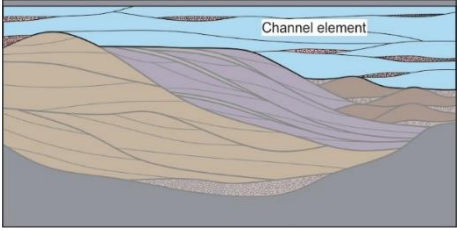
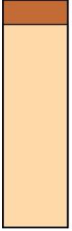
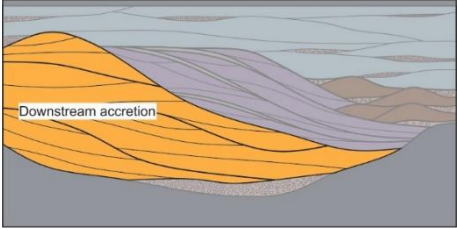
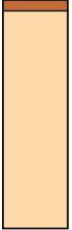
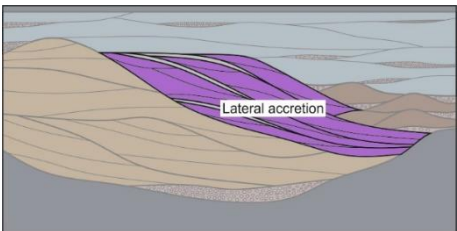
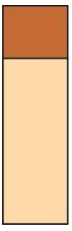
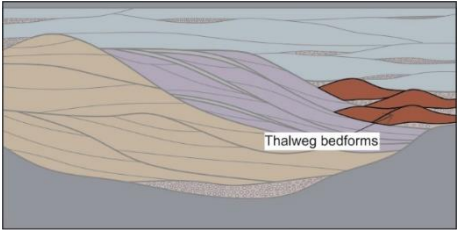
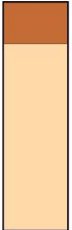


Figure 5.5 - Example of MPS SNESIM algorithm and what the search tree obtains A) Shows a simple block two-dimensional TI, with three types of data. B) A TI of channelised sandstones in a mudstone background facies used to borrow data events from. A simulation grid with conditioning data showing the predetermined facies at those give node locations. Finally, the output of the SNESIM algorithm. Where channel sands have been projected between conditioning node points (Modified from Strebelle and Cavelius 2013). C) The use of Communian (2012) method of probability projection, using z-axis coordinate based probabilities to project outcrops into three-dimensions. The lower four images show gridded models based upon differing probability weightings between the two outcrops.

5.3 Modelling elements

The elements used herein to constrain the heterogeneity of architecture in the Tuscher Canyon (Section 3.3) are those presented in Chapter 3 with one minor difference: the upstream accretion elements are considered genetic sub-units of the downstream accretion elements, based upon their similar grain-scale textural characteristics. In addition, a new element is defined here. These are thalweg bedform complexes. The thalweg bedform complex element (Figure 5.6, Table 5.1) has been characterised as non-net as it is extremely poorly sorted and contains pebble-grade material within its sandy matrix.

Table 5.1 – *Architectural element summary of the Lower Castlegate at Tuscher Canyon. The table describes each element individually by: their top, bottom and internal bounding surface framework according to Miall (1996), the idealised facies succession (in the order the facies are shown), the reservoir characteristics of the element and whether they are considered net or gross when modelled in this study, and finally an internal two-dimensional schematic architectural framework. Note, the scale of these schematics is 100 m horizontally by 10 m vertically, and no foreset laminae have been illustrated. Finally, a summary of the quantified statistical characteristics of each element: net-gross, palaeocurrent data and average width:thickness ratios are given.*

Element	Surfaces	Facies	Reservoir characterisation	Internal architecture of element	Net-Gross
Channel (CH)	Basal surface: 5 th order Top surface: 4 th order Internal surfaces: 3 rd order	Sh, St, Sp, Smv	Channel lag deposits provide vertical element scale permeability, only to be considered a horizontal flow conduit (North and Taylor, 1996; Eschard <i>et al.</i> , 1998; Puig <i>et al.</i> , 2019). This study: Non-net		 88%
Downstream accretion (DA)	Basal surface: 5 th order Top surface: 4 th order Internal surfaces: 1 st , 2 nd and 3 rd order	Sm, Sh, St, Sr	Extremely homogeneous, minor pebble lags but the majority of the element is uniform climbing bedforms comprising DA (Hornung and Ainger, 1999; Best <i>et al.</i> , 2003; Miall and Jones, 2003; Ghinassi and Ielpi, 2018). This study: Net		 96%
Lateral accretion (LA)	Basal surface: 5 th order Top surface: 4 th order Internal surfaces: 1 st , 2 nd and 3 rd order	Sm, Sh, St, Sp, Shv, Sr,	Inclined heterolithic strata of the element provide significant baffles to flow (Pranter <i>et al.</i> , 2007; Ghinassi <i>et al.</i> , 2014; Ielpi and Ghinassi 2014; Colombera <i>et al.</i> , 2017; Cabello <i>et al.</i> , 2018b). This study: Non-net		 75%
Thalweg bedform complex (TB)	Basal surface: 5 th order Top surface: 4 th order Internal surfaces: 1 st , 2 nd and 3 rd order	Sm, St, Sp, Sr	May be considered a baffle to flow relative to other elements, due to its immature make-up, basal lag deposits and the pebble lining of foresets. This study: Non-net		 81%

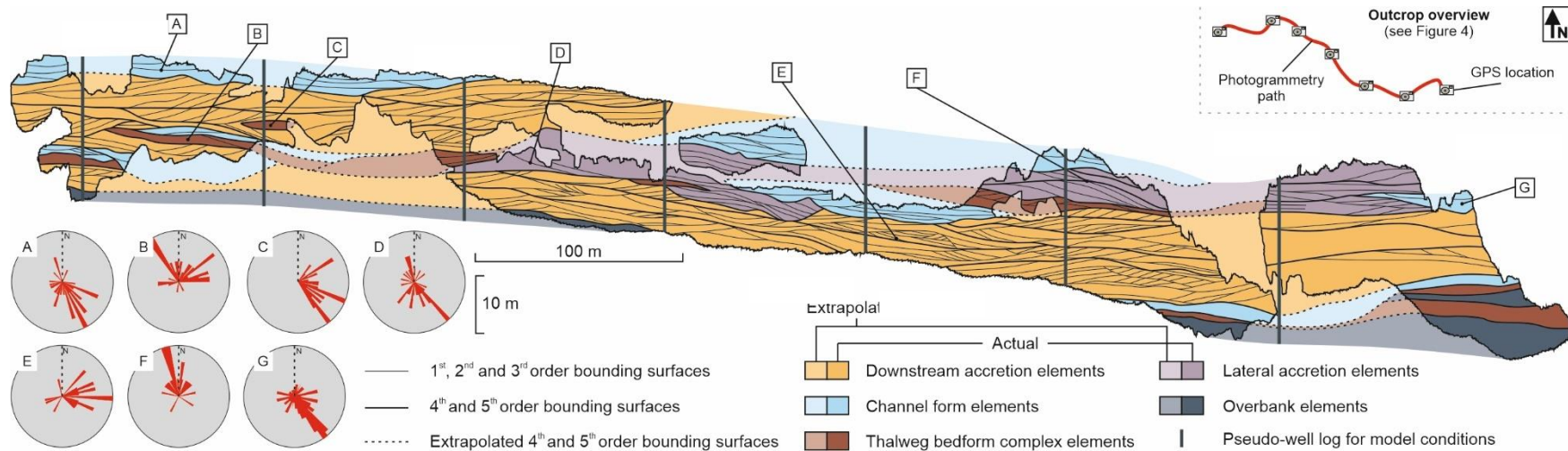


Figure 5.6 – Complete interpretation of the Lower Castlegate Tuscher Canyon outcrop, Utah, USA (see Figure 3.3D for location). Schematic shows the distribution of architectural elements and dominance of the downstream accretion element. Pseudo-well logs have also been incorporated to show positions of wells used to condition reservoir models. Measured palaeocurrent data (respective positions marked) of individual sedimentary architectural elements are also shown. Note the 2.5x vertical exaggeration. Detailed panel is available in Appendix C.

5.4 Methodology

The three-dimensional reservoir models used in this study were generated in Schlumberger™ Petrel v.2016 software. The top and base of the Lower Castlegate Sandstone from the Tuscher Canyon outcrop, Utah, USA, were picked as key digital stratigraphic surfaces and marker horizons (Section 3.3). These two horizons form the top and base of the modelling grid, which was modelled as a single zone. This forms a deterministic stratigraphic framework for the modelling grid (following common practice, see Enge *et al.*, (2007) and references therein), that is proportionally layered, and is extended beyond the dimensions of the Lower Castlegate outcrop to fit with the spatial extent of the modern Jamuna River data (see Pringle *et al.*, 2010 for specific methodology). The resultant reservoir model grid is 4,000 m x 3,000 m x 40 m, and contains 4.8 million cells, at a cell resolution of 10 m x 10 m x 0.5 m honour the input datasets (*c.f.* Enge *et al.*, 2007).

The three modelling techniques used in the development of the reservoir models for this study are: multi-point statistics (MPS), sequential-indicator simulation (SIS) and object-based modelling (OBM). In each model iteration was conditioned to six pseudo-well logs taken from the photogrammetric model interpretation of Tuscher Canyon, Utah, the positions of which are indicated in Figure 5.6 (Pringle *et al.*, 2010; Colombera *et al.*, 2016b; Cabello *et al.*, 2018b; Puig *et al.*, 2019). The pseudo-well logs lock the position of elements within the reservoir model volume and force the modelling algorithms to populate around the real data. Ten iterations of each modelling process were generated (Goovaerts, 1999; Falivene *et al.*, 2006),

so that a qualitative visual and quantitative statistical analysis of each model could be undertaken.

The MPS models were created using the depositionally conditioned three-dimensional training image. The TI was then incorporated into the model volume by aligning the centraloid cell of the TI to that of the MPS model. The TI was then subjected to a neural-network-type analysis, where each pixel away from the TI volume and centraloid cell was given a value (see Strebelle and Journel, 2001; Strebelle, 2002; Caers and Zhang, 2004; Strebelle and Levy, 2008; Daly and Caers, 2010), based upon the TI and the patterns and geometries it contains. The network continues to populate the modelled reservoir volume until the framework is populated by the MPS algorithm (Strebelle and Chevron, 2012).

To generate the SIS models, variograms for each of the architectural elements were generated. Variograms of the major (east-west) and minor (north-south) directions were generated from measured sections through the Jamuna River data (Section 5.6), and a variogram for the vertical dimension was generated from measured section through the Tusher Canyon data (Figure 5.6), following standard practice of Deutsch and Journel (1992), Kupfersberger and Deutsch (1999), Seifert and Jensen (1999, 2000), Martinius *et al.* (2017) and Mullins *et al.* (2019). The variograms are used, in conjunction with the element proportion statistics derived from the input datasets, to populate the SIS reservoir model.

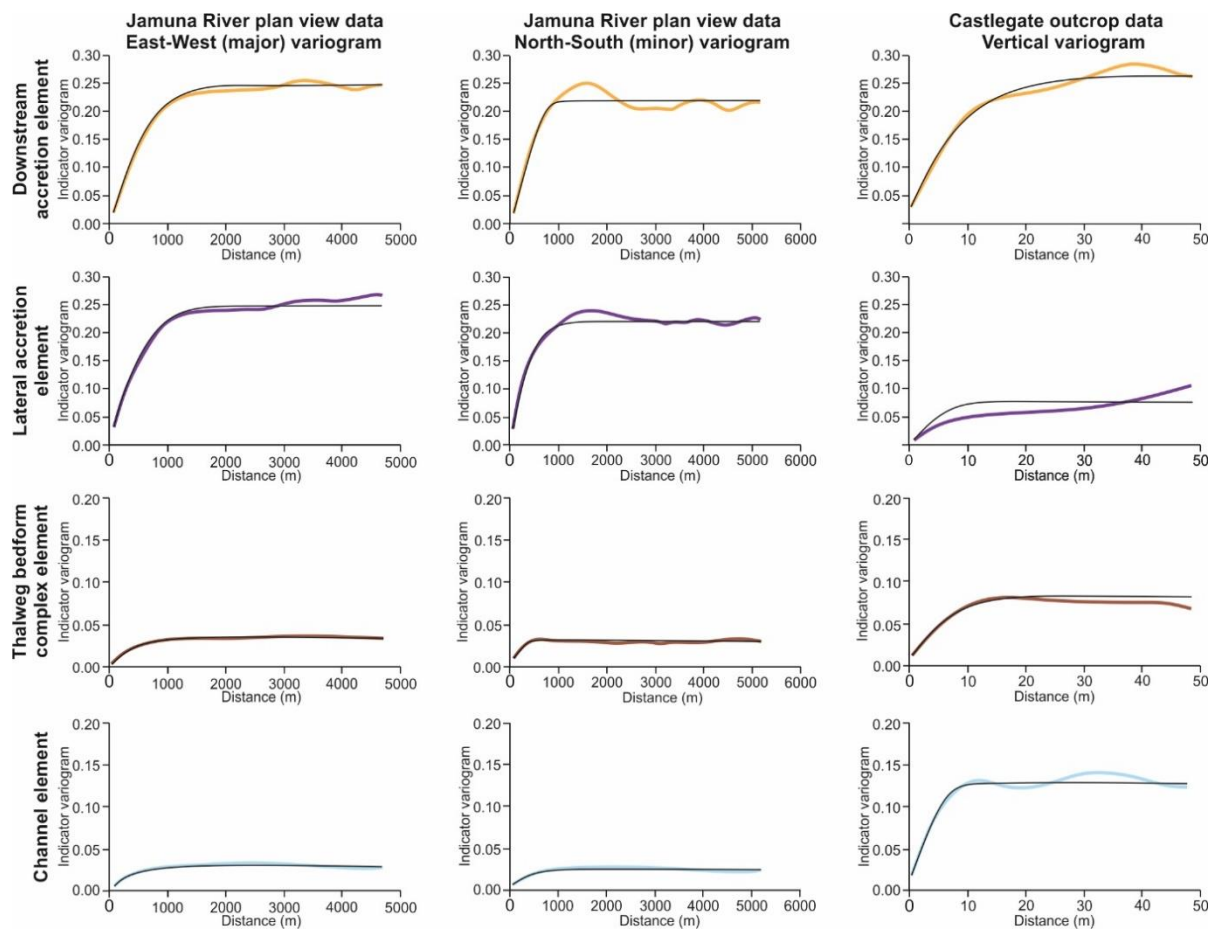


Figure 5.7 – Indicator variograms (coloured lines) showing the variance of the four architectural elements (DA = Downstream accretion element; CH = Channel element; LA = Lateral accretion element; TB = Thalweg bedform complex) across both data sets, providing input conditions for the SIS model iterations. Respective experimental variograms (black lines) are also shown, see text for details.

The OBM were generated using the downstream accretion element as the background facies, as this is the host barform of the channels. The channels were built using the geometric and dimensional statistics derived from the outcrop and modern data sets (Table 5.1 and 5.2), with the channel sinuosity derived from the Jamuna River modern plan-view data (Table 5.2). Lateral accretion elements were constructed as ellipsoid bodies that erode

into the downstream accretion elements, so as to maintain channel proportions. Thalweg bedform complex elements were modelled as small ellipses to erode into channel elements, and were trended to occur in the base and middle of the channel-fill elements, as they occur in the studied examples. These predefined shapes and relationships were modelled as a hierarchy within one-run (Holden, 1998; Seifert and Jensen, 2000; Vevle *et al.*, 2018), iteratively correcting to enable the elementary proportions (or global target fraction) to be maintained.

5.4.1 Model analysis tests

Qualitative analysis was conducted through visual comparison of each model iteration individually, and for each model algorithm, to test if the input parameters of depositional conditions imposed by the depositional environment had been met. Quantitative whole model analysis was also conducted by comparing dimensional characteristics of individual architectural elements for each model iteration. The results of these analyses were compared to the mean input data, with architectural element proportions also compared to their target fractions. Individual element thicknesses for each model iteration across the three algorithms were measured and compared to the dispersion in mean element thicknesses. Maximum element unit thicknesses were also compared to see how the model algorithms replicated the extreme cases of the element simulations, and whether they produced any anomalously thick element units that were unrealistic.

Finally, a single vertical well, penetrating the entire vertical extent of the model, was placed through the centraloid cell of all model iterations to provide a quantitative measure of static

net-connectivity (Falivene *et al.*, 2006). Static net-connectivity, also known as reservoir-to-well, is defined here as the volume of net-rock intersected and drainable by a single well (Laure and Hodavik, 2006, Hodavik and Larue, 2007). Quantitative measures of net-connectivity were supplemented by looking at the maximum, mean and variability in the thicknesses of net connectivity. This enabled, not only the proportion of interconnected net reservoir to be evaluated, but also the nature of the connections.

5.5 Two-dimensional training images

In this section the development and implementation of two-dimensional TIs is discussed. The use of two-dimensional TIs is common (Corbett *et al.* 2012; Strebelle and Chevron 2012; Zhou *et al.* 2018) as they are easily obtainable from outcrop and satellite imagery. However, this then requires the translation of two-dimensional data events into a three-dimensional space. This led to the development of sc2Dcd by Comunian *et al.* (2012). This algorithm takes an outcrop image and translates data events away, in space, from the TI. This projects the TI in three-dimensions, however, it also aggregates the probabilities of data events that may well be over represented in the two-dimensional parent TI.

The following section presents a similar methodology to sc2Dcd (Comunian *et al.* 2012), by using probability trends found within a two-dimensional TI, developed from the interpretation of Tuscher Canyon, Utah, USA (Figure 5.7). The section then looks at constructing multi-point statistics reservoir models, based upon the resultant two and a half-dimensional TI, and develops traditional sequential indicator variograms for the outcrop so that a comparison of purely geostatistical techniques can be conducted. Object-based

simulations are not constructed here, due to the lack of plan view control that is a consequence of using outcrop only.

5.5.1 MPS from a deterministic two-dimensional training image

The Tuscher Canyon outcrop and its interpretation (Figure 5.7) was incorporated into Petrel as a 1 m x 1000 m x 25 m simple grid at a cell resolution of 1 m x 10 m x 0.5 m, giving a 5000 cell grid. A numerical framework was digitally painted onto the grid, providing the TI (Figure 5.7).

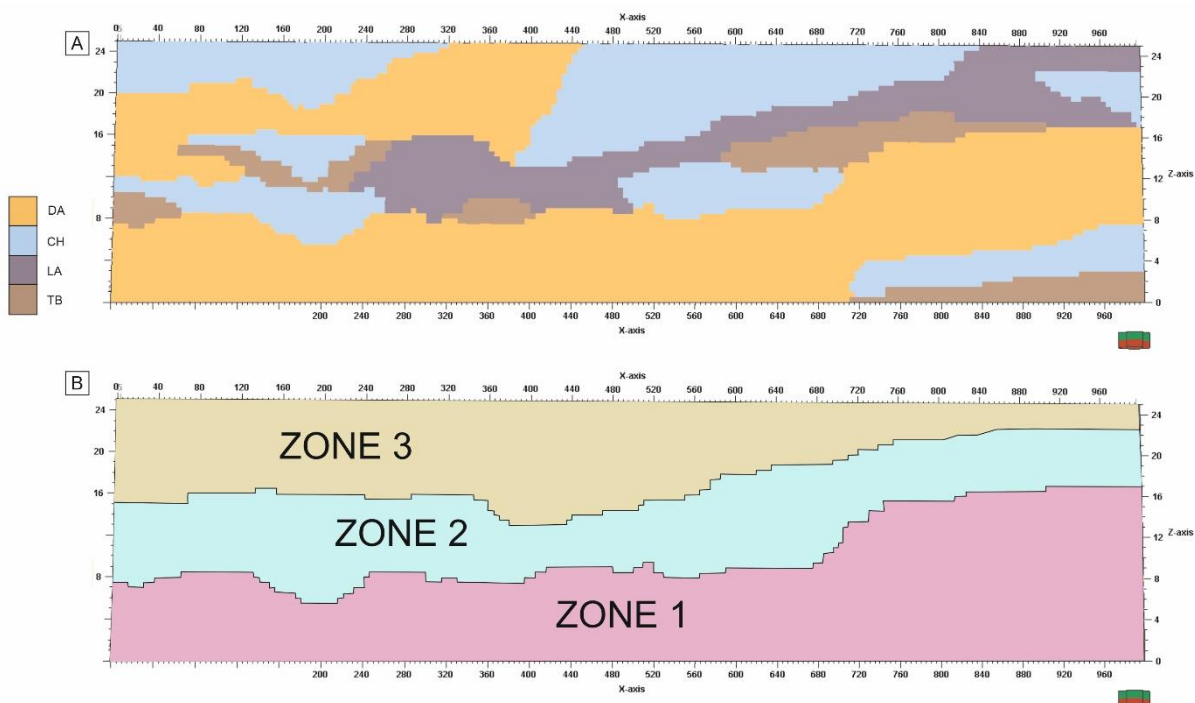


Figure 5.8 – Digitally painted two-dimensional TI of Tuscher Canyon, Utah, USA, for multi-point statistics simulations. This is a painted grid (using the 1 x 10 x 0.5 m cell size) of the interpreted Tuscher Canyon outcrop seen in Figure 5.6. Note, DA – downstream accretion, CH - channel element, LA – lateral accretion and TB – thalweg bedform complex.

A test of the resulting multi-point statistics algorithm, when applied to the two-dimensional TI, was conducted in a 1000 m x 1000 m x25 m cell grid model. This test was conducted without conditioning to see how the multi-point statistics would simulate three-dimensional geobodies from two-dimensional inputs. The resultant model is shown in Figure 5.9. From the model it is evident that there is a plan view problem with the multi-point statistics algorithm, simply stacking the two-dimensional TI laterally, gives a visual effect of a shuffled pack of cards. This affect is due to the lack of control in the projection of data events in three dimensions. The algorithm assumes that, because an axis of data is missing, the relationships of data events within the TI are purely two-dimensional. This is therefore unsuitable to translate into a larger grid for testing against sequential indicator simulation, as it would provide no statistical relevance in three-dimensions.

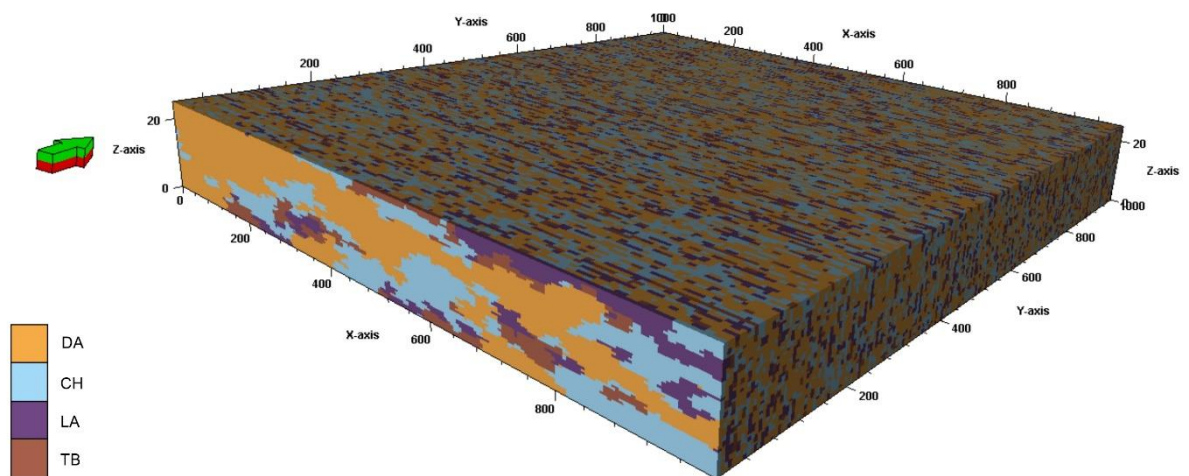


Figure 5.9 – Test product of two-dimensional TI used in the production of three-dimensional multi-point statistics generated in Schlumberger Petrel v.2016 software, see text for details.

5.5.2 *Generating two and a half-dimensional training images*

In an attempt to develop a third dimension for the simulation of geobodies using two-dimensional TIs, the probability trend for an element was then incorporated into the TI. This trend translates the probability of data events in the two-dimensional TI across another spatial axis within the model, following the procedure of Comunian et al. (2012). This enables a two and a half-dimensional TI to be created. First, the model grid was divided into three model zones, based upon facies abundance (Figure 5.10, 5.11 and 5.12). The next stage was to construct a surface based upon the proportion of a specific element within each zone (Figure 5.10, 5.11 and 5.12). This was done by inserting points along the TI, their position being dictated by the proportion of the element in the zone (z-axis) and the spatial positioning of the element (x-axis). This was done for all elements in all zones. The points were then projected through the y-axis by a simple “y+constant” function, projecting the points through the three-dimensional volume of the 1000 m x 1000 m x 25 m model grid. This creates a stationary distribution through the y-axis, enabling the points to be converted to a surface.

These distribution surfaces are then digitally smoothed, to remove any anomalous data (Figure 5.10, 5.11 and 5.12). The resulting surface attributes are then equalized to a percentage of the z-axis, equating to the probability of an elements occurrence at a given point in space. This probability is then put through a gaussian transform filter, so that the distribution of elements is truly stationary and weighted to their point in space and not their proportion comprising the total model volume (Comunian et al. 2012) (Figure 5.13). This is

done so that trends can be honoured when multi-point statistics models are generated. The target fraction, or proportion of elements, is taken directly from the TI, as in the two-dimensional model work flow.

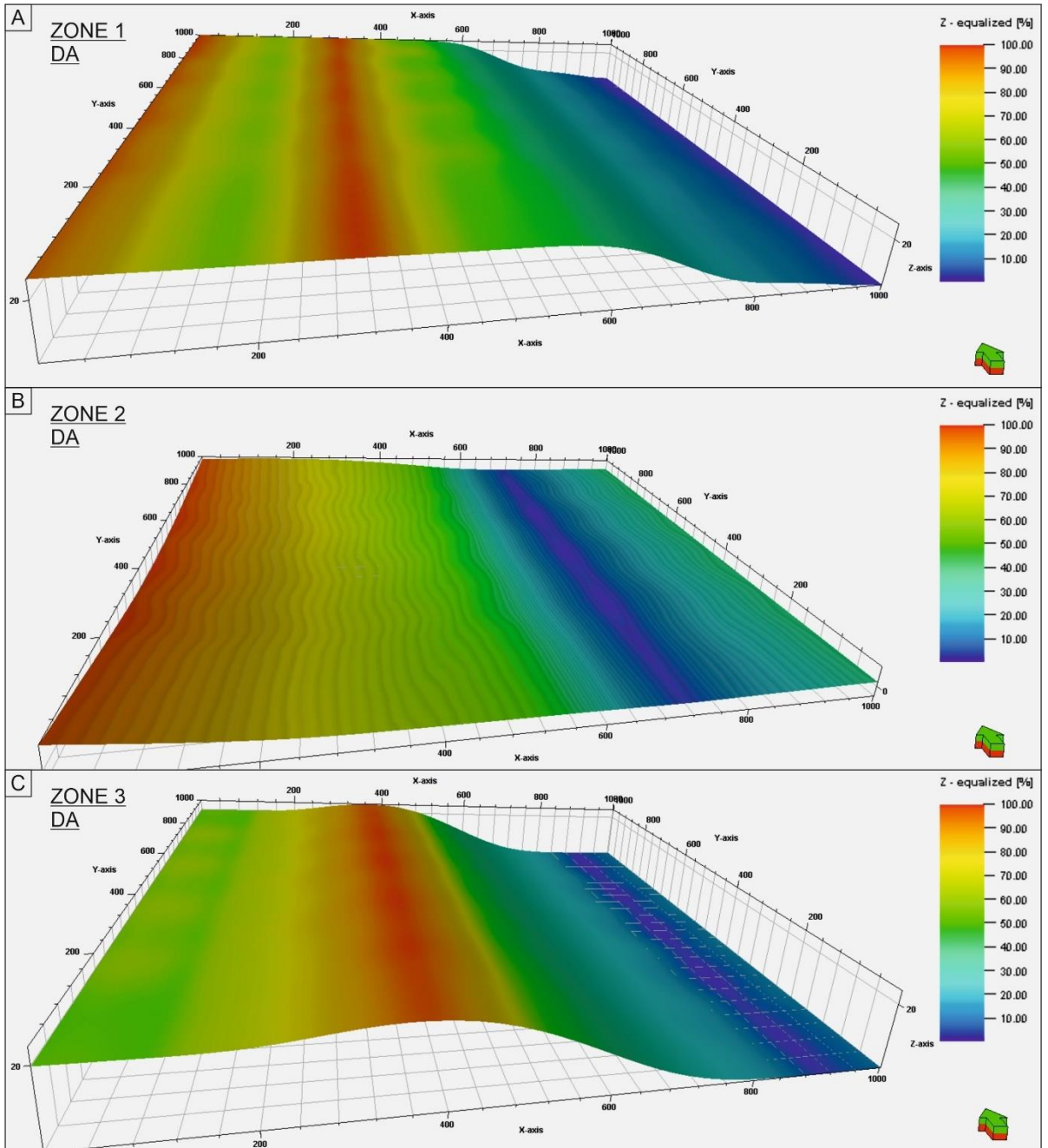


Figure 5.10 – Smoothed digital surfaces showing the relative proportions of the Downstream accretion element (DA) across the three model zones.

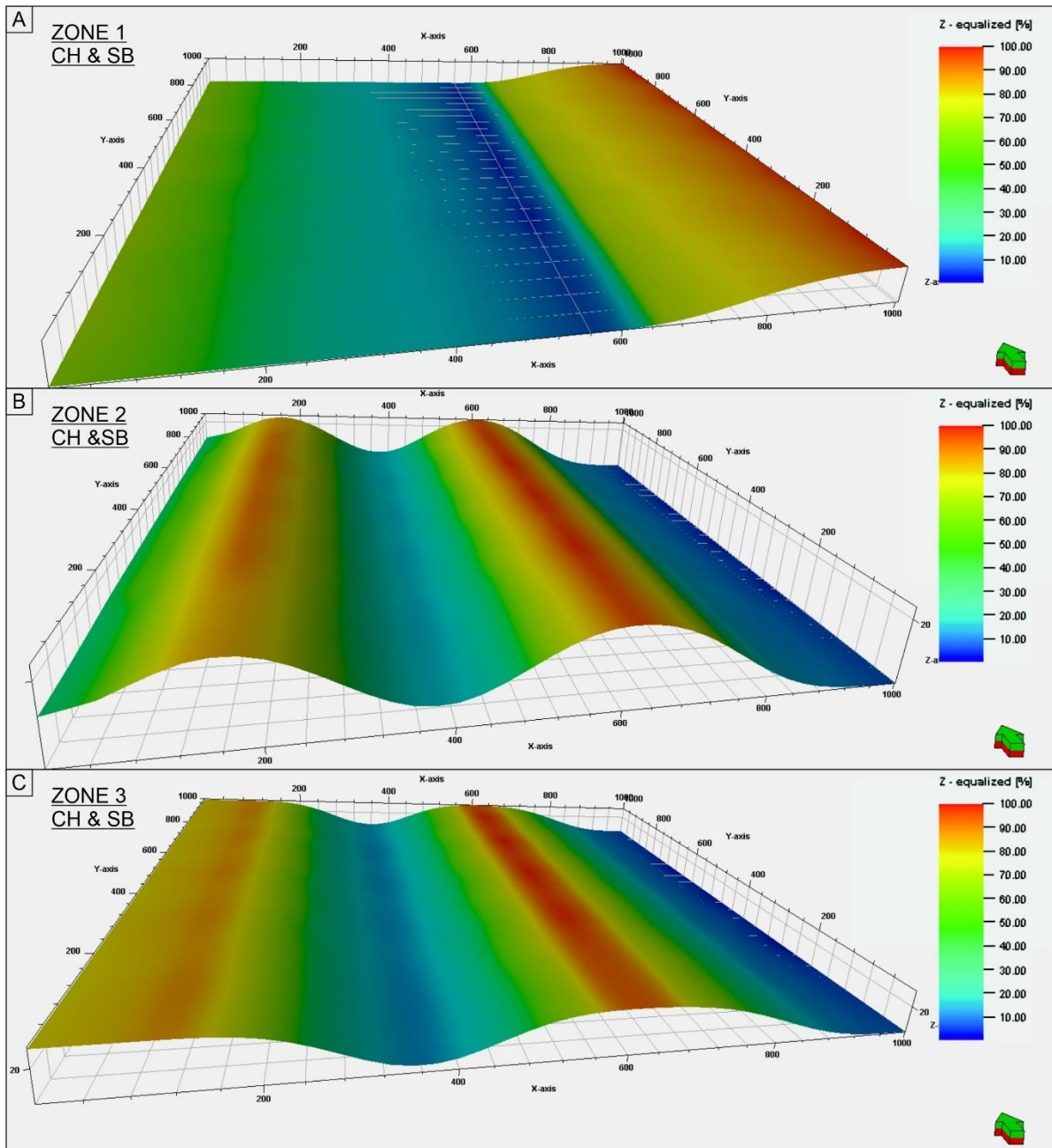


Figure 5.11 – Smoothed digital surfaces showing the relative proportions of channel element (CH) and thalweg bedform complex (TB) element across the three model zones.

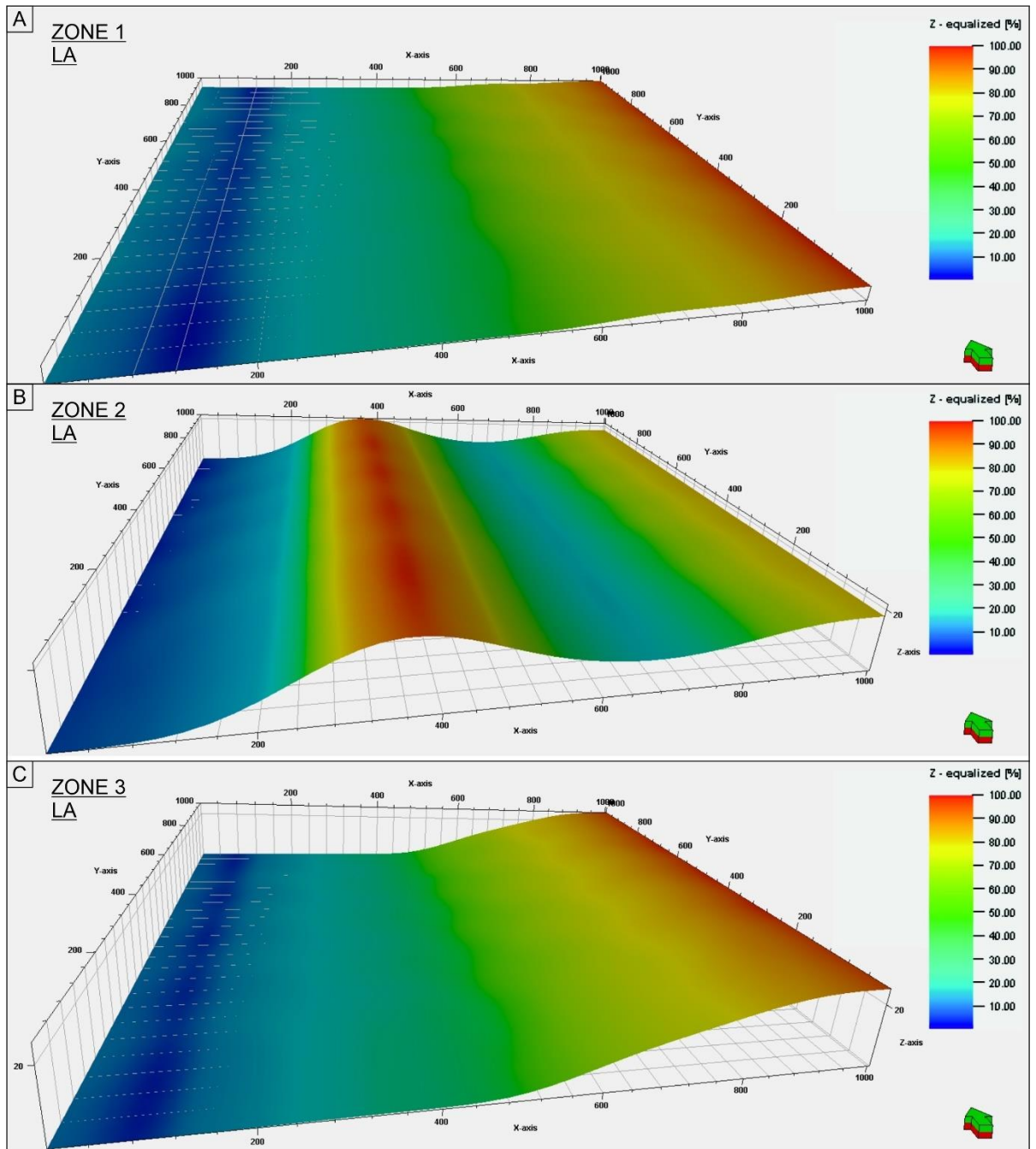


Figure 5.12 – Smoothed digital surfaces showing the relative proportions of lateral accretion (LA) element across the three model zones.

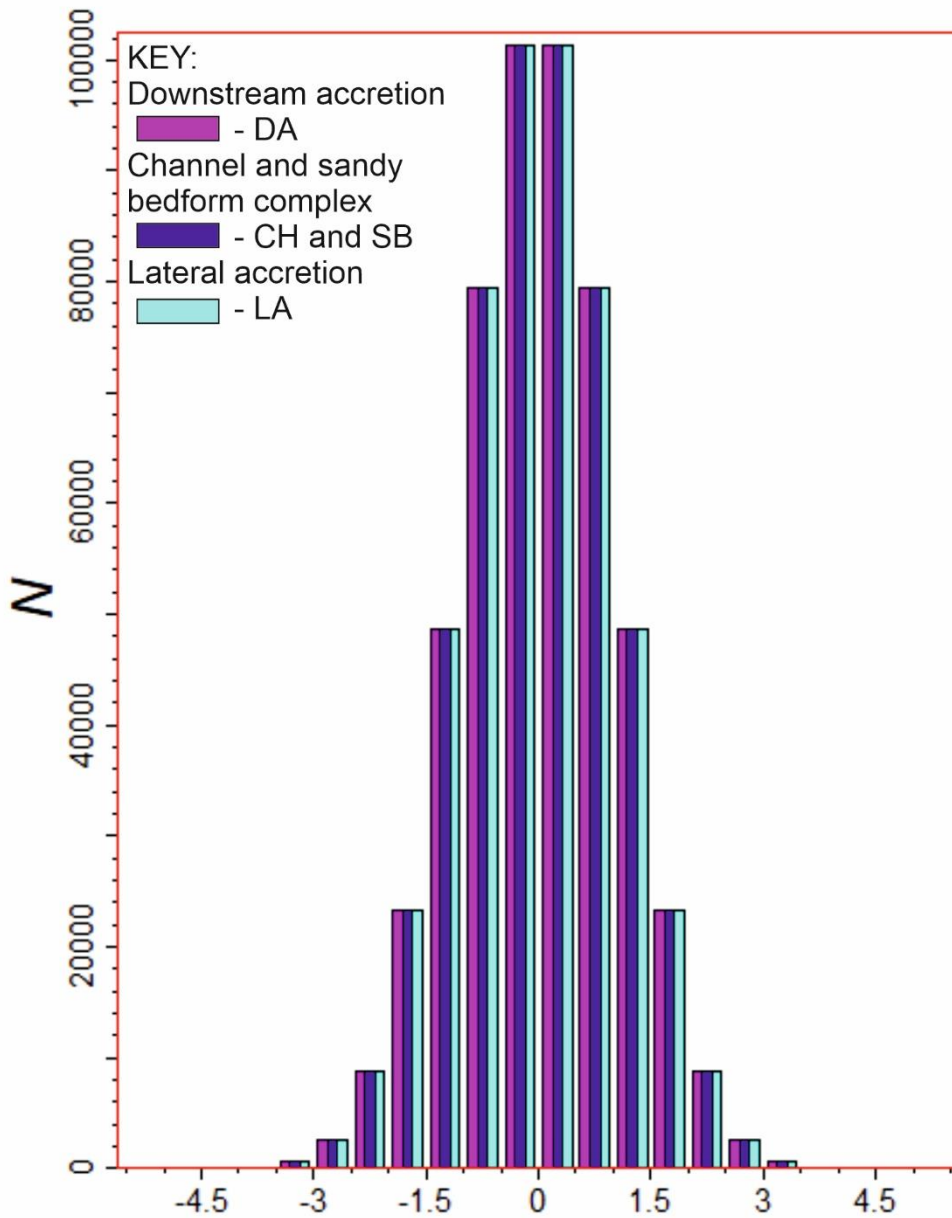


Figure 5.13 – Histogram showing the trend data for each modelled element (see key) across all model zones showing into a normal Gaussian distribution. The x-axis shows gaussian transformed values for the relative proportions of elements across the trended surface. The y-axis, N , is the frequency of those values. Notice the values are now in a stationary gaussian space enabling the use of kriging. The legend shows the elements plotted on the histogram.

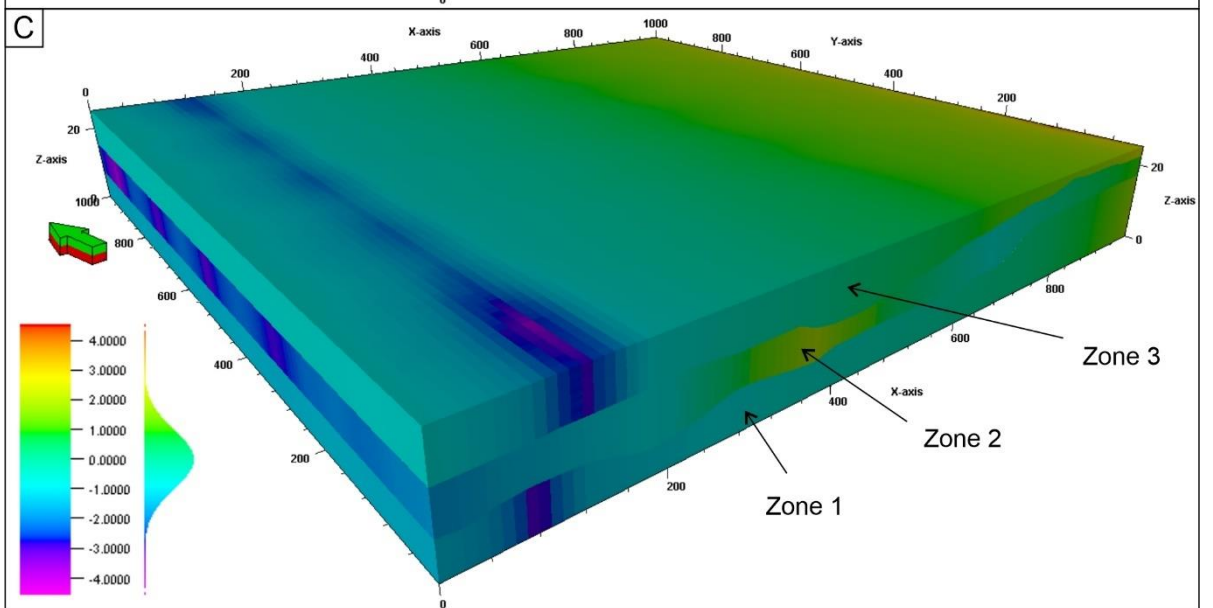
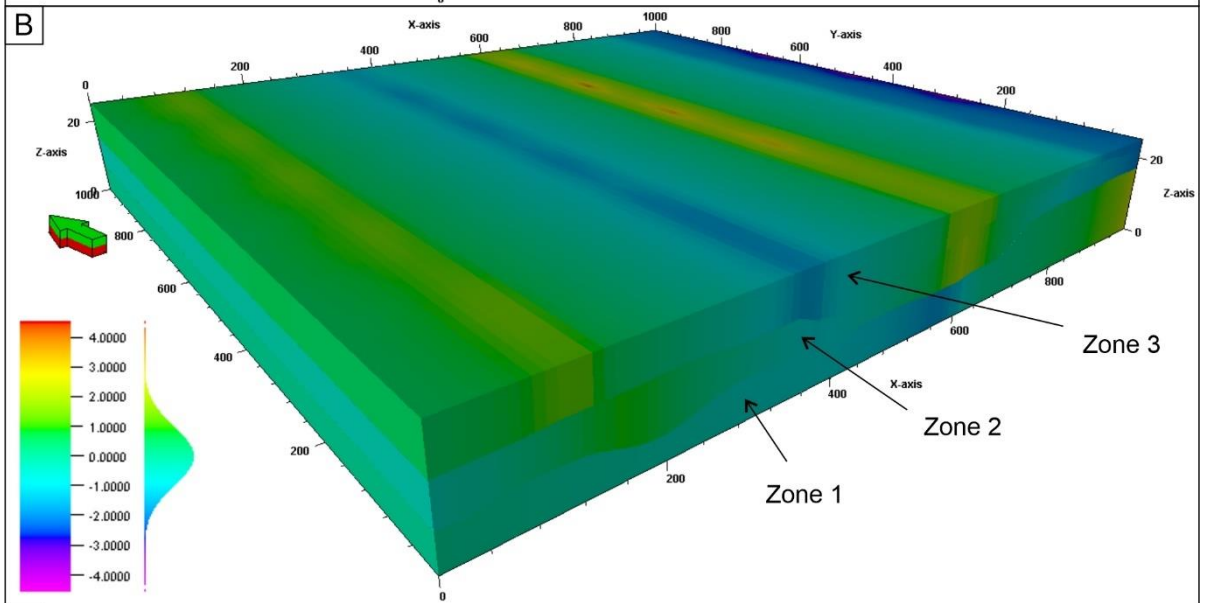
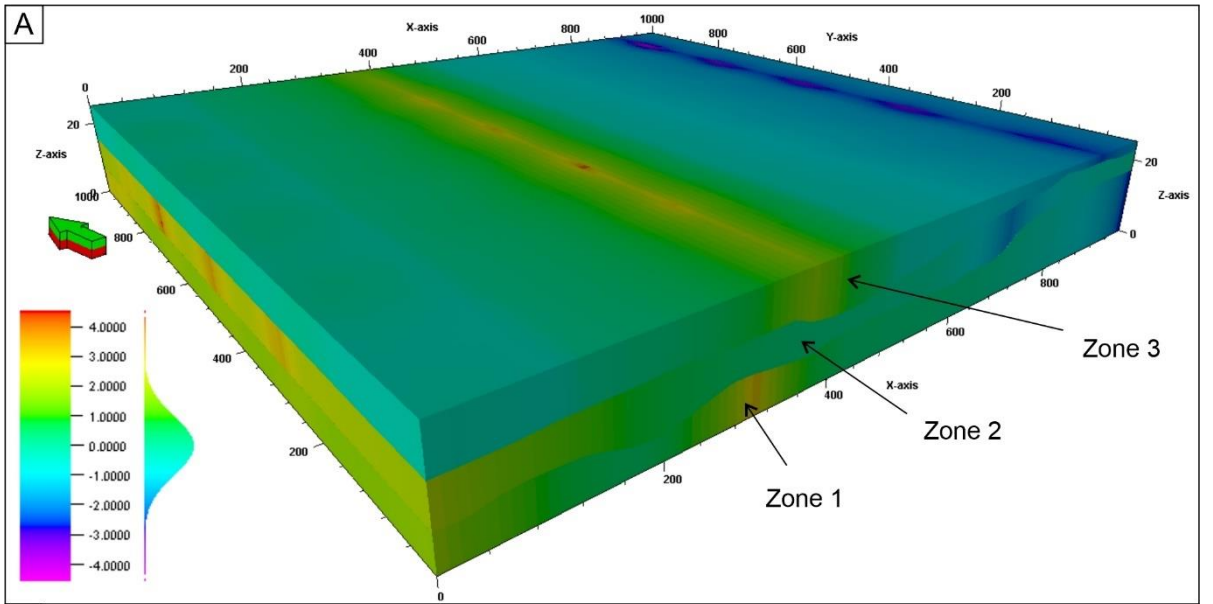


Figure 5.14 – Kriged trend models using the probability surfaces shown in figures 5.10, 5.11 and 5.12.

A) Trend across zones for DA element. B) Trends across zones for CH and TB. C) Trends across zones for LA.

Finally, the digital surfaces are converted into three-dimensional trend models by kriging. Each zone is trended independently so that the distribution of elements within that zone of the TI is honoured. The resulting trend model (Figure 5.13), is used as an additional constraint to the multi-point statistics algorithm, providing relative probability proportions for each element in each zone of the three-dimensional volume. This produces a two-and a half-dimensional TI (Figure 5.15).

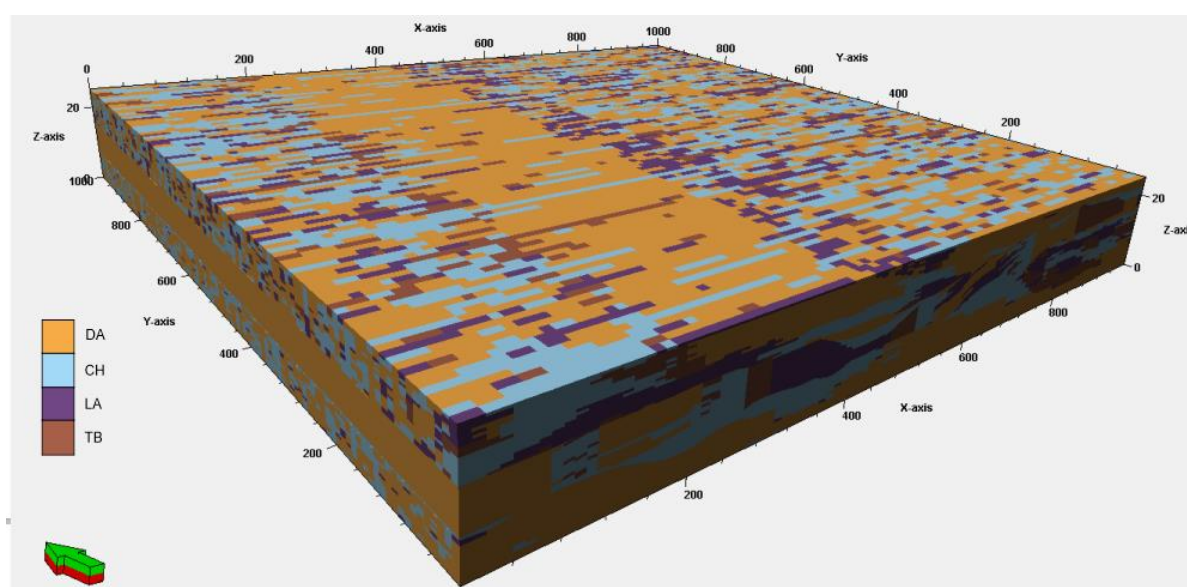


Figure 5.15 – Resulting multi-point statistics two and a half-dimensional TI developed from the original two-dimensional TI and the trended volumes shown in Figure 5.14.

The resulting TI begins to show some recognisable sedimentary barform element geometries in cross section and has some plan view extensive geometries and connections. This shows

that the TI is being some-what projected spatially, however, the TI affect seen before the inclusion of trends is still evident. This is seen as a methodological limitation, as the MPS is still reading data events from two-dimensions alone.

5.6 Two-dimensional conditioned reservoir models

The two and a half-dimensional TI was used to condition a three-dimensional reservoir volume. The TI was then incorporated into the model volume by aligning the centraloid cell of the TI to that of the MPS model. The TI was subjected to a neural-network-type analysis, where each pixel away from the TI volume and centraloid cell was given a value (see Strebelle and Journel, 2001; Strebelle, 2002; Caers and Zhang, 2004; Strebelle and Levy, 2008; Daly and Caers, 2010), based upon the TI and the patterns and geometries it contains. The network continues to populate the modelled reservoir volume until the framework is populated by the MPS algorithm (Strebelle and Chevron, 2012).

To generate the SIS models, variograms for each of the architectural elements were generated. Variograms of the major (east-west) and vertical dimensions were generated from measured sections through the Tusher Canyon data (Figure 5.6) (following the standard practice of Deutsch and Journel, 1992; Kupfersberger and Deutsch, 1999; Seifert and Jensen, 1999, 2000; Martinius *et al.*, 2017; Mullins *et al.*, 2019). The variograms are used, in conjunction with the element proportion statistics derived from the input datasets, to populate the SIS reservoir model.

A visual comparison of the two suites of model simulations show an extremely patchy texture to the MPS-generated models (Figure 5.15a). Limited channel connectivity, in both a lateral

and downstream sense, is coupled with lateral accretion elements that occur as a series of aligned cells 45° to strike. The downstream accretion elements within the model are small but do show some connectivity in cross section and plan-view. The location of the thalweg bedform complex elements are well placed and only occur within the channel elements. This is possibly the only data event well represented from the TI.

In contrast, the SIS simulated model (Figure 5.15b) shows good channel connectivity in the down dip and lateral directions. The channel elements bifurcate and shows some sinuosity (probably a chance representation considering the use of two-point statistics). However, lateral accretion and thalweg bedform complex elements form large (in both plan view and cross section) and unrealistic geometries. The downstream accretion element is extremely large in plan view and laterally extensive, probably beyond what is realistic of the Lower Castlegate system.

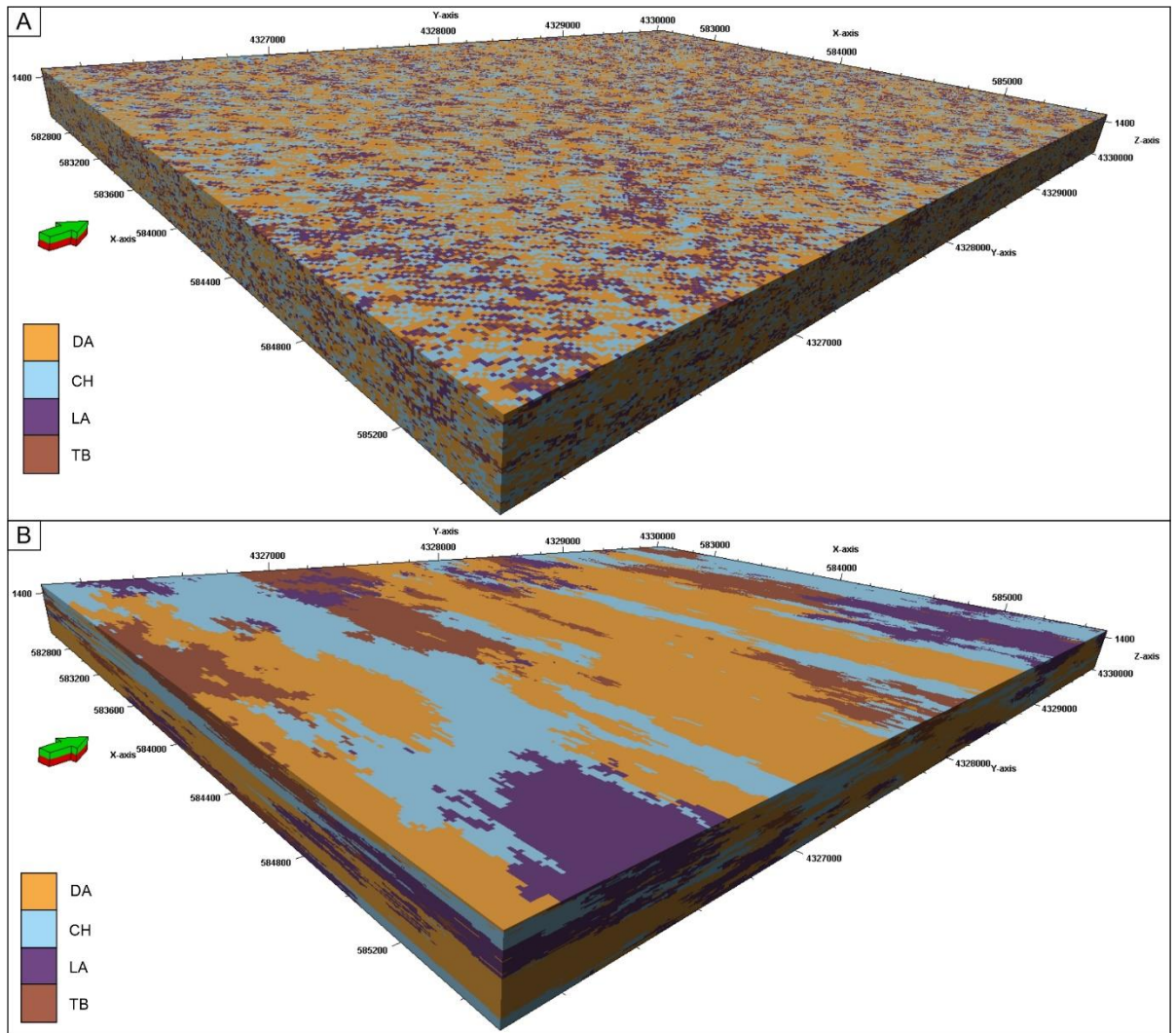


Figure 5.16 – A) MPS-generated, three-dimensional reservoir model developed from the two and a half-dimensional TI. B) SIS generated three-dimensional reservoir model developed from the variograms taken from Tuscher Canyon dataset, Utah, USA, generated in Schlumberger Petrel v.2016 software.

The two-dimensional MPS models gave a true reflection of the thalweg bedform complex proportions, but underestimated the downstream accretion elements by ~6% and overestimated channel elements by ~1%. The MPS algorithm estimated the mean thickness

of the elements to approximately 20% relative to the input data and reproduced more of the minimum element thicknesses (Figure 5.17; Table 5.3). The deviation away from the mean element thicknesses were well replicated. The lateral accretion elements showed a lower mean thickness (~1.0 m) across their reproduction in the MPS models. The maximum thicknesses of the elements produced within the model were mostly realistic and approximately replicated those seen within the input data, apart from the downstream accretion elements which are probably over estimated by about five metres.

The SIS models produced the largest amount of variance across the element thicknesses. SIS generated iterations reproduced the mean element proportions best for downstream accretion and lateral accretion elements. The mean and variability of the reproduced element thickness for the lateral accretion was closely related to that of the input data. However, it proved the least effective at replicating the mean thicknesses of the thalweg bedform complex and downstream and lateral accretion elements. The maximum thicknesses of all the elements were over represented, for example, the maximum thicknesses of the downstream accretion elements was 40 m (the entire modelled reservoir thickness), and over 20 m for the thalweg bedform complex.

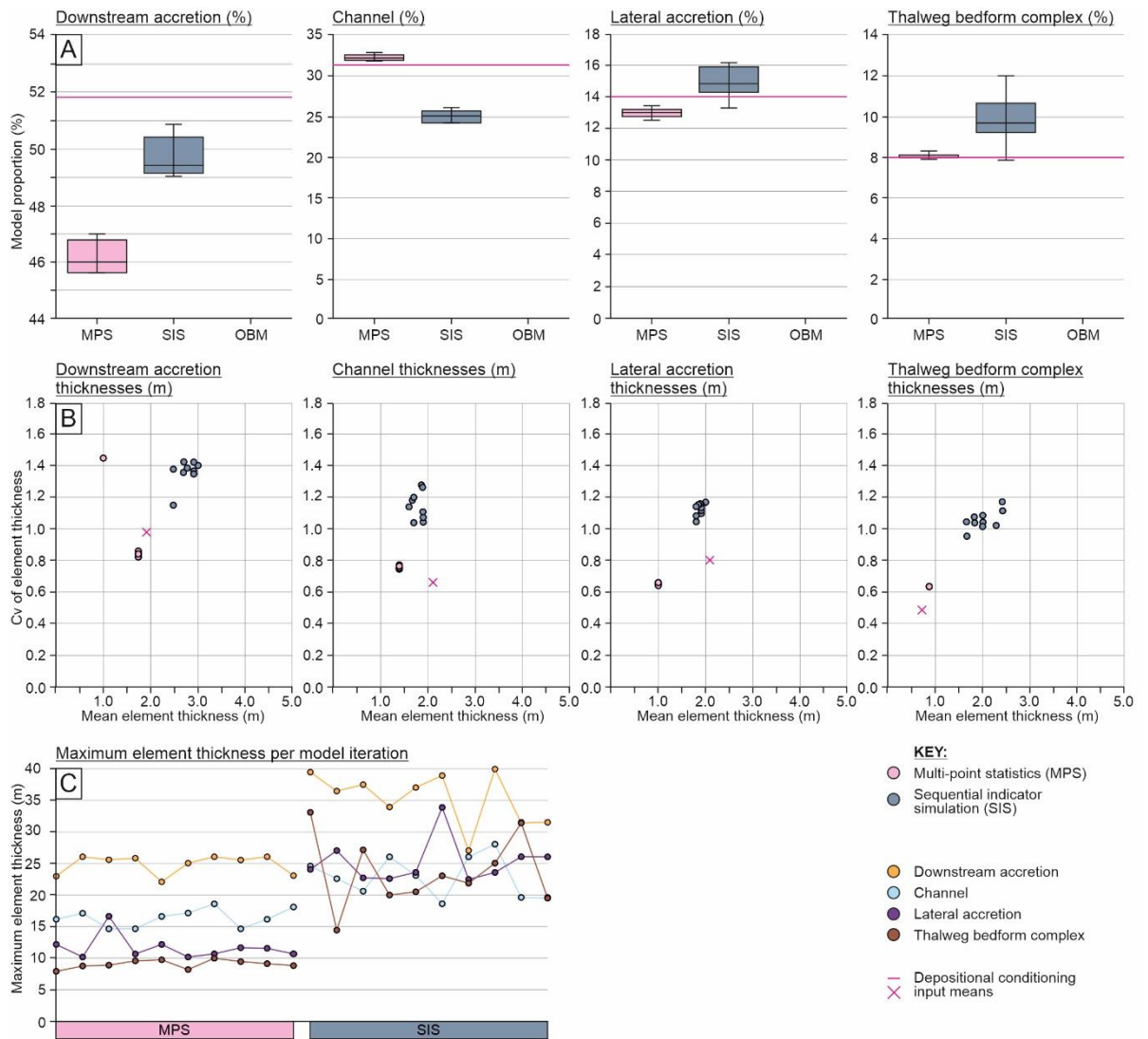


Figure 5.17 - Summary model statistics derived from the two-dimensional summaries of the reservoir models generated using each iteration of both algorithms. A) The relative proportions of each architectural element modelled within the reservoir model algorithms. The pink line highlights the model input data derived from the sedimentary analysis. B) Mean element thicknesses for each element plotted against the covariance (Cv) of each element, to highlight the thickness and dispersion in thickness across each element. C) Maximum element thickness plot for each model iteration in each algorithm to show how overestimations of vertical connectivity were affected by the choice of

algorithm. Note, the depositional conditioning input means are indicated on the graph showing where the input data and TI values plot.

Both algorithms produced differing static connectivity test results of net reservoir proportions that were drainable. The single production well was able to drain half of the SIS modelled volume (Figure 5.18), equivalent to a total drainable volume of $\sim 229,000,000 \text{ m}^3$ at $\sim 49\%$. However, MPS models returned 5% less drainable volumes across the model iterations, with the largest variance in the drainable volumes produced.

The SIS model produced a 48.63/49.14/50.72 (min/mean/max) percentage drainable volume with a standard deviation of 0.88. The MPS model iterations produced a 43.55/44.02/45.36 (min/mean/max) percentage drainable volume with a standard deviation of 1.12. This suggests that the range and standard deviation was much greater for the two- and a half-dimensional conditioned MPS models, when compared to those models generated by SIS. Consequently, the MPS realisations were far less effective in their reproduction of reproducible meso-scale heterogeneity within the reservoir volumes.

The vertical thickness of connected net was also measured to derive its vertical connectivity and the pathway thickness replicated within the models. The MPS generations produced a much smaller vertical connectivity (0.5 mean and ~ 26 maximum) when compared to the SIS generated ones. The SIS iterations generated vertical connectivity thicknesses equal to the entire reservoir thickness ($\sim 40 \text{ m}$), with large variability with approximately 5 to 6 m standard deviation. This is unrealistic when comparing to the maximum thicknesses within the input

data (Figure 5.7), which show vertical connections of net (downstream accretion elements) were no bigger than approximately 15 m.

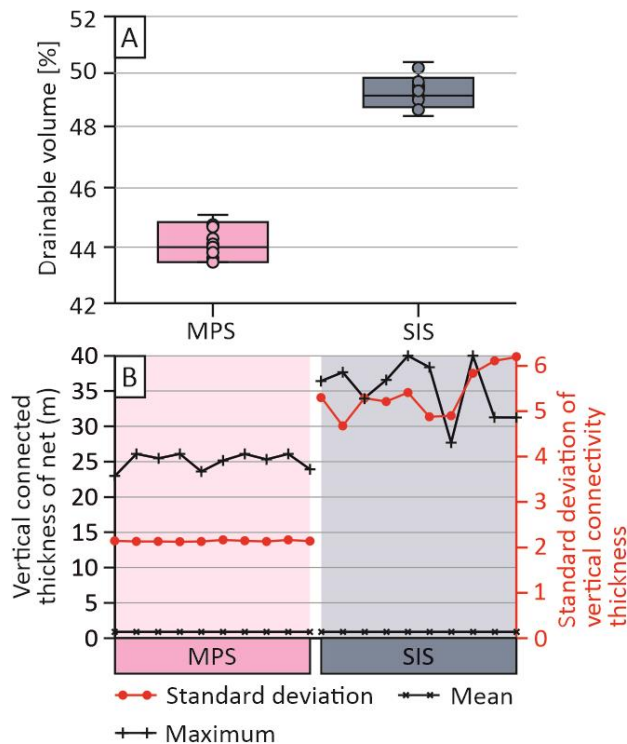


Figure 5.18 - Drainable volumes and vertical connectivity statistics from all thirty model iterations across the three algorithms of the generated reservoir models. A) Drainable percentage volume box-plots of the SIS- and MPS-generated models, showing the variance in results across the ten iterations of SIS-generated reservoir volumes and a narrow variance in MPS-generated iterations. B) Maximum, mean and standard deviation of the vertical thickness of net connectivity across all iterations of MPS- and SIS-generations.

5.7 Three-dimensional TI

In modelling fluvial strata studies, either outcrop or modern plan-view data are used to create TIs. This renders the input data reliable in two dimensions only and it has been shown

to be a major limitation of TIs that are applied to MPS models (Strebelle, 2002; Comunian *et al.*, 2012), as shown above. This section uses quantitative and qualitative data, derived from both ancient (the Lower Castlegate at Tuscher Canyon, Utah, USA) and the Jamuna River, India datasets, to condition a three-dimensional TI. The current study refers to this as depositional conditioning. Concepts of depositional conditioning have been suggested by previous workers using outcrop (Buckley *et al.*, 2006; Falivene *et al.*, 2006; Cabello *et al.*, 2018b; Puig *et al.*, 2019) or modern plan view data (Gershenzon *et al.*, 2015; Zhou *et al.*, 2018). The technique for the development of three dimensional depositively conditioned TIs presented here provides a more geologically realistic basis for reservoir model generation than working in two dimensions only.

5.7.1 *Depositional conditioning*

Depositional conditions fall under four categories; (1) the spatial distribution of types of architectural elements relative to others, (2) the dimensions of the elements; 3) the geometric shape of the elements and finally, (4) the relative proportion of elements within a total reservoir volume. These standard sedimentary inputs can be used to develop a simple set of conditional rules for the TI, derived from empirical patterns of deposition. The sedimentary characteristics used to develop depositional conditions can be derived for any representative elementary volume of sediment (Nordhal and Ringrose, 2008) at or above facies scale, making the approach extremely versatile. Consequently, the level of heterogeneity applied to a TI may depend upon the specific reservoir complexity, the abundance of data and interpretation, or reservoir type.

Recent studies combine multiple datasets to develop library-based approaches (e.g. the FAKTS database; Colombera *et al.*, 2012, 2013, 2016a) from which quantitative conditioning data can be extracted for the construction of sequential indicator simulation and object-based models. Such object based-models could be used for the development of three-dimensional TIs. These techniques draw upon large amounts of data to increase their statistical validity. However, in the absence of such databases, depositional conditions must be generated from more limited datasets. In this work, depositional conditions are derived from both an outcrop analogue dataset and a modern-day satellite image, to create a TI that realistically constrains meso-scale heterogeneity, in three dimensions. The use of standardised sedimentary inputs into TIs provides a step to a reproducible set of input parameters for TIs, a common problem creation of TIs (Tahmasebi, 2018).

5.7.2 *The Jamuna River, northern India*

The modern-day bar complex within the Jamuna River is situated between the border of Bangladesh and Bhutan, in northern India (Figure 5.19). The Jamuna River has been studied extensively as an analogue for dynamic, sandy bedload dominated low-sinuosity river systems (see, for example, Coleman, 1969; Bristow, 1993; Bristow *et al.*, 1999; Ashworth *et al.*, 2000; Best *et al.*, 2003). It transports material from the Himalaya down into the Bay of Bengal and feeds the Brahmaputra-Ganges river-deltaic system (Best *et al.*, 2007). The bar complex in the study area is dominantly downstream accreting and has subordinate channel flows, re-working the top of the barform and impeding soil formation and vegetation growth (Bristow, 1993; Ashworth *et al.*, 2000; Best *et al.*, 2003).

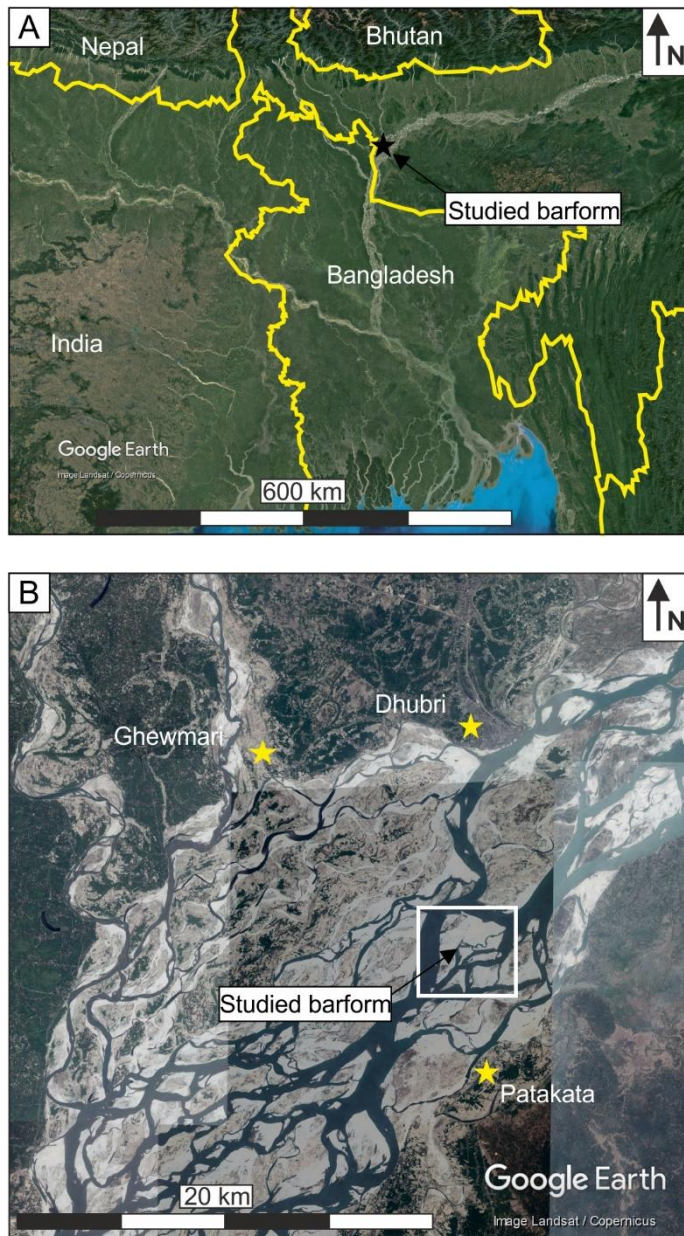


Figure 5.19 – A) Study site location map of the Jamuna River, northern India and B) close-up of the study area (box), modified from Mitten et al. (2018).

The satellite image of the Jamuna River was captured on 24/04/14 and was subsequently interpreted using the same bounding surface nomenclature as the Tuscher Canyon outcrops (Miall, 1985, 1996). The image was imported into ImageJ (v.1.51; Rasband, 2009) software

as a 32-bit image, where accurate measurements of sedimentary architecture could be made (Potere, 2008; Yu and Gong, 2012; Colombera *et al.*, 2012, 2013, 2016; Zhou and Wang, 2015; Gorelick *et al.*, 2017). Thirty-eight channel and barform widths, and twenty-seven barform lengths were measured from the 8 km² downstream accreting bar complex. Width:length element ratios were calculated. Finally, the image was put into the equal surface area measurement tool within ImageJ (Rasband, 2009; Grove and Jerram, 2011) to analyse sedimentary architecture proportions.

The studied section of the analysed Jamuna River, northern India, shows a large downstream accreting barform complex; with sub-ordinate channel forms migrating along the bar top (Figure 8). The downstream accreting bar complex is ~4,300 m in length and ~3,330 m wide.

Within the studied barform, channel elements are bar-top modification channels, eroding into the larger downstream-accreting element complex. The proportion of these subordinate channels is 35.6% of the totally imaged area. The channels have two distinct groupings of their widths which were ~290 m and ~110 m (mean values), dependent on the degree of bifurcation.

The downstream accretion elements dominate the majority of the surface area at 57%. They are confined within major channel margin erosion surfaces (fourth and fifth-order bounding surfaces; Figure 5.20) and are eroded by subordinate channel forms (Figure 5.20). The barforms show a wide range of sizes, but have a consistent width:length ratio of 1:1.3. Thalweg barform complexes are poorly imaged by satellite data, due to them being rarely emergent bedform complexes. These elements are confined within channel forms and

appear structureless in character, with a width:length ratio of 1.3:3.1 with a maximum length of 400 m (Figure 5.20).

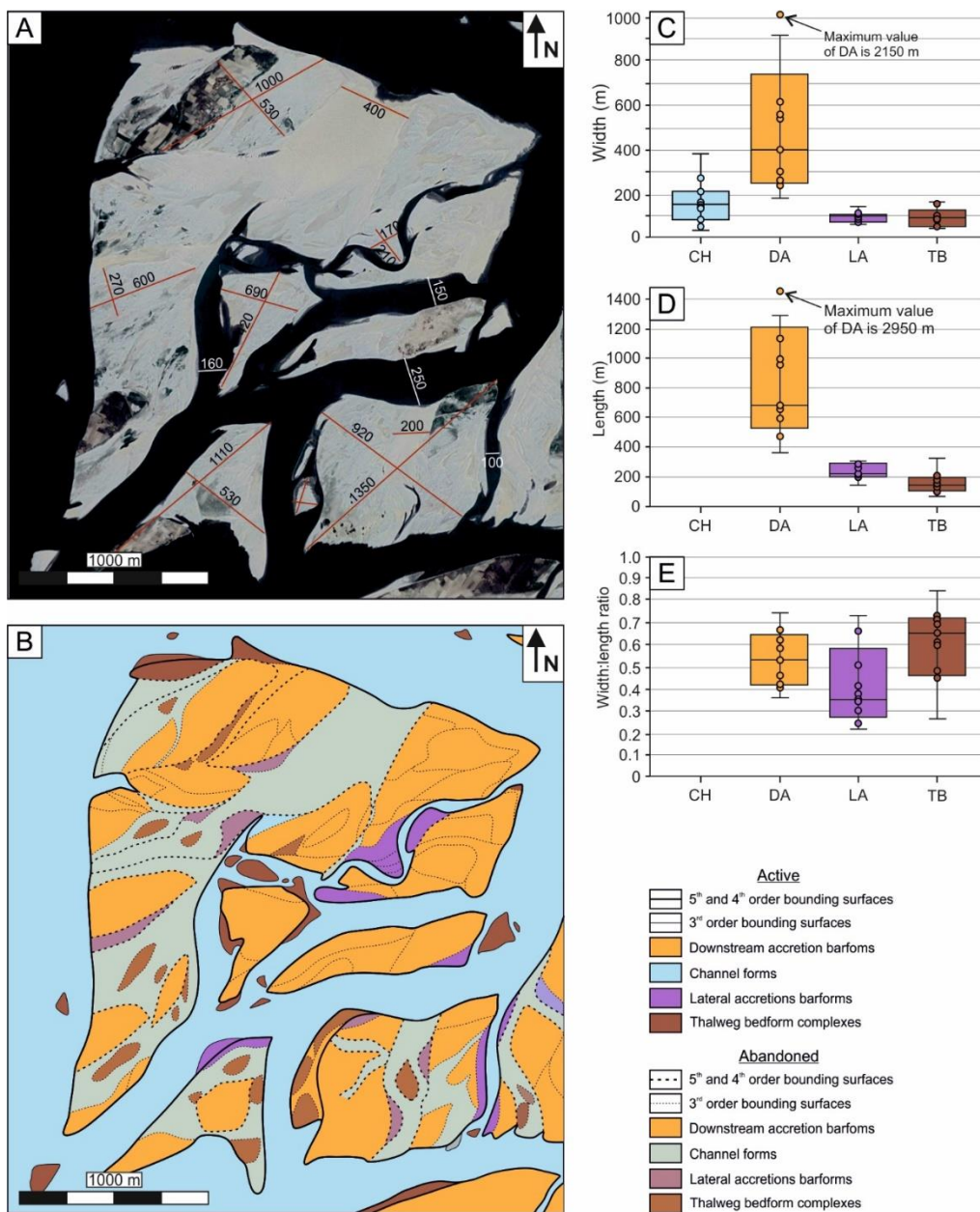


Figure 5.20 – A) The Jamuna downstream accreting barform in northern India (see Figure 3 for location), annotated with width and length measurements of active and abandoned fluvial sedimentary architectures. B) Interpretive line drawing (see key and text) – note colours are the same

as for the Tuscher Canyon outcrop (Figure 5.6). C) Box plots of the width, D) length and E) width:length ratio of sedimentary architectural elements within the interpreted Jamuna River barform complex (CH = Channel element, TB = Thalweg bedform complex, DA = Downstream accretion element, LA = Lateral accretion element). Note the maximum measurements of the downstream accretion element exceeds the scope of the graph.

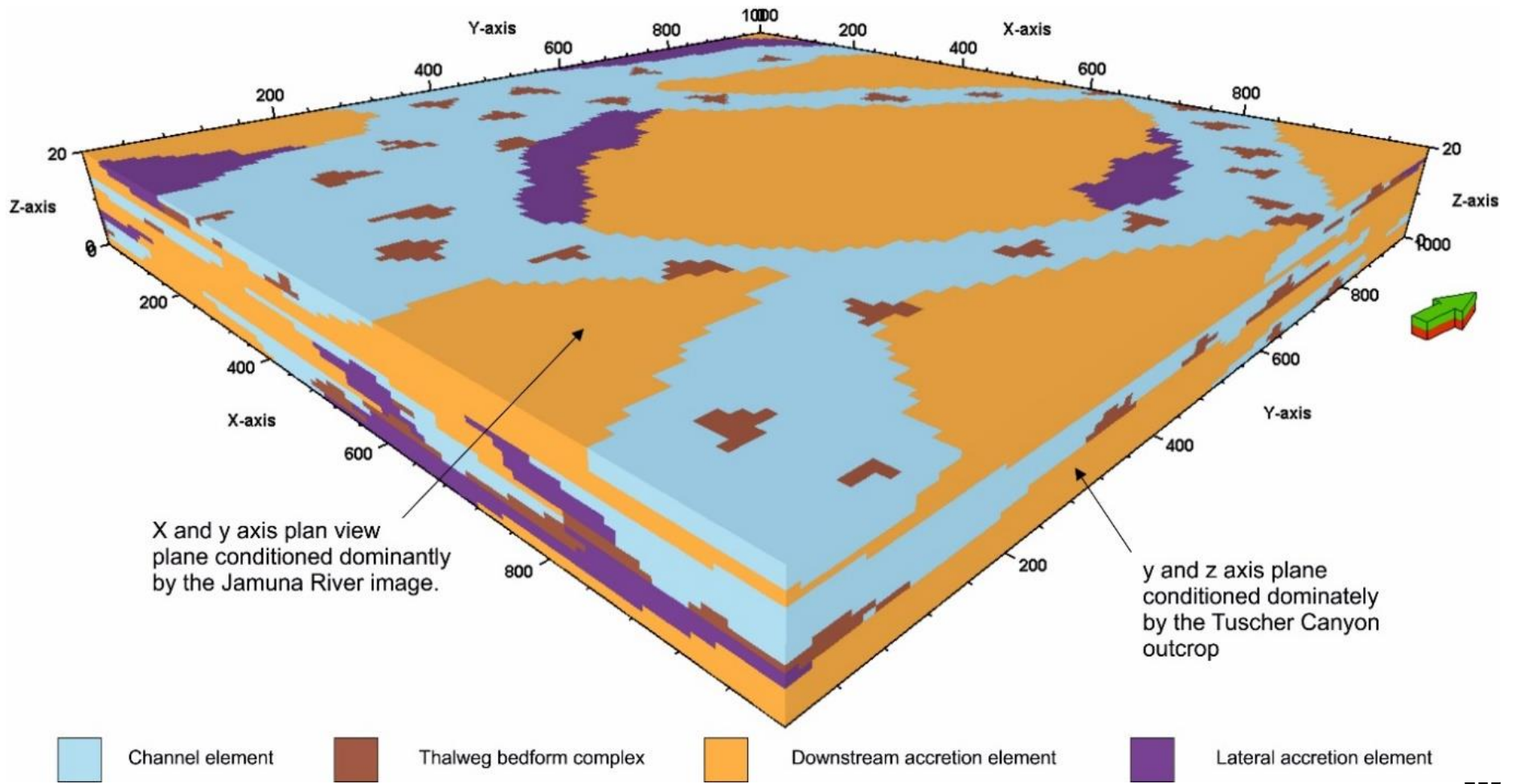
Lateral accretion elements represent a low proportion of the bedforms in the image, these are not large point bars but lateral accretion deposits associated with the sinuosity of bar-top modification channels. The architectures are confined within a channel margin (fifth-order) bounding surface and are usually located on the margins of a channel. Typically, the element has a width:length ratio of 1:2 and has a lower surface area proportion compared to what is preserved within the Tuscher Canyon section. This may be due to higher than usual preservation potential, due to the lateral migration during deposition of the element, or the imaged bar-top channels are not as sinuous as those preserving lateral accretion within the Castlegate outcrops.

5.7.3 Constructing a three-dimensional TI

The TI, presented here, is produced in a simple three-dimensional grid generated in Schlumberger™ Petrel v.2016 software, using the top and base of the Tuscher Outcrop as deterministic surfaces (Enge *et al.*, 2007). The simple grid is a single zone, 1,000 m x 1,000 m x 20 m, with a cell resolution of 10 m x 10 m x 0.5 m. The TI was manually filled by digitally painting the simple grid with the proportions, geometries, dimensions and juxtaposition of elements highlighted in the quantitative three-dimensional geological concept model (Figure

5.20) that used the depositional conditions (Table 5.2) extracted from the outcrop and modern study. The Castlegate outcrop at Tuscher Canyon provides constraints for the cross-sectional plane (parallel to flow; Figure 5.20) as this is the orientation of the studied section. The plan view (Figure 5.20) is constrained by the modern day Jamuna River data (Howell *et al.*, 2014). The target fractions (elementary proportions), element dimensions and geometries were monitored during the painting of the three-dimensional volume to ensure input data were matched. Corrections were made iteratively to the TI until the manually filled simple grid honoured the input parameters (or depositional conditions) developed from the input datasets.

Figure 5.21 – Numerical depositionally-conditioned 3D TI used in this study, created within Schlumberger™ Petrel v.2016 software, using the input parameters given in Table 5.2. The TI is 1,000 m x 1,000 m x 20 m at a cell resolution of 10 m x 10 m x 0.5 m. The datasets providing the major conditions for the planes are marked. The image provides the basis for the MPS model generation (see text).



Channel elements are conditioned to be cross- and down-cutting into the underlying downstream accretion element. They have widths between 90 m to 400 m, they are 1 m to 8 m thick, and they have a lensoidal cross-sectional geometry but ribbon plan-view geometry (Figure 5.21). The element occupies 26 % of the total model volume. Thalweg bedform complex elements must be confined within channel elements. They have lengths of 50 m to 400 m, widths of 50 m to 300 m and depths of 1 m to 3 m. Thalweg bedform complex elements occupy 8 % of the total model volume and have lensoidal geometries (Table 5.2). Due to thalweg bedform complexes being poorly imaged by satellite, respective element proportions are weighted against those exposed at the Tuscher Canyon outcrop, where they are preserved and visible. Lateral accretion elements must be located at the margins of channel elements and downstream accretion elements. They have lengths of 150 m to 800 m, widths of 75 m to 800 m and depths of 1 m to 5 m, with lensoidal plan views and tabular cross-sectional geometries (Table 5.1). The element has its volumetric percentage weighted against the preserved Tuscher Canyon outcrop to account for preservation. The lateral accretion architecture must cover 14% of the total modelled volume. Lateral accretion, as well as channel and thalweg bedform complex, should be considered as strata that contain baffles to fluid flow, thus considered as non-net reservoir.

Downstream accretion elements are the only elements in this model considered net, due to them being relatively homogenous (Best *et al.*, 2003; Miall, 2003; Ghinassi and Ielpi, 2018). They have lengths of 400 m to 2000 m, widths of 200 m to 2000 m and depths of 4 m to 12 m. The downstream accretion element should populate 52 % of the total model volume

(Table 5.2), and be distributed within CH elements as kite-like shapes in plan view and lensoidal geometries in cross section.

Table 5.2 – Depositional conditions of mega-bar complexes for the TI construction. This details the main sedimentary architectural elements and their respective conditional requirements: distribution, dimensions, geometry, and proportions. * indicates values weighted to the data from the Tuscher Canyon outcrop due to imaging issues in the satellite images, see text for details. Note, channel sinuosity values are included, obtained from the Jamuna River satellite imagery data.

Architectural element	(1) Distributions	(2) Dimensions	(3) Prop.	(4) Geometry	
Channel Fill (CH)	Subordinate elements cross cut DA.	length	N/A	26 %	Plan: Ribbon Cross-section: Lensoidal
		width	Min: 90 m Max: 400 m		
		depth	Min: 1 m Max: 8 m		
		Sinuosity amplitude	Min: 50 m Max: 575 m		
		Sinuosity wavelength	Min: 370 m Max: 3400 m		
Thalweg barform complex (TB)	TB must be confined within CH.	length	Min: 50 m Max: 400 m	8* %	Plan: Irregular asymmetric lens Cross-section: Lensoidal
		width	Min: 50 m Max: 300 m		
		depth	Min: 1 m Max: 3 m		
Lateral Accretion (LA)	LA must be located at the CH/DA boundary.	length	Min: 150 m Max: 800 m	14* %	Plan: Lensoidal Cross-section: Tabular
		width	Min: 75 m Max: 800 m		
		depth	Min: 1 m Max: 5 m		
Downstream accretion (DA)	DA must be contained within CH on a large scale.	length	Min: 400 m Max: 2000 m	52%	Plan: Irregular kite Cross-section: Lensoidal
		width	Min: 200 m Max: 2000 m		
		depth	Min: 4 m Max: 12 m		

5.8 Three-dimensional conditioned reservoir model

In this section the comparison of conventional reservoir modelling techniques is discussed and the qualitative and quantitative results of the reservoir models generated are shown.

5.8.1 *Object-based models of the Lower Castlegate*

The OBMs produced channels that showed distinct concave-up geometries and amalgamations brought on by avulsion events. The thalweg bedform complexes were replicated to be only within the channel elements, and were mostly located in the middle to basal portions of the channel elements (Figure 5.22). The lateral accretion elements formed ellipse plan-view geometries and were adjacent to channel elements in the majority of cases. Downstream accretion elements have over-represented thickness and showed no discernible geometry as they have been modelled as background sedimentation.

OBMs accurately reproduced the elementary proportions, and produced the lowest degree of variance in the element proportions between each model iteration. The OBMs overrepresented the mean thickness of downstream accretion elements and thalweg bedform complexes (by 4.1 m and 1.6 m respectively). The variance replicated in the thicknesses of channel element ($C_v = 0.8$) and downstream accretion element ($C_v = 1.0$; Figure 5.22) was well produced. The maximum thicknesses of these elements were, however, over estimated at 40 m and 18 m respectively. The mean and maximum thicknesses of the lateral accretion elements (mean = 1.96 m, maximum = 13 m) and thalweg bedform complex (mean = 1.50 m maximum = 10 m) were similar to those of the MPS generated models and those found in the input datasets.

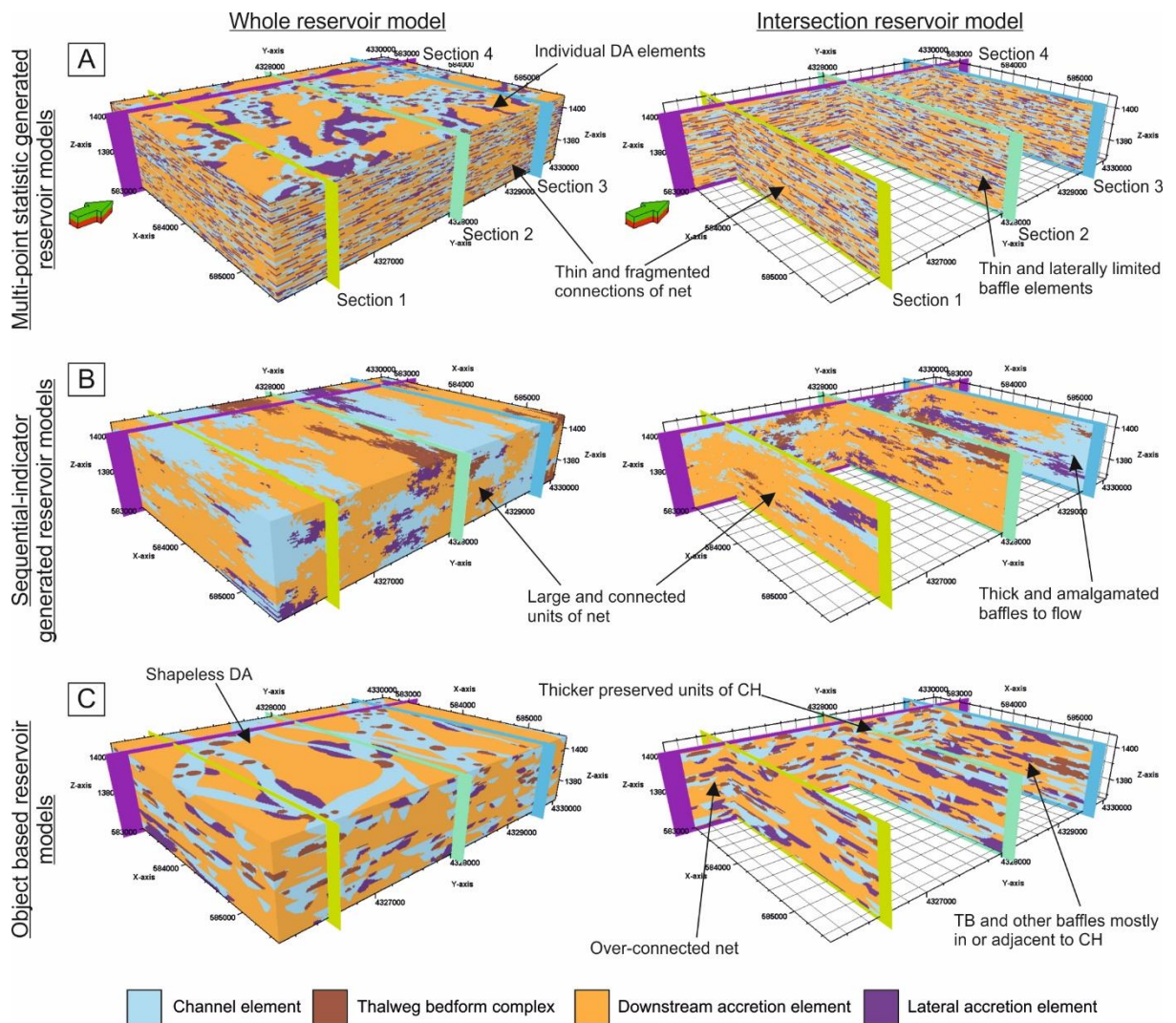


Figure 5.22 - Comparison of (A) Multi-point statistics (MPS)-, (B) sequential indicator simulation (SIS)-generated and (C) Object-based (OBM) reservoir models as whole models and in cross-sections. Models were generated using the same input parameters derived from the outcrop and modern studies (see text for details). A) MPS model generated from the TI shown in figure 5.20. This evidences thin and laterally restricted baffles, individual plan-view downstream accretion elements that showed some recognisable geometries and thin and fragmented net connectivity in cross section. B) SIS model generated from the variograms (see text). Model shows large and connected net reservoir and thick laterally extensive amalgamations of non-net baffle heterogeneity. C) OBM models generated from

the quantitative statistics extracted to make the depositional conditioning rules. Model shows an over-connected net reservoir and thicker preserved channel elements. Note, all models have a 20x vertical exaggeration.

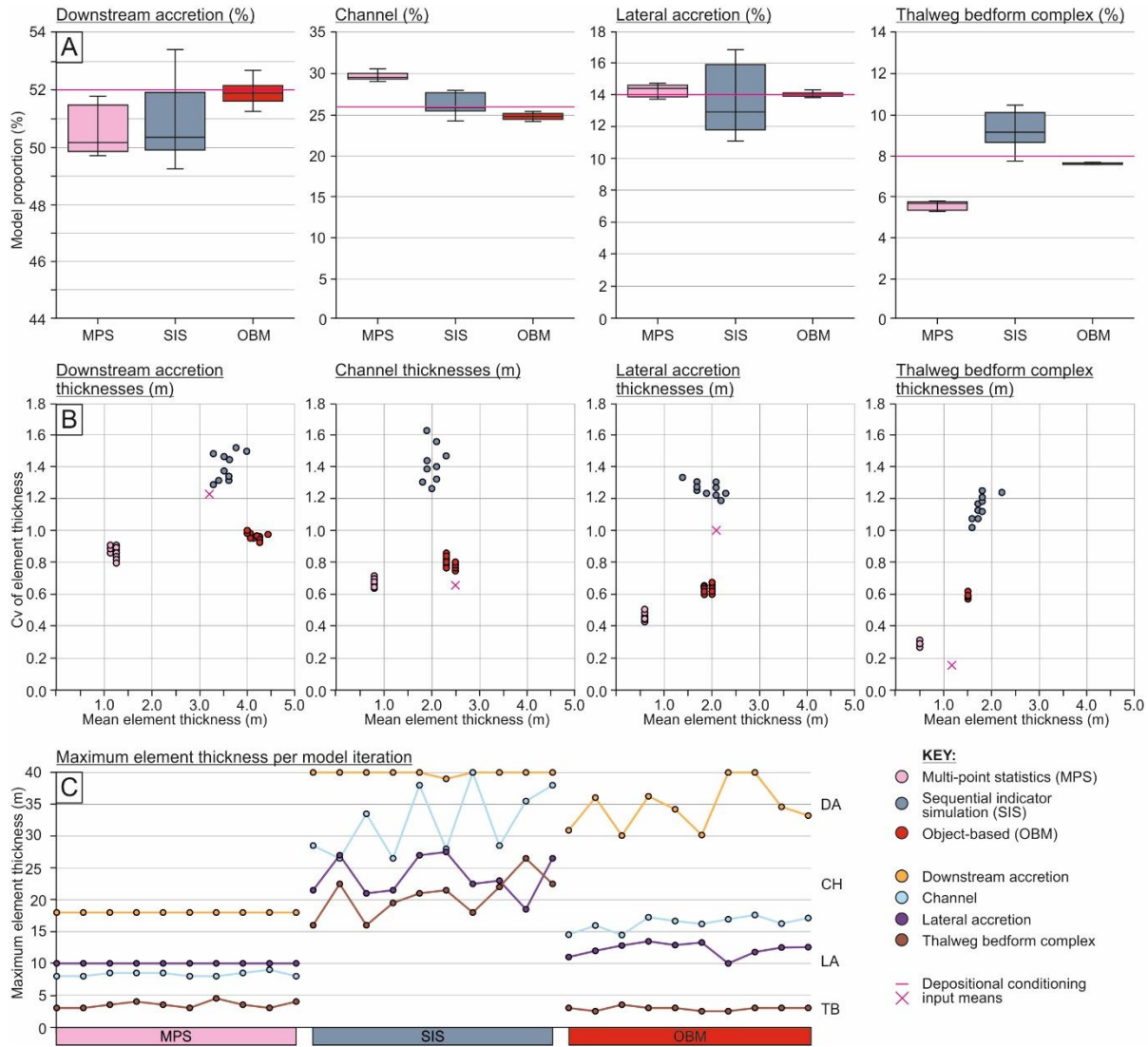


Figure 5.23 – Summary model statistics derived from the three-dimensional summaries of the reservoir models generated using each iteration of the three algorithms. A) The relative proportions of each architectural element modelled within the reservoir model algorithms. The pink line highlights the model input data derived from the sedimentary analysis. B) Mean element thicknesses for each element plotted against the covariance (Cv) of each element, to highlight the thickness and dispersion

in thickness across each element. C) Maximum element thickness plot for each model iteration in each algorithm to show how overestimations of vertical connectivity were affected by the choice of algorithm. Note, the depositional conditioning input means are indicated on the graph showing where the input data and TI values plot.

5.8.2 Sequential indicator simulations of the Lower Castlegate

The SIS generated models honoured some realistic depositional rules. For example, lateral accretion elements were generally adjacent to channel fill elements. However, lateral accretion elements were typically represented as one large unit rather than separate, smaller discrete elements, and the model did not recreate the long ribbon-like, cross-cutting planforms of the channel element. The thalweg bedform complexes were not confined to the channel elements and were again reproduced at a much larger scale than was realistic (Figure 5.22). Very large volumes of downstream accretion elements were connected (Figure 5.22).

The SIS models produced the largest amount of variance across the element thicknesses. SIS generated iterations reproduced the mean element proportions best of the three algorithms. The SIS algorithm statistically best reproduced the downstream accretion element with the mean element thickness (3.48 m) and variability (Covariance (Cv) = 1.33) of mean thickness (Figure 5.23; Table 5.3). The mean and variability of the reproduced element thickness for the lateral accretion was also closely related to that of the input data. However, it proved the least effective at replicating the mean thicknesses of the thalweg bedform complex and lateral accretion elements. The maximum thicknesses of all the elements were over

represented, for example, the maximum thicknesses of the downstream accretion elements was 40 m (the entire modelled reservoir thickness), and ~20 m for the thalweg bedform complex.

5.8.3 *Multi-point statistics models of the Lower Castlegate based upon a three-dimensional*

TI

The depositionally-conditioned MPS models reproduced the distribution, geometry, dimensions and proportions of the modelled sedimentary architectures. The lateral accretion elements were always placed adjacent to the channel fill and downstream accretion elements. The channel elements replicated the ribbon-like plan view geometries of the depositional conditioning. The downstream accretion elements always displayed sensible trends of thickening and thinning, both laterally and vertically throughout the modelled volume and commonly occurred as small discrete bar-like packages in plan-view (Figure 5.22). Avulsion events were observed with both the channel and lateral accretion element architectures across the reservoir volume, on similar scales to those observed in both ancient (Smith *et al.*, 1989; McLaurin and Steel 2007; Hajek and Heller, 2012; Li *et al.*, 2015) and modern systems (Bristow *et al.*, 1999; Pickering *et al.*, 2014; Sarker *et al.*, 2014). Thalweg bedform complex elements were only observed within channel fills. However, the square geometry of some of the smaller depositional elements (lateral accretion and thalweg bedform complex elements) appeared to differ from the original input data, with square geometries in cross section.

The MPS models underestimated the thalweg bedform complex proportions and downstream accretion elements by ~2% and overestimated channel elements by ~3%. The MPS algorithm underestimated the mean thickness of the elements relative to the input data and reproduced more of the minimum element thicknesses (Figure 5.23; Table 5.2). The deviation away from the mean element thicknesses were well replicated, except for the lateral accretion elements. The lateral accretion elements showed a lower mean thickness (0.60 m) and a lower variation (Covariance (Cv) = 0.39) in thickness across their reproduction in the MPS models. The maximum thicknesses of the elements produced within the model were realistic and approximately replicated those seen within the input data.

5.8.4 Static connectivity tests

All three algorithms produced broadly similar results in the static connectivity test of net reservoir. The single production well was able to drain over half of the modelled volume (Figure 5.24), equivalent to a total drainable volume of ~229,000,000 m³. However, OBMs returned greater drainable volumes across the model iterations, with the smallest variance in the drainable volumes produced. The SIS algorithm produced the greatest range in connected net (Figure 5.24).

The SIS model produced a 48.84/50.44/53.23 (min/mean/max) percentage drainable volume with a standard deviation of 1.38. The MPS model iterations produced a 49.48/50.25/51.54 (min/mean/max) percentage drainable volume with a standard deviation of 0.76 (Table 5.3). This suggests that, although the two models were similar in terms of average in drainable volume, the range and standard deviation was much greater for the SIS models when

compared to those models generated by MPS. The OBM iterations produced 49.44/51.67/52.51 (min/mean/max) in the drainable volumes, which is a much tighter distribution than SIS and MPS generated iterations, with a range of only 1.21%. Consequently, the MPS realisations were far more repeatable and representative in their reproduction of realistic meso-scale heterogeneity within the reservoir volumes.

The vertical thickness of connected net was also measured to derive its vertical connectivity and the pathway thickness replicated within the models. The MPS generations produced a much smaller vertical connectivity (1.2 mean and ~18 maximum; Table 5.3) than SIS or OBM. The SIS and OBM iterations generated vertical connectivity thicknesses equal to the entire reservoir thickness (~40 m), with large variability with approximately 5 m and 4 m standard deviation respectively. This is unrealistic when comparing to the maximum thicknesses within the input data (Figure 5.21), which show vertical connections of net (downstream accretion elements) were no bigger than approximately 15 m.

Table 5.3 – Output data for the architectural elements and net connectivity for the multi-point statistics, sequential indicator and object-based model iterations. Note, Min. = minimum, Mean = arithmetic mean, Max. = maximum, Sd = standard deviation, Cv = covariance.

	Statistic		Multi-point statistics	Sequential-indicator simulation	Object-based models
Downstream accretion element	Proportions	Min.	49.7	49.26	49.62
		Mean	50.48	50.84	51.77
		Max.	51.79	53.44	52.66
		Sd	0.77	1.24	0.79
	Thickness	Min.	0.50	0.50	0.50
		Mean	1.20	3.48	4.18
		Max.	18.00	40.00	40.00
		Cv	0.78	1.33	0.94
Channel element	Proportions	Min.	29.01	24.49	25.28
		Mean	29.56	26.08	32.02
		Max.	30.17	27.68	32.38
		Sd	0.33	1.07	0.60
	Thickness	Min.	0.50	0.50	0.50
		Mean	1.80	2.00	2.33
		Max.	9.00	38.00	31.50
		Cv	0.60	1.35	0.76
Lateral accretion element	Proportions	Min.	13.81	10.99	13.78
		Mean	14.29	13.57	13.93
		Max.	14.72	16.87	14.27
		Sd	0.31	2.01	0.16
	Thickness	Min.	0.50	0.50	0.50
		Mean	0.60	1.92	1.96
		Max.	10.00	27.50	13
		Cv	0.39	1.19	0.65
Thalweg bedform complex element	Proportions	Min.	5.39	7.52	8.00
		Mean	5.67	9.51	8.00
		Max.	5.85	12.42	8.00
		Sd	0.18	1.25	0.00
	Thickness	Min.	0.50	0.50	0.50
		Mean	0.50	1.76	1.50
		Max.	3.00	26.50	10.00
		Cv	0.29	1.09	0.59
Net connectivity	Proportions	Min.	49.48	48.84	49.44
		Mean	50.25	50.44	51.67
		Max.	51.54	53.23	52.51
		Sd	0.76	1.38	0.81
	Thickness	Min.	0.50	0.50	0.50
		Mean	1.20	3.60	4.21
		Max.	18.00	40.00	40.00
		Sd	0.92	4.71	3.89

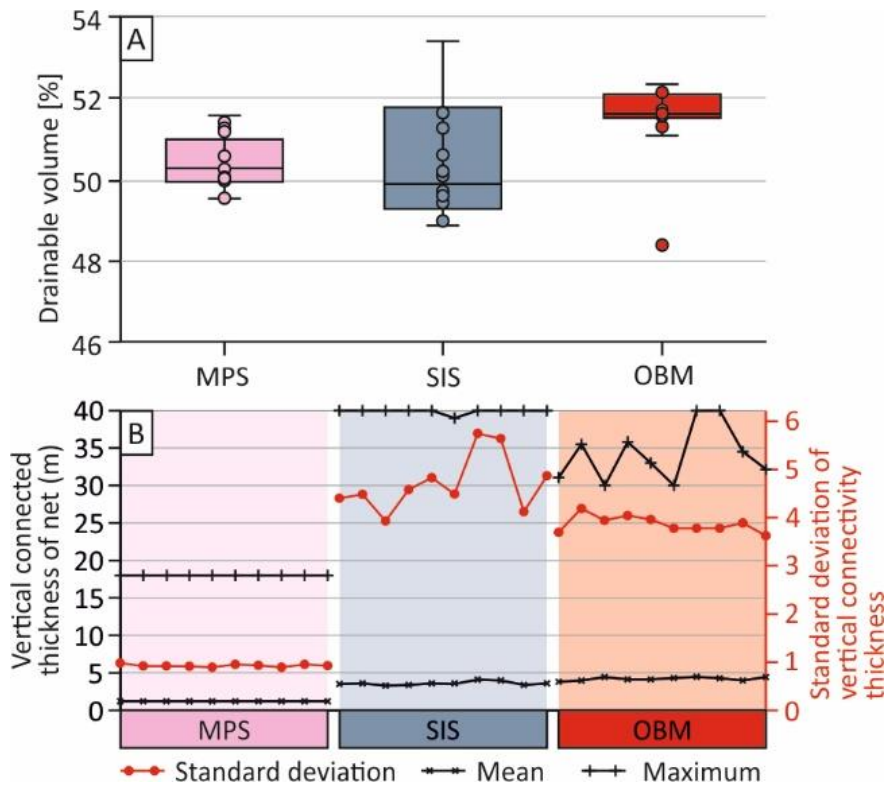


Figure 5.24 – Drainable volumes and vertical connectivity statistics from all thirty model iterations across the three algorithms. A) Drainable percentage volume box-plots of the SIS-, MPS- and OBM-generated models, showing the variance in results across the ten iterations of SIS-generated reservoir volumes and a narrow variance in MPS-generated and OBM-generated iterations. B) Maximum, mean and standard deviation of the vertical thickness of net connectivity across all iterations of MPS-, SIS- and OBM-generations. OBM and SIS show a maximum thickness equal to that of the entire model, whereas MPS shows a maximum connectivity thickness of 18. The standard deviations of the SIS and OBM models also showed a high variance, whereas the MPS showed less of a variation away from the mean.

5.9 Discussion

Current common practice in the construction of reservoir models is to rely on OBM or SIS methods, because of the inherent complexities associated with generating appropriate TIs for MPS. To-date, using MPS is limited by the re-usability of TIs and the lack of standardized methods for their development, particularly in three dimensions (Comunian *et al.*, 2012; Ringrose and Bentley, 2015; Tahmasebi, 2018), the overprinting of local controls upon reservoir models, and the inability of MPS to reproduce non-stationary patterns within a TI (Strebelle and Zhang, 2004).

This study presents a repeatable method for the generation of geologically realistic TIs, by conditioning them to the depositional environment. Depositional conditioning uses four key characteristics of sedimentary architecture: (1) distributions, (2) dimensions, (3) geometries and (4) proportions (Table 5.2; Figure 5.21). These four categories can be used to develop TIs that are representative of a sedimentary environment rather than an individual dataset.

The depositional conditioning workflow proposed (Figure 5.25), provides a simpler but standardized methodology, when compared with traditional MPS and SIS simulated reservoir models (Deutsch and Journel, 1992; Seifert and Jensen, 1999, 2000; Caers and Zhang, 2002, Strebelle and Levy, 2008; Le Coz *et al.*, 2011; Hu *et al.*, 2014). Developing depositional conditioning is heavily dependent on the studied geology, and thus helps sedimentology to translate into reservoir modelling, simplifying the relationship between the two disciplines. Depositional conditioning also allows the modeller to input their own level of stationarity

into a TI as well as heterogeneity (Figure 5.20). The biggest advantage, shown in this study, is the visual impact they have upon subsurface models.

The manual development of TIs is laborious, as it requires multiple iterations and manual checks of intersectional planes through the TI volume and target fractions to ensure that input statistics were being honoured. This is the biggest remaining issue in the production of geologically conceptual TIs and is therefore dependent upon low human error.

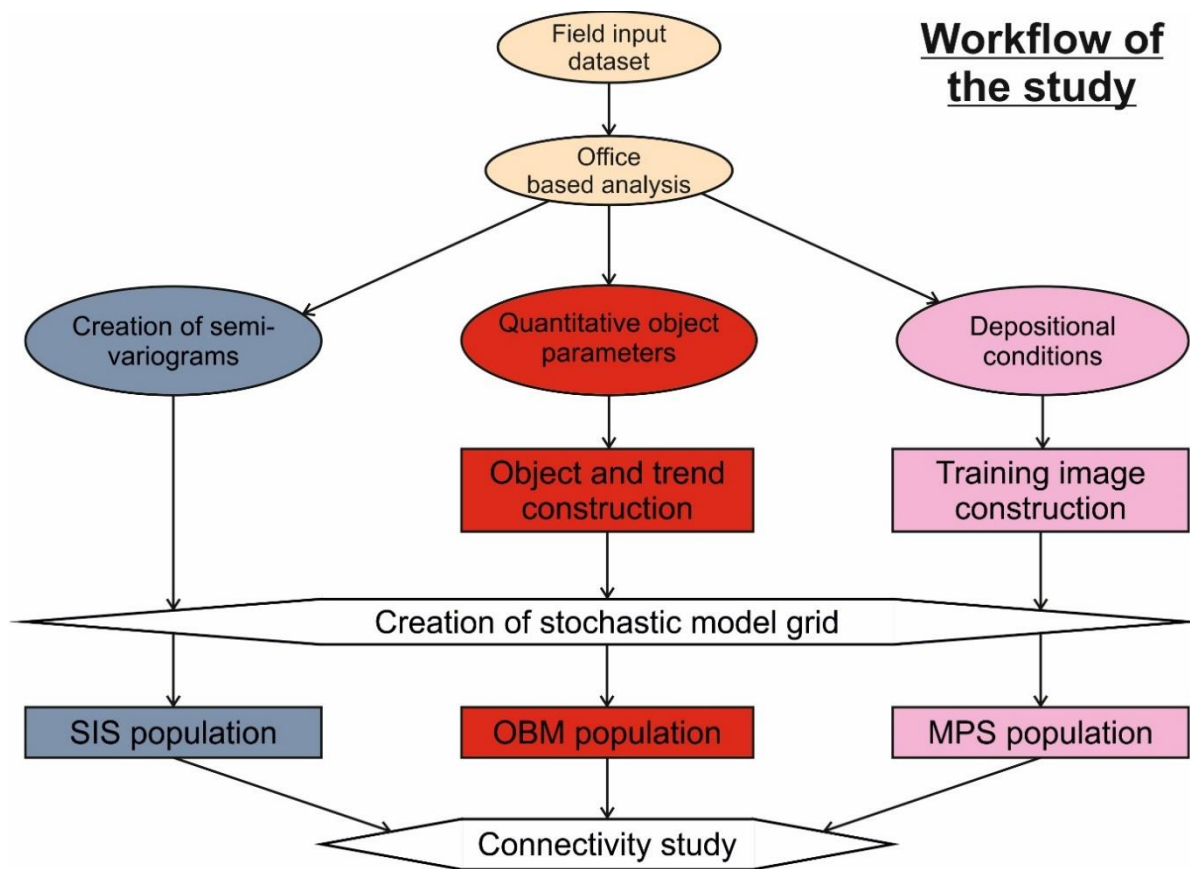


Figure 5.25 – Generalised workflow of this study to generate the reservoir models. Note, SIS = Sequential Indicator Simulation, MPS = Multi-Point Statistics, OBM = Object-based Modelling.

5.9.1 *The reproducibility of geologically realistic data*

During this study, more emphasis was placed on the reproduction of the patterns, geometries, architectures and relationships contained in the TI, than to match the exact target fractions (element proportions) to keep computing simulations times to a reasonable level.

OBFs, while producing visually and statistically realistic outputs, are notoriously difficult to match to hard data (Holden, 1998; Seifert and Jensen, 2000; Vevle *et al.*, 2018). They are also extremely limited to their pre-defined geometries (Holden *et al.*, 1998; Stephen *et al.*, 2001; Manzocchi *et al.*, 2007), and have shown in the current work to over represent the maximum thickness of the background facies (Figure 5.23); in this study, the downstream accretion element). This problem leads to a large overestimation in the dimensions of net-connectivity (Figure 5.23). Furthermore, the use of the downstream accretion element as background leads to a poor representation of its geometry and dimensions in OBFs. However, OBFs do produce models that visually represent the environment they are simulating, with the dimensions, proportions and juxtapositions of the other elements being well represented.

SIS is a method that uses the probability and variance of one model unit to another to populate a model framework. This provided little visual resemblance to the system being simulated (Figure 5.22; Seifert and Jensen, 1999; 2000 and references therein; Martinius *et al.*, 2017). The resultant dimensions of net connectivity were also extremely over estimated (Figure 5.24). The standard deviations reported for the static connectivity of the SIS models were anomalously high, this may, in part, be due to the use of 10 model iterations

(Goovaerts, 1999); however this is sufficient to negate any sequential fluctuations in the model reproduction (Falivene *et al.*, 2006), and further iterations would have been computationally expensive for a relatively small improvement on the standard deviations (Goovaerts, 1999). Although SIS simulations honoured some of the rules within the conditioning dataset, the geological realism of the resulting models was poor.

The depositional conditioning of TIs in MPS modelling provides a more realistic visual representation of a fluvial system. This work shows that the distribution of sedimentary architectures and therefore, the distribution of heterogeneity within a reservoir, is better constrained when using MPS than SIS. The MPS model honoured the depositional conditions imposed and produced models that visually were recognisable as the environments in which they simulated in. Despite the minor differences between the depositional conditioning proportions and those of the MPS simulations, the MPS results were closer to those in the original depositional conditioning rules, when compared to the SIS or the OBM generated models. In the MPS simulations, the juxtaposition of one element to another was extremely well constrained (Zhang *et al.*, 2006; Daly and Caers, 2010; Zhou *et al.*, 2018), and the dimensions of the four sedimentary architectures fell within the minimum and maximum values imposed in the depositional conditions (Table 5.2; Figure 5.21).

MPS provided the most geologically realistic distributions of the net reservoir facies and associated heterogeneities. The relative portions of the elements in the depositionally conditioned TIs may have minor variations from the input data, due to the algorithm reproducing the other three aspects of depositional conditioning. The smaller sized

geometric rules, such as minor fluctuations in the size of thalweg bedform complexes, imposed by the TI were not followed by the MPS models. This may be because the MPS algorithm does not recognise such small-scale variations (Strebelle, 2002; Comunian *et al.*, 2012) in shape, or be due to the model resolution, or it may be due to the number of variations in the size of thalweg bedform complexes repeated within the TI volume. A low number of repetitions within a TI volume may lead to poor reproduction by MPS (Strebelle, 2002). The reproduction of thalweg bedform complexes was far more realistically reproduced by the OBM generated models.

The connectivity study showed that almost all of the net-defined reservoir rock was connected to the single penetrating well (Figure 5.24). The SIS iterations showed a large range in their drainable volumes. By contrast, the depositionally conditioned MPS and OBM simulations showed very little variance in their results (Figure 5.24), indicating more reliable and repeatable methodologies. However, both OBM and SIS model iterations did show an unrealistic over estimation in the thickness of the net reservoir connectivity. These results contrast those of Zhou *et al.* (2018), where MPS provided a higher connectivity than OBM with no significant improvement of reproduction accuracies. Zhou *et al.*, (2018) concluded that MPS were limited by the robustness of TIs. This study provides a method of constructing TIs that are directly fit-for-purpose in a more accurate and realistic manner than previously presented.

5.9.2 *Constructing an MPS model for a confined fluvial system*

This chapter has shown the construction of reservoir models for an unconfined fluvial system, the Lower Castlegate, Utah. The construction of a depositionally conditioned TI for confined fluvial systems is far more complex than for unconfined. Temporally erosional juxtapositions of different facies zones makes constraining architectural elements within these images difficult when modelled as a simple gridded zone. It is therefore proposed that a multi-zonal approach is adopted. The two distinct channel sets imaged in (Figure 4.8; Figure 5.25), provide two facies zones. Following the process outlined in Section 5.4, deterministic surfaces can be placed at the base and top of the analysed unit, and a third can be placed between the two channel sets, dividing the dramatically different channel set architecture. The lower channel set being characterised by more downstream accreting and mid-channel bar with channel cut-and-fill architecture. Whilst the upper channel set is dominated by more lateral accretion within the system (Figure 5.26).

The possibility of constructing an MPS model from such a succession is possible using depositional conditioning in three ways: 1) the development of a non-stationary TI, 2) a TI with multiple zones and 3) the construction of multiple TIs and zones within the model framework and not the TI. There are inherent problems for the first two methods in the construction of TIs. A TI should be stationary both spatially and temporally, meaning there should be no trend in the image. Whilst there have been works to overcome this (Strebbele and Zhang 2005; de Vries et al. 2009) and to maintain the spatial and temporal probability of

a data event occurring equally, this is an extremely laborious method when the construction of two stationary TIs is much simpler.

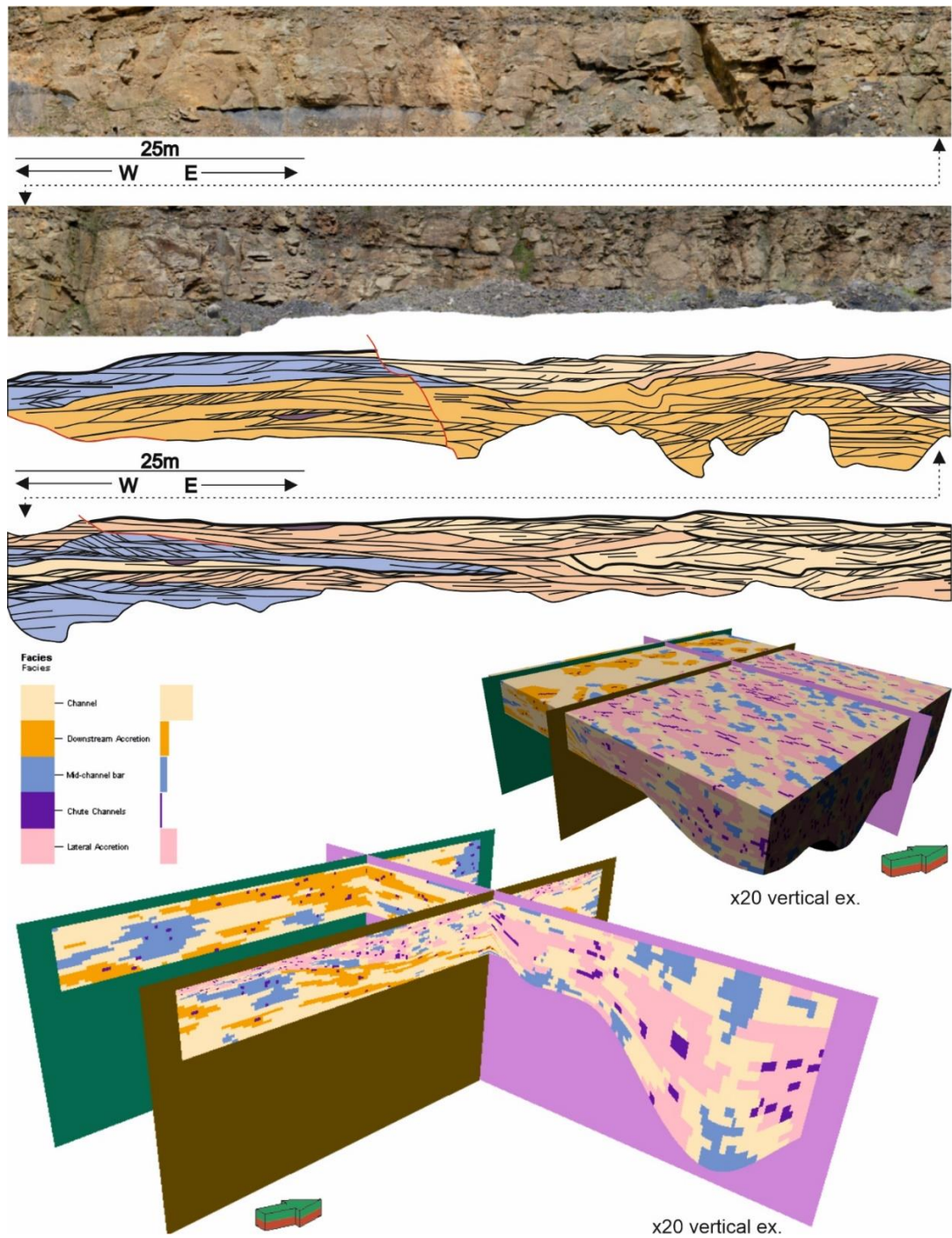


Figure 5.26 (previous page) – *The B1 Face of the Spireslack Sandstone, as interpreted in Figure 4.8 and associated multi-zonal MPS model. Note model is 400 m wide with a cell resolution of 10 m, complete model shown on the right and intersection model at the bottom (20 x vertical exaggeration).*

In Figure 2.25 an MPS model is generated for the Spireslack Sandstone as two zones, two individual TIs were constructed for this. This allowed the distinctly architecturally different architectures of the two channel sets to be constrained. This method does, however, require considerable control upon the depositional system and a surface defining the two zones must be imaged within the data set, to construct a reliable model.

5.10 Summary

The work presented here showcases a method of inputting heterogeneity and stationarity into a three-dimensional TI. The concept of depositional conditioning is shown as a simple and standardized method of generating geologically realistic TIs, based upon limited data. Depositional conditioning uses four categories inputting sedimentary properties: (1) spatial distribution of an architectural element relative to others, (2) 3D dimension of the respective depositional element; 3) geometric shape of the depositional elements and finally, (4) the proportion of a depositional element of the total reservoir volume.

A depositionally conditioned three-dimensional TI was produced from architectural element scale analysis of heterogeneity within the Lower Castlegate Sandstone, Tuscher Canyon, Utah, and the Jamuna River, northern India. The use of two datasets, one modern and one outcrop, allowed the TI to constrain the heterogeneity of the environment of deposition in three dimensions, based upon limited input data. After deterministic surfaces were

generated from the input data to form a model framework, 10 iterations of multi-point statistic (MPS), sequential-indicator simulation (SIS) and object-based (OBM) reservoir models were generated and statically tested.

Results showed MPS and OBM models to have more geologically realistic element distributions. Whilst similar connectivity means were achieved, through the MPS and SIS generations, smaller ranges were achieved through OBM and MPS-generated reservoir models. This study presents one depositional environment, four architectural elements and static testing of reservoir models, results showed that MPS models could be generated in a reproducible and realistic manner. The results demonstrated real potential for the use of outcrop data libraries to improve reservoir model of architectural element scale heterogeneity. Study implications suggest the reduction of uncertainty surrounding secondary and tertiary phases of production, which are commonly more susceptible to the influences of sedimentary heterogeneity.

This work demonstrates the difficulties and complexities in the numerical representation of fluvial multi-storey sandbodies. Models that statistically honour input data whilst appearing geologically realistic are difficult to produce and fraught with problems. This chapter highlights, whilst using limited data, that a realistic and statistically honoured model can be produced using depositional conditioning of TIs for MPS simulation.

6 Discussion

This discussion will first look at the application of confined and unconfined nature to fluvial systems, highlighting the stratigraphic and sedimentological signatures that may be diagnostic of lateral confinement. A discussion of stochastic workflow best-practices for these systems is then undertaken. Finally, the discussion will provide a summary of the limitations associated with this study.

6.1 Multi-storey sandbodies

This section of the discussion will discuss the findings from Chapters 3 and 4, bringing in modern and more ancient examples to help support the observations made in those chapters.

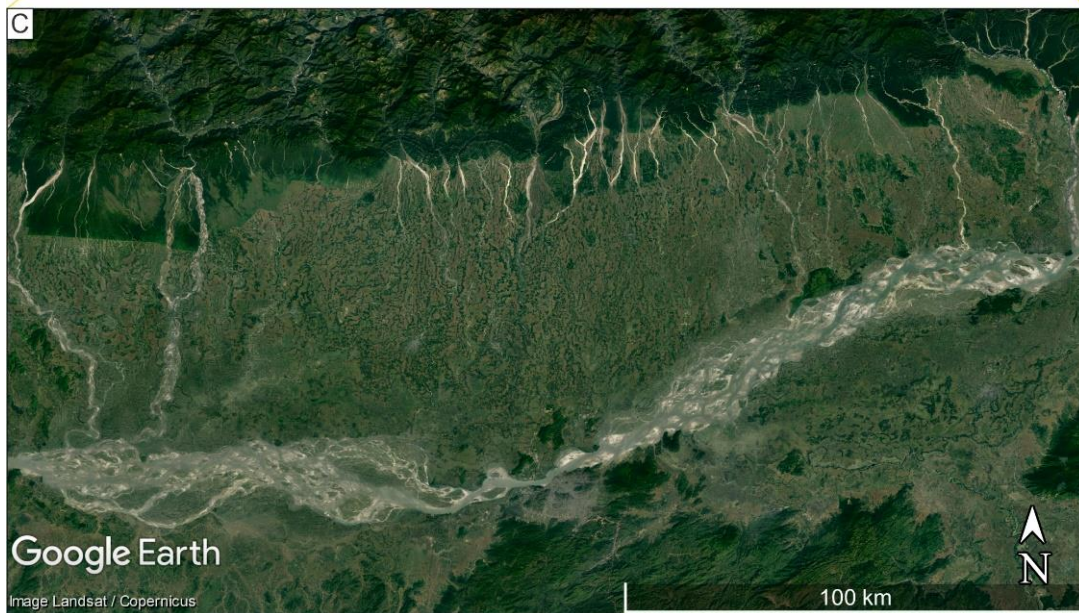
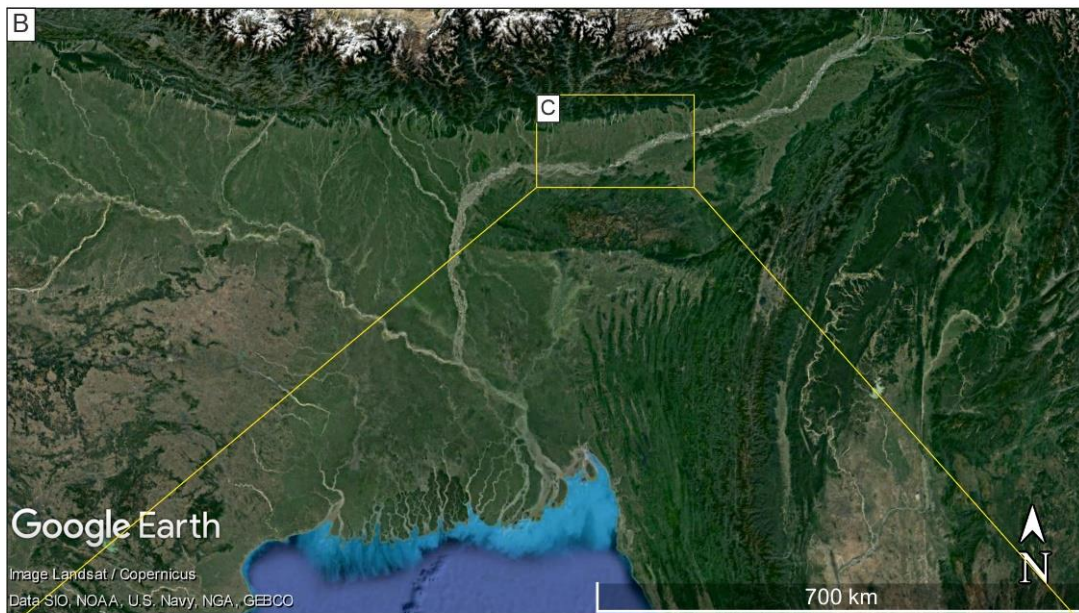
6.1.1 *Unconfined multi-storey sandbodies*

At the stratigraphic and morphological scale, unconfined fluvial systems can show radial or distributive plan view drainage patterns (Nichols and Fisher 2007). They typically occur in endoheric basins (Weismann et al. 2010), those without marine influence. However, radial patterns of deposition can be noted at different scales, regardless of the attachment to marine influence. Many fluvial systems show a distributive pattern from a mountain front (Nichols and Fisher 2007; Weismann et al. 2010) but can also show a tributive morphology (Fielding et al. 2012) at the larger scale, as seen in the Lower Castlegate (Section 3.8). This is

an issue with the pigeon-holing of the definitions of tributive (Fielding et al. 2012) and “axial” in the distributive fluvial system model (Weismann et al. 2010; Owen et al. 2015).

This poses the question: is scale and definition the cause of confusion? The axial system here is considered as one that influences stream capture (i.e. the confluence of one system with another) (Mikesell 2010), which then changes sedimentation downstream of the confluence between the two systems. This is typical of fluvial systems. However, what can be noted from, particularly from aerial photography in Figure 6.1, is the proportion of sand-grade sediment within these systems. Both systems shown in Figure 6.1 show evidence of a distributive nature, and both show stream capture in the medial to distal zones of their distributive systems. However, the grade of bedload material seems to be significantly higher in the major stream capturing the distributive systems.

Figure 6.1 – *Examples of modern fluvial systems that show both distributary and tributary morphologies, at differing scales. A) The Rio Senguerr fluvial system, Argentina. The system shows a distinct distributive pattern from the eastern Andean margin; however, stream capture is evident on three occasions, at the fan margin, with drainage from either side of the fan, and finally, with the large basin feeding north-south fluvial system. The Rio Senguerr fluvial system may then be considered both distributive and tributive. B) The Jamuna River, Bhutan and northern India, on the southern Himalayan margin. Note the yellow box location for C. C) Smaller scale view of the Jamuna River in B. This portion of the Jamuna River shows a much larger fluvial system than in A, presenting similar traits in a vastly different climatic regime. Mountain elongate run-off fans are intersected at their toes by the major axial system, fitting to the DFS model well. However, as is clear in B, the larger scale plan-view of the Jamuna is tributive.*



The scale of observation may have an impact upon the fluvial morphology observed. The Rio Senguerr fluvial system, Argentina (Figure 6.1A) shows a distinct distributive pattern in the form of a semi-arid mountain run-off system from the eastern Andean margin. However, at the larger scale, instances of stream capture are observed. Stream capture and a more tributive nature can be seen on three levels: at the fan margin, with respect to drainage from either side of the fan, and with respect to the large basin feeding north-south fluvial system. Therefore, at the small scale the Rio Senguerr fluvial system may then be considered distributive but when looking across the entire back-arc a tributive morphology may be implied.

The Jamuna River, Bhutan and northern India, on the southern Himalayan margin shows similar characteristics. The system (Figure 6.1B) shows an overall tributive morphology but at the smaller scale, the Jamuna River shows mountain elongate run-off fans that are in confluence at their toes with an axial system (Figure 6.1C). This again provides evidence of scale based-observations fitting to both the tributive and distributive morphological models. These observations suggest that whilst many systems show distributive patterns, many also show evidence of stream capture at a number of orders (Figure 3.21A), which in plan-view appears to be both distributive and tributive, traits that may be complicit with observation scale.

At an architectural element scale, little has been done to understand the sedimentary architecture of such systems. A modern endoheric example from central China (Figure 6.2) shows similar barform preservation and deposition as is found in the Lower Castlegate

(Chapter 3). Whilst at a channel belt – or stratigraphic scale – the unconfined fluvial system shows a radial pattern that has its own fan-like topography and a distally decreasing channel belt width. However, when architectural elements at a barform scale are considered, the results are somewhat counterintuitive.

The channel elements (cut-and-fill scale elements) of the Northern Quilian Mountains DFS, China, show minimal variation in widths, from approximately 22-25 m. The proportion of channel elements within the proximal to medial zones of the fluvial system show a slow decline from proximal to distal from approximately 60% to 30%. The unit bar elements are seen throughout the fluvial system, however, they become larger towards the medial zone (from approximately 10 to 25 m wide, proximal to medial) and decrease in size to the distal zone to approximately 11m. The proportions of these unit bars decrease downstream, from approximately 40% to 18%. Compound bar elements increase in size distally. Compound elements are not found in the proximal zone of the fluvial system, whilst in the medial and distal zones an increase in compound barform size from 44 m to approximately 75 m width is seen. The proportions of compound barforms increases downstream to a total proportion in the distal reaches of 52%, becoming the dominant architectural element of the fluvial system. It is proposed that the decreased unit bar size in the distal zone is due to the construction of compound bars.

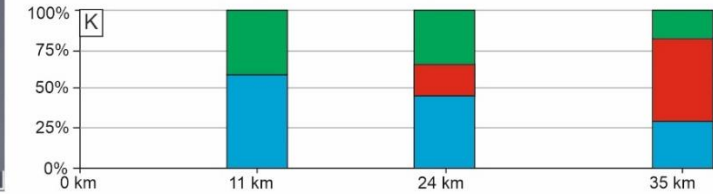
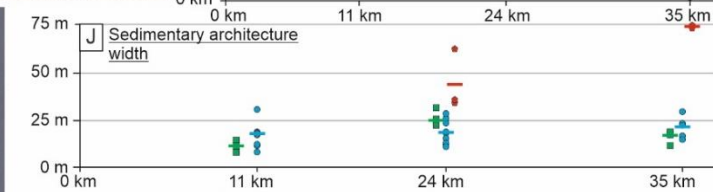
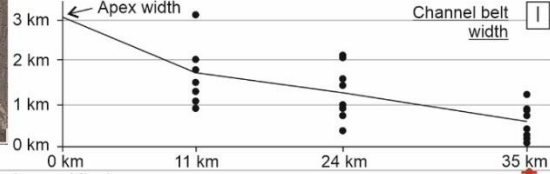
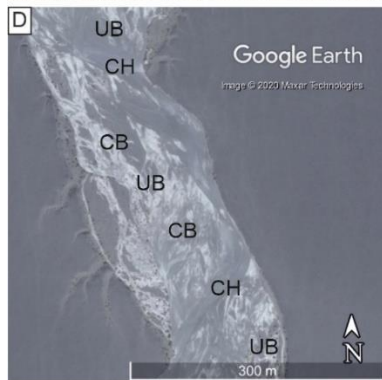
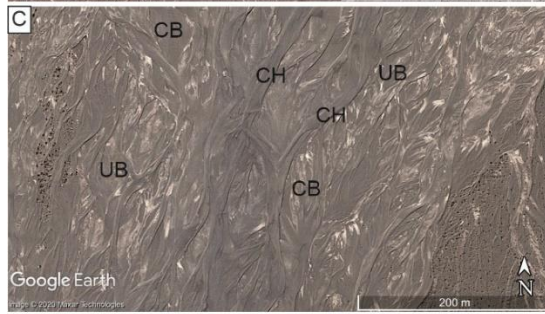
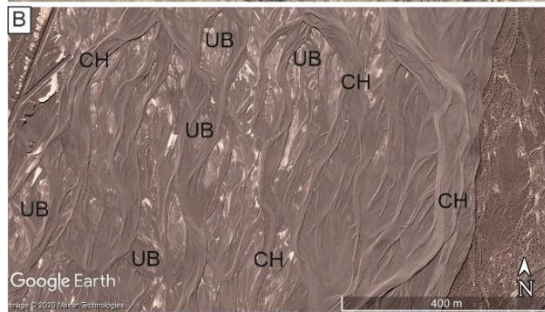
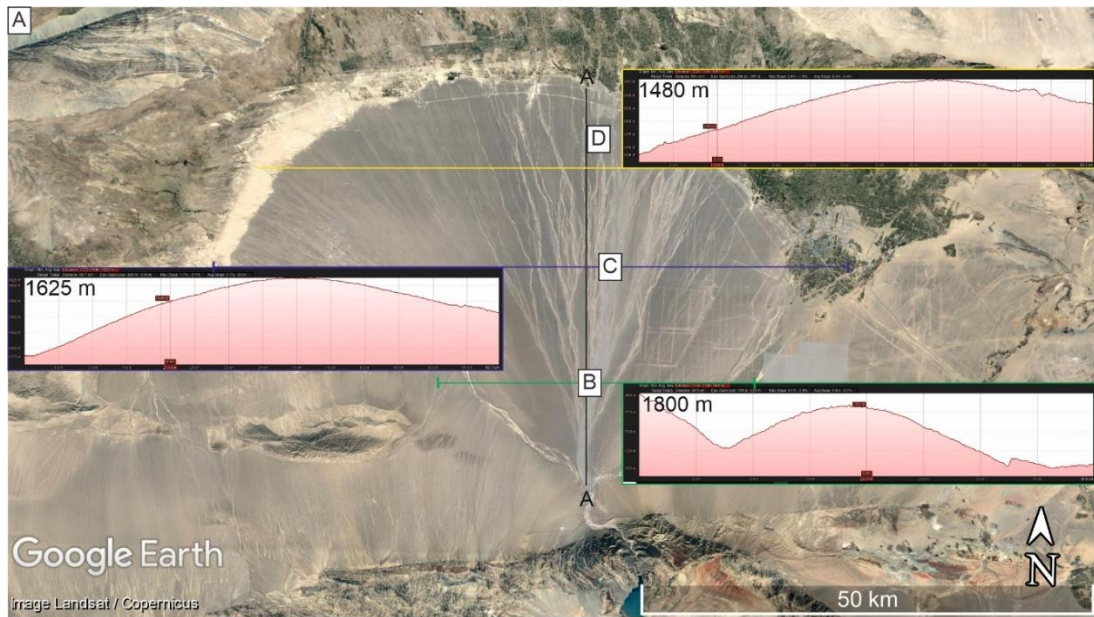


Figure 6.2 – A) Northern Quilian Mountains DFS, China from Hartley et al. (2010) and figure 2.15. Showing the locations of higher resolution channel belt images from B, C, and D. The transect of elevation profile in E is shown. Topographic transects of proximal, medial and distal fan zones are also shown. This shows steeper topographic relief on the margins of the fluvial system in the proximal zone. B) High resolution image of proximal DFS zone channel belt showing channel cut-and-fill elements and unit bars. C) High resolution image of medial DFS zone channel belt showing channel cut-and-fill elements, unit bars and some compound barform deposition. D) High resolution image of distal DFS zone channel belt showing channel cut-and-fill elements, unit bars and compound bars. E) Topographic profile from proximal (left) to distal (right) of the northern Quilian Mountain DFS. F) High resolution topographic profile through the proximal zone. G) High resolution topographic profile through the medial zone. H) High resolution topographic profile through the distal zone. I) Channel belt widths displaying the typical DFS profile of decreasing widths in the distal direction. J) Architectural element widths from the proximal medial and distal zones. Green indicates unit bar, blue indicates channel cut-and-fill elements, red indicates compound barforms. Note, line indicates mean and dot raw data value. K) Element proportions for proximal, medial and distal fan zones. Colours are as indicated for J.

6.1.2 Confined multi-storey sandbodies

Confined modern fluvial systems, as highlighted in Chapter 4 can have high sediment load depositional features in the lower part of their depositional units. The nature of these high sediment load deposits may be indicative of allogenic processes at the time of deposition with forced regressions acting upon a basin causing the fluvial system to incise (Catuneanu 2019) and provide higher sediment input rates as a result of re-equilibration to the graded

fluvial profile (Holbrook et al. 2006). However, not all confined fluvial systems are undergoing forced regression, structural features and palaeotopography may also provide lateral confinement to a fluvial system.

What is clear from the Spireslack data presented here and in the findings of Wang et al. (2020) is that confined fluvial systems, particularly incised valley fill successions, show characteristics that are unique compared to those of unconfined systems. The water depths of confined systems may be much higher than what barform top heights may indicate. Wang et al. (2020) provide evidence using maximum flow depth reconstructions and bar-top heights to determine the depths of flows within incised valley systems. The common result when compared is that the resultant maximum flow depths from cross strata greatly exceed those derived from cross-bed thicknesses. It is therefore proposed that water depths are much greater than what bars may indicate due to limited sediment supply allowing barforms to build up to the total water depth. This is also in the proximal region of the Jamuna River, northern India (Figure 6.3). Here, well proximal of any backwater effects and incised valley's produced by forced regressions, similar characteristics can be seen. Submerged unit bars can be seen within the confined system, however, are not emergent.



Figure 6.3 – Jamuna River, northern India, showing a confined morphology with submerged unit bars and a large amount of sediment deposited distal of the confinement.

Furthermore, Wang et al. (2020) provide evidence of extremely stable flow conditions within confined fluvial systems. The Spierslack Sandstone cross-bed thicknesses (Figure 6.4A) show a low standard deviation, this standard deviation be even lower without one erroneously large reading. When removing that reading the standard deviation is approximately 0.15 (coefficient of variation equal to 0.30), significantly lower than that of the Lower Castlegate (Chapter 3), that shows a standard deviation of 0.23 (coefficient of variation equal to 0.39), even in generally smaller cross-bed thicknesses. Wang et al. (2020) also use the coefficient of variation of cross-set thicknesses across all of their studied incised valley fill successions, highlighting that all fall below the variability dominated successions line.

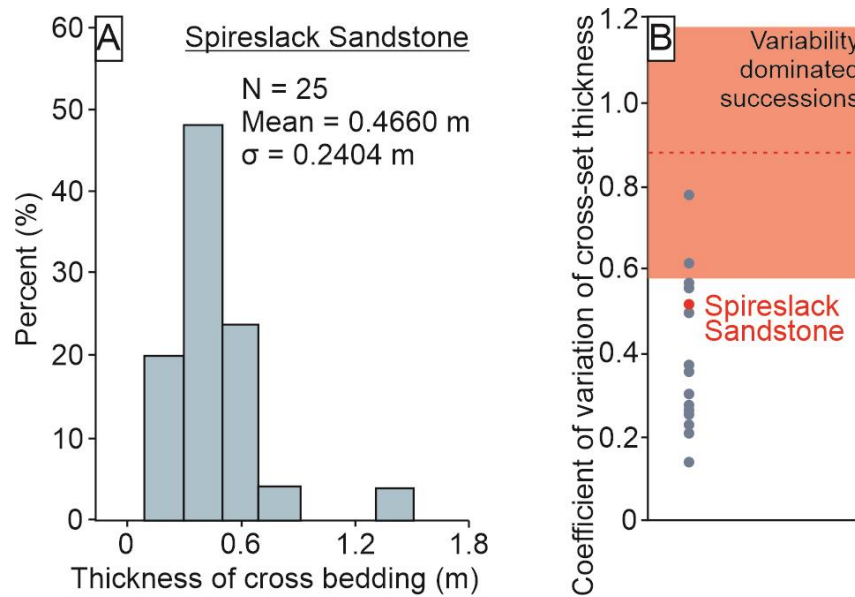


Figure 6.4 – Cross-bedding thickness data from Wang et al. (2020). A) Histogram of cross-bed thicknesses from the Spireslack Sandstone (Modified from Wang et al. 2020). B) Plot showing the coefficient of variation from cross-set thicknesses from the Spireslack Sandstone (red dot) relative to other incised valley fill successions (blue dots). The line for a variability dominated succession is also highlighted.

The above section has helped to understand possible identifiers of confined fluvial systems, when applied to incised valley strata. However, only one example from the Jamuna River has produced similar characteristics. Further comparisons can be drawn with other published studies.

The mid-Carboniferous Fell Sandstone of northern England was deposited during a period of rifting in north-west Europe (Fraser and Gawthorpe, 1990). It comprises the upstream fluvial portion of a major fluvio-deltaic system that prograded southwards (Kearsey et al. 2019) through the Tweed, Northumberland and Solway basins of northern England. The Fell

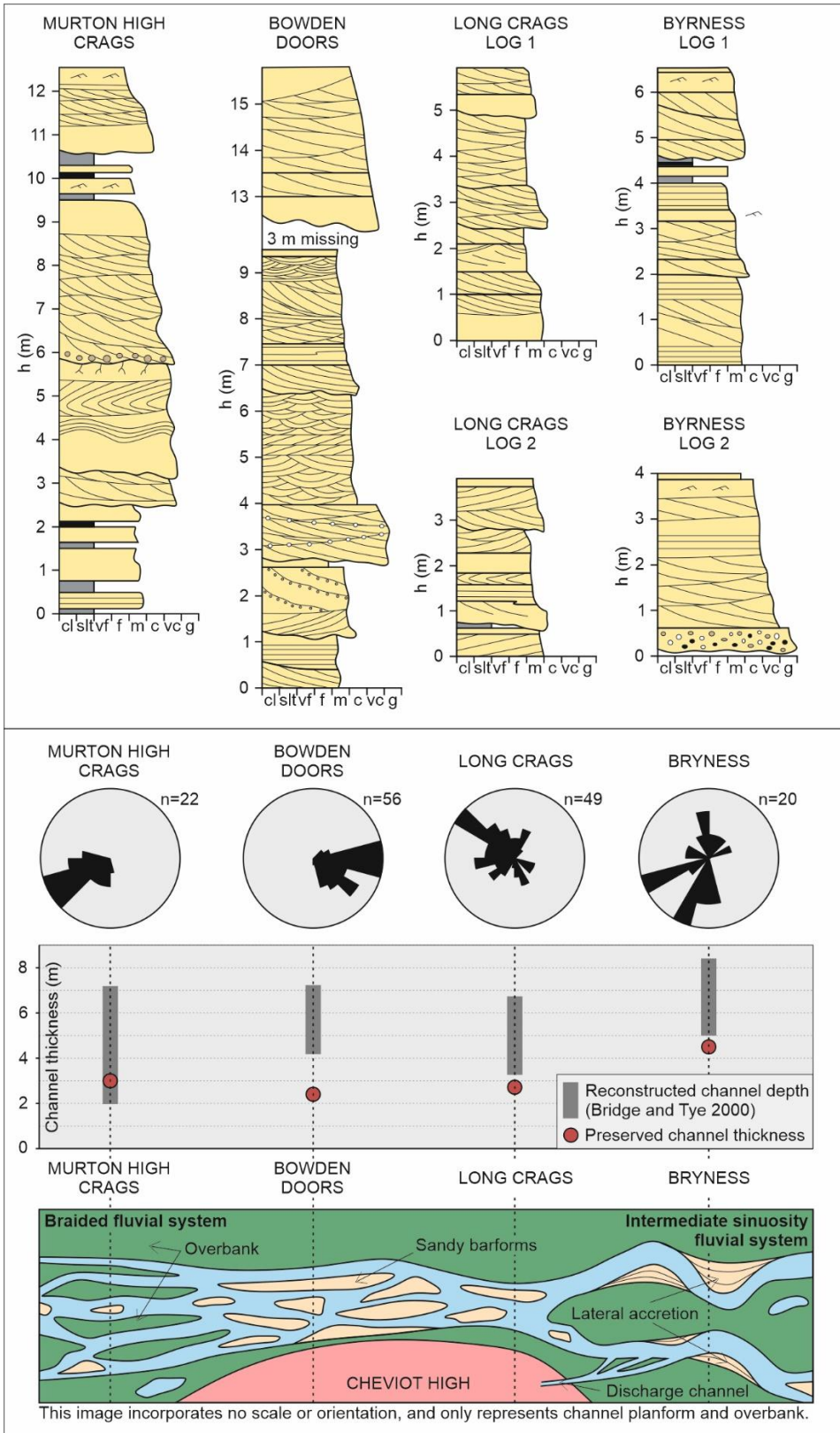
Sandstone received significant divergence of flow by the uplift of a buoyant low-density granitic body that underpins the Cheviot High (highlighted by the palaeocurrents given in Figure 6.5) (Howell et al. 2019).

The fluvial system grades downstream as its graded fluvial profile changes downstream with gradient (Holbrook et al. 2006), from a braided fluvial system, in the northern Tweed Basin, to a high-sinuosity meandering system in the northern Northumberland Basin. The two basins are separated by the Cheviot High that was uplifting during this time confining the fluvial system to within its margin (Howell et al. 2019; Howell et al. 2020). This is seen at the Bowden Doors location (Figure 6.5).

Throughout most of the outcrop of the Fell Sandstone, preserved channel thicknesses and bar-top heights give an estimate for flow depth of approximately three to four metres. This is supported by maximum flow depth reconstructions of cross-bed thicknesses using Bridge and Tye (2000). However, at the point of confinement along the Cheviot High, similar observations are observed to those made by Wang et al. (2020) from the Spireslack Sandstone. Here bar-top heights are approximately two and a half metres. However, reconstructed flow depths are considerably higher by a factor of at least two (Figure 6.5). This may be attributed to the overestimation of flow depths (Section 4.8.1) although the regularity with which confined systems show this characteristic suggests otherwise, given this is noted throughout all incised valley successions studied by Wang et al. (2020) and in the Spireslack Sandstone succession.

Furthermore, the range in maximum flow depth reconstruction seen in more braided proximal regions (Murton High Crag) is approximately five metres (Figure 6.5), and in more meandering sections (Long Crag and Bryness) is approximately four metres. The range in maximum flow depths observed from cross-bed thicknesses in Bowden Doors is much smaller, at three metres.

Figure 6.5 – Data from the Fell Sandstone taken from Howell et al. (2020). The logged sections show proximal (left) to distal (right) variations in sedimentation. Palaeocurrent data show the significant divergence of the fluvial system around the Cheviot High at Bowden Doors. Maximum reconstructed flow depths and channel thicknesses plotted with relative distance downstream. Finally, a small schematic example of the plan view evolution of the Fell Sandstone fluvial system (Modified from Howell et al. 2019).



6.1.3 *Unconfined and confined multi-storey sandbodies*

The nature morphological nature of unconfined fluvial systems maybe scale dependant, based upon the observations above. However, in the absence of large scale-satellite imagery or in limited sub-surface and outcrop datasets architectural element make-up may provide an insight into the nature of a multi-storey sandbodies' lateral extent. If a body is unconfined, then stream capture may provide a principle control upon sedimentation and it should not be assumed without significant hydrodynamic constraints that a single fluvial system is in operation within the studied interval. The identification of upstream accretion elements may help to identify such hydrodynamic fluctuations.

Confined fluvial systems may exhibit larger water depths regardless of downstream controls such as transgressions and backwater reach affects. From the material presented above, the observation of deep confined fluvial systems may occur in any reach of a fluvial system. Sediment supply within these regions may, without forced regression, be higher relative to the speed of flow through the concentration of the flow laterally. This relative concentration may provide pseudo-high sediment load conditions inhibiting bedform preservation, but yet not provide enough sediment to construct barforms to the total water depth. The nature of confined fluvial systems being deeper than the surrounding unconfined system (if there is any) may be determined through the use of hydrodynamic reconstructions and their comparison to bar-top heights.

Diagnostic features

Upstream accretion elements occur as a result of bank-low discharge when bedforms amalgamate on the upstream margin of unit bars and stack to the water depth (Bristow, 1993; Skelly et al., 2003; Wang and Plink-Björklund, 2019b). These elements have been found within modern analogues such as the Niobrara River, Nebraska (Skelly et al., 2003) and the Jamuna River (Ashworth et al., 2000). The stacking nature on the upstream margin of a unit bar provide the initial formation of compound barforms and change the length-to-width relationship of the barform in plan-view. This can have a knock-on effect on the change in local flow conditions and may promote more lateral growth and further compound barform development (Ashworth et al., 2000). In all instances where upstream accretion elements have been identified, they are in unconfined settings. These include modern analogues such as the Niobrara River, Nebraska (Skelly et al., 2003) and the Jamuna River (Ashworth et al., 2000) and the ancient Green River Formation, Utah (Wang and Plink-Björklund, 2019b). The variable discharge required to develop such barforms, and their reliance to stack to water-depth makes such accretionary unit's indicative of unconfined fluvial systems.

Confined fluvial systems may be characterised by greater water depths in maximum flow depths reconstructions from cross-set thicknesses (using methods such as Bridge and Tye (2000)) compared to those of the bar-top heights. This is due to the amount of sediment in the systems being retained but the water depth being increased, therefore, cross-set thickness increases however, constructed barforms never fulfil the total vertical accommodation provided by the water depth.

Another potential diagnostic criteria for confined fluvial systems is lower variable discharge rates, as highlighted in Section 4.8.1 and as described above. This is maybe due to the increased water depths, such that any fluctuation in flow in shallower water depths will have a greater effect on the cross-set thicknesses produced at the sediment water interface as it occupies a greater percentage of the total water column. However, in larger water depths such a change will have less of an affect upon cross-set thicknesses as the fluctuation has a minimal effect on the flow's sediment water interface.

6.2 Reservoir modelling of multi-storey sandbodies

The first thing to ascertain in the production of reservoir models is the heterogeneity being constrained. This is dependent upon the depositional environment, scale of observation, data density, resolution of model and level of depositional complexity (Ringrose and Bentley 2015). This study (Chapter 5) constrains a different set of architectural elements based upon notable differences in sorting. The models presented here do not constrain upstream accretion elements as they are characteristically very similar to the downstream accretion element, at the facies scale. The models instead constrain a thalweg bedform complex which consist of moderately high sediment load material migrating through the middle of the channel cut-and-fill element and are extremely poorly sorted (Eschard et al. 1998). This enables a more accurate constraint on the petrophysical properties to be applied.

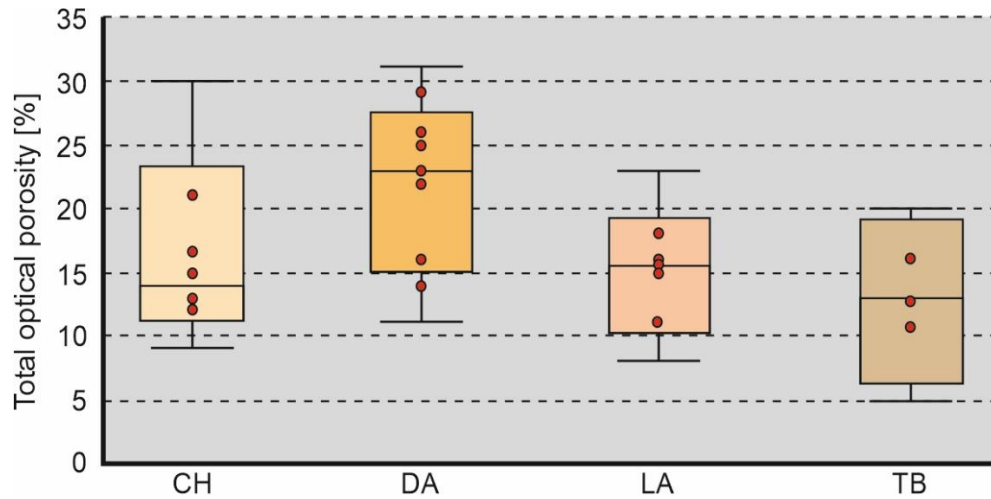


Figure 6.5 - Total optical porosity measurements, derived using JPor (Grove and Jerram 2011), taken from samples collected from the Lower Castlegate data set. Total optical porosity is in two-dimensions and is plotted as all locations based upon the architectural element.

6.2.1 Training image development for confined multi-storey sandbodies

The production of three-dimensionally constrained multi-point statistics reservoir models (Chapter 5) was on balance (visually and statistically) best suited for the reproduction of the unconfined Tuscher Canyon section, when compared to those generated by OBM and SIS. The TI was built using depositional conditioning of a single zone. However, the construction of a TI and a model for a confined multi-storey sandbody is not presented in any major detail here. This section highlights the nature of their construction.

The modelling of confined and unconfined multi-storey sandbodies is best represented through MPS, particularly in the realistic reproduction of architectural element thickness. MPS may be more suited for the development of effective drilling plans, given the realistic nature of its connectivity results (Section 5.8.4). However, in order to de-risk any

assumptions upon the reservoir and the choice of the MPS algorithm SIS and OBM should also be constructed. With this suite of models, reliable statistical constraints such as net-connectivity can be used.

The construction of confined and unconfined multi-storey sandbody reservoir models is dependent upon their nature. For unconfined systems a single zone, temporally, is sufficient. However, with the affects of stream capture, if imaged within the data, spatial zoning should be considered. For confined fluvial systems, depending upon their temporal evolution, multiple zones should be used in the development of such models. To constrain these possible differences, the modeller must define whether the multi-storey sandbody is confined or unconfined. As stated above, in the presence of upstream accretion elements (although not used directly in the construction of reservoir models) the spatial change in architecture need to be considered in the data, if not present then the modeller can build an MPS model with a single zone, as the multi-storey sandbody is likely unconfined. If upstream accretion is not present and cross-set thicknesses provide limited variance and are significantly overestimating the maximum reconstructed flow depths, when compared to bar-top heights, then temporal zonations should be considered as it is likely the multi-storey sandbody is confined.

6.3 Study limitations

The study of confined fluvial systems (Chapter 4) was limited by the poor outcrop exposure across the basin and poor data with regards to coal board borehole data. Whilst the engineered faces of the SGP provided excellent exposure from which this study is based,

comments on basin wide fluvial palaeomorphology and sandbody distribution is limited to rather poorly described borehole cutting descriptions. Furthermore, given the limitations of the study, and the interpretation of an incised valley fill succession, this work does not take into consideration the backwater reach effects associated with such an environment. Due to this, comparisons made in section 6.1.2 have attempted to utilise further examples both proximal and distal of backwater reach effects and to determine common diagnostic criteria for confined fluvial systems.

The work on determining the avulsion styles of confined and unconfined multi-storey sandbodies has been limited by outcrop orientation relative to palaeoflow directions and the erosional extent of geobody margins. If the amalgamated nature of the studied sandbodies was more limited, then an aggradation index (Gibling 2006) study would have been undertaken to provide insight into the avulsive nature of the deposits.

Overall, the results showcased in this thesis apply solely to the MSBs generated by perennial fluvial systems. This should be taken into account as hydrodynamic fluctuations, which may be diagnostic criteria for MSB confinement, are characteristic of ephemeral fluvial systems. Further caution is required when using maximum flow depth reconstructions, and indeed any empirical relationship derived from nature. The use of flow reconstructions from cross-set thicknesses is limited by variations in aggradation rate, angles of bedform climb and the conformity of cosets (Paola and Borgman 1991), all having a control upon preserving cross-set thickness. A second limitation to this methodology is flow depth estimations can lead to

overestimations of palaeoflow depths. This is due to the preferential preservation of thicker dune deposits (Holbrook and Wanas 2014).

Despite showcasing the successful model generation using modern and ancient data together to produce a three-dimensional TI, there are limitations in the use of modern and ancient datasets for depositional conditioning and TI development. The two systems correspond to two different timescales of observation, and it is difficult to determine whether the sedimentation rate across the two systems is equal. The Jamuna River represents a snap shot of a specific fluvial system, whereas the Castlegate at Tuscher Canyon provides a much broader view of time but preserved as snapshots of past depositional events.

The scales of analyses with the preserved volumes of the Castlegate and the actively depositing modern day Jamuna River may provide further limitations to the study. These must be considered as an unavoidable limitation in the analysis of sedimentary environments (Miall, 2006). Furthermore, despite the fact that both datasets are proximal of the backwater reach (Samuels, 1989; Ashworth *et al.*, 2000; Best *et al.*, 2003; Marra *et al.*, 2014; Trower *et al.*, 2018), differences in the proximity of the data to their respective reaches is not considered in this study. However, differences in proximity to the backwater reach may add natural variability to TIs and increase their recyclability, a key issue TI production and use (Ringrose and Bentley 2015; Tahmasebi 2018).

Furthermore, the generated depositional conditioning example above is limited to one outcrop and environment of deposition. How its application translates into other

environments is unknown. The generation of the models themselves, with regards to number of stochastic iterations undertaken is taken from Gooverts (1999), however, Gooverts (1999) only studied 2-point statistical methods of representing depositional environments. This study uses Boolean, multi-point and two-point statistics to generate such models, therefore, whilst the two-point SIS simulations may be statistically relevant, the number of iterations required for multi-point and Boolean simulations is unknown. It is therefore possible that the number of model iterations for the other two methods is insufficient.

7 Conclusions

The meso-scale architectural elements that comprise confined and unconfined multi-storey sandbodies, whilst similar, are dependent upon the lateral confinement of a multi-storey sandbody during deposition. These works use multiple approaches to analyse the controls on deposition and preservation of architectural elements within unconfined and confined MSBs. This study demonstrates that downstream profiles, discharge variations, avulsion scales and subsidence rates play a key role in the preservation of fluvial architectural elements.

In unconfined systems, discharge variability and position along the fluvial profile provide control over the upstream accretion of barforms, whereas subsidence rates control the preservation of lateral accretion and overbank elements. Such an understanding may prove critical as a diagnostic feature of the lateral confinement on a fluvial system and therefore provide insight into sandbody location and palaeogeographic interpretation in basin analysis and basin-scale interpretations of sequence stratigraphy. Unconfined fluvial MSBs can be identified by palaeohydrodynamic reconstructions, based upon their variable discharge. Given the nature of formation of upstream accreting architectural elements, these can be a key diagnostic criteria in the identification of unconfined MSBs, where outcrop and spatial data is limited.

Confined multi-storey sandbodies may have a relatively high-sediment load and may also exhibit water depths greater than analysis of the bar tops suggest. Unit bar and high

sediment load conditions dominate deposition in the basal portion of confined fluvial systems. Consistent flow depths are also highlighted as a potential diagnostic criteria for the fluvial system confinement, where any fluctuation proximal or distal of the confinement would be minimal in comparison to the larger water depths compared to the sediment available for deposition.

Results showed MPS and OBM models to have more geologically realistic element distributions, in the stochastic modelling of multi-storey sandbodies. Whilst similar connectivity means were achieved, through the MPS and SIS generations, smaller ranges were achieved through OBM and MPS-generated reservoir models. Given the findings of this thesis on balance of qualitative and quantitative analysis the results showed that MPS models could be generated in a reproducible and realistic manner. The results demonstrated real potential for the use of outcrop data libraries to improve reservoir model of architectural element scale heterogeneity.

The construction of confined and unconfined multi-storey sandbody reservoir models is dependent upon their nature. The affects of stream capture, if imaged within the data, in unconfined multi-storey sandbodies may require spatial zonation of a model. For confined fluvial systems, depending upon their temporal evolution, multiple temporal zones should be used in the development of such models. To constrain the applications of differing model requirements a multi-storey sandbody should be defined as confined or unconfined. In the presence of upstream accretion elements, the spatial changes in architecture need to be considered in the data, if not present then the modeller can build an MPS model with a single

zone, as the multi-storey sandbody is likely unconfined. If upstream accretion is not present and cross-set thicknesses provide limited variance and are significantly overestimating the maximum reconstructed flow depths, when compared to bar-top heights, then temporal zonations should be considered as it is likely the multi-storey sandbody is confined.

7.1 Further work

This work has demonstrated that there are key diagnostic features within the classification of architectural elements, that dictate confined and unconfined multi-storey sandbodies interpretation and how they can most realistically be represented numerically. However, various questions and research niches have been identified. This section describes the further work that could be done to answer these questions.

7.1.1 *Multi-storey sandbodies*

This study has only presented a limited number of examples from multi-storey sandbodies. Whilst the observations made herein honour the data incorporated, significant investigation into more modern and ancient systems should be undertaken across different climatic and tectonic regimes. This will enable broader scale controls of these deposits to be commented on more rigorously, and discussions on how these systems preserve with regards to avulsion frequencies be made. From this dataset an attempt to construct a large secondary dataset of confined and unconfined fluvial systems hydrodynamic regimes should be made to develop a test base for the observations highlighted in section 6.1.3.

Finally, given the significance of upstream accretion elements as a potential diagnostic tool for the interpretation of potential confinement. Work should be undertaken to establish the genesis and characterisation of these elements in a self-contained study. Once the nature of the element is critically understood, studies on how common the elements are, their formation in variable discharge systems, their implications for palaeogeographical and fluvial sedimentological understanding can be undertaken.

7.1.2 Reservoir modelling

Stochastic simulations

Rigorous work into how many stochastic realisations are required to make a statistically relevant dataset is currently lacking. Work to continue from Gooverts (1999) attempt at validating the number of realisations required to develop an effective reservoir model suite using two-point simulation should be done applying the techniques to multi-point statistical simulations and object-based modelling algorithms. Once this has been done an investigation into the controls onto number of iterations should be undertaken. For instance, does increased heterogeneity or the size of heterogeneity provide a control? If so, does this mean that differing depositional environments require differing numbers of model iterations for the establishment of a statistically rigorous risk profile?

Depositional conditioning

Subsequent work on depositional conditioning would benefit from projecting the input cross-sectional and plan-view planes through the three-dimensional volume in an automated fashion, projecting logical rules dictated by the depositional conditioning throughout the TI.

This may be a future application for how machine learning algorithms receive and read two-dimensional data and use multi-iterative analysis in their reproduction of sedimentary products into three dimensional volumes. This could be done effectively with the incorporation of a two-dimensional predictive panel-forming algorithm based upon empirical relationships found in nature, such as those presented by Bridge and Tye (2000), with the establishment of two-dimensional control as a conditional panel, built using GeoStatsPy python package (coupled with those of input pseudo-well data from analogue outcrop). This could then be translated into three dimensions where the user can provide co-ordinates to determine the position of elements in three-dimensions, using the GemPy python package as a basis for three-dimensional visualisation.

Finally, a test of the depositional conditioning methodology would be useful. How does the technique stand up to further data inclusion? At what point does the model become over-saturated in data? If it does (which is the current hypothesis), would it then be more realistic to use library-based suites such as FAKTS (Colombera et al. 2012). Trials of depositional conditioning to other depositional environments should be conducted, where a TIs for deepwater, carbonate and shoreface successions are made. Results presented herein (Chapter 5) applications to environments that are composed of discrete geobodies such as carbonate environments and deepwater mass transport complexes may be successful. However, application may be more difficult to those that show definitive non-stationarity and are better modelled for truncated gaussian simulation, such as shoreface successions.

7.2 Summary

This thesis demonstrates that confined and unconfined fluvial multi-storey sandbodies, whilst appearing visually similar in limited outcrops, have genetic differences that can prove diagnostic in their identification. Unconfined fluvial systems may have been formed by more hydrodynamically varied fluvial systems, with stream capture playing a large control upon the discharge rates along the fluvial systems course. The nature of the unconfined flow and variable discharge promotes the deposition of upstream accretion elements, a diagnostic feature of this type of system. Confined multi-storey sandbodies, however, show a different discharge regime that is more stable, relative to the amount of sediment within the system. This means that the system has water depths too great for sediment to stack to, impeding the depth to which barforms can build and therefore the genesis of upstream accretion elements. This is a diagnostic feature of confined systems, with no upstream accretion elements and maximum flow depth reconstructions showing a significant difference from those of maximum barform heights. Finally, this work has demonstrated a more realistic method of representing such barforms and fluvial multi-storey sandbodies numerically in reservoir modelling workflows. The use of depositionally conditioned TIs in MPS, over two-dimensional TIs, has proven to provide realistic and statistically accurate representations of potential fluvial reservoirs. Furthermore the use of such MPS techniques provides better compromise between visual and statistical representations of such environments compared to the more traditional SIS or OBM techniques.

8 References

- Adams, M.M. and Bhattacharya, J.P., 2005. No change in fluvial style across a sequence boundary, Cretaceous Blackhawk and Castlegate Formations of central Utah, USA. *Journal of Sedimentary Research*, **75**, (6), 1038-1051.
- Alexander, J. and Fielding, C., 1997. Gravel antidunes in the tropical Burdekin River, Queensland, Australia. *Sedimentology*, **44**, (2), 327-337.
- Alexander, J. and Leeder, M.R., 1987. Active tectonic control on alluvial architecture. In: Ethridge, F.G. and Flores, R.M. and Harvey, M.D. (Eds.). *Recent developments in fluvial sedimentology*. Society of Economic Palaeontologists and Mineralogists, **39**, 243-252.
- Allen, J.R.L., 1967. Notes on some fundamentals of palaeocurrent analysis, with reference to preservation potential and sources of variance. *Sedimentology*, **9**, 75-88.
- Allen, J., 1970. Studies in fluvial sedimentation: a comparison of fining-upwards cyclothems, with special reference to coarse-member composition and interpretation. *Journal of Sedimentary Research*, **40**, (1), 298-323.
- Allen, J., 1982. *Sedimentary structures: their character and physical basis*, vol. I. *Developments in Sedimentology*, **30A**, Elsevier Scientific Publishing Company, Amsterdam.
- Allen, J., 1983. Studies in fluvial sedimentation: bars, bar-complexes and sandstone sheets (low-sinuosity braided streams) in the Brownstones (L. Devonian), Welsh Borders. *Sedimentary Geology*, **33**, (4), 237-293.
- Almeida, R.P., Freitas, B.T., Turra, B.B., Figueiredo, F.T., Marconato, A., Janikian, L., 2016. Reconstructing fluvial bar surfaces from compound cross-strata and the interpretation of bar accretion direction in large river deposits. *Sedimentology*, **63**, 609-628.
- Armitage, J.J., Duller, R.A., Whittaker, A.C. and Allen, P.A., 2011. Transformation of tectonic and climatic signals from source to sedimentary archive. *Nature Geoscience*, **4**, (4), 231-235.
- Arnott, R., Zaitlin, B. and Potocki, D., 2002. Stratigraphic response to sedimentation in a net-accommodation-limited setting, Lower Cretaceous Basal Quartz, south-central Alberta. *Bulletin of Canadian Petroleum Geology*, **50**, (1), pp. 92-104.
- Aschoff, J., Steel, R., 2011a. Anomalous clastic wedge development during the Sevier-Laramide transition, North American Cordilleran foreland basin, USA. *AAPG Bulletin*, **123**, 1822-1835.
- Aschoff, J.L., Steel, R.J., 2011b. Anatomy and development of a low-accommodation clastic wedge, upper Cretaceous, Cordilleran Foreland Basin, USA. *Sedimentary Geology*, **236**, 1-24.

- Ashley, G.M., 1990. Classification of large-scale subaqueous bedforms: a new look at an old problem. *Journal of Sedimentary Research*, **60**, (1), 160-172.
- Ashworth, P.J., Best, J.L., Roden, J.E., Bristow, C.S., Klaassen, G.J., 2000. Morphological evolution and dynamics of a large, sand braid-bar, Jamuna River, Bangladesh. *Sedimentology*, **47**, 533-555.
- Ashworth, P.J., Sambrook Smith, G.H., Best, J.L., Bridge, J.S., Lane, S.N., Lunt, I.A., Reesink, A.J., Simpson, C.J., Thomas, R.E., 2011. Evolution and sedimentology of a channel fill in the sandy braided South Saskatchewan River and its comparison to the deposits of an adjacent compound bar. *Sedimentology*, **58**, 1860-1883.
- Aslan, A. and Blum, M.D., 1999. Contrasting styles of Holocene avulsion, Texas Gulf coastal plain, USA. *Fluvial sedimentology VI*, 193-209.
- Baas, J.H., 1994. A flume study on the development and equilibrium morphology of current ripples in very fine sand. *Sedimentology*, **41**, (2), 185-209.
- Baas, J.H., 1999. An empirical model for the development and equilibrium morphology of current ripples in fine sand. *Sedimentology*, **46**, (1), 123-138.
- Baas, J.H., Oost, A.P., Sztano, O.K., Boer, P.L. and Postma, G., 1993. Time as an independent variable for current ripples developing towards linguoid equilibrium morphology. *Terra Nova*, **5**, (1), 29-35.
- Barazzetti, L., Scaioni, M. and Remondino, F., 2010. Orientation and 3D modelling from markerless terrestrial images: combining accuracy with automation. *The Photogrammetric Record*, **25**, (132), 356-381.
- Batezelli, A., Ladeira, F.S.B., Nascimento, D.L.D., Da Silva, M.L., 2019. Facies and palaeosol analysis in a progradational distributive fluvial system from the Campanian–Maastrichtian Bauru Group, Brazil. *Sedimentology* **66**, 699-735.
- Bemis, S.P., Micklethwaite, S., Turner, D., James, M.R., Akciz, S., Thiele, S.T. & Bangash, H.A. 2014. Ground-based and UAV-based photogrammetry: A multi-scale, high-resolution mapping tool for structural geology and paleoseismology. *Journal of Structural Geology*, **69**, 163-178.
- Best, J., 2005. The fluid dynamics of river dunes: A review and some future research directions. *Journal of Geophysical Research: Earth Surface*, **110**, (F4).
- Best, J.L., Ashworth, P.J., Bristow, C.S. and Roden, J., 2003. Three-dimensional sedimentary architecture of a large, mid-channel sand braid bar, Jamuna River, Bangladesh. *Journal of Sedimentary Research*, **73**, (4), 516-530.
- Bhattacharya, J.P., 2011. Practical problems in the application of the sequence stratigraphic method and key surfaces: integrating observations from ancient fluvial–deltaic wedges with Quaternary and modelling studies. *Sedimentology*, **58**, (1), pp. 120-169.

- Bhattacharya, J.P., Copeland, P., Lawton, T.F. and Holbrook, J., 2016. Estimation of source area, river paleo-discharge, paleoslope, and sediment budgets of linked deep-time depositional systems and implications for hydrocarbon potential. *Earth-Science Reviews*, **153**, 77-110.
- Bilmes, A., D'Elia, L., Lopez, L., Richiano, S., Varela, A., Alvarez, M. P., Bucher, J., Eymand, I., Muravichik, M., Franzese, J., Ariztegui, D. 2019. Digital outcrop modelling using "structure-from-motion" photogrammetry: Acquisition strategies, validation and interpretations to different sedimentary environments. *Journal of South American Earth Science*, 96, 102325.
- Bilton, J. N. 2019. The sub-seismic stratigraphic architecture of an IVF succession from the Middle Carboniferous of the Midland Valley, Scotland. MSc Thesis. Keele University. *Unpublished*.
- Blum, M.D., 1993. Genesis and Architecture of Incised Valley Fill Sequences: A Late Quaternary Example from the Colorado River, Gulf Coastal Plain of Texas, Chapter 10 In: Weimer, P. and Posamentier, H.W., *Recent Applications of Siliciclastic Sequence Stratigraphy*, **M58**.
- Blum, M., 2001. Importance of falling stage fluvial deposition: Quaternary examples from the Texas Gulf Coastal Plain and Western Europe. *Seventh International Conference on Fluvial Sedimentology, Lincoln*, August 2001, 6-10.
- Blum, M.D. and Aslan, A., 2006. Signatures of climate vs. sea-level change within incised valley-fill successions: Quaternary examples from the Texas Gulf Coast. *Sedimentary Geology*, **190**, 177-211.
- Blum, M.D. and Törnqvist, T.E., 2000. Fluvial responses to climate and sea-level change: a review and look forward. *Sedimentology*, **47**, 2-48.
- Bowman, M.B.J., McClure, N.M., Wilkinson, D.W., 1993. Wytch Farm oilfield: deterministic reservoir description of the Triassic Sherwood Sandstone. In: Parker, J.R. (Ed.) *Petroleum geology of Northwest Europe Proceedings of the 4th conference*. Geological Society of London, Petroleum Geology Conference series, 1513-1517.
- Boyd, R., Dalrymple, R.W. and Zaitlin, B.A., 2006. Estuarine and incised-valley facies models. In: Posamentier, H.W. and Walker, R.G. (Eds.), *Facies Models Revisited*, Society of Sedimentary Geology, Special Publication, **84**, 171.
- Boyd, R., Diessel, C., Wadsworth, J., Chalmers, G., Little, M., Leckie, D. and Zaitlin, B., 1999. Development of a non-marine sequence stratigraphic model. *American Association of Petroleum Geologists Annual Meeting 1999*, A15.
- Bridge, J., 1993. The interaction between channel geometry, water flow, sediment transport and deposition in braided rivers. In: Best, J.L., Bristow, C.S. (Eds.), *Braided Rivers*. Geological Society Of London, Special Publication 75, 13-71.
- Bridge, J.S. and Jarvis, J., 1976. Flow and sedimentary processes in the meandering river South Esk, Glen Clova, Scotland. *Earth surface processes*, **1**, (4), 303-336.

- Bridge, J.S., 1993. Description and interpretation of fluvial deposits: a critical perspective. *Sedimentology*, **40**, (4), 801-810.
- Bridge, J.S., 2009. Rivers and floodplains: forms, processes, and sedimentary record. John Wiley & Sons.
- Bridge, J.S., Leeder, M.R., 1979. A simulation model of alluvial stratigraphy. *Sedimentology*, **26**, 617–644.
- Bridge, J.S., MacKey, S.D., 1992. A theoretical study of fluvial sandstone body dimensions, In: Flint, S.S., Bryant, I.D., (Eds.), *The Geological Modelling of Hydrocarbon Reservoirs and Outcrop Analogues*. IAS, Special Publications, 15, 213–236.
- Bridge, J.S., Tye, R.S., 2000. Interpreting the dimensions of ancient fluvial channel bars, channels, and channel belts from wireline-logs and cores. *AAPG Bulletin*, **84**, 1205-1228.
- Bridge, J.S., Jalfin, G.A., Georgieff, S.M., 2000. Geometry, lithofacies, and spatial distribution of Cretaceous fluvial sandstone bodies, San Jorge Basin, Argentina: outcrop analog for the hydrocarbon-bearing Chubut Group. *Journal of Sedimentary Research*, **70**, 341-359.
- Bristow, C.S., 1987. Brahmaputra River: channel migration and deposition. Recent developments in fluvial sedimentology, SEPM, Special Publications 39.
- Bristow, C.S., 1993. Sedimentary structures exposed in bar tops in the Brahmaputra River, Bangladesh. In: Best, J.L., Bristow, C.S. (Eds.), *Braided Rivers*. Geological Society of London, Special Publication, 75, pp. 277-289.
- Bristow, C.S., 1995. Internal geometry of ancient tidal bedforms revealed using ground penetrating radar. In: Flemming, B.W., Bartoloma, A. (Eds), *Tidal signatures in modern and ancient sediments*. International Association of Sedimentologists. 24, 313-328.
- Browne, M.A.E. and Monro, S.K., 1989. Evolution of the coal basins of Central Scotland. *Congrès international de stratigraphie et de géologie du Carbonifère*, 1-19.
- Browne, M., Dean, M., Hall, I.H., McAdam, A.D., Monro, S.K. and Chisholm, J.I., 1999. A lithostratigraphical framework for the Carboniferous rocks of the Midland Valley of Scotland. Version 2.
- Buckley, S., Howell, J.A., Enge, H.D., Leren, B.L.S., Kurz, T.H., 2006. Integration of terrestrial laser scanning, digital photogrammetry and geostatistical methods for high-resolution modelling of geological outcrops, ISPRS Commission V Symposium, September 25–27. International Archives of the Photogrammetry, Remote Sensing and Spatial Information Sciences, Dresden, Germany.
- Burgess, P.M., Gayer, R.A., 2000. Late Carboniferous tectonic subsidence in South Wales: implications for Variscan basin evolution and tectonic history in SW Britain. *Journal of the Geological Society*, **157**, 93-104.
- Burnham, B.S., Hodgetts, D., 2018. Quantifying spatial and architectural relationships from fluvial outcrops. *Geosphere*, **15**, 236-253.

- Burns, C.E., Mountney, N.P., Hodgson, D.M. and Colombera, L., 2017. Anatomy and dimensions of fluvial crevasse-splay deposits: Examples from the Cretaceous Castlegate Sandstone and Neslen Formation, Utah, USA. *Sedimentary Geology*, **351**, 21-35.
- Cabello, P., Lopez, C., Gamba, N., Dussán, M.I., Torres, E., Ballesteros-Torres, C.I., Cantisano, M.T., Marfisi, N., Calvo, R., Vázquez-Taset, Y.M., Ramos, E., 2018a. An integrated approach to define new plays in mature oil basins: the example from the Middle Magdalena Valley basin (Colombia). *AAPG Bulletin*, **102**, 2201 - 2238.
- Cabello, P., Domínguez, D., Murillo-López, M.H., López-Blanco, M., García-Sellés, D., Cuevas, J.L., Marzo, M. and Arbués, P., 2018b. From conventional outcrop datasets and digital outcrop models to flow simulation in the Pont de Montanyana point-bar deposits (Ypresian, Southern Pyrenees). *Marine and Petroleum Geology*, **94**, 19-42.
- Caers, J., and Zhang, T., 2004, Multiple-point Geostatistics: A quantitative vehicle for integrating geologic analogs into multiple reservoir models, in *Integration of outcrop and modern analogs in reservoir modelling*, AAPG Memoir, **80**, 383-394.
- Caldwell, W.G.E. and Young, G.M., 2013. Structural controls in the western offshore Midland Valley of Scotland: implications for Late Palaeozoic regional tectonics. *Geological Magazine*, **150**, (4), 673-698.
- Cameron, I.B. and Stephenson, D., 1985. *British regional geology: the Midland Valley of Scotland* (No. 5). Hmsco Books.
- Cant, D.J., 1996. Sedimentological and sequence stratigraphic organization of a foreland clastic wedge, Mannville Group, Western Canada Basin. *Journal of Sedimentary Research*, **66**, (6), 1137-1147.
- Cant, D.J., Walker, R.G., 1978. Fluvial processes and facies sequences in the sandy braided South Saskatchewan River, Canada. *Sedimentology*, **25**, 625-648.
- Catuneanu, O., 2006. Sequence Models. In: *Principles of sequence stratigraphy*, Elsevier, 253.
- Catuneanu, O., 2019. Model-independent sequence stratigraphy. *Earth-science reviews*, **188**, 312-388.
- Catuneanu, O. and Sweet, A.R., 1999. Maastrichtian-Palaeocene foreland-basin stratigraphies, western Canada: a reciprocal sequence architecture. *Canadian Journal of Earth Sciences*, **36**, (5), 685-703.
- Catuneanu, O. and Elango, H.N., 2001. Tectonic control on fluvial styles: The Balfour Formation of the Karoo Basin, South Africa. *Sedimentary Geology*, **140**, (3), 291-313.
- Catuneanu, O., Galloway, W.E., Kendall, Christopher G ST C, Miall, A.D., Posamentier, H.W., Strasser, A. and Tucker, M.E., 2011. Sequence stratigraphy: methodology and nomenclature. *Newsletters on stratigraphy*, **44**, (3), 173-245.
- Chamberlin, E.P., Hajek, E.A., 2015. Interpreting paleo-avulsion dynamics from multistory sand bodies. *Journal of Sedimentary Research*, **85**, 82-94.

- Chamberlin, E.P., Hajek, E.A., 2019. Using bar preservation to constrain reworking in channel-dominated fluvial stratigraphy. *Geology*, **47**, 531-534.
- Chan, M.A. and Pfaff, B.J., 1991. Fluvial sedimentology of the Upper Cretaceous Castlegate Sandstone, Book Cliffs, Utah. In: Chidsey Jr., T.C. (Ed.). *Geology of East-Central Utah*. Utah Geological Association Special Publication 19, 95-110.
- Clymo, R.S., 1987. The ecology of peatlands. *Science Progress (1933-)*, 593-614.
- Collinson, J.D., 1970. Bedforms of the Tana river, Norway. *Geografiska Annaler: Series A, Physical Geography*, **52**, 31-56.
- Collinson, J.D.; Mountney, N. P. and Thompson, D. B. 2006. *Sedimentary Structures*, Third edition, Terra Publishing, Hertfordshire.
- Colombera, L., Mountney, N.P. and McCaffrey, W.D., 2012. A relational database for the digitization of fluvial architecture concepts and example applications. *Petroleum Geology*, **18**, 129-140.
- Colombera, L., Mountney, N.P. and McCaffrey, W.D., 2013. A quantitative approach to fluvial facies models: methods and example results. *Sedimentology*, **60**, (6), 1526-1558.
- Colombera, L., Mountney, N.P., McCaffrey, W.D., 2015. A meta-study of relationships between fluvial channel-body stacking pattern and aggradation rate: implications for sequence stratigraphy. *Geology*, **43**, 283-286.
- Colombera, L., Mountney, N.P., Hodgson, D.M. and McCaffrey, W.D., 2016a. The Shallow-Marine Architecture Knowledge Store: a database for the characterization of shallow-marine and paralic depositional systems. *Marine and Petroleum Geology*, **75**, 83-99.
- Colombera, L., Mountney, N.P., Howell, J.A., Rittersbacher, A., Felletti, F. and McCaffrey, W.D., 2016b. A test of analog-based tools for quantitative prediction of large-scale fluvial architecture. *AAPG Bulletin*, **100**, 237-267.
- Comunian, A., Renard, P., and Straubhaar, J., 2012, 3D multiple-point statistics simulation using 2D TIs, *Computer Geoscience*, **40**, 49-65.
- Cope, J.C.W., Ingham, J.K., and Rawson, P.F. 1992. *Atlas of palaeogeography and lithofacies*. Geological Society of London Memoir, 13.
- Corbett, P.W., Hamdi, H. and Gurav, H., 2012. Layered fluvial reservoirs with internal fluid cross flow: a well-connected family of well test pressure transient responses. *Petroleum Geoscience*, **18**, (2), 219-229.
- Corfield, S.M., Gawthorpe, R.L., Gage, M., Fraser, A.J. and Besly, B.M., 1996. Inversion tectonics of the Variscan foreland of the British Isles. *Journal of the Geological Society*, **153**, (1), 17-32.
- Costello, W.R., 1974. *Development of bed configurations in coarse sands*, Massachusetts Institute of Technology.

- Cowan, E., 1991. The large-scale architecture of the fluvial Westwater Canyon Member, Morrison Formation (Upper Jurassic), San Juan Basin, New Mexico. In: Miall, A.D., Tyler, N. (Eds) *The three-dimensional facies architecture of terrigenous clastic sediments and its implications from hydrocarbon discovery and recovery. Concepts in Sedimentology and Paleontology, SEPM*, **3**, 80-93.
- Cross, T.A., 1986. Tectonic controls of foreland basin subsidence and Laramide style deformation, western United States. *Foreland basins*, 13-39.
- Curry, J.R., 1956. The analysis of two-dimensional orientation data. *Journal of Geology*, **64**, 117-131.
- Dahle, K., Flesja, K., Talbot, M. and Dreyer, T., 1997. Correlation of fluvial deposits by the use of Sm-Nd isotope analysis and mapping of sedimentary architecture in the Escanilla Formation (Ainsa Basin, Spain) and the Statfjord Formation (Norwegian North Sea), *Sixth International Conference on Fluvial Sedimentology*, Cape Town, 46.
- Daly, C. and Caers, J., 2010. Multi-point geostatistics—an introductory overview. *First Break*, **28**, (9), 39-47.
- DeCelles, P.G., 2004. Late Jurassic to Eocene evolution of the Cordilleran thrust belt and foreland basin system, western USA. *American Journal of Science*, **304**, 105-168.
- DeCelles, P.G., Giles, K.A., 1996. Foreland basin systems. *Basin research*, **8**, 105-123.
- Deutsch, C.V. and Tran, T.T., 2002. FLUVSIM: a program for object-based stochastic modeling of fluvial depositional systems. *Computers & Geosciences*, **28**, (4), 525-535.
- Deutsch, C.V. and Wang, L., 1996. Hierarchical object-based stochastic modeling of fluvial reservoirs. *Mathematical geology*, **28**, (7), 857-880.
- Deutsch, C.V., 2006, A sequential indicator simulation program for categorical variables with point and block data: BlockSIS, *Computer and Geoscience*, **10**, 1669-1681.
- Deutsch, C.V., and Journal, A., 1992, *GSLIB: Geostatistical Software Library and User's Guide*, Oxford University Press, New York.
- Dickinson, W.R., Klute, M.A., Hayes, M.J., Janecke, S.U., Lundin, E.R., McKittrick, M.A. and Olivares, M.D., 1988. Paleogeographic and paleotectonic setting of Laramide sedimentary basins in the central Rocky Mountain region. *Geological Society of America Bulletin*, **100**, (7), 1023-1039.
- Dickinson, W.R., Klute, M.A., Swift, P.N., 1986. The Bisbee basin and its bearing on Late Mesozoic paleogeographic and paleotectonic relations between the Cordilleran and Caribbean regions. In: P.L. Abbott (Ed.), *Cretaceous Stratigraphy, Western North America. Pacific Sect., SEPM*, 51-62.
- Dubrule, O., 1998. *Geostatistics in petroleum geology*. AAPG Course Notes 38, 52.
- Durkin, P.R., Boyd, R.L., Hubbard, S.M., Shultz, A.W. and Blum, M.D., 2017. Three-dimensional reconstruction of meander-belt evolution, Cretaceous McMurray

- Formation, Alberta foreland basin, Canada. *Journal of Sedimentary Research*, **87**, (10), 1075-1099.
- Durkin, P.R., Hubbard, S.M., Holbrook, J. and Boyd, R., 2018. Evolution of fluvial meander-belt deposits and implications for the completeness of the stratigraphic record. *GSA Bulletin*, **130**, (5-6), 721-739.
- Ellen, R., Browne, M.A.E., Mitten, A.J., Clarke, S.M., Leslie, A.G., Callaghan, E., 2019. Sedimentology, architecture and depositional setting of the fluvial Spireslack Sandstone of the Midland Valley, Scotland: insights from the Spireslack surface coal mine. In: Corbett, P.W.M., Owen, A., Hartley, A.J., Pla-Pueyo, S., Barreto, D., Hackney, C., Kape, S.J. (Eds.), *Rain, Rivers and Reservoirs*. Geological Society of London Special Publication, 488.
- Emery, D. and Myers, K., 2009. *Sequence stratigraphy*. John Wiley & Sons, Oxford.
- Enge, H.D., Buckley, S.J., Rotevatn, A. and Howell, J.A., 2007. From outcrop to reservoir simulation model: Workflow and procedures. *Geosphere*, **3**, (6), 469-490.
- Eschard, R., Lemouzy, P., Bacchiana, C., Desaubliaux, G., Parpant, J. and Smart, B., 1998. Combining sequence stratigraphy, geostatistical simulations, and production data for modelling a fluvial reservoir in the Chaunoy field (Triassic, France). *AAPG Bulletin*, **82**, (4), 545-568.
- Ethridge, F.G. and Schumm, S.A., 1978. Reconstructing paleochannel morphologic and flow characteristics. *Fluvial Sedimentology*. Canadian Society of Petroleum Geologists, Memoir 5, 703-721.
- Ethridge, F. and Schumm, S., 2007. Fluvial seismic geomorphology: a view from the surface. *Geological Society, London, Special Publications*, **277**, (1), 205-222.
- Falivene, O., Arbues, P., Gardiner, A., Pickup, G., Munoz, J.A. and Cabrera, L., 2006. Best practice stochastic facies modeling from a channel-fill turbidite sandstone analog (the Quarry outcrop, Eocene Ainsa basin, northeast Spain). *AAPG Bulletin*, **90**, (7), 1003-1029.
- Fanti, F. and Catuneanu, O., 2010. Fluvial sequence stratigraphy: The Wapiti Formation, west-central Alberta, Canada. *Journal of Sedimentary Research*, **80**, (4), 320-338.
- Favalli, M., Fornaciai, A., Isola, I., Tarquini, S. and Nannipieri, L., 2012. Multiview 3D reconstruction in geosciences. *Computers & Geosciences*, **44**, 168-176.
- Fielding C.R., Ashworth P.J., Best J.L., Prokocki E.W., Sambrook Smith G.H., 2012. Tributary, distributary and other fluvial patterns: What really represents the norm in the continental rock record? *Sedimentary Geology*, **261–262**, 15–32.
- Fielding C.R., Paola C., 2013. Sequence boundaries generated by climate change. Proceedings of the 10th International Conference on Fluvial Sedimentology, Leeds, UK, 14-19th, 305-306.

- Fielding, C.R., Ashworth, P.J., Best, J.L., Prokocki, E.W. and Smith, G.H.S., 2012. Tributary, distributary and other fluvial patterns: What really represents the norm in the continental rock record? *Sedimentary Geology*, **261**, 15-32.
- Floyd, J.D., 1994. The derivation and definition of the 'Southern Upland Fault': a review of the Midland Valley–Southern Uplands terrane boundary. *Scottish Journal of Geology*, **30**, (1), 51-62.
- Fouch, T.D., Lawton, T.F., Nichols, D.J., Cashion, W.B. and Cobban, W.A., 1983. Patterns and timing of synorogenic sedimentation in Upper Cretaceous rocks of central and northeast Utah. Mesozoic Paleogeography of the West-Central United States: Rocky Mountain Symposium. Rocky Mountain Section (SEPM). 305-336.
- Fouch, T.D., Lawton, T.F., Nichols, D.J., Cashion, W.B. and Cobban, W.A., 1983. Patterns and timing of synorogenic sedimentation in Upper Cretaceous rocks of central and northeast Utah. In: Reynolds, M.W., Dolly, E.D. (Eds.), Mesozoic Paleogeography of the West Central United States, SEPM. Rocky Mountain Section. Second Rocky Mountain Paleogeography Symposium, 305-336.
- Fraser, A.J. and Gawthorpe, R.L., 1990. Tectono-stratigraphic development and hydrocarbon habitat of the Carboniferous in northern England. *Geological Society, London, Special Publications*, **55**, (1), pp.49-86.
- Friend, P.F., 1983. Towards the field classification of alluvial architecture or sequence. In: Collinson, J.D. and Lewin, J. (Eds.) *Modern and ancient fluvial systems*, Special Publications, International Association of Sedimentologists, 345-354.
- Frothingham, K.M. and Rhoads, B.L., 2003. Three-dimensional flow structure and channel change in an asymmetrical compound meander loop, Embarras River, Illinois. *Earth Surface Processes and Landforms: The Journal of the British Geomorphological Research Group*, **28**, (6), 625-644.
- Froude, M.J., Alexander, J., Barclay, J. and Cole, P., 2017. Interpreting flash flood palaeoflow parameters from antidunes and gravel lenses: An example from Montserrat, West Indies. *Sedimentology*, **64**, (7), 1817-1845.
- Galloway, W.E., 1981. Fluvial and Deltaic Depositional Systems and Hydrocarbon Exploration, 1-55.
- Gershenson, N.I., Soltanian, M., Ritzi, R.W. and Dominic, D.F., 2015. Understanding the impact of open-framework conglomerates on water–oil displacements: the Victor interval of the Ivishak Reservoir, Prudhoe Bay Field, Alaska. *Petroleum Geoscience*, **21**, (1), 43-54.
- Ghazi, S. and Mountney, N.P., 2009. Facies and architectural element analysis of a meandering fluvial succession: The Permian Warchha Sandstone, Salt Range, Pakistan. *Sedimentary Geology*, **221**, (1-4), 99-126.

- Ghinassi, M., 2011. Chute channels in the Holocene high-sinuosity river deposits of the Firenze plain, Tuscany, Italy. *Sedimentology*, **58**, (3), 618-642.
- Ghinassi, M. and Ielpi, A., 2018. Precambrian snapshots: Morphodynamics of Torridonian fluvial braid bars revealed by three-dimensional photogrammetry and outcrop sedimentology. *Sedimentology*, **65**, (2), 492-516.
- Ghinassi, M., Ielpi, A., 2018. Stratal Architecture and Morphodynamics of Downstream-Migrating Fluvial Point Bars (Jurassic Scalby Formation, U.K.). *Journal of Sedimentary Research*, **85**, 1123–1137.
- Ghinassi, M., Nemec, W., Aldinucci, M., Nehyba, S., Özaksoy, V. and Fidolini, F., 2014. Plan-form evolution of ancient meandering rivers reconstructed from longitudinal outcrop sections. *Sedimentology*, **61**, (4), 952-977.
- Ghinassi, M., Ielpi, A., Aldinucci, M. and Fustic, M., 2016. Downstream-migrating fluvial point bars in the rock record. *Sedimentary Geology*, **334**, 66-96.
- Ghosh P., 2000. Estimation of channel sinuosity from paleocurrent data: a method using fractal geometry. *Journal of Sedimentary Research*, **70**, 449–455.
- Gibling M.R., 2006. Width and thickness of fluvial channel bodies and valley fills in the geological record: a literature compilation and classification. *Journal of Sedimentary Research*, **76**, 731–770.
- Gibling, M.R., Fielding, C.R. and Sinha, R., 2011. Alluvial valleys and alluvial sequences: towards a geomorphic assessment. In: Davidson, S.K., Leleu, S., and North, C.P. (Eds.) *From River to Rock Record*, Society of Sedimentary Geology, Special Publication **97**, 423-447.
- Gilvear, D.J., 1993. River management and conservation issues on formerly braided river systems; the case of the River Tay, Scotland. *Geological Society, London, Special Publications*, **75**, (1), 231-240.
- Glennie, K.W. and Underhill, J.R., 1998. Origin, development and evolution of structural styles. In: Glennie, K. W. (Ed) *Petroleum geology of the North Sea: Basic concepts and recent advances*, 42-84.
- Goovaerts, P., 1997. *Geostatistics for natural resources evaluation*. Oxford University Press on Demand.
- Goovaerts, P., 1999. Impact of the simulation algorithm, magnitude of ergodic fluctuations and number of realizations on the spaces of uncertainty of flow properties. *Stochastic and Environmental Research for Risk Analysis*, **13**, (3), 161-182.
- Gorelick, N., Hancher, M., Dixon, M., Ilyushchenko, S., Thau, D. and Moore, R., 2017. Google Earth Engine: Planetary-scale geospatial analysis for everyone. *Remote Sensing Environment*, **202**, 18-27.

- Greensmith, J.T., 1965. Calciferous Sandstone Series sedimentation at the eastern end of the Midland Valley of Scotland. *Journal of Sedimentary Research*, 35, (1), pp.223-242.
- Gringarten, E. and Deutsch, C.V., 1999, January. Methodology for variogram interpretation and modeling for improved reservoir characterization. In: *Spe annual technical conference and exhibition*. Society of Petroleum Engineers.
- Grove, C., Jerram, D.A., 2011. jPOR: An ImageJ macro to quantify total optical porosity from blue-stained thin sections. *Computers and Geoscience*, 37, 1850-1859.
- Guardiano, F. and Srivastava, M., 1993. Multivariate geostatistics: Beyond bivariate moments, In: Soares, A. (Ed), *Geostatistics Troia*, 133-144.
- Guin, A.R., Ramanathan, R.W., Ritzi, D.F., Dominic, I.A., Lunt, I.A., Scheibe, T.D., Freedman, V.L., (2010). Simulating the heterogeneity in braided channel belt deposits: 2. Examples of results and comparison to natural deposits, *Water Resource Research*, 46, W04516.
- Guiseppe, A.C., Heller, P.L., 1998. Long-term river response to regional doming in the Price River Formation, central Utah. *Geology*, 26, 239-242.
- Gulliford, A.R., Flint, S.S. and Hodgson, D.M., 2017. Crevasse splay processes and deposits in an ancient distributive fluvial system: The lower Beaufort Group, South Africa. *Sedimentary Geology*, 358, 1-18.
- Guy, H.P., Simons, D.B. and Richardson, E.V., 1966. *Summary of alluvial channel data from flume experiments, 1956-61* (Vol. 462). US Government Printing Office.
- Hajek, E.A., Heller, P.L., 2012. Flow-depth scaling in alluvial architecture and nonmarine sequence stratigraphy: example from the Castlegate Sandstone, central Utah, USA. *Journal of Sedimentary Research*, 82, 121-130.
- Hajek, E.A., Huzurbazar, S.V., Mohrig, D., Lynds, R.M. and Heller, P.L., 2010. Statistical characterization of grain-size distributions in sandy fluvial systems. *Journal of Sedimentary Research*, 80, (2), 184-192.
- Haldorsen, H.H. and Damsleth, E., 1993. Challenges in reservoir characterization: GEOHORIZONS. *AAPG bulletin*, 77, (4), 541-551.
- Hampson, G.J., Davies, W., Davies, S.J, Howell, J.A., Adamson, K.J. 2005. Use of spectral gamma-ray data to refine subsurface fluvial stratigraphy: late Cretaceous strata in the Book Cliffs, Utah, USA. *Journal of the Geological Society of London*, 162, 603–621.
- Haq, B.U. and Schutter, S.R., 2008. A chronology of Paleozoic sea-level changes. *Science*, 322, (5898), 64-68.
- Hartley, A.J., Weissmann, G.S., Nichols, G.J., Warwick, G.L., 2010. Large distributive fluvial systems: characteristics, distribution, and controls on development. *Journal of Sedimentary Research*, 80, 167-183.

- Hazeldine, R.S., 1983. Fluvial bars reconstructed from a deep, straight channel. *Upper Carboniferous coalfield of Northeast England: Journal of Sedimentary Petrology*, **53**, 1233-1247.
- Heller P.L., Paola C., 1996. Downstream changes in alluvial architecture: an exploration of controls on channel-stacking patterns. *Journal of Sedimentary Research*, **66**, 297-306.
- Heller, P.L., Winslow, N.S. and Paola, C., 1986. Sedimentation and subsidence across a foreland basin, observations and results from the Western Interior. In: *Geological Society of America Abstracts with Programs*, **18**, 634.
- Heller, P.L., Angevine, C.L., Winslow, N.S. and Paola, C., 1988. Two-phase stratigraphic model of foreland-basin sequences. *Geology*, **16**, (6), 501-504.
- Henares, S., Caracciolo, L., Viseras, C., Fernández, J. and Yeste, L.M., 2016. Diagenetic constraints on heterogeneous reservoir quality assessment: A Triassic outcrop analogue of meandering fluvial reservoirs. *AAPG Bulletin*, **100**, (9), 1377-1398.
- Herbert, C., Alexander, J., Fielding, C.R., Amos, K.J., 2020. Unit bar architecture in a highly-variable fluvial discharge regime: Examples from the Burdekin River, Australia: Unit bar architecture. *Sedimentology*, **67**, 576-605.
- Hodgetts, D., Seers, T., Head, W., Burnham, B.S., 2015. High performance visualisation of multiscale geological outcrop data in single software environment. In: 77th EAGE Conference and Exhibition, Proceedings for the 2015 EAGE meeting in Madrid, Spain.
- Holbrook, J. and Wanas, H., 2014. A fulcrum approach to assessing source-to-sink mass balance using channel paleohydrologic parameters derivable from common fluvial data sets with an example from the Cretaceous of Egypt. *Journal of Sedimentary Research*, **84**, (5), 349-372.
- Holbrook, J., Scott, R.W., Oboh-Ikuenobe, F.E., 2006. Base-level buffers and buttresses: a model for upstream versus downstream control on fluvial geometry and architecture within sequences. *Journal of Sedimentary Research*, **76**, 162-174.
- Holden, L., Hauge, R., Skare, Ø., and Skorstad, A., 1998. Modeling of fluvial reservoirs with object models, *Mathematical Geology*, **30**, (5), 473-496.
- Hornung, J. and Aigner, T., 1999. Reservoir and aquifer characterization of fluvial architectural elements: Stubensandstein, Upper Triassic, southwest Germany. *Sedimentary Geology*, **129**, (3-4), 215-280.
- Hovadik, J., and Laure, D.K., 2007. Static characterizations of reservoirs: Refining the concept of connectivity and continuity, *Petroleum Geoscience*, **13**, 237-252.
- Howard, A.D., Dietrich, W.E. and Seidl, M.A., 1994. Modeling fluvial erosion on regional to continental scales. *Journal of Geophysical Research: Solid Earth*, **99**, (B7), 13971-13986.

- Howell, J.A., Martinius, A.W. and Good, T.R., 2014. The application of outcrop analogues in geological modelling: a review, present status and future outlook. Geological Society of London, Special Publication, **387**, 1-25.
- Howell, J., Eide, C., Hartley, A. 2018. No evidence for sea level fall in the Cretaceous strata of the Book Cliffs of Eastern Utah. EarthArXiv.
- Howell, L., Egan, S., Leslie, G. and Clarke, S., 2019. Structural and geodynamic modelling of the influence of granite bodies during lithospheric extension: application to the Carboniferous basins of northern England. *Tectonophysics*, **755**, 47-63.
- Howell, L., Mitten, A. J., Egan, S., Clarke, S., and Leslie, G. (2020). The influence of local low-density basement anomalies on the distribution of fluvio-deltaic sediment in rift basins: the early Carboniferous Fell Sandstone Formation, northern England. EarthArXiv.
- Hsu, K.J., 2004. *Physics of sedimentology: textbook and reference*. Springer Science & Business Media, Heidelberg.
- Hu, L.Y., Liu, Y., Scheepens, C., Shultz, A.W. and Thompson, R.D., 2014. Multiple-point simulation with an existing reservoir model as TI. *Mathematical Geology*, **46**, 227-240.
- Hubbard, S.M., Smith, D.G., Nielsen, H., Leckie, D.A., Fustic, M., Spencer, R.J. and Bloom, L., 2011. Seismic geomorphology and sedimentology of a tidally influenced river deposit, Lower Cretaceous Athabasca oil sands, Alberta, Canada. *AAPG bulletin*, *95*(7), pp.1123-1145.
- Ielpi, A., Ghinassi, M., 2014. Planform architecture, stratigraphic signature and morphodynamics of an exhumed Jurassic meander plain (Scalby Formation, Yorkshire, UK). *Sedimentology*, **61**, 1923-1960.
- Jackson, R.G., 1976. Depositional model of point bars in the lower Wabash River. *Journal of Sedimentary Research*, **46**, (3), 579-594.
- Jones, J.A. and Hartley, A.J., 1993. Reservoir characteristics of a braid-plain depositional system: the Upper Carboniferous Pennant Sandstone of South Wales. *Journal of the Geological Society of London*, **73**, 143-156.
- Jordan, D.W., Pryor, W.A., 1992. Hierarchical levels of heterogeneity in a Mississippi River meander belt and application to reservoir systems: Geologic note. *AAPG Bulletin*, **76**, 1601-1624.
- Kauffman, E.G. 1977. Geological and biological overview. *Mountain Geologist*, **14**, 79–99.
- Kauffman, E.G., Caldwell, W.G.E., 1993. The Western Interior Basin in space and time. In: Caldwell, W.G.E., Kauffman, E.G. (Eds.). *Evolution of the Western Interior Basin*, Geological Association of Canada, Special Paper, **39**, 1-30.
- Kearsey, T.I., Millward, D., Ellen, R., Whitbread, K. and Monaghan, A.A., 2019. Revised stratigraphic framework of pre-Westphalian Carboniferous petroleum system elements

- from the Outer Moray Firth to the Silverpit Basin, North Sea, UK. *Geological Society, London, Special Publications*, **471**, (1), 91-113.
- Kolla, V., Posamentier, H.W. and Wood, L.J., 2007. Deep-water and fluvial sinuous channels— Characteristics, similarities and dissimilarities, and modes of formation. *Marine and Petroleum Geology*, **24**, (6-9), 388-405.
- Koneshloo, M., Aryana, S.A. and Hu, X., 2018. The impact of geological uncertainty on primary production from a fluvial reservoir. *Petroleum Science*, **15**, (2), 270-288.
- Kraus, M.J. and Middleton, L.T., 1987. Dissected paleotopography and base-level changes in a Triassic fluvial sequence. *Geology*, **15**, (1), 18-21.
- Kupfersberger, H. and Deutsch, C.V., 1999. Methodology for integrating analog geologic data in 3-D variogram modeling. *AAPG bulletin*, **83**, (8), 1262-1278.
- Labourdette, R., 2011. Stratigraphy and static connectivity of braided fluvial deposits of the lower Escanilla Formation, south central Pyrenees, Spain. *AAPG Bulletin*, **95**, 585-617.
- Laure, D.K., and Hodavik, J., 2006. Connectivity of channelized reservoirs: A modelling approach, *Petroleum Geoscience*, **12**, 291-308.
- Lawton, T.F., 1986. Fluvial systems of the Upper Cretaceous Mesaverde Group and Paleocene North Horn Formation, central Utah: a record of transition from thin skinned to thick-skinned in the foreland region. In Peterson, J.A. (Ed.), *Paleotectonics and Sedimentation in the Rocky Mountain Region, United States: American Association of Petroleum Geologists, Memoir 41*, 423–442.
- Le Coz, M., Genthon, P., and Adler, P.M., 2011, Multiple-point statistics for modelling facies heterogeneities in a porous medium: The Komadugu-Yobe alluvium, Lake Chad Basin, *Mathematical Geology*, **43**, 861-878.
- Le Roux J.P., 1992. Determining the channel sinuosity of ancient fluvial systems from paleocurrent data. *Journal of Sedimentary Petrology*, **62**, 283-291.
- Le Roux. J.P., 1994. The angular deviation of paleocurrent directions as applied to the calculation of channel sinuosities. *Journal of Sedimentary Research*, **64**, 86-87.
- Leckie, D.A., Boyd, R., 2003. Towards a nonmarine sequence stratigraphic model. In: *American Association of Petroleum Geologists Annual Convention, Salt Lake City*, 11, 14.
- Leckie, D.A., Wallace-Dudley, K.E., Vanbeselaere, N.A. and James, D.P., 2004. Sedimentation in a low-accommodation setting: nonmarine (Cretaceous) Mannville and marine (Jurassic) Ellis Groups, Manyberries Field, southeastern Alberta. *AAPG bulletin*, **88**, (10), 1391-1418.
- Leeder, M.R., 1973. Fluvial fining-upwards cycles and the magnitude of palaeochannels. *Geological Magazine*, **110**, (3), 265-276.

- Leeder, M., 1980. On the stability of lower stage plane beds and the absence of current ripples in coarse sands. *Journal of the Geological Society*, **137**, (4), 423-429.
- Leeder, M.R., 1982. *Sedimentology: process and product*. Chapman and Hall, London.
- Leeder, M., 1983. On the dynamics of sediment suspension by residual Reynolds stresses—confirmation of Bagnold's theory. *Sedimentology*, **30**, (4), 485-491.
- Leeder, M.R., 1993. Tectonic controls upon drainage basin development, river channel migration and alluvial architecture: implications for hydrocarbon reservoir development and characterization. Geological Society of London Special Publications, **73**, 7-22.
- Leeder, M.R., 2011. *Sedimentology and sedimentary basins: from turbulence to tectonics*. 2nd edn. Wiley-Blackwell, Chichester.
- Leopold, L., Wolman, G. and Miller, J., 1964. *Fluvial processes in geomorphology*. W. H. Freeman, San Francisco.
- Lesemann, J-E., Piotrowski, J.A. & Wysota, W. 2010. "Glacial curvilineations": New glacial landforms produced by longitudinal vortices in subglacial meltwater flows. *Geomorphology*, **120**, 153-161.
- Leslie, A.G., Browne, M.A., Cain, T. and Ellen, R., 2016. From threat to future asset—The legacy of opencast surface-mined coal in Scotland. *International Journal of Coal Geology*, **164**, 123-133.
- Li, H. and White, C.D., 2003. Geostatistical models for shales in distributary channel point bars (Ferron Sandstone, Utah): From ground-penetrating radar data to three-dimensional flow modeling. *AAPG bulletin*, **87**, (12), 1851-1868.
- Li, S., Yu, X., Chen, B., Li, S., 2015. Quantitative Characterization of Architecture Elements and Their Response To Base-Level Change In A Sandy Braided Fluvial System At A Mountain Front. *Journal of Sedimentary Research*, **85**, 1258-1274.
- Littke, R., Büker, C., Hertle, M., Karg, H., Stroetmann-Heinen, V., Oncken, O., 2000. Heat flow evolution, subsidence and erosion in the Rheno-Hercynian orogenic wedge of central Europe. In: Franke, W., Haak, V., Oncken, O., Tanner, D., (Eds.), *Orogenic Processes: Quantification and Modelling in the Variscan Belt*. Geological Society of London Special Publications, **179**, 231-255.
- Liu, S. and Nummedal, D., 2004. Late Cretaceous subsidence in Wyoming: Quantifying the dynamic component. *Geology*, **32**, (5), 397-400.
- Liu, S., Nummedal, D. and Liu, L., 2011. Migration of dynamic subsidence across the Late Cretaceous United States Western Interior Basin in response to Farallon plate subduction. *Geology*, **39**, (6), 555-558.

- Long, D., 2011. Architecture and depositional style of fluvial systems before land plants: a comparison of Precambrian, early Palaeozoic and modern river deposits. *From River to Rock Record*, Society of Sedimentary Geology, Special Publication **97**, 37-61.
- López-Gómez, J., Arche, A., Vargas, H., Marzo, M., 2010. Fluvial architecture as a response to two-layer lithospheric subsidence during the Permian and Triassic in the Iberian Basin, eastern Spain. *Sedimentary Geology*, **223**, 320-333.
- Lunt, I.A., Sambrook Smith, G.H., Best, J.L., Ashworth, P.J., Lane, S.N., Simpson, C.J., 2013. Deposits of the sandy braided South Saskatchewan River: Implications for the use of modern analogs in reconstructing channel dimensions in reservoir characterization. *AAPG Bulletin*, **97**, 553-576.
- Lynds R., Hajek E., 2006. Conceptual model for predicting mudstone dimensions in sandy braided-river reservoirs. *AAPG Bulletin*, **90**, 1273-1288
- Mackin, J.H., 1948. Concept of the graded river. *Geological Society of America Bulletin*, **59**, (5), 463-512.
- Maharaja, A., 2008. TiGenerator: Object-based TI generator. *Computers & Geoscience*, **34**, (12), 1753-1761.
- Mantz, P.A., 1980. Low sediment transport rates over flat beds. *Journal of the Hydraulics Division*, **106**, (7), 1173-1190.
- Manzocchi, T., Walsh, J.J., Tomasso, M., Strand, J., Childs, C. and Haughton, P.D., 2007. Static and dynamic connectivity in bed-scale models of faulted and unfaulted turbidites. Geological Society, London, Special Publications, **292**, (1), 309-336.
- Marra, W.A., Kleinhans, M.G. and Addink, E.A., 2014. Network concepts to describe channel importance and change in multichannel systems: test results for the Jamuna River, Bangladesh. *Earth Surface Processes*, **39**, (6), 766-778.
- Martinius, A.W., Fustic, M., Garner, D.L., Jablonski, B.V.J., Strobl, R.S., MacEachern, J.A. and Dashtgard, S.E., 2017. Reservoir characterization and multiscale heterogeneity modelling of inclined heterolithic strata for bitumen-production forecasting, McMurray Formation, Corner, Alberta, Canada. *Marine and Petroleum Geology*, **82**, 336-361.
- McDonough, K.J. and Cross, T.A., 1991. Late Cretaceous sea level from a paleoshoreline. *Journal of Geophysical Research: Solid Earth*, **96**, (B4), 6591-6607.
- McLaurin, B.T. and Steel, R.J., 2007. Architecture and origin of an amalgamated fluvial sheet sand, lower Castlegate Formation, Book Cliffs, Utah. *Sedimentary Geology*, **197**, 291-311.
- Merritts, D.J., Vincent, K.R. and Wohl, E.E., 1994. Long river profiles, tectonism, and eustasy: A guide to interpreting fluvial terraces. *Journal of Geophysical Research: Solid Earth*, **99**, 14031-14050.

- Miall, A.D., 1973. Markov chain analysis applied to an ancient alluvial plain succession. *Sedimentology*, **20**, 347-364.
- Miall, A.D., 1978. Lithofacies types and vertical profile models in braided river deposits: a summary. In: Miall, A.D. (Ed.), *Fluvial Sedimentology*, Canadian Society of Petroleum Geologists, Memoir **5**, 1-47.
- Miall, A.D., 1979. Tertiary fluvial sediments in the Lake Hazen intermontane basin, Ellesmere Island, arctic Canada.
- Miall, A.D., 1981. Alluvial sedimentary basins: tectonic setting and basin architecture. In: Miall, A.D. (Ed.). *Sedimentation and tectonics in alluvial basins*. Geological Association of Canada, Special Paper **21**, pp. 1-33.
- Miall, A.D., 1985. Architectural-element analysis: a new method of facies analysis applied to fluvial deposits. *Earth-Science Reviews*, **22**, (4), pp. 261-308.
- Miall, A.D., 1988a. Architectural elements and bounding surfaces in fluvial deposits: anatomy of the Kayenta Formation (Lower Jurassic), southwest Colorado. *Sedimentary Geology*, **55**, (3-4), 233247-240262.
- Miall, A.D., 1988b. Reservoir heterogeneities in fluvial sandstones: lessons from outcrop studies. *AAPG Bulletin*, **72**, 682–697.
- Miall, A.D., 1991. Hierarchies of architectural units in terrigenous clastic rocks, and their relationship to sedimentation rate. In: Miall, A.D. and Tyler, N. (Eds.) *The three-dimensional facies architecture of terrigenous clastic sediments and its application for hydrocarbon discovery and recovery*. Society of Sedimentary Geology, Special Publication **3**, pp. 6-12.
- Miall, A.D., 1992b. Alluvial Deposits. In: Walker, R.J. and James, N. (Eds.). *Facies Models Response to Sea Level Change*. Geological Association of Canada, Ontario, 119-143.
- Miall, A.D., 1993. The architecture of fluvial-deltaic sequences in the Upper Mesaverde Group (Upper Cretaceous), Book Cliffs, Utah. In: Best, J.L. and Bristow, C.S. (Eds.). *Braided Rivers*, Geological Society of London Special Publications, **75**, pp. 305-332.
- Miall, A.D., 1994. Reconstructing fluvial macroform architecture from two-dimensional outcrops: examples from the Castlegate Sandstone, Book Cliffs, Utah. *J. Sediment. Res.*, **B64** (2). 146-158. <https://doi.org/10.1306/D4267F78-2B26-11D7-8648000102C1865D>
- Miall, A.D., 1996. *The Geology of Fluvial Deposits: Sedimentary Facies, Basin Analysis and Petroleum Geology*. Springer-Verlag, New York.
- Miall, A.D., 2002. Architecture and sequence stratigraphy of Pleistocene fluvial systems in the Malay Basin, based on seismic time-slice analysis. *AAPG Bulletin*, **86**, (7), pp. 1201-1216.
- Miall, A.D., 2008. Sedimentary Basins of the United States and Canada. In: Miall, A.D. (Ed) *The Sedimentary Basins of the World*, Volume 5. Elsevier Science & Technology.

- Miall, A., 2010. *The geology of fluvial deposits: sedimentary facies, basin analysis, and petroleum geology*. Springer, Heidelberg.
- Miall, A.D., 2014. *Fluvial depositional systems*. Springer.
- Miall, A.D., 2016. Facies analysis. In *Stratigraphy: A Modern Synthesis*. Springer, Cham, 77-159.
- Miall, A.D. and Arush, M., 2001. The Castlegate Sandstone of the Book Cliffs, Utah: sequence stratigraphy, paleogeography, and tectonic controls. *Journal of Sedimentary Research*, **71**, (4), 537-548.
- Miall, A.D. and Jones, B.G., 2003. Fluvial architecture of the Hawkesbury sandstone (Triassic), near Sydney, Australia. *Journal of Sedimentary Research*, **73**, (4), 531-545.
- Mikesell, L.R., Weissmann, G.S., Karachewski, J.A., 2010. Stream capture and piracy recorded by provenance in fluvial fan strata. *Geomorphology*, **115**, 267-277.
- Mitten, A.J., Clarke, S.M., Pringle, J.K., Richards, P.C., 2018. 2854396 Combining Terrestrial Photogrammetry, Applied Sedimentology and Hand-Held Gamma Ray Spectrometry to Characterise the Cretaceous Lower Castlegate Formation, Tuscher Canyon, Utah, U.S.A. Search and Discovery, AAPG database.
- Mitten, A.J., Mullins, J., Pringle, J.K., Howell, J., Clarke, S.M., 2020. Depositional conditioning of TIs: improving the reproduction and representation of architectural elements in sand-dominated fluvial reservoir models. *Marine and Petroleum Geology*, **113**, 104156.
- Mohrig, D., Heller, P.L., Paola, C., Lyons, W.J., 2000. Interpreting avulsion process from ancient alluvial sequences: Guadalope-Matarranya system (northern Spain) and Wasatch Formation (western Colorado). *Geological Society of America Bulletin*, **112**, 1787-1803.
- Molenaar, C.M., Rice, D.D. and Sloss, L.L., 1988. Cretaceous rocks of the Western Interior basin. *The Geology of North America*, **2**, 77-82.
- Morad, S., Al-Ramadan, K., Ketzer, J.M. and De Ros, L.F., 2010. The impact of diagenesis on the heterogeneity of sandstone reservoirs: A review of the role of depositional facies and sequence stratigraphy. *AAPG Bulletin*, **94**, (8), 1267-1309.
- Muir, R.O., 1963. Petrography and provenance of the Millstone Grit of Central Scotland. *Transactions of the Edinburgh Geological Society*, **19**, (4), 439-485.
- Mullins, J.R., Nyberg, B., Eide, C., Comunian, Renard, P., Straubhaar, J., Howell, J. 2019. Automated workflows for reservoir modelling, can we get there? AAPG ACE, San Antonio. Search and Discovery.
- Murray, M.R. and Dorobek, S.L., 2004. Sediment Supply, Tectonic Subsidence, and Basin-Filling Patterns Across the Southwestern South China Sea During Pliocene to Recent Time. In: Clift, P., Kuhnt, W., Wang, P. and Hayes, D. (Eds.), *Continent-ocean interactions within East Asian marginal seas*, American Geophysics Union, 235-254.

- Nanson, G.C., 1980. Point bar and floodplain formation of the meandering Beatton River, northeastern British Columbia, Canada. *Sedimentology*, **27**, (1), 3-29.
- Nanson, G.C., Croke, J.C., 1992. A genetic classification of floodplains. *Geomorphology*, **4**, 459-486.
- Nanson, G.C. and Page, K., 1983. Lateral accretion of fine-grained concave benches on meandering rivers. *Modern and ancient fluvial systems*, 133-143.
- Nichols, G. 2009. *Sedimentology and Stratigraphy* (2nd Edition). Chapter 4: Processes of transport and sedimentary structures, 44-68.
- Nichols, G.J., Fisher, J.A., 2007. Processes, facies and architecture of fluvial distributary system deposits. *Sedimentary Geology*, **195**, 75-90.
- Nordahl, K. and Ringrose, P.S., 2008. Identifying the representative elementary volume for permeability in heterolithic deposits using numerical rock models. *Mathematical geosciences*, **40**, (7), 753.
- North, C.P. and Taylor, K.S., 1996. Ephemeral-fluvial deposits: integrated outcrop and simulation studies reveal complexity. *AAPG Bulletin*, **80**, (6), 811-830.
- Obradovich, J.D., 1993. A Cretaceous time scale. In: Caldwell, W.G.E., Kauffman, E.G., (Eds.), *Evolution of the Western Interior Basin*. Geological Association, Canada, Special Paper, **39**, 379–396.
- Olsen, T., Steel, R., Hogseth, K., Skar, T. and Roe, S.L., 1995. Sequential architecture in a fluvial succession: sequence stratigraphy in the Upper Cretaceous Mesaverde Group, Price Canyon, Utah. *Journal of Sedimentary Research*, **65**, (2), 265-280.
- Owen, A., Nichols, G.J., Hartley, A.J., Weissmann, G.S., Scuderi, L.A., 2015. Quantification of a distributive fluvial system: the Salt Wash DFS of the Morrison Formation, SW USA. *Journal of Sedimentary Research*, **85**, 544-561.
- Owen, A., Ebinghaus, A., Hartley, A.J., Santos, M.G. and Weissmann, G.S., 2017. Multi-scale classification of fluvial architecture: An example from the Palaeocene–Eocene Bighorn Basin, Wyoming. *Sedimentology*, **64**, (6), 1572-1596.
- Paola, C. and Borgman, L., 1991. Reconstructing random topography from preserved stratification. *Sedimentology*, **38**, (4), 553-565.
- Pang, M., Nummedal, D., 1995. Flexural subsidence and basement tectonics of the Cretaceous Western Interior basin, United States. *Geology*, **23**, 173-176.
- Paola, C., Straub, K., Mohrig, D. and Reinhardt, L., 2009. The “unreasonable effectiveness” of stratigraphic and geomorphic experiments. *Earth-Science Reviews*, **97**, (1-4), 1-43.
- Pattison, S.A., 2018. Rethinking the Incised-Valley Fill Paradigm For Campanian Book Cliffs Strata, Utah–Colorado, USA: Evidence For Discrete Parasequence-Scale, Shoreface-Incised Channel Fills. *Journal of Sedimentary Research*, **88**, 1381-1412.

- Pattison, S.A., 2019a. High resolution linkage of channel-coastal plain and shallow marine facies belts, Desert Member to Lower Castlegate Sandstone stratigraphic interval, Book Cliffs, Utah-Colorado, USA. *Geological Society of America Bulletin*, **131**, 1643-1672.
- Pattison, S.A., 2019b. Re-evaluating the sedimentology and sequence stratigraphy of classic Book Cliffs outcrops at Tuscher and Thompson canyons, eastern Utah, USA: Applications to correlation, modelling, and prediction in similar nearshore terrestrial to shallow marine subsurface settings worldwide. *Marine and Petroleum Geology*, **102**, 202-230.
- Peeters, J., Busschers, F.S., Stouthamer, E., Bosch, J.H.A., Van den Berg, M.W., Wallinga, J., Versendaal, A.J., Bunnik, F.P.M. and Middelkoop, H., 2016. Sedimentary architecture and chronostratigraphy of a late Quaternary incised-valley fill: a case study of the late Middle and Late Pleistocene Rhine system in the Netherlands. *Quaternary Science Reviews*, **131**, 211-236.
- Perrier, R., Quiblier, J., 1974. Thickness changes in sedimentary layers during compaction history; methods for quantitative evaluation. *AAPG Bulletin*, **58**, 507-520.
- Petit, J.P., Beauchamp, J., 1986. Synsedimentary faulting and palaeocurrent patterns in the Triassic sandstones of the High Atlas (Morocco). *Sedimentology*, **33**, 817-829.
- Pettit, B.S., Blum, M., Pecha, M., McLean, N., Bartschi, N.C., Saylor, J.E. 2019. Detrital-Zircon U-Pb Paleodrainage Reconstruction and Geochronology of the Campanian Blackhawk–Castlegate Succession, Wasatch Plateau and Book Cliffs, Utah, U.S.A. *J. Sediment. Res.*, **89**, 273–292.
- Pickel, A., Frechette, J.D., Comunian, A. and Weissmann, G.S., 2015. Building a TI with Digital Outcrop Models. *Journal of Hydrology*, **531**, 53-61.
- Pitman, W.C., 1978. Relationship between eustacy and stratigraphic sequences of passive margins. *Geological Society of America Bulletin*, **89**, (9), 1389-1403.
- Pitman, J.K., Franczyk, K.J., Anders, D.E., 1987. Marine and nonmarine gas-bearing rocks in Upper Cretaceous Blackhawk and Neslen formations, eastern Uinta Basin, Utah: sedimentology, diagenesis, and source rock potential. *AAPG Bulletin*, **71**, 76-94.
- Posamentier, H., 1988. Eustatic controls on clastic deposition II—sequence and systems tract models. In: Wilgus, C.K., Ross, C.A. and Posamentier, H.W. (Eds.). *Sea Level Changes: An Integrated Approach*, Society of Economic Palaeontologists and Mineralogists, Special Publication **42**, 125-155.
- Posamentier, H., Jervey, M. and Vail, P., 1988. Eustatic controls on clastic deposition I—conceptual framework. In: Wilgus, C.K., Ross, C.A. and Posamentier, H.W. (Eds.). *Sea Level Changes: An Integrated Approach*, Society of Economic Palaeontologists and Mineralogists, Special Publication **42**, 110-124.
- Posamentier, H.W. and Weimer, P., 1993. Siliciclastic sequence stratigraphy and petroleum geology—where to from here?. *AAPG bulletin*, **77**, (5), 731-742.

- Potere, D., 2008. Horizontal positional accuracy of Google Earth's high-resolution imagery archive. *Sensors*, **8**, (12), 7973-7981.
- Pranter, M.J., Ellison, A.I., Cole, R.D., Patterson, P.E., 2007. Analysis and modelling of intermediate-scale reservoir heterogeneity based on a fluvial point-bar outcrop analogy, Williams Fork Formation, Piceance Basin, Colorado. *AAPG Bulletin*, **91**, 1025-1051.
- Priddy, C.L., Pringle, J.K., Clarke, S.M., Pettigrew, R.P., 2019. Application of Photogrammetry to Generate Quantitative Geobody Data in Ephemeral Fluvial Systems. In: Granshaw, S.I. (Ed.) *VGC2018 Special Issue. Photogrammetry Record*, **34**, 428-444.
- Priddy, C.L. and Clarke, S.M., 2020. The sedimentology of an ephemeral fluvial–aeolian succession. *Sedimentology*.
- Pringle, J.K., Howell, J.A., Hodgetts, D., Westerman, A.R., Hodgson, D.M., 2006. Virtual outcrop models of petroleum reservoir analogues: a review of the current state-of-the-art. *First break*, **24**, 33-42.
- Pringle, J.K., Brunt, R.L., Hodgson, D.M. and Flint, S.S. 2010. Capturing stratigraphic and sedimentological complexity in 3D digital outcrop models of submarine channel complexes, Karoo Basin, South Africa. *Petroleum Geoscience*, **16**, (4), 307-330.
- Puig, J.M., Cabello, P., Howell, J. and Arbués, P., 2019. Three-dimensional characterisation of sedimentary heterogeneity and its impact on subsurface flow behaviour through the braided-to-meandering fluvial deposits of the Castissent Formation (late Ypresian, Tremp-Graus Basin, Spain). *Marine and Petroleum Geology*, **103**, 661-680.
- Purkait, B., 2002. Patterns of grain-size distribution in some point bars of the Usri River, India. *Journal of Sedimentary Research*, **72**, (3), 367-375.
- Pyrzcz, M.J. and Deutsch, C.V., 2014. *Geostatistical reservoir modeling*. Oxford university press.
- Ramaekers, P. and Catuneanu, O., 2004. Development and sequences of the Athabasca basin, early Proterozoic, Saskatchewan and Alberta, Canada. In: Eriksson, P.G., Altermann, W., Nelson, D., Mueller, W. and Catuneanu, O. (Eds.). *The Precambrian Earth: Tempos and Events*. *Developments in Precambrian Geology*, **12**, 705-723.
- Rasband, W.S., 2009. ImageJ, US National Institutes of Health, Bethesda, Maryland, USA, <http://rsb.info.nih.gov/ij/>.
- Read, W.A., 1994. High-frequency, glacial—eustatic sequences in early Namurian coal-bearing fluviodeltaic deposits, central Scotland. In: de Boer, P.L., Smith, D.G. (Eds) *Orbital forcing and cyclic sequences*. Blackwell Scientific Oxford. 413-428.
- Read, W.A. and Johnson, S.R.H., 1967. The sedimentology of sandstone formations within the Upper Old Red Sandstone and lowest Calciferous Sandstone Measures west of Stirling, Scotland. *Scottish Journal of Geology*, **3**, (2), 242-267.

- Read, W.A., Browne, M.A.E., Stephenson, D. & Upton, B.J.G. 2002. Carboniferous. *In*: Trewin, N.H. (ed.) *The Geology of Scotland*. 4th Geological Society, London, 251-300.
- Reinfelds I., Nanson G., 1993. Formation of braided river floodplains, Waimakariri River, New Zealand. *Sedimentology*, **40**, 1113-1127.
- Richards, M.T., 1996. Fluvial systems. *In*: Emery, D. and Myers, K. (Eds) *Sequence stratigraphy*, 109-133.
- Ringrose, P. and Bentley, M., 2015. The Property Model. *In* *Reservoir Model Design*. Springer, Dordrecht. 173-231
- Ringrose, P.S., Martinius, A.W. and Alvestad, J., 2008. Multiscale geological reservoir modelling in practice. *In*: Robinson, A., Griffiths, P., Price, S., Hegre, J., and Muggeridge, A., (Eds.) *The Future of Geological Modelling in Hydrocarbon Development*, Geological Society of London, Special Publications, **309**, 123-134.
- Ritchie, J.D., Johnson, H., Browne, M.A.E. and Monaghan, A.A., 2003. Late Devonian–Carboniferous tectonic evolution within the Firth of Forth, Midland Valley; as revealed from 2D seismic reflection data. *Scottish Journal of Geology*, **39**, (2), 121-134.
- Rittersbacher, A., Howell, J.A. and Buckley, S.J., 2014. Analysis of fluvial architecture in the Blackhawk Formation, Wasatch Plateau, Utah, USA, using large 3D photorealistic models. *Journal of Sedimentary Research*, **84**, (2), 72-87.
- Robinson, J.W. and McCabe, P.J., 1997. Sandstone-body and shale-body dimensions in a braided fluvial system: Salt Wash Sandstone Member (Morrison Formation), Garfield County, Utah. *AAPG Bulletin*, **81**, (8), 1267-1291.
- Robinson, R.A., Slingerland, R.L., 1998. Grain-size trends, basin subsidence and sediment supply in the Campanian Castlegate Sandstone and equivalent conglomerates of central Utah. *Basin Research*, **10**, 109-127.
- Ronayne, M.J., Gorelick, S.M., Zheng, C., 2010. Geological modeling of submeter scale heterogeneity and its influence on tracer transport in a fluvial aquifer. *Water Resources Research*, **46**.
- Ross, G.M., Patchett, P.J., Hamilton, M., Heaman, L., DeCelles, P.G., Rosenberg, E. and Giovanni, M.K., 2005. Evolution of the Cordilleran orogen (southwestern Alberta, Canada) inferred from detrital mineral geochronology, geochemistry, and Nd isotopes in the foreland basin. *GSA Bulletin*, **117**, (5-6), 747-763.
- Rust, B.R., 1972. Pebble orientation in fluvial sediments. *Journal of Sedimentary Research*, **42**, (2), 384-388.
- Sahoo, H., Gani, M.R., Hampson, G.J., Gani, N.D. Ranson, A., 2016. Facies-to sandbody-scale heterogeneity in a tight-gas fluvial reservoir analog: Blackhawk Formation, Wasatch Plateau, Utah, USA. *Marine and Petroleum Geology*, **78**, 48-69.

- Salter, T., 1993. Fluvial scour and incision: models for their influence on the development of realistic reservoir geometries. In: North, C.P., Posser, D.J. (Eds.). Characterisation of Fluvial and Aeolian Reservoirs. Geological Society of London Special Publication, **73**, 33-51.
- Sambrook Smith, G.H., Ashworth, P.J., Best, J.L., Woodward, J. and Simpson, C.J., 2006. The sedimentology and alluvial architecture of the sandy braided South Saskatchewan River, Canada. *Sedimentology*, **53**, (2), 413-434.
- Sarker, M.H., Thorne, C.R., Aktar, M.N. and Ferdous, M.R., 2014. Morpho-dynamics of the Brahmaputra–Jamuna River, Bangladesh. *Geomorphology*, **215**, 45-59.
- Schumm, S., 1993. River response to base-level change: implications for sequence stratigraphy. *The Journal of geology*, **101**, 279-294.
- Schumm, S. and Ethridge, F., 1991. The effect of base level change on the fluvial system, *Geological Society of America, Abstracts with Programs*, 170.
- Schumm, S.A., Schumm, S.A., Dumont, J.F., Holbrook, J.M., 2002. Active tectonics and alluvial rivers. Cambridge University Press.
- Seifert, D. and Jensen, J.L., 1999. Using sequential indicator simulation as a tool in reservoir description: issues and uncertainties. *Mathematical Geology*, **31**, (5), 527-550.
- Seifert, D. and Jensen, J.L., 2000. Object and pixel-based reservoir modelling of a braided fluvial reservoir. *Mathematical Geology*, **32**, (5), 581-603.
- Seymour, D.L., Fielding, C.R., 2013. High resolution correlation of the Upper Cretaceous stratigraphy between the Book Cliffs and the western Henry Mountains Syncline, Utah, USA. *Journal of Sedimentary Research*, **83**, 475-494.
- Shanley, K.W. and McCabe, P.J., 1994. Perspectives on the sequence stratigraphy of continental strata. *AAPG Bulletin*, **78**, (4), 544-568.
- Shanley, K.W. and McCabe, P.J., 1998. *Relative role of eustasy, climate, and tectonism in continental rocks*. Society of Sedimentary Geology, Special Publication **58**.
- Skelly, R.L., Bristow, C.S., Ethridge, F.G., 2003. Architecture of channel-belt deposits in an aggrading shallow sandbed braided river: the lower Niobrara River, northeast Nebraska. *Sedimentary Geology*, **158**, 249-270.
- Sloss, L., 1962. Stratigraphic models in exploration. *Journal of Sedimentary Research*, **32**, (3), 415-422.
- Smith, N.D., 1971. Transverse bars and braiding in the lower Platte River, Nebraska. *Geological Society of America Bulletin*, **82**, (12), 3407-3420.
- Southard, J.B., 1971. Representation of bed configurations in depth-velocity-size diagrams. *Journal of Sedimentary Research*, **41**, (4), 903-915.

- Southard, J.B. and Boguchwal, L.A., 1990. Bed configurations in steady unidirectional water flows. Part 2. Synthesis of flume data. *Journal of Sedimentary Research*, **60**, (5), 658-679.
- Stephen, K.D., Clark, J.D. and Gardiner, A.R., 2001. Outcrop-based stochastic modelling of turbidite amalgamation and its effects on hydrocarbon recovery. *Petroleum Geoscience*, **7**, (2), 163-172.
- Storz-Peretz, Y., Laronne, J.B., Surian, N. and Lucía, A., 2016. Flow recession as a driver of the morpho-texture of braided streams. *Earth Surface Processes and Landforms*, **41**, (6), 754-770.
- Stott, D.F., 1984. Cretaceous sequences of the foothills of the Canadian Rocky Mountains.
- Straub, K.M., Paola, C., Mohrig, D., Wolinsky, M.A. and George, T., 2009. Compensational stacking of channelized sedimentary deposits. *Journal of Sedimentary Research*, **79**, (9), 673-688.
- Strebelle, S., 2002. Conditional simulation of complex geological structures using multiple-point statistics. *Mathematical Geology*, **34**, (1), 1-21.
- Strebelle, S.B. and Journel, A.G., 2001, Reservoir modelling using multiple-point statistics. In: SPE Annual Technical Conference and Exhibition. Society of Petroleum Engineers.
- Strebelle, S., and Levy, M., 2008, Using multiple-point statistics to build geologically realistic reservoir models: the MPS/FDM workflow. In: Robinson, A., Griffiths, P., Price, S., Hegre, J., and Muggeridge, A., (Eds.) *The Future of Geological Modelling in Hydrocarbon Development*, Geology Society of London, Special Publications, **309**, 67-74.
- Strebelle, S. and Chevron, E.T.C., 2012. Multiple-point geostatistics: from theory to practice. In: Expanded Abstract Collection from Ninth International Geostatistics Congress. Norwegian Computing Center, 1-65.
- Strebelle, S., Payrazyan, K. and Caers, J., 2002, January. Modeling of a deepwater turbidite reservoir conditional to seismic data using multiple-point geostatistics. In *SPE Annual Technical Conference and Exhibition*. Society of Petroleum Engineers.
- Strebelle, S.B. and Cavelius, C.E., Chevron USA Inc, 2015. System and method for optimizing the number of conditioning data in multiple point statistics simulation. U.S. Patent 9,164,193.
- Sweet, A., Long, D. and Catuneanu, O., 2003. Sequence boundaries in fine-grained terrestrial facies: biostratigraphic time control is key to their recognition. *Geological Association of Canada, Mineralogical Association of Canada joint annual meeting*, May 25-28, 165.
- Sweet, A., Catuneanu, O. and Lerbekmo, J., 2005. Uncoupling the position of sequence-bounding unconformities from lithological criteria in fluvial systems. *American Association of Petroleum Geologists Annual Convention*, June 19-22, A136.

- Syvitski, J.P., Morehead, M.D., Bahr, D.B. and Mulder, T., 2000. Estimating fluvial sediment transport: the rating parameters. *Water resources research*, **36**, (9), 2747-2760.
- Tahmasebi P. (2018) Multiple Point Statistics: A Review. In: Daya Sagar, B., Cheng, Q., Agterberg, F., (Eds.). *Handbook of Mathematical Geosciences*. Springer, Cham.
- Törnqvist, T.E., Bridge, J.S., 2002. Spatial variation of overbank aggradation rate and its influence on avulsion frequency. *Sedimentology*, **49**, 891-905.
- Trower, E.J., Ganti, V., Fischer, W.W. and Lamb, M.P., 2018. Erosional surfaces in the Upper Cretaceous Castlegate Sandstone (Utah, USA): Sequence boundaries or autogenic scour from backwater hydrodynamics? *Geology*, **46**, (8), 707-710.
- Tubino, M., Repetto, R. and Zolezzi, G., 1999. Free bars in rivers. *Journal of Hydraulic Research*, **37**, (6), 759-775.
- Tyler, N., Finley, R.J., 1991. Architectural controls on the recovery of hydrocarbons from sandstone reservoirs. In: Miall, A.D., Tyler, N., (Eds.), *The three-dimensional facies architecture of terrigenous clastics sediments and its implications for hydrocarbon discovery and recovery—SEPM Concepts in Sedimentology and Palaeontology*, 1–5.
- Tyler, K., Henriquez, A. and Svanes, T., 1994. Modeling heterogeneities in fluvial domains: a review of the influence on production profiles. In: Yarus, J.M. and Chambers, R.L. (Eds.) *Stochastic modelling and geostatistics: principles, methods, and case studies*. AAPG Computer Applications in Geology; No. 3.
- Underhill, J.R., Gayer, R.A., Woodcock, N.H., Donnelly, R., Jolley, E.J. and Stimpson, I.G., 1988. The Dent Fault System, northern England—reinterpreted as a major oblique-slip fault zone. *Journal of the Geological Society*, **145**, (2), 303-316.
- Underhill, J.R. and Brodie, J.A., 1993. Structural geology of Easter Ross, Scotland: implications for movement on the Great Glen fault zone. *Journal of the Geological Society*, **150**, (3), 515-527.
- Underhill, J.R., Monaghan, A.A. and Browne, M.A., 2008. Controls on structural styles, basin development and petroleum prospectivity in the Midland Valley of Scotland. *Marine and Petroleum Geology*, **25**, (10), 1000-1022.
- Van de Graaff, F.R., 1972. Fluvial--deltaic facies of the Castlegate Sandstone (Cretaceous), east-central Utah. *Journal of Sedimentary Research*, **42**, (3).
- Van Wagoner, J.C., 1995. Sequence stratigraphy and marine to nonmarine facies architecture of foreland basin strata, Book Cliffs, Utah, USA. In: Van Wagoner, J.C. and Bertram, G.T. (Eds.), *Sequence Stratigraphy of Foreland Basin Deposits*. AAPG Special Volumes M64. Pp. 137-223.
- Van Wagoner, J.C., Mitchum, R., Campion, K. and Rahmanian, V., 1990. Siliciclastic sequence stratigraphy in well logs, cores, and outcrops: concepts for high-resolution correlation of time and facies. *AAPG Methods in Exploration Series*, **7**.

- Veevers, J.T. and Powell, C.M., 1987. Late Paleozoic glacial episodes in Gondwanaland reflected in transgressive-regressive depositional sequences in Euramerica. *Geological Society of America Bulletin*, **98**, (4), 475-487.
- Vevle, M.L., Skorstad, A. and Vonnet, J., 2018. Recent developments in object modelling opens new era for characterization of fluvial reservoirs. *First Break*, **36**, (6), 85-89.
- Viero, D.P., Dubon, S.L. and Lanzoni, S., 2018. Chute cutoffs in meandering rivers: formative mechanisms and hydrodynamic forcing. *Fluvial Meanders and Their Sedimentary Products in the Rock Record*, International Association of Sedimentologists, Special Publications, **48**, 201-230.
- Villamizar, C.A., Hampson, G.J., Flood, Y.S., and Fitch, P.J.R., 2015. Object-based modelling of avulsion-generated sandbody distributions and connectivity in a fluvial reservoir analogue of low to moderate net-to-gross ration, *Petroleum Geoscience*, **21**, 249-270.
- Visser, C.A., Chessa, A.G. 2000. Estimation of length distributions from outcrop datasets – application to the Upper Permian Cutler Formation, Utah. *Petroleum Geoscience*, **6**, 29–36.
- Wakefield, O.J.W., Hough, E., and Peatfield, A.W. 2015. Architectural analysis of a Triassic fluvial system: The Sherwood Sandstone of the East Midlands Shelf, UK. *Sedimentary Geology*, **327**, 1-13.
- Wang, J., Plink-Björklund, P., 2019a. Stratigraphic complexity in fluvial fans: Lower Eocene Green River Formation, Uinta Basin, USA. *Basin Research*, **31**, 892-919.
- Wang, J., Plink-Björklund, P., 2019b. Variable-discharge-river macroforms in the Sunnyside Delta Interval of the Eocene Green River Formation, Uinta Basin, USA. *Sedimentology*.
- Wang, R., Colombera, L. and Mountney, N.P., 2020. Palaeohydrological characteristics and palaeogeographic reconstructions of incised-valley-fill systems: Insights from the Namurian successions of the United Kingdom and Ireland. *Sedimentology*.
- Watkind, I.J., 1995. Geologic Map of the Price 1 x 2 Quadrangle, Utah. Miscellaneous investigations Map I-2462. U.S. Geological Survey.
- Weissmann, G.S., Hartley, A.J., Nichols, G.J., Scuderi, L.A., Olson, M., Buehler, H., Banteah, R., 2010. Fluvial form in modern continental sedimentary basins: distributive fluvial systems. *Geology*, **38**, 39-42.
- Weissmann, G., Hartley, A., Nichols, G., Scuderi, L., Olson, M., Buehler, H. and Massengill, L., 2011. Alluvial facies distributions in continental sedimentary basins—distributive fluvial systems. In: Davidson, S.K., Leleu, S., and North, C.P. (Eds.) *From River to Rock Record*, Society of Sedimentary Geology, Special Publication **97**, 327-355.
- Wells, N.A. and Dorr, J.A., 1987. Shifting of the Kosi river, northern India. *Geology*, **15**, (3), 204-207.

- Wescott, W.A., 1993. Geomorphic thresholds and complex response of fluvial systems--some implications for sequence stratigraphy. *AAPG Bulletin*, **77**, (7), 1208-1218.
- Westoby, M.J., Brasington, J., Glasser, N.F., Hambrey, M.J. and Reynolds, J.M., 2012. 'Structure-from-Motion' photogrammetry: A low-cost, effective tool for geoscience applications. *Geomorphology*, **179**, 300-314.
- Whittaker, A.C., Duller, R.A., Springett, J., Smithells, R.A., Whitchurch, A.L. and Allen, P.A., 2011. Decoding downstream trends in stratigraphic grain size as a function of tectonic subsidence and sediment supply. *AAPG Bulletin*, **123**, (7-8), 1363-1382.
- Williams, G.P., 1970. *Flume width and water depth effects in sediment-transport experiments*. US Government Printing Office.
- Willis, A., 2000. Tectonic control of nested sequence architecture in the Sejo Sandstone, Neslen Formation and upper Castlegate Sandstone (Upper Cretaceous), Sevier foreland basin, Utah, USA. *Sedimentary Geology*, **136**, 277-317.
- Wright, V.P., Marriott, S.B., 1993. The sequence stratigraphy of fluvial depositional systems: the role of floodplain sediment storage. *Sedimentary Geology*, **86**, 203-210.
- Yoshida, S., 2000. Sequence and facies architecture of the upper Blackhawk formation and the lower Castlegate Sandstone (Upper Cretaceous), Book Cliffs, Utah, USA. *Sedimentary Geology*, **136**, (3), 239-276.
- Yoshida, S., Willis, A. and Miall, A.D., 1996. Tectonic control of nested sequence architecture in the Castlegate Sandstone (Upper Cretaceous), Book Cliffs, Utah. *Journal of Sedimentary Research*, **66**, (4), 737-748.
- Yu, L. and Gong, P., 2012. Google Earth as a virtual globe tool for Earth science applications at the global scale: progress and perspectives. *International Journal of Remote Sensing*, **33**, (12), 3966-3986.
- Yue, D., Li, W., Wang, W., Hu, G., Qiao, H., Hu, J., Zhang, M. and Wang, W., 2019. Fused spectral-decomposition seismic attributes and forward seismic modelling to predict sand bodies in meandering fluvial reservoirs. *Marine and Petroleum Geology*, **99**, 27-44.
- Zhang, T., Switzer, P. and Journel, A., 2006. Filter-based classification of TI patterns for spatial simulation. *Mathematical Geology*, **38**, (1), 63-80.
- Zhou, X. and Wang, H., 2015. Application of google earth in modern river sedimentology research. *Journal of Geological and Environmental Protection*, **3**, (08), 1-8.
- Zhou, F., Shields, D., Tyson, S. and Esterle, J., 2018. Comparison of sequential indicator simulation, object modelling and multiple-point statistics in reproducing channel geometries and continuity in 2D with two different spaced conditional datasets. *Journal of Petroleum Science and Engineering*, **166**, 718-730.

Appendix A – Castlegate facies photoplates

The following contains facies photoplates for those facies presented in Table 3.1. These facies comprise the Lower Castlegate Sandstone, Utah.

Facies - Matrix supported conglomerate - Cm



Facies Description

Architecture	Matrix-support, massive, cobble- to pebble-size clasts, fine- to very coarse-sandstone matrix
Texture	Poorly sorted, moderate- to well-rounded, equant sphericity
Colour	Grey to cream matrix, clasts are most commonly grey
Interpretation	Non-Newtonian laminar flow with high sediment load

Key Feature

Matrix supported, large clasts, poorly sorted

Location

Observed in most of the studied locations.

Facies - Trough crossbedded sandstone - St



Facies Description

Architecture	Clast-support, trough crossbedded, fine- to very coarse- sandstone matrix, some pebble sized material lining basal surface
Texture	Poorly sorted, sub- to well-rounded, equant sphericity
Colour	Grey to brown
Interpretation	Migration of subaqueous sinuous bedforms

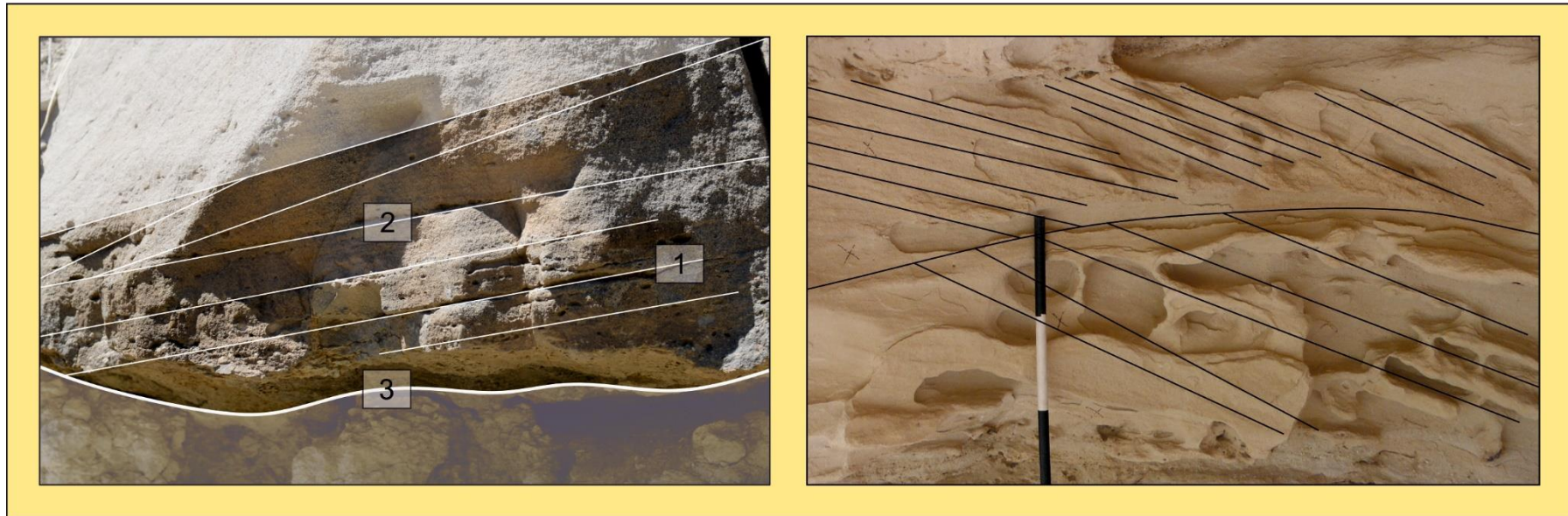
Key Feature

Trough cross bedding, poorly sorted.

Location

Observed in most of the studied locations.

Facies - Planar crossbedded sandstone - Sp



Facies Description

Architecture	Clast-supported, planar crossbedding, fine- to coarse-grained sandstone
Texture	Moderately sorted, sub-rounded to rounded, equant sphericity
Colour	Grey to cream coloured sandstone, forsets are often brown
Interpretation	Migration of two-dimensional subaqueous bedforms

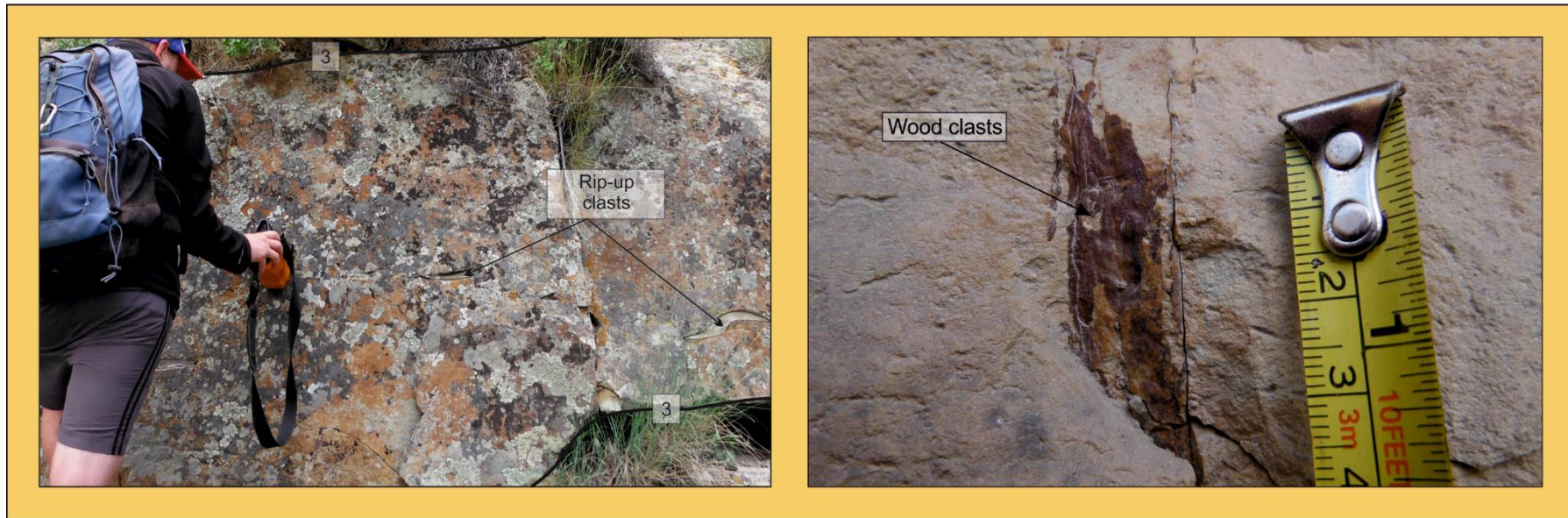
Key Feature

Planar lamination, set and coset stacking

Location

Observed in most of the studied locations.

Facies - Massive sandstone - Sm



Facies Description

Architecture	Clast-support, massive, fine- to very coarse-sandstone, some crude normal grading
Texture	Poorly sorted, sub-angular to well-rounded, equant sphericity
Colour	Brown to yellow
Interpretation	High sediment load newtonian

Key Feature

Massive, darker colour

Location

Observed in most of the studied locations.

Facies - Horizontally bedded sandstones



Facies Description

Architecture	Clast-support, horizontally bedded, fine- to very coarse-grained sandstone
Texture	Poorly sorted, sub- to well-rounded, equant sphericity
Colour	Grey to brown
Interpretation	Plane bed deposition

Key Feature

Horizontal bedding

Location

Observed in most of the studied locations.

Facies - Ripple laminated sandstone - Sr



Facies Description

Architecture	Clast supported, very fine- to fine-grained sandstone, asymmetrical ripples, some crude normal grading
Texture	Sub-rounded, moderate- to well-sorted showing equant sphericity
Colour	Grey to cream, laminations can be a reddish brown, or a very dark brown to black colour
Interpretation	Small asymmetrical ripple migration

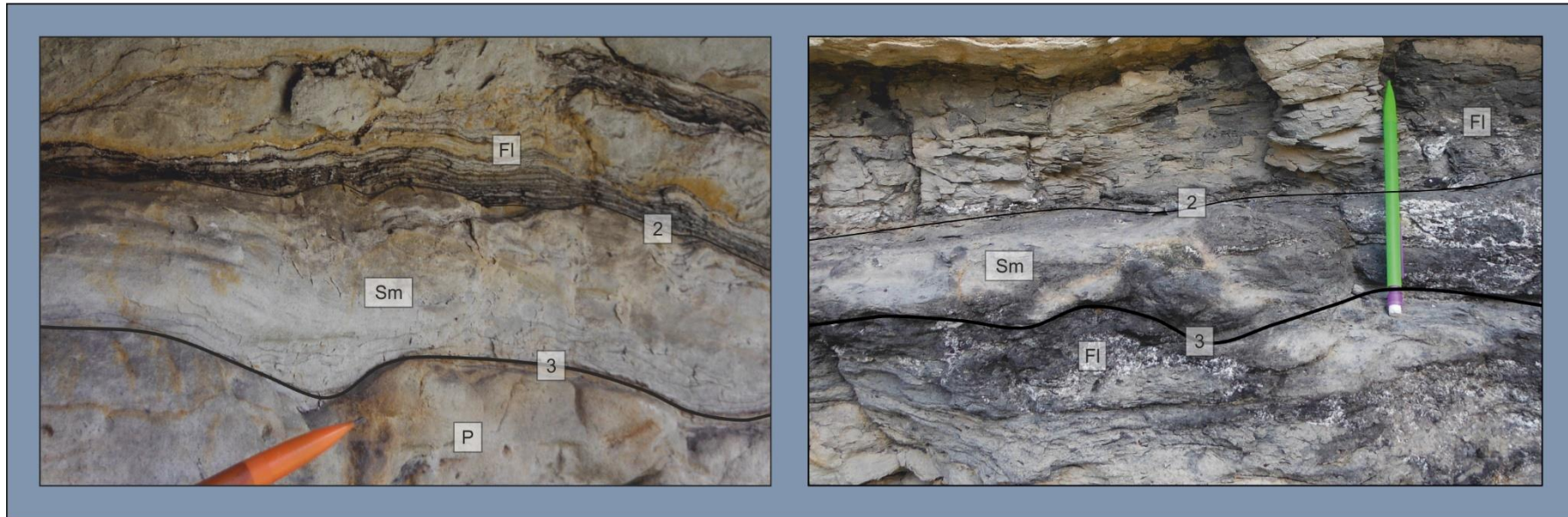
Key Feature

Ripple lamination, thin beds

Location

Observed in most of the studied locations.

Facies - Fine material - FI/Fm



Facies Description

Architecture	Fine silt to mudstones, planar laminated or massive, some minor rooting
Texture	Well to moderately sorted
Colour	Dark grey to brown
Interpretation	Suspension settling followed by sub-areial exposure

Key Feature

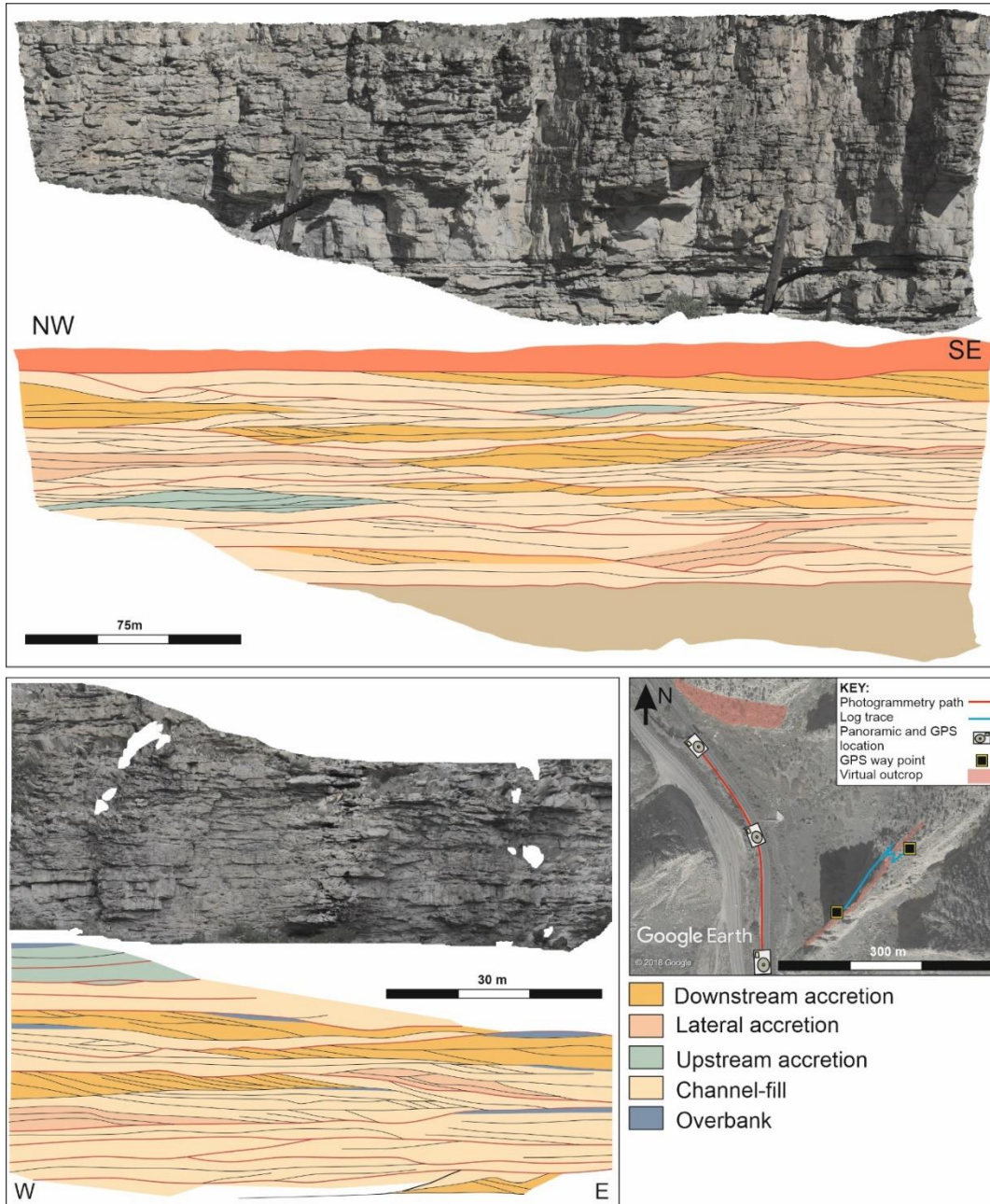
Dark colour, fine grain, low competency

Location

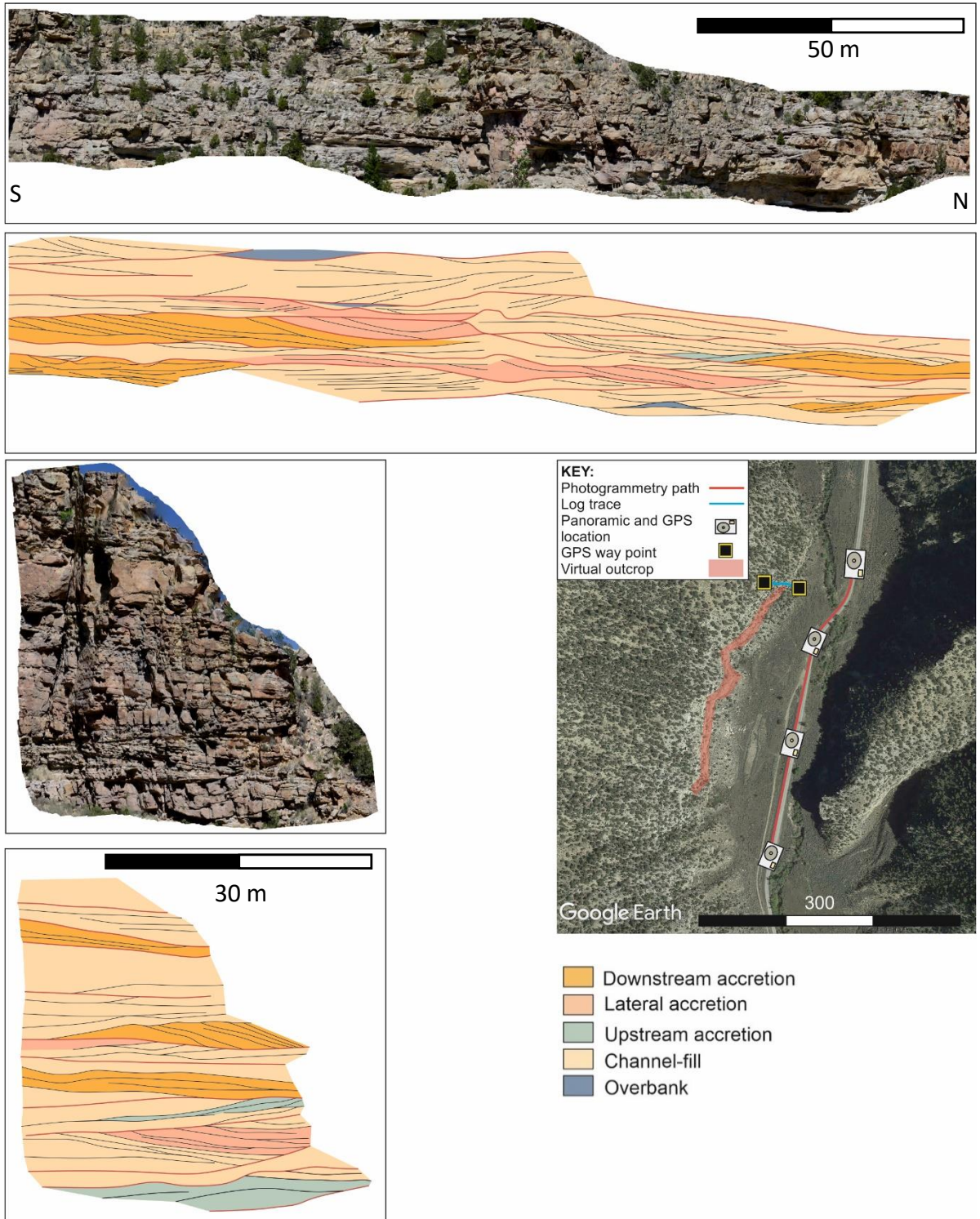
Observed at the type locality, Horse Canyon, Nine-mile canyon and Gray Canyon

Appendix B – Castlegate bounding surface analysis

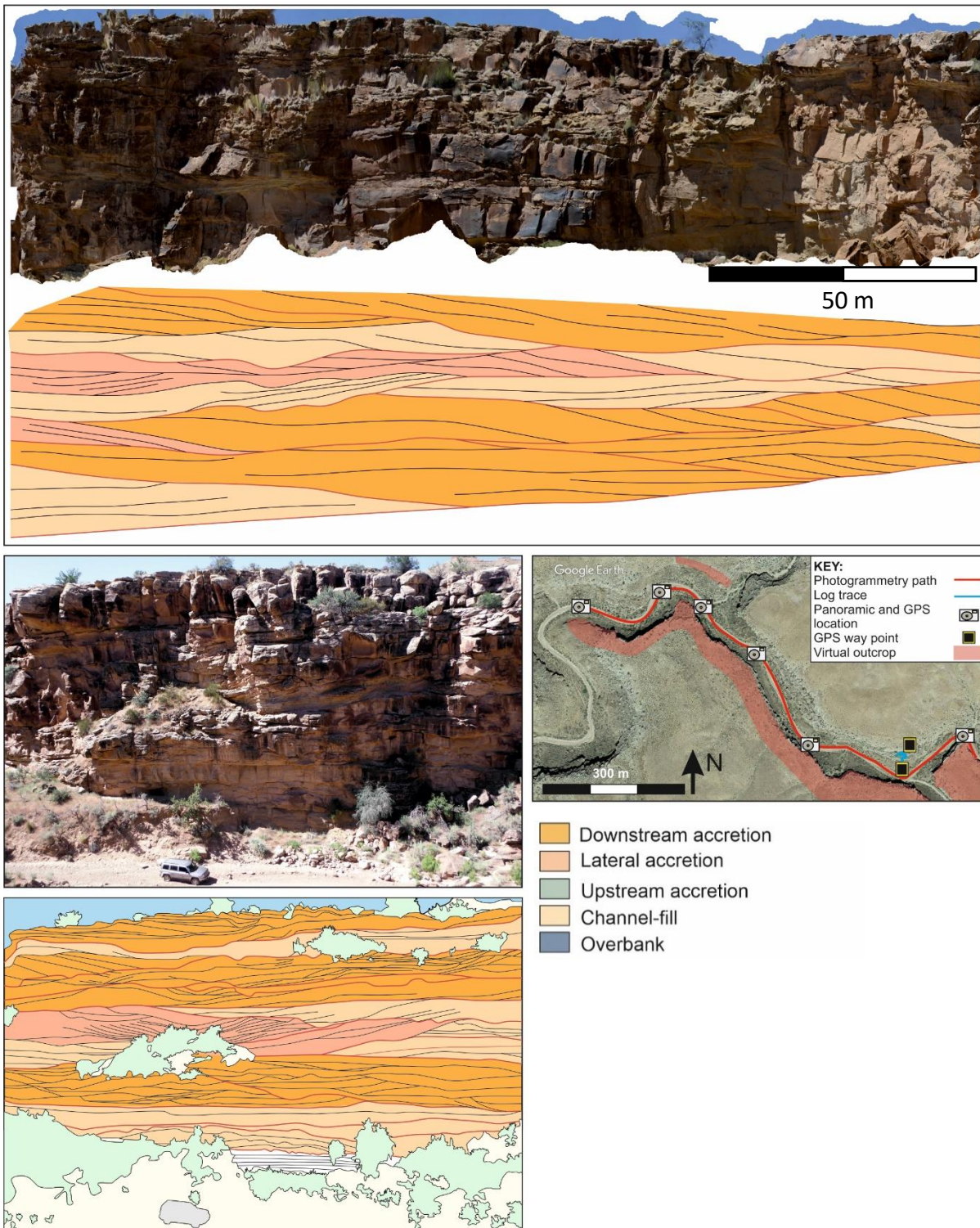
B.1 - Castle Gate



B.2 - Sunnyside

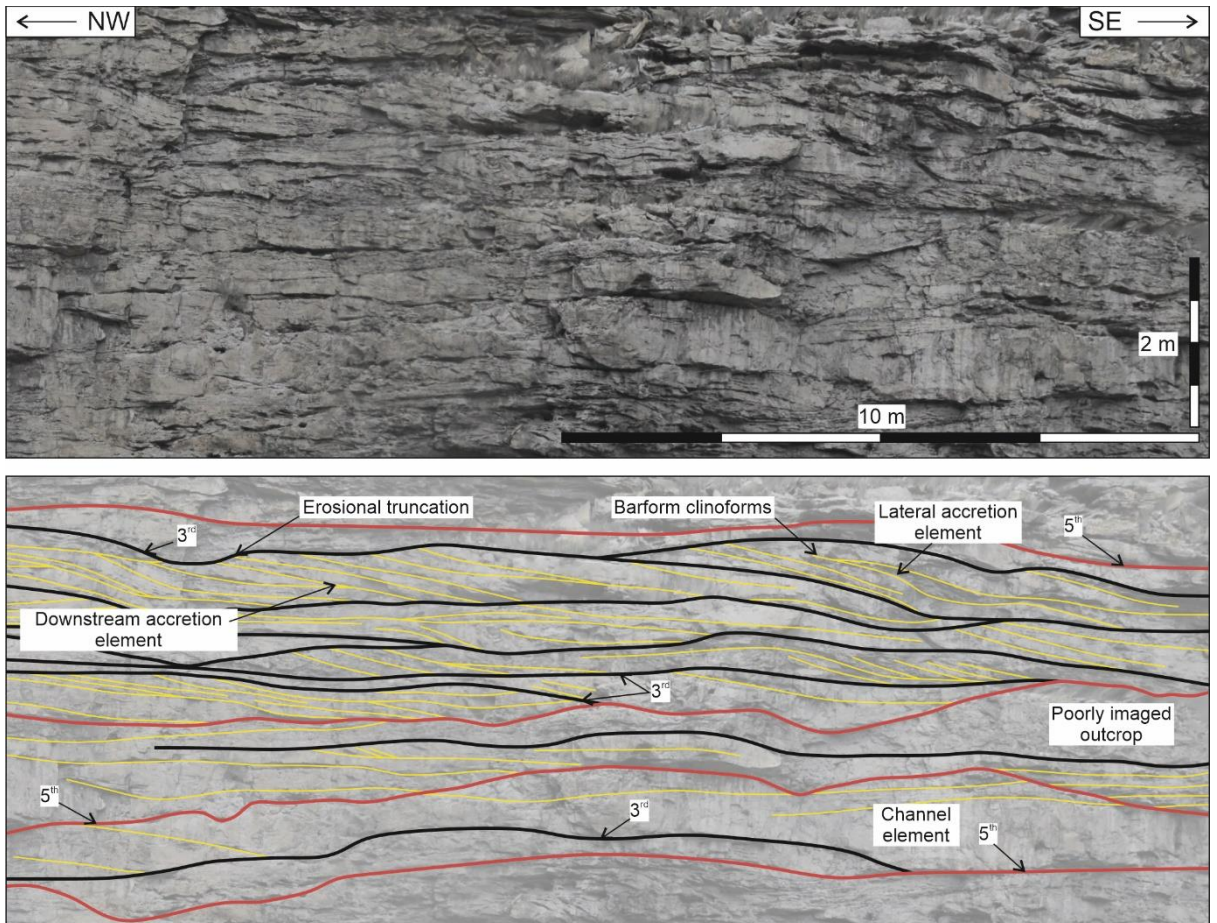


B.3 - Tuscher Canyon



Appendix C – High Resolution bounding surface analysis

C.1 - Bounding surface hierarchy and erosional surfaces – Castle Gate North



C.2 – Bounding surface analysis of the Main Tuscher Canyon Outcrop

